

AD723351

Bulletin 41
(Part 6 of 7 Parts)

THE SHOCK AND VIBRATION BULLETIN

Part 6
Dynamics, Dynamic Stress Analysis

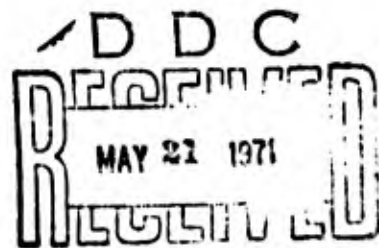
DECEMBER 1970

A Publication of
THE SHOCK AND VIBRATION
INFORMATION CENTER
Naval Research Laboratory, Washington, D.C.



Reproduced by
NATIONAL TECHNICAL
INFORMATION SERVICE
Springfield, Va 22151

Office of
The Director of Defense
Research and Engineering



This document has been approved for public release and sale; its distribution is unlimited.

243

ADDITION BY	
WPS	WHITE SECTION <input checked="" type="checkbox"/>
DS	DIFF SECTION <input type="checkbox"/>
UNANNOUNCED	<input type="checkbox"/>
JUSTIFICATION	
BY	
DISTRIBUTION/AVAILABILITY CODES	
DIST.	AVAIL. and/or SPECIAL
A	21

SYMPOSIUM MANAGEMENT

THE SHOCK AND VIBRATION INFORMATION CENTER

William W. Mutch, Director
 Henry C. Pusey, Coordinator
 Rudolph H. Volin, Coordinator
 Edward H. Schell, Coordinator
 Katherine G. Jahnel, Clerk Typist

Bulletin Production

Graphic Arts Branch, Technical Information Division,
 Naval Research Laboratory

Bulletin 41
(Part 6 of 7 Parts)

THE SHOCK AND VIBRATION BULLETIN

DECEMBER 1970

**A Publication of
THE SHOCK AND VIBRATION
INFORMATION CENTER
Naval Research Laboratory, Washington, D.C.**

The 41st Symposium on Shock and Vibration was held at the Air Force Academy, Air Force Academy, Colorado, on 27-29 October 1970. The U.S. Air Force was host.

**Office of
The Director of Defense
Research and Engineering**

CONTENTS

PAPERS APPEARING IN PART 6

Dynamics

PARAMETRIC RESPONSE OF MONOSYMMETRIC IMPERFECT THIN-WALLED COLUMNS UNDER SINUSOIDAL LOADING	1
Stanley G. Ebner, USAF Academy, Colorado and Martin L. Moody, University of Colorado, Denver, Colorado	
PREDICTION OF UPSTAGE RANDOM VIBRATION ENVIRONMENT USING A STATISTICAL ENERGY APPROACH	9
D. E. Hines, G. R. Parker, and R. D. Hellweg, McDonnell Douglas Astronautics Company- West, Santa Monica, California	
ON THE REDUCTION AND PREVENTION OF THE FLUID-INDUCED VIBRATIONS OF CIRCULAR CYLINDERS OF FINITE LENGTH.	31
Dirse W. Sallet, Department of Mechanical Engineering, University of Maryland, College Park, Maryland and U.S. Naval Ordnance Laboratory, White Oak, Silver Spring, Maryland	
EFFECTS OF LOOSENESS ON DYNAMIC BEHAVIOR.	39
R. E. Beckett, K. C. Pan, U.S. Army Weapons Command, Rock Island, Illinois and D. D. Penrod, The University of Iowa, Iowa City, Iowa	
DYNAMIC DEFLECTIONS OF MULTIPLE-SPAN GUIDEWAYS UNDER HIGH SPEED, AIR CUSHION VEHICLES.	47
James F. Wilson, Duke University, Durham, North Carolina	
ANALYSIS OF THE MOTION OF A LONG WIRE TOWED FROM AN ORBITING AIRCRAFT	61
S. A. Crist, Department of Engineering Mechanics, USAF Academy, Colorado	
A POSTSHOT STUDY OF THE DYNAMIC RESPONSE OF THE LASL MOBILE TOWER DURING THE PLIERS EVENT	75
R. E. Bachman, E. F. Smith, Holmes and Narver, Inc., Las Vegas, Nevada and R. P. Kennedy, Holmes and Narver, Inc., Los Angeles, California	
BOUNDS FOR THE RESPONSE OF A CONSERVATIVE SYSTEM UNDER DYNAMIC LOADING.	87
H. Brauchli, The University of Alabama in Huntsville, Huntsville, Alabama	
THREE DEGREE OF FREEDOM SPRING MASS EJECTION SYSTEM	93
R. Muskat, Aerospace Corporation, San Bernardino, California	
STRUCTURAL DYNAMICS OF A PARABOLOIDAL ANTENNA	103
Myron L. Gossard and William B. Halle, Jr., Lockheed Missiles and Space Company, Sunnyvale, California	
AN APPLICATION OF COMPONENT MODE SYNTHESIS TO ROCKET MOTOR VIBRATION ANALYSIS	115
F. R. Jensen, Hercules Inc., and H. N. Christiansen, Brigham Young University	

COMPARISON OF CONSISTENT AND LUMPED MASS MATRIX SOLUTIONS WITH THE EXACT SOLUTION FOR A SIMPLY-SUPPORTED TIMOSHENKO BEAM	123
C. Baum, J. T. Higney, Gibbs and Cox, Inc., New York, New York and A. Jenks, Esso International Inc., New York, New York	
APPLICATION OF APPROXIMATE TRANSMISSION MATRICES TO DESCRIBE TRANSVERSE BEAM VIBRATIONS	133
R. D. Rocke and Ranjit Roy, University of Missouri-Rolla, Rolla, Missouri	
MEASUREMENT OF MOMENT-CURVATURE RELATIONSHIP FOR STEEL BEAMS.	147
V. H. Neubert and W. Vogel, The Pennsylvania State University, University Park, Pennsylvania	
SELF-SYNCHRONIZATION OF TWO ECCENTRIC ROTORS ON A BODY IN PLANE MOTION.	159
Mario Paz, Associate Professor, University of Louisville, Louisville, Kentucky	
PROPAGATION OF THE ERROR IN COMPUTED FREQUENCIES AND MODE SHAPES RESULTING FROM A DISCRETE MASS REPRESENTATION OF UNIFORM, SLENDER BEAMS WITH VARYING HEIGHT-TO-LENGTH RATIOS	163
Francis M. Henderson, Naval Ship Research and Development Center, Washington, D. C.	

Dynamic Stress Analysis

A DISCUSSION ON THE ANALYTICAL DYNAMICS, STRESS, AND DESIGN INTERFACES	179
Irvin P. Vatz, Teledyne Brown Engineering, Huntsville, Alabama	
DYNAMIC STRESS ANALYSIS IN A STRATIFIED MEDIUM	187
Jackson C.S. Yang, Ames Research Center, NASA, Moffett Field, California	
COMPARISON OF STRUCTURAL LOADS: STATIC VERSUS DYNAMIC	197
Paul J. Jones and William J. Kacena, III, Martin Marietta Corporation, Denver, Colorado	
EGGSHELLING AND VIBRATIONS OF A HIGH SPEED SHAFT WITH NASTRAN ANALYSIS.	203
Dennis J. Martin and William C. Walton, Jr., NASA Langley Research Center, Hampton, Virginia	
PARAMETRIC STUDY OF A BEAM WITH A COMPOUND SIDE-BRANCH RESONATOR AS A DEVICE TO EVALUATE PRELIMINARY DESIGN LOADS	211
J. Roger Ravenscraft, Teledyne Brown Engineering, Huntsville, Alabama	
RAIL LAUNCHING DYNAMICS OF THE SAM-D SURFACE-TO-AIR MISSILE	219
Martin Wohltmann, Leonard A. Van Gulick, H. Carlton Sutphin, Martin Marietta Corporation, Orlando, Florida	

PAPERS APPEARING IN PART 1 Part 1 - Classified (Unclassified Titles)

CASC (CAPTIVE AIR SPACE CRAFT) - A POSSIBLE CONCEPT FOR RIVERINE BOAT DESIGN
V. H. Van Bibber, Naval Ship Research and Development Laboratory, Panama City, Florida, and N. Elmore, Naval Ship Research and Development Center, Portsmouth, Va.

PROBLEMS OF DAMPING THE WINDOW AREAS OF SONAR DOMES

Howard N. Phelps, Jr., Naval Underwater Systems Center, New London, Connecticut

APPLICATION OF THE FINITE ELEMENT METHOD TO THE SHOCK ANALYSIS OF SONAR TRANSDUCERS

Vincent D. Godino and George A. Ziegler, General Dynamics/Electric Boat Division, Groton, Connecticut

DYNAMIC RESPONSE OF ABOVE-GROUND TARGETS TO A BLAST WAVE

P. N. Mathur, D. M. Rogers, R. H. Lee, and J. W. Murdock, The Aerospace Corporation, San Bernardino, California

PAPERS APPEARING IN PART 2

Keynote Talk

THE DYNAMIC CENTURY

D. Zonars, Air Force Dynamics Laboratory, Wright-Patterson Air Force Base, Ohio

Physiological Effects

TESTING AND MODELING STANDING MAN'S RESPONSE TO IMPACT

Joseph Gesswein and Paul Corrao, Naval Ship Research and Development Center, Washington, D.C.

EQUAL ANNOYANCE CONTOURS FOR THE EFFECT OF SINUSOIDAL VIBRATION ON MAN

C. Ashley, Mechanical Engineering Department, University of Birmingham, England

Isolation

ISOLATION FROM MECHANICAL SHOCK WITH A MOUNTING SYSTEM HAVING NONLINEAR DUAL-PHASE DAMPING

J. C. Snowdon, Ordnance Research Laboratory, The Pennsylvania State University, University Park, Pennsylvania

INTERACTIVE OPTIMAL DESIGN OF SHOCK ISOLATION SYSTEMS

W. D. Pilkey, University of Virginia, Charlottesville, Virginia

DESIGN OF HIGH-PERFORMANCE SHOCK ISOLATION SYSTEMS

Ronald L. Eshleman, IIT Research Institute, Chicago, Illinois

ELASTIC WAVE PROPAGATION IN A HELICAL COIL WITH VARYING CURVATURE AND ITS APPLICATION AS AN IMPACT LOAD DISPERSER

Nam P. Suh, Department of Mechanical Engineering, Massachusetts Institute of Technology, Cambridge, Massachusetts

ANALYSIS OF THE INVERTING TUBE ENERGY ABSORBER

J. M. Alcone, Sandia Laboratories, Livermore, California

THE EFFECTS OF PAYLOAD PENETRATION AND VARIOUS ANALYTICAL MODELS ON THE DESIGN OF A SPHERICAL CRUSHABLE CASING FOR LANDING ENERGY ABSORPTION

Robert W. Warner and Margaret Covert, NASA Ames Research Center

Damping

EFFECT OF FREE LAYER DAMPING ON RESPONSE OF STIFFENED PLATE STRUCTURES

David I. G. Jones, Air Force Materials Laboratory, Wright-Patterson AFB, O

- VIBRATION CONTROL BY A MULTIPLE-LAYERED DAMPING TREATMENT**
A. D. Nashif, University of Dayton Research Institute, Dayton, Ohio and T. Nicholas,
Air Force Materials Laboratory, Wright-Patterson Air Force Base, Ohio
- DETERMINATION OF DAMPING PROPERTIES OF SOFT VISCOELASTIC MATERIALS**
Fakhruddin Abdulhadi, IBM General Systems Division, Rochester, Minnesota
- IMPROVING RELIABILITY AND ELIMINATING MAINTENANCE WITH ELASTOMERIC DAMPERS FOR ROTOR SYSTEMS**
J. L. Potter, Lord Manufacturing Company, Erie, Pennsylvania
- EFFECT OF HIGH POLYMER ADDITIVES ON DIFFUSER FLOW NOISE**
B. M. Ishino, California State College, Fullerton, California and R. C. Binder,
University of Southern California, Los Angeles, California
- HAWK SUSPENSION SYSTEM PERFORMANCE ON M754 TRACKED VEHICLE**
Paul V. Roberts, Raytheon Company, Missile Systems Division, Bedford, Massachusetts

PAPERS APPEARING IN PART 3

Instrumentation

- A PRACTICAL APPLICATION OF ACCELEROMETER CALIBRATIONS**
R. R. Bouche, Endevco, Dynamic Instrument Division, Pasadena, California
- DESIGNING AN INSTRUMENTED TEST EGG FOR DETECTING IMPACT BREAKAGE**
William L. Shupe, USDA, Agricultural Research Service, Transportation and Facilities
Research Div., University of California, Davis, California and Robert M. Lake, Mayo
Clinic, Rochester, Minnesota
- AN ACCELEROMETER DESIGN USING FERROFLUID ULTRASONIC INTERFEROMETRY**
Jack G. Parks, U.S. Army Tank-Automotive Command, Warren, Michigan
- HYBRID TECHNIQUES FOR MODAL SURVEY CONTROL AND DATA APPRAISAL**
Robert A. Salyer, TRW Systems, Inc., Redondo Beach, California
- OBJECTIVE CRITERIA FOR COMPARISON OF RANDOM VIBRATION ENVIRONMENTS**
F. F. Kazmierczak, Lockheed Missiles and Space Company, Sunnyvale, California
- THE APPLICATION OF ANALOG TECHNIQUES TO REAL TIME ANALYSIS AND SCREENING OF DYNAMIC DATA**
Roger C. Crites, McDonnell Aircraft Co., St. Louis, Mo.
- SHOCK LOADING AND HOLOGRAPHIC INTERFEROMETRY IN NDT**
R. L. Johnson, R. Aprahamian and P. G. Bhuta, TRW Systems Group,
Redondo Beach, California

Data Analysis

- A NEW SYNTHESIS TECHNIQUE FOR SHOCK SPECTRUM ANALYSIS**
William G. Pollard, Spectral Dynamics Corporation of San Diego, San Diego, California
- THE ROLE OF LATENT INFORMATION IN INFORMATION PROCESSING IN MEASURING SYSTEMS**
Peter K. Stein, Arizona State University, Tempe, Arizona

Test Facilities

USBR VIBRATION TEST SYSTEM

R. M. McCafferty, U.S. Bureau of Reclamation, Denver, Colorado

MULTI-DEGREE OF FREEDOM MOTION SIMULATOR SYSTEMS FOR TRANSPORTATION ENVIRONMENTS.

T. K. DeClue, R. A. Arone and C. E. Deckard, Wyle Laboratories, Huntsville, Alabama

DESIGN AND FABRICATION OF AN AIRCRAFT SEAT CRASH SIMULATOR

Nelson M. Isada, State University of New York at Buffalo, Buffalo, New York

DESCRIPTION OF A SHOCK AND VIBRATION DISPLACEMENT AMPLIFIER

D. Cerasuolo and J. Chin, Raytheon Company, Sudbury, Massachusetts

ARTILLERY SIMULATOR FOR FUZE EVALUATION

H. D. Curchack, Harry Diamond Laboratories, Washington, D.C.

GAS SPRING FIRING AND THE SOFT RECOVERY OF A HARD-WIRE INSTRUMENTED 155 MM PROJECTILE

S. L. Fluent, Heat, Plasma, Climatic, Towers Division, Sandia Laboratories, Albuquerque, New Mexico

FULL-SCALE RECOIL MECHANISM SIMULATOR (FORCED FLUID FLOW THROUGH A CONCENTRIC ORIFICE)

W. J. Courtney, IIT Research Institute, Chicago, Illinois and R. Rossmiller and R. Reade, U.S. Army Weapons Command, Rock Island, Illinois

ISOTOPE FUEL IMPACT FACILITY

Larry O. Seamons, Sandia Laboratories, Albuquerque, New Mexico

A REVERBERATION CHAMBER FOR USE AT REDUCED PRESSURES

M. H. Hieken, J. N. Olson, and G. W. Olmsted, McDonnell Aircraft Company, St. Louis, Missouri

DESIGN OF AN OFF-ROAD VEHICLE MOTION SIMULATOR

Nelson M. Isada, Cornell Aeronautical Laboratory, Inc., and State University of New York at Buffalo, Buffalo, New York and Robert C. Sugarman, and E. Donald Sussman, Cornell Aeronautical Laboratory, Inc., Buffalo, New York

AN AERIAL CABLE TEST FACILITY USING ROCKET POWER

C. G. Coalson, Sandia Laboratories, Albuquerque, New Mexico

PAPERS APPEARING IN PART 4

Vibration

SURVEY OF SPACE VEHICLE VIBRATION ANALYSIS AND TEST TECHNIQUES

W. Henricks, R. J. Herzberg, B. G. Wrenn, Lockheed Missiles and Space Company, Sunnyvale, California

METHODS USED TO REALISTICALLY SIMULATE VIBRATION ENVIRONMENTS

J. V. Otts, Centrifuge, Vibration, and Acoustics Division, Sandia Laboratories, Albuquerque, New Mexico

SIMULATION OF COMPLEX-WAVE PERIODIC VIBRATION

A. J. Curtis, H. T. Abstein, Jr., and N. G. Tinling, Hughes Aircraft Company, Culver City, California

RATIONAL ES APPLYING TO VIBRATION FOR MAINTENANCE

A. H. Grundy, Canadian Forces Headquarters, Ottawa, Canada

**SPECIFICATION OF SINE VIBRATION TEST LEVELS USING A FORCE-ACCELERATION
PRODUCT TECHNIQUE**

A. F. Witte, Vibration and Acoustics Test Division, Sandia Laboratories,
Albuquerque, New Mexico

**SOME EFFECTS OF EQUALIZATION WITH A SINGLE MASS VS AN ELASTIC
SYSTEM ON ACCELERATIONS AND STRESSES**

R. M. Mains, Washington University

**A METHOD FOR PREDICTING STRUCTURAL RESPONSES FROM LOWER LEVEL
ACOUSTIC TESTS**

D. O. Smallwood, Centrifuge, Vibration, Acoustics Division, Sandia Laboratories,
Albuquerque, New Mexico

SWEEP SPEED EFFECTS IN RESONANT SYSTEMS

Ronald V. Trull, USAF, 4750th Test Squadron, Tyndall AFB, Florida

**THE DYNAMIC RESPONSE OF A STEEL EYEBAR CHAIN SUSPENSION BRIDGE
OVER THE OHIO RIVER TO VARIOUS EXCITATIONS**

R. F. Varney, J. G. Viner, Federal Highway Administration, Department of
Transportation, Washington, D.C.

**DUAL SPECIFICATIONS IN RANDOM VIBRATION TESTING, AN APPLICATION
OF MECHANICAL IMPEDANCE**

A. F. Witte, Vibration and Acoustics Test Division, Sandia Laboratories, Albuquerque,
New Mexico and R. Rodeman, Applied Mechanics Division, Sandia Laboratories,
Albuquerque, New Mexico

VIBRATION — A DIAGNOSTIC TOOL FOR SHOCK DESIGN

Culver J. Floyd, Raytheon Company, Submarine Signal Division, Portsmouth,
Rhode Island

**THE RESONANT RESPONSE OF A MECHANICAL SYSTEM SUBJECTED TO
LOGARITHMICALLY SWEPT AND NOTCHED BASE EXCITATION, USING
ASYMPTOTIC EXPANSION**

B. N. Agrawal, COMSAT Laboratories, Clarksburg, Maryland

**EFFECTS OF FLIGHT CONDITIONS UPON GUNFIRE INDUCED VIBRATION
ENVIRONMENT**

J. A. Hutchinson and B. G. Musson, LTV Aerospace Corporation, Vought Aeronautics
Division, Dallas, Texas

THE BOX CAR DYNAMIC ENVIRONMENT

Robert W. Luebke, C and O/B and O Railroad Companies, Baltimore, Maryland

THE NOISE ENVIRONMENT OF A DEFLECTED-JET VTOL AIRCRAFT

S. L. McFarland and D. L. Smith, Air Force Flight Dynamics Laboratory, Wright-
Patterson Air Force Base, Ohio

VIBRATION SIGNATURE ANALYSIS OF BEARINGS AND ELECTRONIC PACKAGES

Charles H. Roos, General Electric Company, Aerospace Electronic Systems,
Utica, New York

OUTER LOOP CONTROL FOR VIBRATION TESTING

Gordon Lester, Perkin-Elmer Corporation, Danbury, Connecticut and James Gay Helmuth,
Chadwick-Helmuth Company, Inc., Monrovia, California

EMPIRICAL PREDICTION OF MISSILE FLIGHT RANDOM VIBRATION

A. E. Kartman, The Bendix Corporation, Mishawaka, Indiana

STRUCTURAL VIBRATIONS IN THE BELL AH-1G HELICOPTER DURING WEAPON FIRING

R. Holland, Kinetic Systems, Inc., Boston, Massachusetts and D. Marcus and J. Wiland, U.S. Army Frankford Arsenal, Philadelphia, Pennsylvania

CHARACTERISTICS OF GUNFIRE INDUCED VIBRATION IN HELICOPTERS

C. E. Thomas and V. C. McIntosh, Air Force Flight Dynamics Laboratory, Wright-Patterson Air Force Base, Ohio

INFLIGHT VIBRATION AND NOISE STUDY OF THREE HELICOPTERS

Phyllis G. Bolds and John T. Ach, Air Force Flight Dynamics Laboratory, Wright-Patterson Air Force Base, Ohio

PAPERS APPEARING IN PART 5

Shock

A DISCUSSION OF PYROTECHNIC SHOCK CRITERIA

M. B. McGrath, Martin Marietta Corporation, Denver, Colorado

A SUMMARY OF PYROTECHNIC SHOCK IN THE AEROSPACE INDUSTRY

W. P. Rader, Martin Marietta Corporation, Denver, Colorado and William F. Bangs, Goddard Space Flight Center, Greenbelt, Maryland

MEASURES OF BLAST WAVE DAMAGE POTENTIAL

C. T. Morrow, LTV Research Center, Western Division, Anaheim, California

SHOCK RESPONSE OF A BILINEAR, HYSTERETIC BEAM AND SUPPORT SYSTEM

Bruce E. Burton, Ohio Northern University and Robert S. Ayre, University of Colorado, Boulder, Colorado

DIGITAL FOURIER ANALYSIS OF MECHANICAL SHOCK DATA

H. A. Gaberson, and D. Pal, Naval Civil Engineering Laboratory, Port Hueneme, California

THE COMPUTER DETERMINATION OF MECHANICAL IMPEDANCE FOR SMALL ARMS FROM THE RESPONSE TO RECOIL

L. B. Gardner, R. K. Young, and D. E. Frericks, U.S. Army Weapons Command, Rock Island, Illinois

SHOCK PULSE SHAPING USING DROP TEST TECHNIQUES

R. E. Keeffe and E. A. Bathke, Kaman Sciences Corporation, Colorado Springs, Colorado

ANALYSIS OF PROJECTILE IMPACT ON COMPOSITE ARMOR

Richard A. Fine, IBM Corporation, Rochester, Minnesota and Raymond R. Hagglund, Worcester Polytechnic Institute, Worcester, Massachusetts

A SYSTEMATIC APPROACH TO SHOCK HARDENING

J. L. Lipeles, Littleton Research and Engineering Corporation, Littleton, Massachusetts and D. Hoffman, Naval Ammunition Depot, Crane, Indiana

THE DEVELOPMENT OF SHOCK TEST CRITERIA FOR AIRCRAFT DISPENSER WEAPON EJECTION MECHANISMS

K. D. Denton, K. A. Herzing, and S. N. Schwantes, Honeywell, Inc., Ordnance Division, Hopkins, Minnesota

**SHOCK LOAD RESPONSE OF AN ELASTIC ANNULAR PLATE ON A
DISTRIBUTED FOUNDATION**

John R. Mays, Department of Civil and Environmental Engineering, University of
Colorado, Denver, Colorado and James E. Nelson, Space Systems Dynamics, Martin
Marietta Corporation, Denver, Colorado

Fragility

METHODOLOGY AND STANDARDIZATION FOR FRAGILITY EVALUATION

R. C. Rountree, Logicon, San Pedro, California and F. B. Safford, TRW Systems Group,
Redondo Beach, California

**CONTROLLING PARAMETERS FOR THE STRUCTURAL FRAGILITY OF LARGE
SHOCK ISOLATION SYSTEMS**

Robert J. Port, Air Force Weapons Laboratory, Kirtland Air Force Base, New Mexico

HARDNESS EVALUATION

W. H. Rowan, TRW Systems Group, Redondo Beach, California

INITIAL DESIGN CONSIDERING STATISTICAL FRAGILITY ASSESSMENT

R. L. Grant, the Boeing Company, Seattle, Washington

TRANSIENT PULSE DEVELOPMENT

J. Crum and R. L. Grant, The Boeing Company, Seattle, Washington

FRAGILITY TESTING FOR HYDRAULIC SURGE EFFECTS

D. M. Eckblad, The Boeing Company, Seattle, Washington and W. L. Hedrick, TRW
Systems Group, Redondo Beach, California

PAPERS APPEARING IN PART 7

Mathematical Analysis

**ROCKET-SLED MODEL STUDY OF PREDICTION TECHNIQUES FOR FLUCTUATING
PRESSURES AND PANEL RESPONSE**

Eric E. Ungar, Bolt Beranek and Newman Inc., Cambridge, Massachusetts

DETERMINATION OF STRUCTURAL PROPERTIES FROM TEST DATA

A. E. Galef and D. L. Cronin, TRW Systems Group, Redondo Beach, California

**VALIDITY OF MATHEMATICAL MODELS OF DYNAMIC RESPONSE OF STRUCTURES
TO TRANSIENT LOADS**

Willfred E. Baker, Southwest Research Institute, San Antonio, Texas

DYNAMIC RESPONSE OF PLATES WITH CUT-OUTS

Nicholas L. Basdekas, Office of Naval Research, Arlington, Virginia and
Michael Chi, Catholic University of America, Washington, D. C.

**NATURAL FREQUENCIES AND MODE SHAPES OF PLATES WITH
INTERIOR CUT-OUTS**

Jon Monahan, P. J. Nemergut, USAF Air Force Institute of Technology,
G.E. Maddux, Air Force Flight Dynamics Laboratory Wright-Patterson AFB, Ohio

FINITE BEAM ELEMENTS FOR DYNAMIC ANALYSIS

V. H. Neubert, The Pennsylvania State University, State College, Pennsylvania and
H. Lee, Westinghouse Research Laboratory, Pittsburgh, Pennsylvania

EVALUATION OF MODELS FOR ONE-DIMENSIONAL VIBRATION SYSTEMS

R. D. Rocke, University of Missouri-Rolla, Rolla, Missouri

**DYNAMIC ELASTOPLASTIC RESPONSE OF GEOMETRICALLY NONLINEAR
ARBITRARY SHELLS OF REVOLUTION UNDER IMPULSIVE AND
THERMAL LOADINGS**

T. J. Chung, J. T. Oden, R. L. Eidson, J. F. Jenkins, and A. E. Masters,
Research Institute, The University of Alabama in Huntsville, Huntsville, Alabama

**RIGID BODY MOTIONS OF ELASTICALLY RESTRAINED UNDERWATER STRUCTURES
FROM DETONATION-INDUCED SHOCK**

H. S. Zwibel and J. G. Hammer, Naval Civil Engineering Laboratory,
Port Hueneme, California

EXTENSION OF CLASSICAL BINARY FLUTTER MODEL USING ROOT LOCUS

J. C. Hornbuckle, and R. L. Sierakowski, University of Florida, Gainesville, Florida

STIFFNESS AND MASS MATRICES FOR A TRIANGULAR ELEMENT

Mario Paz, Associate Professor, Civil Engineering Department, University of
Louisville, Louisville, Kentucky and Earl Berry, Jr., Graduate Student,
University of Louisville, Louisville, Kentucky

**HELICOPTER FUSELAGE VIBRATION RESPONSE ANALYSIS USING THE
HYBRID COMPUTER**

James D. Cronkhite, Bell Helicopter Company, Fort Worth, Texas

**VIBRATION OF A CLASS OF NONCONSERVATIVE SYSTEMS WITH TIME-DEPENDENT
BOUNDARY CONDITIONS**

Shoel-sheng Chen, Argonne National Laboratory, Argonne, Illinois

Fluid-Structure Interactions

**A VARIATIONAL APPROACH TO THE FLUID-SHELL DYNAMIC
INTERACTION PROBLEM**

A. S. Benson, Lockheed Missiles and Space Company, Sunnyvale, California

**EQUIVALENT MECHANICAL MODEL OF PROPELLANT FREE-SURFACE
VIBRATIONS IN THE SATURN S-IVB WORKSHOP CONFIGURATION**

Franklin T. Dodge and Luis R. Garza, Southwest Research Institute,
San Antonio, Texas

**THE EFFECT OF LIQUID OSCILLATIONS ON THE LM PROPELLANT QUANTITY
GAUGE SYSTEM**

M. Rimer, Grumman Aerospace Corporation, Bethpage, New York and
D. G. Stephens, NASA Langley Research Center, Hampton Virginia

**DERIVATION OF SKYLAB PROPELLANT STORAGE MODULE RANDOM VIBRATION
ENVIRONMENT**

A. E. Chirby, R. A. Stevens, H.C. Allen and W.R. Wood, Jr., North American
Rockwell Corporation, Space Division, Downey, California

THE FLUTTER OF A HYDROFOIL

Thomas M. Ward, California Institute of Technology, Pasadena, California and
Raymond C. Binder, University of Southern California, Los Angeles, California

SUPPLEMENT

AN AIR PULSER FOR VIBRATION TESTING

J. R. Peoples, Naval Ship Research and Development Center, Washington, D.C.
and J. G. Viner, Federal Highway Administration, Washington, D. C.,

STATISTICAL APPROACH TO OPTIMIZE RANDOM VIBRATION TEST SPECTRA
David L. Earls and John F. Dreher, Air Force Flight Dynamics Laboratory,
Wright-Patterson AFB, Ohio

**THE EFFECT OF TAILFINS ON THE VIBRACOUSTIC ENVIRONMENT OF
EXTERNALLY CARRIED AIRCRAFT STORES**
John F. Dreher, Air Force Flight Dynamics Laboratory, Wright-Patterson
Air Force Base, Ohio

**THE EFFECTS OF VISCOUS DAMPING ON DYNAMIC LOAD FACTORS FOR
SINGLE DEGREE-OF-FREEDOM SYSTEMS**
Harry Price Gray, Naval Ship Research and Development Center, Washington, D.C.

**THE EFFECT OF CAVITATION ON THE FLAT PLATE HULL UNDERWATER
SHOCK MODEL**
R. J. Scavuzzo, Rensselaer Polytechnic Institute, Hartford Graduate Center,
East Windsor Hill, Connecticut, and D. D. Raftopoulos, The University of Toledo,
Toledo, Ohio

DYNAMICS

PARAMETRIC RESPONSE OF MONOSYMMETRIC IMPERFECT THIN-WALLED COLUMNS UNDER SINUSOIDAL LOADING

Stanley G. Ebner
USAF Academy
USAF Academy, Colorado

Martin L. Moody
University of Colorado
Denver, Colorado

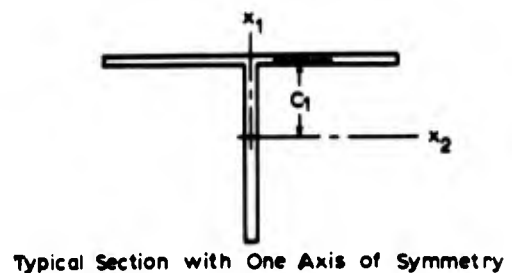
This investigation considers the vibrational response and dynamic stability of thin-walled columns with small initial crookedness and twist. The columns investigated are simply supported, of low torsional stiffness, and the cross sections of the columns have a single plane of symmetry. The columns are subjected to a constant plus a harmonic longitudinal load which causes parametric vibrations. Partial differential equations for this problem were first derived by Vlasov and are solved herein by separation of variables and an analog computer. The unstable regions in the plane of the loading and frequency parameters are located using a unique analog computer technique. Typical amplitude time responses of the two transverse modes and the torsional mode are presented which clearly show the subharmonic, harmonic and superharmonic frequencies characteristic of the Mathieu equation. Amplitude response spectra are also included.

INTRODUCTION

It has been known for many years [1] that transverse parametric oscillations can occur when a longitudinal periodic load is applied to a column. Up to the present time, the majority of investigations of this problem have been directed toward vibration in a single plane. The purpose of this paper is to present a portion of the results of an unpublished study [3] of the nonplanar problem which investigated the parametric vibrations of thin-walled elastic columns having small initial crookedness and twist. The columns considered herein are simply supported and the cross sections have a single plane of symmetry, as shown in Fig. 1. An axial periodic load $P(t) = P_0 + P_1 \cos \theta t$ is assumed to be applied* where P_0 is a static load, P_1 is the magnitude of the dynamic overload, θ is the frequency of application and t is time. The resulting motion consists of the interaction of twisting motion with the bending motion.

Bolotin's classic work [2] derives the equations which define the dynamic stability boundaries for thin-walled columns. Whereas an approximate method proposed by Bolotin gives excellent results in certain regions, analog computer solutions contained herein show that the utility in other regions may be limited. Other results in this paper include amplitude time responses and frequency response curves.

*Symbols are defined on first appearance in this paper.



Typical Section with One Axis of Symmetry

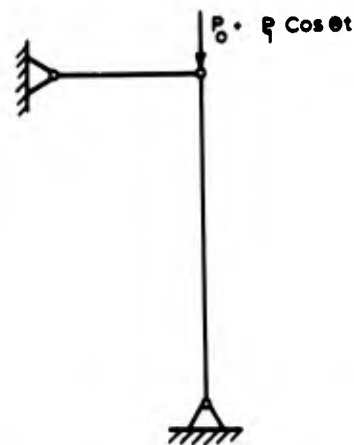


Fig. 1 Simply Supported Column Acted upon by a Periodic Axial Force

BASIC EQUATIONS

Thin-walled structural columns are distinguished by the fact that their three dimensions are of a different order of magnitude. Accordingly, the dimensions of the cross section are small when compared to the length of the column but are large when compared to the thickness of the walls of the column. The theory of St. Venant torsion is not sufficient to analyze the case of twisting of a thin-walled column because the longitudinal fibers can also undergo extension. In this case the warping of cross sections will vary along the length of the column, and a nonuniform torsion analysis is required.

The equations of motion are obtained by adding the transverse inertia forces to the two moment curvature equations, and adding the inertia moment taken about the longitudinal axis through the shear center to the nonuniform torsion equation. The resulting partial differential equations were first derived by Vlasov [11] in connection with problems of free vibrations. For the case of a column with small initial crookedness and twist loaded by a longitudinal force $P(t)$, the equations have the following linear form:

$$\begin{aligned} EI_2 \frac{\partial^4 (u_1 - u_1^e)}{\partial x_3^4} + P \frac{\partial^2 u_1}{\partial x_3^2} + m \frac{\partial^2 u_1}{\partial t^2} &= 0 \\ EI_1 \frac{\partial^4 (u_2 - u_2^e)}{\partial x_3^4} + P \frac{\partial^2 u_2}{\partial x_3^2} - PC_1 \frac{\partial^2 \phi}{\partial x_3^2} + m \frac{\partial^2 u_2}{\partial t^2} &= 0 \\ - mC_1 \frac{\partial^2 \phi}{\partial t^2} &= 0 \\ EC_w \frac{\partial^4 (\phi - \phi^e)}{\partial x_3^4} - GJ_e \frac{\partial^2 (\phi - \phi^e)}{\partial x_3^2} + P \frac{J_0}{A} \frac{\partial^2 \phi}{\partial x_3^2} &= 0 \\ - PC_1 \frac{\partial^2 u_2}{\partial x_3^2} + \frac{mJ_0}{A} \frac{\partial^2 \phi}{\partial t^2} - mC_1 \frac{\partial^2 u_2}{\partial t^2} &= 0 \end{aligned} \quad (1)$$

The notation used in these equations is as follows: x_3 is the longitudinal axis and passes through the centroid of the cross section, x_1 and x_2 in Fig. 1 are principal axes of the cross section, u_1 and u_2 are the total bending deformations measured from the initially straight configuration; C_1 is the coordinate distance to the center of rotation (shear center), and ϕ is the total angular displacement about the x_3 axis; I_1 and I_2 are the principal moments of inertia of the cross section, E is the modulus

of elasticity, G is the shearing modulus of elasticity, C_w is the warping coefficient, and J_0 is St. Venant's torsional constant for the cross section; u_1^e and u_2^e represent the initial unstressed crookedness in the x_1x_3 plane and the x_2x_3 plane respectively; ϕ^e is the initial unstressed twist, J_0 is the polar moment of inertia with respect to the shear center and A denotes the area of the cross section; m is the mass per unit length of the column, and t is the time.

The boundary conditions for a column simply supported at both ends are

$$u_1(0) = u_2(0) = \phi(0) = u_1(L) = u_2(L) = \phi(L) = 0$$

$$\frac{\partial^2 u_1(0)}{\partial x_3^2} = \frac{\partial^2 u_2(0)}{\partial x_3^2} = \frac{\partial^2 \phi(0)}{\partial x_3^2} \quad (2)$$

$$= \frac{\partial^2 u_1(L)}{\partial x_3^2} = \frac{\partial^2 u_2(L)}{\partial x_3^2} = \frac{\partial^2 \phi(L)}{\partial x_3^2} = 0$$

and can be satisfied by assuming solutions of the form

$$\begin{aligned} u_1(x_3, t) &= r_1 f_1(t) \sin \frac{\pi x_3}{L} \\ u_2(x_3, t) &= r_2 f_2(t) \sin \frac{\pi x_3}{L} \end{aligned} \quad (3)$$

$$\phi(x_3, t) = f_3(t) \sin \frac{\pi x_3}{L}$$

where L is the column length, r_1 and r_2 are radii of gyration, $f_1(t)$, $f_2(t)$ and $f_3(t)$ are unknown dimensionless displacement functions hereafter called temporal modes, and $\sin(\pi x_3/L)$

is the first spatial mode. * Whereas, a more rigorous analysis would include the contributions for all the modes, experimental results [2, 6, 10] indicate that the elastic curve differs only slightly from the first spatial mode provided the longitudinal force does not greatly exceed the fundamental Euler buckling

* The spatial mode is the fundamental eigenfunction of the corresponding static stability problem.

load. The imperfections in the column are, in general, random curves which may be defined by Fourier sine series. This investigation assumes that the first terms of the sine series adequately define the crookedness. Accordingly:

$$\begin{aligned} u_1^c &= r_1 u_1 \sin \frac{\pi x}{L} \\ u_2^c &= r_2 u_2 \sin \frac{\pi x}{L} \\ u^c &= a_3 \sin \frac{\pi x}{L} \end{aligned} \quad (4)$$

in which a_i 's are initial midspan displacements. Certain identities are introduced at this point in order to put the final equations in a more useable form.

$$\begin{aligned} P^* &= \frac{P}{P_{cr}} & C_1^* &= \frac{C_1}{r_2} \\ P_{cr} &= \frac{\pi^2 EI_2}{L^2} & J_1^* &= \frac{I_1}{J_0} \\ I_1^* &= \frac{I_1}{I_2} = \left(\frac{r_2}{r_1} \right)^2 & J_2^* &= \frac{I_2}{J_0} \\ I_2^* &= \frac{GAJ_e}{P_{cr} J_0} + \frac{C_w A}{I_2 J_0} \end{aligned} \quad (5)$$

In Eqs. (5) P_{cr} is the Euler load for the column (assuming $I_1 \geq I_2$).

Substituting Eqs. (3) and (4) into Eqs. (1) allows separation of variables. Using the identities given in Eqs. (5) the resulting set of ordinary differential equations with variable coefficients can be written as follows:

$$\begin{aligned} \ddot{f}_1 + (1 - P^*) f_1 &= a_1 \\ \ddot{f}_2 + (I_1^* - P^*) f_2 - C_1^* (\ddot{f}_3 - P^* f_3) &= I_1^* a_2 \\ \ddot{f}_3 + (I_2^* - P^*) f_3 - C_1^* J_1^* (\ddot{f}_2 - P^* f_2) &= I_2^* a_3 \end{aligned} \quad (6)$$

The equations are expressed in nondimensional form by using the following expressions:

$$\begin{aligned} x &= \left(\frac{\pi}{L} \right) \sqrt{\frac{EI_2}{P_0}} \xi \\ t &= \tau \\ \ddot{f}_1 &= \frac{P_0}{EI_2} \ddot{f}_1^* \\ \ddot{f}_2 &= \frac{P_0}{EI_2} \ddot{f}_2^* \\ \ddot{f}_3 &= \frac{P_0}{EI_2} \ddot{f}_3^* \\ \ddot{f} &= \frac{d^2 f}{d\tau^2} = \frac{1}{\Omega^2} \ddot{f}^* \end{aligned} \quad (7)$$

$$\begin{aligned} A_1 &= (1 - C_1^* J_1^*) (1 - P_0^*) \\ A_2 &= I_1^* a_2 + C_1^* I_2^* a_3 \\ A_3 &= C_1^* J_1^* I_1^* a_2 + I_2^* a_3 \\ A_4 &= C_1^* I_2^* \\ A_5 &= C_1^* I_1^* J_1^* \end{aligned}$$

where ω_1 is the fundamental frequency of vibration in the plane of symmetry for a simply supported column, Ω is the ratio of the driving frequency to the natural frequency of the unloaded column; λ is one-half the ratio of the frequency of loading (θ) and the natural frequency of the loaded column ($\omega_1 \sqrt{1 - P_0^*}$), and will be referred to as the frequency parameter; α is the loading parameter and the values of α and P completely define the stability of the column.

Substituting Eqs. (7) into Eqs. (6) and eliminating \ddot{f}_3 from Eq. (6b) and \ddot{f}_2 from Eq. (6c), gives:

$$\ddot{f}_1 + \frac{1}{4\tau^2} [1 - 2\lambda^2 \cos T] f_1 = \frac{a_1}{\Omega^2} = \frac{a_1}{4\lambda^2 (1 - P_0^*)} \quad (8a)$$

$$\ddot{f}_2 = \frac{1}{4} \left[\frac{1}{\lambda_1^2} - \frac{1}{1-\beta} \right] f_2 - 2 \cos t \cdot f_3$$

$$= \begin{pmatrix} 1 \\ 1 \end{pmatrix} \begin{pmatrix} \lambda_1 \\ \lambda_1 \end{pmatrix} f_2 - \begin{pmatrix} 1 \\ 1 \end{pmatrix} \begin{pmatrix} \lambda_2 \\ \lambda_1 \end{pmatrix} \quad (8a)$$

$$\ddot{f}_3 = \frac{1}{4} \left[\frac{1}{\lambda_2^2} - \frac{1}{1-\beta} \right] f_3 - 2 \cos t \cdot f_2$$

$$= \begin{pmatrix} 1 \\ 1 \end{pmatrix} \begin{pmatrix} \lambda_2 \\ \lambda_1 \end{pmatrix} f_3 - \begin{pmatrix} 1 \\ 1 \end{pmatrix} \begin{pmatrix} \lambda_3 \\ \lambda_1 \end{pmatrix} \quad (8c)$$

where t is the nondimensional time and $\ddot{f}_i = \frac{d^2 f_i}{dt^2}$

The amplitude time responses for the two bending vibrations and the torsional vibrations are obtained by solving Eqs. (8). The first of these equations is the Mathieu equation with a nonzero right side and indicates that the motion in the plane of symmetry is independent of the twisting and nonsymmetrical bending. The other two equations are coupled Mathieu type equations which indicate the interaction of the twisting and nonsymmetrical bending motion.

Stability of the column is dependent upon the parameters λ and β . The unstable regions

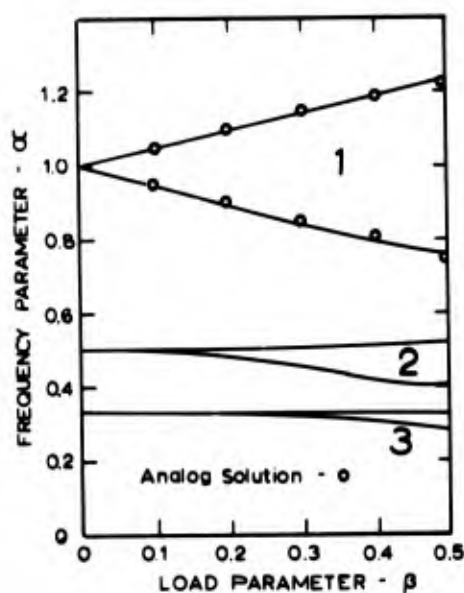


Fig. 2 - Unstable Regions for Mathieu Equation

are defined by those parameter points, λ and β , at which increasing amplitudes occur. For the case of the single Mathieu equation the unstable regions have been well defined [1, 2, 5, 8, 9] and for the particular form used in this paper are shown in Fig. 2.

The remaining two equations (8b and 8c) define two sets of unstable regions in the λ - β plane. The overall stability of the column is determined by superimposing the regions defined by all three equations.

DETERMINATION OF UNSTABLE REGIONS

It has been shown in the case of a single Mathieu equation, that determination of the boundaries of the regions of instability is reduced to finding the conditions under which the given differential equation has periodic solutions with periods of 2π and 4π [2]. Accordingly, if the unstable regions are labeled 1, 2, 3, ... starting from the primary unstable region, the odd numbered unstable boundaries can be determined by assuming solutions of the form

$$f(t) = \sum_{1,3,5,\dots} (a_k \sin \frac{k}{2}t + b_k \cos \frac{k}{2}t) \quad (9)$$

Similarly, the even numbered unstable boundaries can be obtained by assuming solutions of the form

$$f(t) = \sum_{2,4,6,\dots} (a_k \sin \frac{k}{2}t + b_k \cos \frac{k}{2}t) \quad (10)$$

It is clear from Eqs. (9) and (10) that the oscillations corresponding to the odd regions have a period of 4π and the oscillations corresponding to the even regions have a period of 2π .

Using the principle of harmonic balance [7] (Rayleigh's method) infinite sets of homogeneous algebraic equations are obtained in the unknowns a_k and b_k . The condition for the non-trivial solutions requires that the infinite determinants composed of the coefficients of the systems be identically zero. It can be shown [12] that these determinants belong to a known class of converging determinants. Thus, satisfactory approximations can be obtained by considering determinants of relatively low order.

With regard to the stability boundaries for thin-walled columns, Bolotin asserts that sufficiently accurate results defining the boundaries of the principal* regions can be

*These regions correspond to exponentially growing oscillations at a frequency one-half that of the applied longitudinal force and consequently could be called one-half harmonic regions.

obtained by using the "first order determinant". This is equivalent to using the following approximations:

$$\begin{aligned} f_2 &= a \cos \frac{1}{2} \\ f_3 &= b \cos \frac{1}{2} \end{aligned} \quad (11)$$

Substituting Eqs. (11) into Eqs. (8a) and (8c) and equating the coefficients of $\cos(1/2)$ to zero, gives two homogeneous algebraic equations.

$$\begin{aligned} \left[-\frac{1}{4} + \frac{1}{4\lambda} \left(\frac{I_1^*}{\lambda_1} - \frac{P_0^*}{1-P_0^*} \right) \right] a + \frac{1}{4\lambda} \left(\frac{\lambda_4}{\lambda_1} \right) b &= 0 \\ \frac{1}{4\lambda} \left(\frac{\lambda_5}{\lambda_1} \right) a + \left[-\frac{1}{4} + \frac{1}{4\lambda} \left(\frac{I_2^*}{\lambda_1} - \frac{P_0^*}{1-P_0^*} \right) \right] b &= 0 \end{aligned} \quad (12)$$

The condition for the nontrivial solution yields a fourth degree polynomial in λ which defines the unstable boundaries of the primary region in terms of λ .

$$\begin{vmatrix} -\frac{1}{4} + \frac{1}{4\lambda} \left(\frac{I_1^*}{\lambda_1} - \frac{P_0^*}{1-P_0^*} \right) & \frac{\lambda_4}{\lambda_1} \\ \frac{\lambda_5}{\lambda_1} & -\frac{1}{4} + \frac{1}{4\lambda} \left(\frac{I_2^*}{\lambda_1} - \frac{P_0^*}{1-P_0^*} \right) \end{vmatrix} = 0 \quad (13)$$

SOLUTIONS

The preceding results are now applied to a particular column. Equations (8) are solved on the TR-48 analog computer and the unstable boundaries defined by Eq. (13) are compared with the results of an analog computer technique for determining unstable regions. In the discussion which follows, standard structural sizes and dimensions of a tee cross section column are used [4]. Important parameters for a S1 7W 21.5 which is used as an example follow:

$$\begin{aligned} I_1^* &= 1.018 & J_1^* &= 0.4827 \\ I_2^* &= 1.061 & C_1^* &= 0.5661 \end{aligned} \quad (14)$$

Investigation of other monosymmetric cross sections would proceed in essentially the same manner.

Figure 3 shows only the principal unstable regions for the S1 7W 21.5 column, with $P_0^* = 0.5535$. Although solutions can also be obtained for the higher order (harmonic and superharmonic) unstable regions, the second, third and higher order unstable regions

are generally considered less important than the so-called principal regions because they are much narrower in size. Moreover, damping further decreases the size of the higher order unstable regions to the point that they are not emphasized in this paper. The unstable region centered around $\lambda = 1$ corresponds to the uncoupled bending motion in the plane of symmetry, see Fig. 2. The other two regions located (for $\beta = 0$) at approximately $\lambda = 1.43$ and $\lambda = 0.78$ correspond to the twisting motion coupled with the bending motion perpendicular to the plane of symmetry. The harmonic regions (not shown) are located (for $\beta = 0$) at approximately $\lambda = 0.72$, 0.75 and $\lambda = 0.39$.

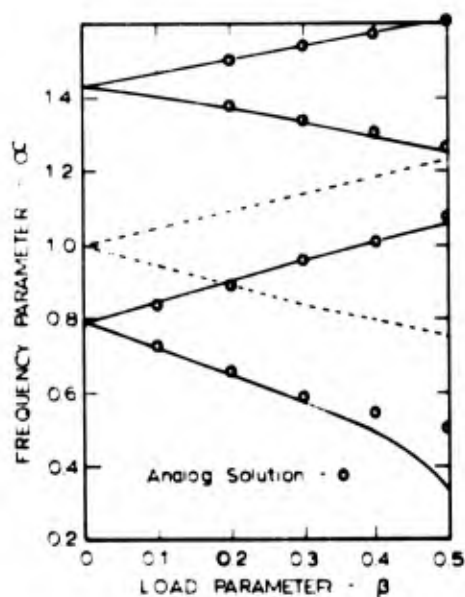


Fig. 3 - Primary Unstable Regions for Structural Tee (S1 7W 21.5)

The unstable boundaries shown in Fig. 3 were obtained by two methods; Eq. (13) and an analog computer technique. The computer technique which is considered reliable and reasonably accurate will now be described.

The boundaries of the unstable regions are not affected by the initial crookedness and twist of the column. Thus, when considering the question of stability, the imperfections were removed. In addition, the initial conditions were set to zero. In such a situation, there exists only the identically zero mathematical solution for the wave forms of the temporal modes. When switched to the "Repetitive operation" mode the analog computer yielded the identically zero solution in the stable regions as expected. It is significant, however, that the primary and higher order unstable regions were defined and located by the existence of exponentially increasing computer solutions for the temporal modes. As stated above, the mathematical formulation of the problem does not predict such solutions. This paradox is ex-

TABLE I

α	Primary Solution for α			
	Upper Boundary		Lower Boundary	
	Analytic	Computer	Analytic	Computer
0.10	1.049	1.050	0.9487	0.9538
0.20	1.095	1.097	0.8944	0.9039
0.30	1.140	1.146	0.8367	0.8485
0.40	1.189	1.190	0.7977	0.8029
0.50	1.233	1.233	0.7559	0.7554

plained by the existence of machine noise (less than 500 microvolts RMS by specification) which provides sufficient perturbations to initiate the unstable solutions. The credibility of the analog computer technique is based upon a comparison with the exact solution [8] for the boundaries of the unstable regions for the Mathieu equation. This comparison is shown in Table I and in Fig. 2. With confidence thus established, the technique was applied to the coupled problem.

As shown in Fig. 3 and in Table II, the analytical approximation for the unstable boundaries defined by Eq. (13) compares favorably to the solutions obtained from the analog computer except for the apparent divergence at the lower boundary of the lower region. The disparity is a consequence of the assumption that f_2 and f_3 are exactly one half harmonic, whereas computer solutions near the divergent

TABLE II

β	Upper Region Solutions for α			
	Upper Boundary		Lower Boundary	
	Analytic	Computer	Analytic	Computer
0.10	1.473	--	1.404	--
0.20	1.507	1.503	1.368	1.376
0.30	1.539	1.539	1.333	1.338
0.40	1.572	1.571	1.293	1.308
0.50	1.603	1.610	1.250	1.266
β	Lower Region Solutions for α			
	Upper Boundary		Lower Boundary	
	Analytic	Computer	Analytic	Computer
0.10	0.8474	0.8410	0.7197	0.7259
0.20	0.9045	0.8927	0.6465	0.6621
0.30	0.9584	0.9562	0.5640	0.5946
0.40	1.009	1.005	0.4897	0.5526
0.50	1.057	1.066	0.3440	0.5116

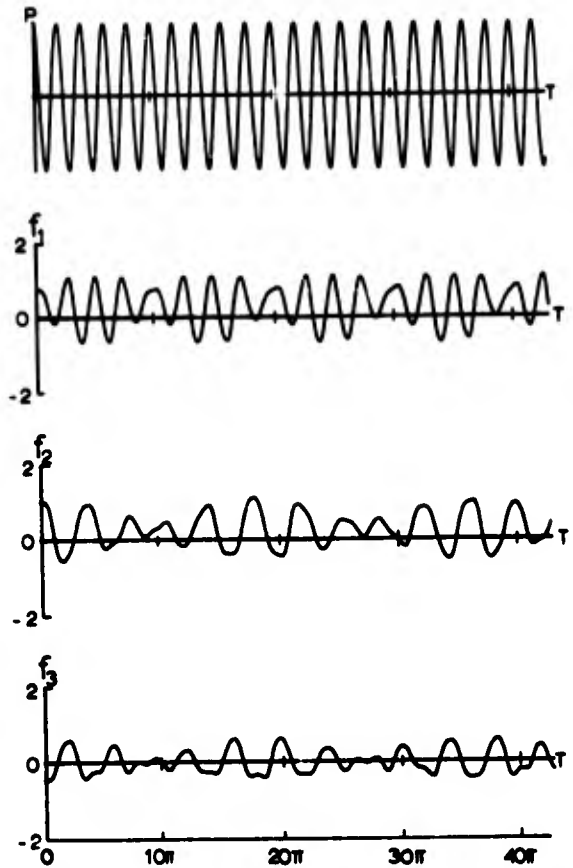


Fig. 4 - Amplitude Time Response Diagrams for Structural Tee (ST 7WF21.5) at $\beta = 0.25$ and $\alpha = 0.612$

region show that the response frequencies are actually higher.

Typical amplitude time responses for the temporal modes at a point below the lower primary unstable region are shown in Fig. 4. The appearance of beats is typical of solutions near the boundary of an unstable region. The period of the beats increase as the unstable region is approached until finally, in the unstable regions, the amplitudes increase exponentially. Near the primary unstable regions the frequency of the response is generally one-half harmonic and for points near the second unstable regions the frequency is generally harmonic. Observe the responses for f_2 and f_3 in Fig. 4 which are nearly one-half harmonic. These responses are not exactly one-half harmonic due to the influence of secondary unstable regions at $\alpha = 0.72$ and $\alpha = 0.39$ (not shown in Fig. 3). It may also be observed in Fig. 4 that the f_1 response is closer to being harmonic due to its nearness to the secondary unstable region ($\alpha = 0.50$) as shown in Fig. 2. A one-half harmonic response within a primary unstable region some-

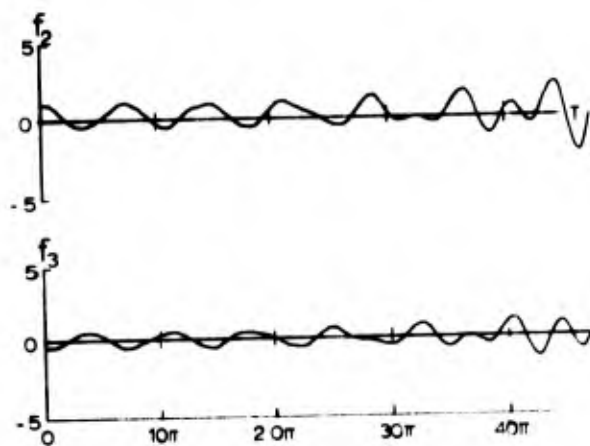


Fig. 5 - Amplitude Time Response Diagrams for Structural Tee (ST 7W21.5) at $\zeta = 0.25$ and $\alpha = 1.445$

times develops slowly as may be observed in Fig. 5 wherein twenty cycles of loading occur before the one-half harmonic response is observed.

If the largest maximum response is taken from a series of solutions then response spectra diagrams can be plotted. For example, fixing $\zeta = 0.25$ and varying α the response spectra for the amplitudes of f_2 and f_3 between the primary unstable regions as shown in Fig. 6 is obtained. These are transient response spectra since only twenty cycles of loading have been used. During the investigation it was found that the phase angle γ for the loading

$$P = P_0 + P_1 \cos(\omega t + \gamma) \quad (15)$$

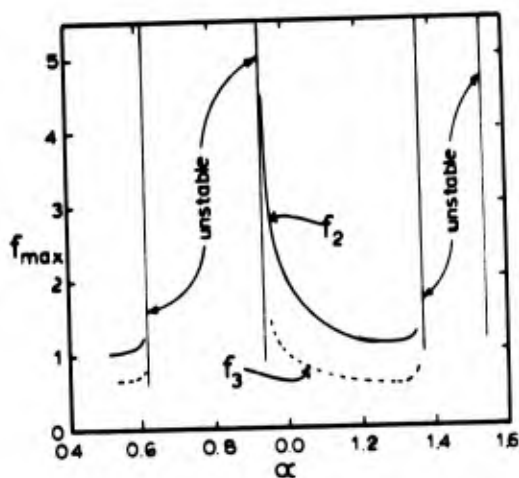


Fig. 6 - Transient Response Spectra for Structural Tee (ST 7W21.5) at $\zeta = 0.25$

had a significant effect on the response diagrams with the largest maximum values dependent on α , ζ , and γ . The maximum usually occurs for $\gamma = 0$. With the addition of a very small amount of uncoupled viscous damping it was observed, as expected, that the steady state solution develops quickly and is independent of the phase angle. A typical example of this is shown in Fig. 7.

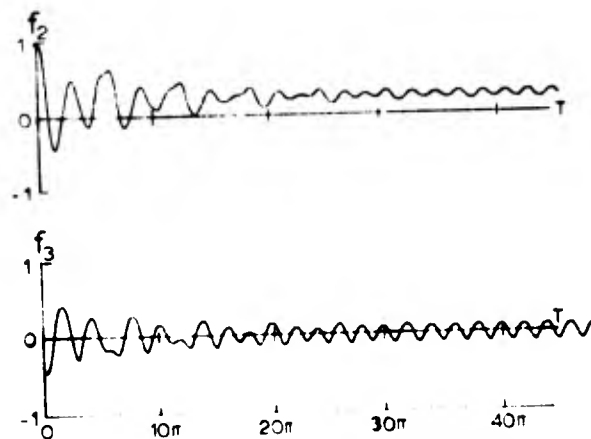


Fig. 7 - Amplitude Time Response Diagrams with damping for Structural Tee (ST 7W21.5) at $\zeta = 0.25$ and $\alpha = 0.548$

CONCLUSIONS

The analog computer is found to be a practical device for locating the unstable regions for coupled Mathieu type equations and also provides a convenient means of looking at a large variety of solutions for this type of system. For design purposes, it may be worthwhile to obtain a sufficient number of solutions so families of response spectra can be plotted by varying α , ζ , and γ .

REFERENCES

1. Beliaev, N. M. "Stability of Prismatic Rods Subject to Variable Longitudinal Forces," Collection of Engineering Construction and Structural Mechanics (Inzhinerne sooruzhenia i stroitel'naya mekhanika), Leningrad, Put' 1924
2. Bolotin, V. V., The Dynamic Stability of Elastic Systems, translated from the Russian by Weingarten, Greszczuk, Trilogoff and Gallegos, Holden-Day, Inc., San Francisco, 1964
3. Ihner, S. G., "Elastic Oscillations of Imperfect Columns of Thin-Walled Open Sections Subjected to Axial Periodic Loads," Thesis submitted to the Department of Civil Engineering, University of Colorado, as partial fulfillment of requirements for the Ph.D. degree, 1968

4. Ishbach, O. W., Handbook of Engineering Fundamentals, 2nd Edition, Wiley Eng. Handbook Series, New York, 1952
5. Evan-Iwanowski, R. M., "On the Parametric Response of Structures," Applied Mech. Review, Vol. 18, pp. 699-702, 1965
6. Iyensen, H. A. and Evan-Iwanowski, R. M., "Effects of Longitudinal Inertia Upon the Parametric Response of Elastic Columns," Journal of Applied Mechanics, pp. 141-148, March 1966
7. Hayashi, Chihiro, Nonlinear Oscillations in Physical Systems, McGraw-Hill Book Co., New York, 1964
8. Lubkin, S., and Stoker, J. J., "Stability of columns and Strings Under Periodically Varying Forces," Quarterly Applied Math., Vol. 1, pp. 215-236, 1915
9. Moody, M. L., "The Parametric Response of Imperfect Columns," Proceedings of the Tenth Midwestern Mechanics Conference, pp. 329-346, Aug. 1967
10. Somerset and Evan-Iwanowski, "Experiments on Parametric Instability of Columns," Developments in Theoretical and Applied Mechanics, Vol. 2, Proceedings of the Second South-eastern Conference on Theoretical and Applied Mechanics, Pergamon Press, 1965
11. Vlasov, V. Z., Thin-Walled Elastic Beams, (translated from the Russian), National Science Foundation OTS 61-11400, Washington, D.C., 1961
12. Whittaker, E. T. and Watson, G. N., A Course of Modern Analysis, 4th Edition, Univ. Press, Cambridge, 1952

PREDICTION OF UpSTAGE RANDOM VIBRATION
ENVIRONMENT USING A STATISTICAL ENERGY APPROACH*

D. E. Hines, G. R. Parker, and R. D. Hellweg
McDonnell Douglas Astronautics Company - West
Santa Monica, California

The "Statistical Energy Approach" (SEA) was used to predict the UpSTAGE high frequency vibration environment. This approach allowed the analysis to account for the high level local excitation induced by the control system, the unique shape of the vehicle and the internal configuration of the vehicle. The topics discussed are (1) development of the SEA as used on UpSTAGE; (2) development of the analytical models; (3) discussion of the tests performed to support the analysis; (4) prediction of the flight levels for the UpSTAGE vehicle.

INTRODUCTION

The UpSTAGE Experiment consists of high performance experimental vehicles which have the form of elliptical cones, as depicted in Fig. 1. Vibration is induced into the vehicle by the aerodynamic noise associated with the attached turbulent boundary layer and the separated flow region just forward of the point of injection of the gasses used for system control. The local high intensity fluctuating pressure field in the

separated flow region and the outer geometry of the vehicle would result in low confidence environmental predictions if they were based on direct scaling of existing data.

*This work has been jointly supported by Army Contract No. DAAH01-68-C-1237 and the "McDonnell Douglas Independent Research and Development Fund."

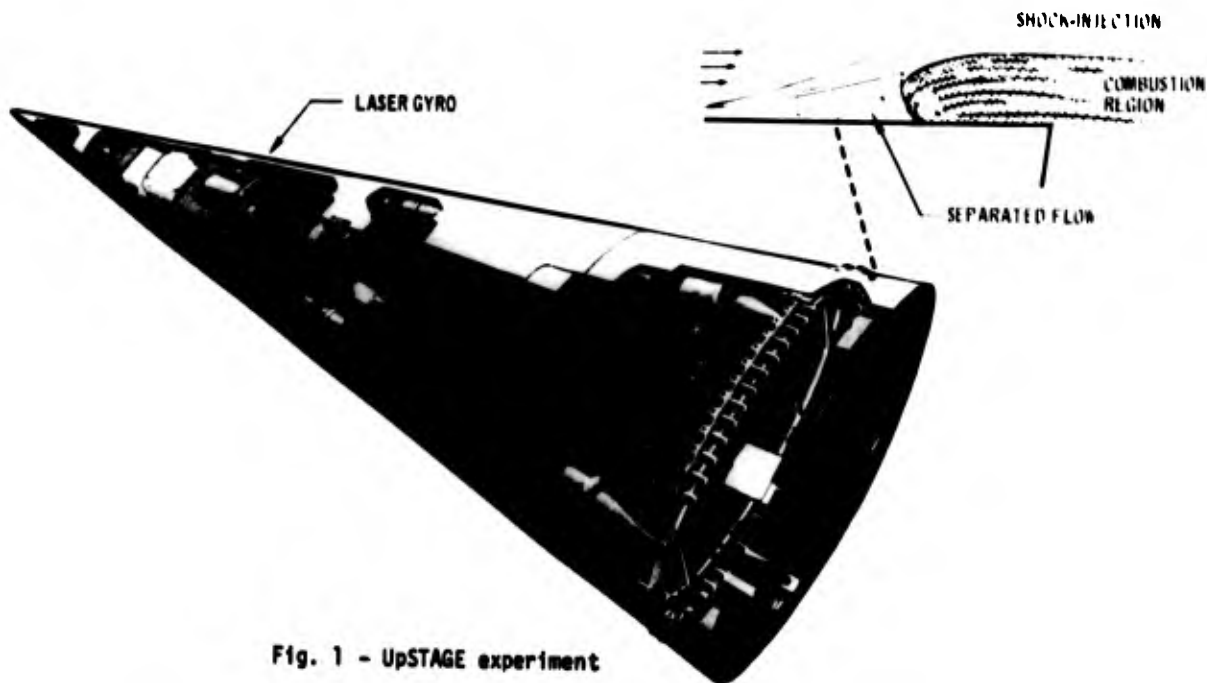


Fig. 1 - UpSTAGE experiment

Therefore, a "Statistical Energy Approach" (SEA) was chosen as the method to be used in predicting these environments. In order to verify that SEA was capable of predicting the vibration levels on a locally excited conical flight vehicle with an elliptical cross section, a model of the UpSTAGE load-carrying structure was constructed and tested. The test results were first compared to the results obtained using a 45-element analysis of the test vehicle and were then used to refine the constants used in the model. The mathematical model of the test specimen was then expanded to a model of the flight vehicle for use in predicting the flight environments. The topics discussed are (1) development of the SEA as it is to be used in this analysis; (2) development of the analytical models; (3) discussion of the tests performed to support the analysis; (4) prediction of the flight levels for the UpSTAGE vehicle.

STATISTICAL ENERGY APPROACH

The development of the SEA* used on UpSTAGE is based on the assumption that all of the vibratory energy contained in a system is contained in the modes of that system. This assumes that the modes of the system are a complete set. Under this assumption, any vibrating (or acoustical) system can be described as a mode set, and the analysis reduces to coupling of these mode sets.

In order to couple these mode sets and to obtain resolution in the frequency domain, each mode set is divided into subsets. Each subset contains all of the modes which fall into a given constant percentage bandwidth. The following assumptions are then made:

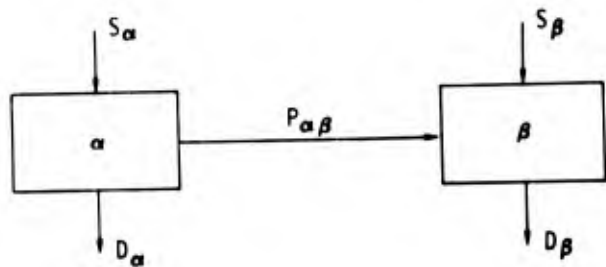
- The modes in a subset contain all of the energy in the bandwidth of that subset.
- The energy in each subset is equally distributed among the modes of that subset.
- Only subsets covering the same frequency range are coupled.
- For two coupled subsets (α and β), each mode in the α subset is equally coupled to each mode in the β subset.

These assumptions can be satisfied only in the average sense. As in all cases where averaging is used, the more samples or, in this case, the wider bandwidth the better the results. However, bandwidths which are too wide may result in problems because of frequency-dependencies and the desired frequency resolution. One-third octave bands were chosen as a compromise bandwidth for the UpSTAGE analysis.

*The development of the SEA theory presented here is consistent with that presented in the literature, but does not parallel that presented in any one document. In the text, only specific points of interest are referenced.

Two Systems

Consider the coupling of two subsets (α and β) as shown below. These subsets belong to two coupled systems and cover the same frequency range.



S_α = Power introduced into α from an outside source other than β

D_α = Power dissipated by α in the form of heat or to an outside source other than β

$P_{\alpha\beta}$ = Power transmitted from α to β and equal to $-P_{\beta\alpha}$.

Consider one of the α modes. The energy of this mode is T_α and the rate at which this energy is dissipated (power) by damping is $2\omega_0\eta_\alpha T_\alpha$.

where

ω_0 = natural frequency of the mode

η = damping factor ($1/Q$) of the mode

T = energy per mode.

The power lost by the α mode to each β mode is $\phi_0 T_\alpha$, and the total power lost by the α mode to β is $\phi_0 T_\alpha N_\beta$.

where

ϕ_0 = the average mode to mode coupling factor between the α and β sets

N_β = the total number of modes in the β set.

The power gained by the α mode of interest is that directly added by an external source (S_α/N_α), plus that gained from β . The power gained from β must equal that gained from each mode ($T_\beta \phi_0$) times the number of modes. Equating the power lost and gained by an α mode leads to

$$2\omega_0\eta_\alpha T_\alpha + \phi_0 T_\alpha N_\beta = \frac{S_\alpha}{N_\alpha} + \phi_0 T_\beta N_\beta \quad (1)$$

The preceeding is the equation for one of the modes in α . The expression for the total subset is obtained by multiplying Equation 1 by N_α yielding

$$N_\alpha 2 \omega_0 \eta_\alpha T_\alpha + \phi_0 T_\alpha N_\beta N_\alpha = S_\alpha + \phi_0 T_\beta N_\beta N_\alpha \quad (2a)$$

or

$$2 \omega_0 \eta_\alpha T_\alpha N_\alpha + \phi_0 N_\alpha N_\beta (T_\alpha - T_\beta) = S_\alpha \quad (2b)$$

The first term of 2b is obviously the power dissipated by α (D_α), and the second term is the net power transmitted to β ($P_{\alpha\beta}$). In addition, $\phi_0 N_\alpha N_\beta$ can be redefined as $\phi_{\alpha\beta}$ giving the form often found in the literature [1].

Equation 2 can be put in terms of total energy of the subsets by letting $E_i = T_i N_i$. Under this substitution, Equation 2 becomes

$$2 \omega_0 \eta_\alpha E_\alpha + \phi_0 N_\beta E_\alpha - \phi_0 N_\alpha E_\beta = S_\alpha \quad (3)$$

Physically, $\phi_0 N_\beta E_\alpha$ represents a loss of power from α to β which is indistinguishable from the loss of power due to damping if only the α set is defined. This being the case, one should be able to define the $\phi_0 N_\beta E_\alpha$ term in the same form as is used for damping. This leads to

$$2 \omega_0 (\eta_\alpha E_\alpha + \eta_{\alpha\beta} E_\alpha - \eta_{\beta\alpha} E_\beta) = S_\alpha \quad (4)$$

where

$$\eta_{\alpha\beta} = \phi_0 N_\beta / 2 \omega_0$$

$$\eta_{\beta\alpha} = \phi_0 N_\alpha / 2 \omega_0$$

This is the form used in Reference 1.

Examination of Equations 2, 3 and 4 leads to several equalities concerning the various energy flow parameters found in the literature. These are

$$\phi_{\alpha\beta} = \phi_{\beta\alpha} = \phi_0 N_\alpha N_\beta = 2 \omega_0 \eta_{\alpha\beta} N_\alpha = 2 \omega_0 \eta_{\beta\alpha} N_\beta$$

$$\phi_0 = \frac{2 \omega_0 \eta_{\alpha\beta}}{N_\beta} = \frac{2 \omega_0 \eta_{\beta\alpha}}{N_\alpha}$$

and

$$\eta_{\alpha\beta} = \eta_{\beta\alpha} \frac{N_\beta}{N_\alpha}$$

If β is the only energy source for α , i.e., $S_\alpha = 0$, then Equation 4 can be rewritten as

$$E_\alpha (\eta_\alpha + \eta_{\alpha\beta}) = E_\beta \eta_{\beta\alpha}$$

or

$$\frac{E_\alpha}{E_\beta} = \frac{\eta_\alpha + \eta_{\alpha\beta}}{\eta_{\beta\alpha}} = \frac{N_\alpha}{N_\beta} \frac{\eta_\alpha + \eta_{\alpha\beta}}{\eta_{\beta\alpha}} = \frac{N_\alpha}{N_\beta} \left(\frac{\eta_\alpha}{\eta_{\beta\alpha}} + \frac{\eta_{\alpha\beta}}{\eta_{\beta\alpha}} \right) \quad (5)$$

This form is presented in Reference 1 and points out two interesting aspects of high frequency vibration. Let α represent a small portion of a vehicle, and β the remainder of the vehicle. In order to appreciably reduce the vibration of α by the addition of damping to α , the energy dissipated by the added damping must be on the order of or greater than the energy being transmitted out of α to β . This usually is difficult to achieve. In the case which usually exists where $\eta_{\alpha\beta} \gg \eta_\alpha$ and Equation 5 reduces to $E_\alpha/E_\beta = N_\alpha/N_\beta$ showing that the energy tends to be equally distributed among the modes of the system.

The purpose of this discussion is to develop a method for deriving a SEA model of a system consisting of many mode sets or sections. Looking ahead, it appears that the above inequality ($\eta_{\alpha\beta} \gg \eta_\alpha$) may be used to define the minimum useful size of a section to be used in an analysis. Any further reduction in size will not alter the distribution of energy away from the section, it will only furnish more definition of the response for that section.

The two basic forms of defining the coupling between sections ($\phi_{\alpha\beta}$) are by using either $\eta_{\alpha\beta}$ or ϕ_0 . The choice should depend on the problem at hand.

For the UpSTAGE analysis, experimental data was available, but not in sufficient detail to define $\phi_{\alpha\beta}$ for each pair of mode sets. Therefore, some assumptions were required concerning its value and properties. The sections of the load-carrying structure used in the model were separated by field joints, or consisted of continuous skin divided into sections for modeling. All of the bulkheads were connected to the load-carrying structure in basically the same way (the majority of components were attached directly to the bulkheads). This gives three types of connections between sections, but the sizes and shapes of these sections vary widely resulting in a large range of modal densities. If the modal densities vary widely, so will the $\eta_{\alpha\beta}$. ϕ_0 which should have a strong dependence only on the boundary, should therefore be approximately described by three values. For this reason, ϕ_0 has been chosen for use in the UpSTAGE analysis.

The general form of the power balance equation used was

$$2 \omega_0 \eta_a E_a + \phi_0 N_b E_a - \phi_0 N_a E_b = S_a \quad (6)$$

Multiple Systems

Now consider a structure divided into many systems or elements, as shown in Fig. 2.

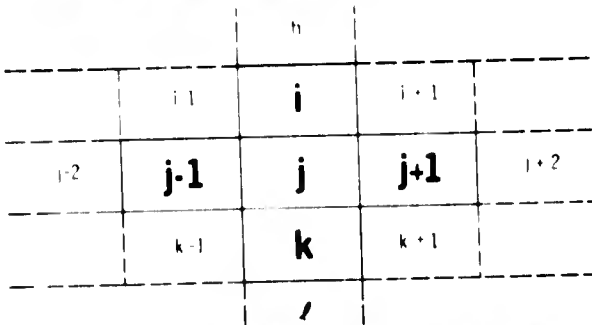


Fig. 2 - Structure divided into systems

The j element is only coupled to the elements having common boundaries (i , $j-1$, $j+1$, and k).

The power lost by the j^{th} element is the result of damping ($2 \omega_0 \eta_j E_j$) plus that lost to adjacent panels ($\phi_0 E_j [N_i + N_{j-1} + N_{j+1} + N_k]$), assuming that coupling across each border can be described by ϕ_0 . The power gained by this element will be that received from some external source (S_j) plus that received from adjacent panels ($\phi_0 N_j [E_i + E_{j-1} + E_{j+1} + E_k]$).

Equating these power flows leads to the form

$$\begin{aligned} & - \phi_0 N_j (E_i + E_{j-1}) \\ & + E_j (2 \omega_0 \eta_j + \phi_0 [N_i + N_{j-1} + N_{j+1} + N_k]) \\ & - \phi_0 N_j (E_{j+1} + E_k) = S_j \end{aligned} \quad (7)$$

If the power balance equations for all of the sections are put into a matrix form, then the above equation would represent the j^{th} row of that matrix, as shown in Fig. 3. In the power balance equation for sections coupled to the j^{th} element, the coefficient for E_j will be j times the modal density of that coupled panel. These terms result in the values in the j^{th} column, as indicated in Fig. 3. It is interesting (and helpful in programming) to note that the positive value of the sum of the off diagonal terms in the j^{th} column plus the damping term is equal to the diagonal term.

TEST SPECIMEN

As was indicated in the Introduction, the UpSTAGE environment was predicted using a combined analysis and test approach. The tests were performed to verify the analytical method and model used as well as to establish some of the constants used in the model. This was done by modeling the test specimen and comparing the results of that model with the experimental results. In addition, the model used to represent the flight vehicle was obtained by altering the model of the test specimen. Therefore, a fairly detailed discussion of the test specimen and the modeling of that specimen is required here.

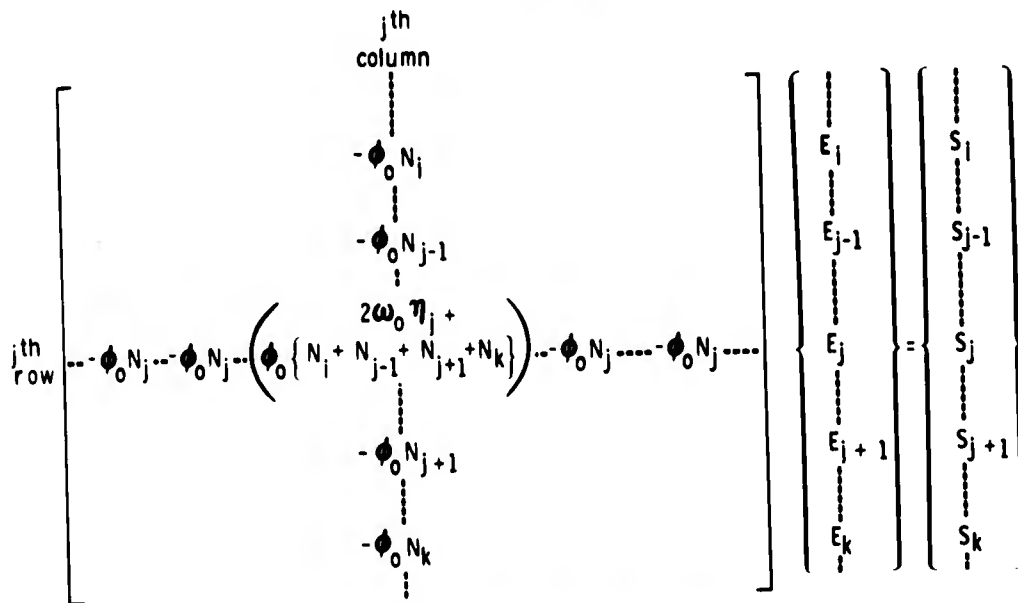


Fig. 3 - Matrix form of mathematical model

The test specimen consisted of the UpSTAGE load-carrying structure up to the ballast point (Station 14.5). This structure included all of the bulkheads, frames, and field joints but did not include a honeycomb section of the skin nor the vehicle ablative. A realistic dynamic model of the laser gyro was available and was the only component included in the test. The location of the gyro is shown in Fig. 1, and external and internal photographs of the specimen are presented in Figs. 4 and 5, respectively.

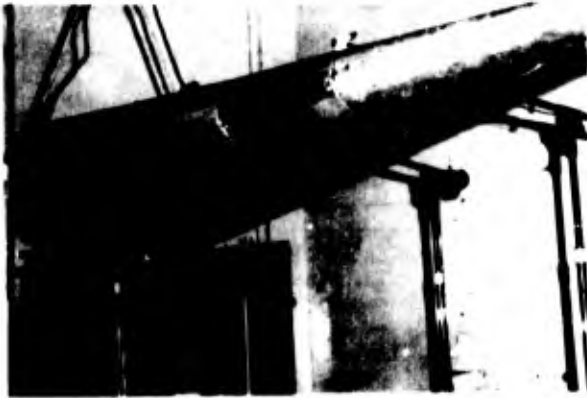


Fig. 4 - UpSTAGE test specimen



Fig. 5 - Internal view of UpSTAGE test specimen

The mathematical model divided the test specimen into four basic sections separated by the three field joints located between Stations 14.6 and 107 (the extent of the model). The aft basic section was further divided into four subsections to allow the mathematical description of the localized excitation. In addition, each

section was assumed to have the shape of an elliptical cylinder yielding the configuration shown in Fig. 6. Each elliptical subsection was approximated by four curved panels of constant radius of curvature, as shown, resulting

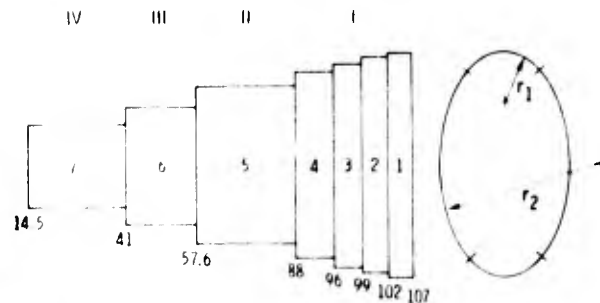


Fig. 6 - Sections used for the mathematical model

in the outer structure of the specimen being defined by 28 curved panels. Additional panels were added to represent the forward and aft bulkheads, at each field joint and each of the remaining bulkheads. The resulting analytical model consisted of 45 mode sets, or sections, which are described in Table 1.

The matrix form of the model previously given can be rewritten in the form

$$([D] + [C]) \{E\} = \{S\} \quad (8)$$

Where D describes the damping and is a diagonal matrix whose elements are of the form

$$d_{ij} = 2\omega_j$$

The [C] is the coupling matrix where

$$c_{jk} = -\phi_i N_j \text{ for } j \neq k$$

$$c_{jk} = -\sum_m c_{jm} \text{ for } j = k$$

c_{jk} are zero for uncoupled panels.

The E and S matrices are the energy and input power, respectively.

The parameters in this equation are discussed below.

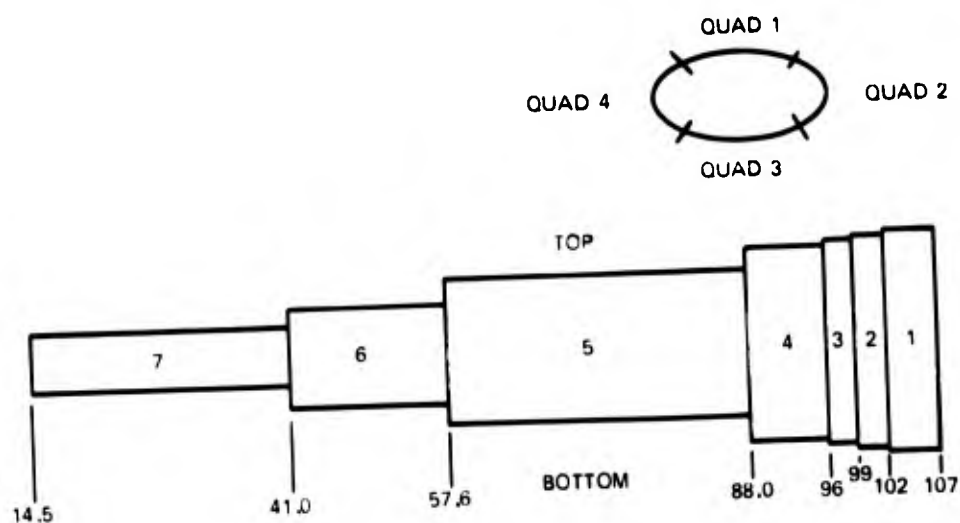
Modal Density

The model for each bandwidth requires calculation of the number of modes in each set contained in that bandwidth (subset). The number of modes (N) was obtained by multiplying the bandwidth ($\Delta\omega$) by the modal densities $[n(\omega)]$.

TABLE 1
UpSTAGE - Model Elements

Sec. No.	Description	Region No.	Quad. No.
1	Skin	1	1
2	Skin	1	2
3	Skin	1	3
4	Skin	1	4
5	Skin	2	1
6	Skin	2	2
7	Skin	2	3
8	Skin	2	4
9	Skin	3	1
10	Skin	3	2
11	Skin	3	3
12	Skin	3	4
13	Skin	4	1
14	Skin	4	2
15	Skin	4	3
16	Skin	4	4
17	Skin	5	1
18	Skin	5	2
19	Skin	5	3
20	Skin	5	4
21	Skin	6	1
22	Skin	6	2
23	Skin	6	3
24	Skin	6	4
25	Skin	7	1
26	Skin	7	2
27	Skin	7	3
28	Skin	7	4

Sec. No.	Description	Sta.	Region No.
29	Aft Bulkhead (B.H.)	107.0	1
30	Forward B.H.	14.5	7
31	Field Joint B.H.	88.2	4-5
32	Field Joint B.H.	57.6	5-6
33	Field Joint B.H.	41.0	6-7
34	Internal B.H.	97.0	3
35	Internal B.H.	92.0	4
36	Internal B.H.	83.5	5
37	Internal B.H.	76.3	
38	Internal B.H.	68.0	
39	Internal B.H.	51.2	6
40	Internal B.H.	46.2	
41	Internal B.H.	36.7	7
42	Internal B.H.	31.9	
43	Internal B.H.	28.0	
44	Internal B.H.	24.0	
45	Internal B.H.	19.4	



The modal densities for flat plates and cylinders are given in Reference 1 as

Plate

$$n_p = A_s / (4\pi \sqrt{D/\rho h})$$

Cylinders

(9)

$$n_c = n_p \text{ for } \omega/\omega_r > 1$$

$$n_c = n_p \left(\frac{\omega}{\omega_r}\right)^{2/3} \text{ for } \omega/\omega_r < 1$$

where

ω_r = ring frequency = speed of sound in the material/radius

$$D = \frac{Eh^3}{12(1-\nu^2)}$$

E = Young's Modulus

ν = Poisson's Ratio

h = panel thickness

In addition, the modal density of a system equals (approximately) the sum of the modal densities of its subsystems [2]. For the purpose of calculating the modal densities of the curved panels the converse of this will be assumed. That is, if a cylinder has a modal density $n(\omega)$ and if that cylinder is divided circumferentially into i equal parts then it is assumed that the modal density of each part will be $n(\omega)/i$.

Therefore, the modal densities of the curved sections are

$$n = A_s / 4\pi \sqrt{D/\rho h}, \omega/\omega_r > 1$$

$$n = (A_s / 4\pi \sqrt{D/\rho h}) (\omega/\omega_r)^{2/3}, \omega/\omega_r < 1$$

For convenience in writing, an equivalent area for curved panels is defined as

$$A_e = A_s \text{ for } \omega/\omega_r > 1$$

$$= A_s (\omega/\omega_r)^{2/3} \text{ for } \omega/\omega_r < 1$$

The modal density for any of the panels to be used is

$$n(\omega) = A_e / 4\pi \sqrt{D/\rho h}$$

Energy

For the systems of interest, the energy is*

$$E = \int_{\text{System}} \langle V^2 \rangle d\rho_s$$

$\langle \rangle$ = time average

ρ_s = local mass

$$m = \text{total mass} = \int_{\text{System}} d\rho_s$$

It is assumed that each panel and its response is sufficiently uniform so that

$$E = \int_{\text{System}} \langle V^2 \rangle d\rho_s = m \langle V^2 \rangle$$

$\langle \rangle$ = space average

It should be noted that this assumption does not affect the results away from the panel of interest. In addition, after the average response has been obtained under the above assumption, local effects can be included using good engineering judgment based on mass loading effects [3], the relationship between energy and modal density previously presented, and the general location of energy sources.

Since we are concerned only with relatively narrow bandwidths

$$E = m \langle V^2 \rangle = \frac{m \langle \ddot{a}^2 \rangle}{\omega^2}$$

Acoustic Excitation

The acoustic excitation can be introduced into the system by one of two ways.

The first method would be to include the acoustic field as an additional mode set coupled to each exposed panel. The coupling factor would include both the acceptance of acoustic energy and the acoustic damping. Energy could be introduced into the acoustic field, and relative values would be obtained between the acoustic field and the vibration in the structure. This is the desired approach for a system excited by a uniform acoustic field, but the local excitation and the change in level as a function of station number for the flight vehicle make this approach difficult. (The change in level with station number will be discussed later.) Therefore an alternate approach was used.

*This expression for energy assumes a conservative system.

The alternate approach consists of first defining the energy balance equation for the j th panel including the acoustic field as an independent system. This results in

$$- \phi_{ac} N_j \sum E_i + E_j (2\omega_0 \eta_j + \phi \sum N_i) + [- \phi_{ac} N_j E_{ac} + \phi_{ac} N_{ac} E_j] = 0 \quad (10)$$

where

ϕ_{ac} = average mode to mode coupling between acoustic field and j

E_{ac} = energy in reverberation room [4]

$$= \frac{\langle \bar{p}^2 \rangle V}{\rho_0 c_0^2}$$

N_{ac} = number of modes in reverberation room in $\Delta\omega$ [4]

$$= \omega_0^2 V \Delta\omega / 2\pi^2 c_0^3$$

V = volume of reverberation chamber

ρ_0 = air density

c_0 = speed of sound in air

Since

$$\phi_{ac} = \frac{2\omega_0 \eta_{jac}}{N_{ac}}$$

then

$$\phi_{ac} N_j E_{ac} = \frac{2\omega_0 \eta_{jac}}{N_{ac}} N_j E_{ac}$$

$$= \frac{4\pi^2 c_0 \eta_{jac} N_j \langle \bar{p}^2 \rangle}{\rho_0 \omega_0 \Delta\omega}$$

in addition [5],

$$\eta_{jac} = \frac{\rho_0 c_0}{\omega_0 m_j} \sigma$$

σ = radiation efficiency

m_j = surface mass density

Substituting this into the preceding yields

$$\phi_{ac} N_j E_{ac} = \frac{4\pi^2 c_0^2 N_j \sigma \langle \bar{p}^2 \rangle}{\omega_0^2 m_j \Delta\omega}$$

Putting this term on the right side of Equation 10 and assuming that the $\phi_{ac} N_{ac} E_j$ term is included in the damping term yields the form shown in Equation 8 where

$$S_j = \phi_{ac} N_j E_{ac}$$

Mathematical Model

Substitution of the appropriate values of E , S and modal density into the previous expression yields

$$\{\langle \bar{a}^2 \rangle\} = [m]^{-1} [[\eta]]$$

$$+ \frac{\Delta\omega}{4\pi \omega_0 \sqrt{E/3\rho} (1-\nu^2)} \left[\frac{\phi_{ac} A_e}{h} \right]^{-1} \quad (11)$$

$$\times \frac{\pi c_0^2}{\omega_0 \sqrt{E/3\rho} (1-\nu^2)} \left[\frac{\sigma A_e \langle \bar{p}^2 \rangle}{h^2} \right]$$

In this expression, Young's Modulus and density have been factored out of the matrices because the entire specimen was aluminum. It should be noted that the units are consistent in the given form, and that $\langle \bar{a}^2 \rangle$ and $\langle \bar{p}^2 \rangle$ are over the same bandwidths.

Constant Evaluation

The remaining constant parameters which must be estimated but cannot be calculated directly are the system coupling factors (ϕ), the system damping (η) and the radiation efficiency (σ). The values of ϕ and σ (as well as modal density) were altered to improve analytical and experimental agreement.

As previously discussed, there are three types of connections for coupled systems on the UpSTAGE vehicle. These are skin panels connected by field joints, skin panels defined only for ease in calculations and not separated by any structured change, and bulkheads connected to the skin.

The field joints are reasonably stiff to displacement. Therefore, the major mode of translating energy across the field joint will be rotation. Since rotation is the only mechanism which will transmit energy into the bulkhead, the mechanism is basically the same for the two. Since data were lacking on these joints, it was assumed that their ϕ values were the same. The value of ϕ was chosen to be of the same order as was found in Reference 6. The initial value used in this study was

$$\frac{\phi_f \Delta \omega_0}{4\pi \omega_0 [E/3\rho (1-\nu^2)]^{1/2}} = 5 \times 10^{-6}$$

f = field joint

The ϕ values for the continuous structure should be greater than the value given above. It was assumed that $\phi_c = 10 \phi_f$. This value did give reasonable analytical results.

The damping of the test specimen was determined by exciting the structure with a hammer and examining the resulting time histories from each accelerometer. The time histories from the various tests were filtered into one-third octave bands, and it was determined that the damping for the total system was $0.005 < \eta < 0.01$ ($\eta = 1/Q = 2 \times$ percent of critical damping). These values were used to calculate the response of the test specimen.

The radiation efficiency used in the preliminary calculations was taken from the experimental data presented in Fig. 7. These data were scaled by both the ring and coincidence frequencies prior to use.

All that remained was to calculate area, thickness, etc., and to perform the required operations. Those constants which are independent of frequency are presented in Table 2, and those which are a function of frequency are given in Table 3 for the 1250 Hz case. The calculations were made at every other third octave. The center frequencies were 500, 800, 1250, 2000, and 3150 Hz.

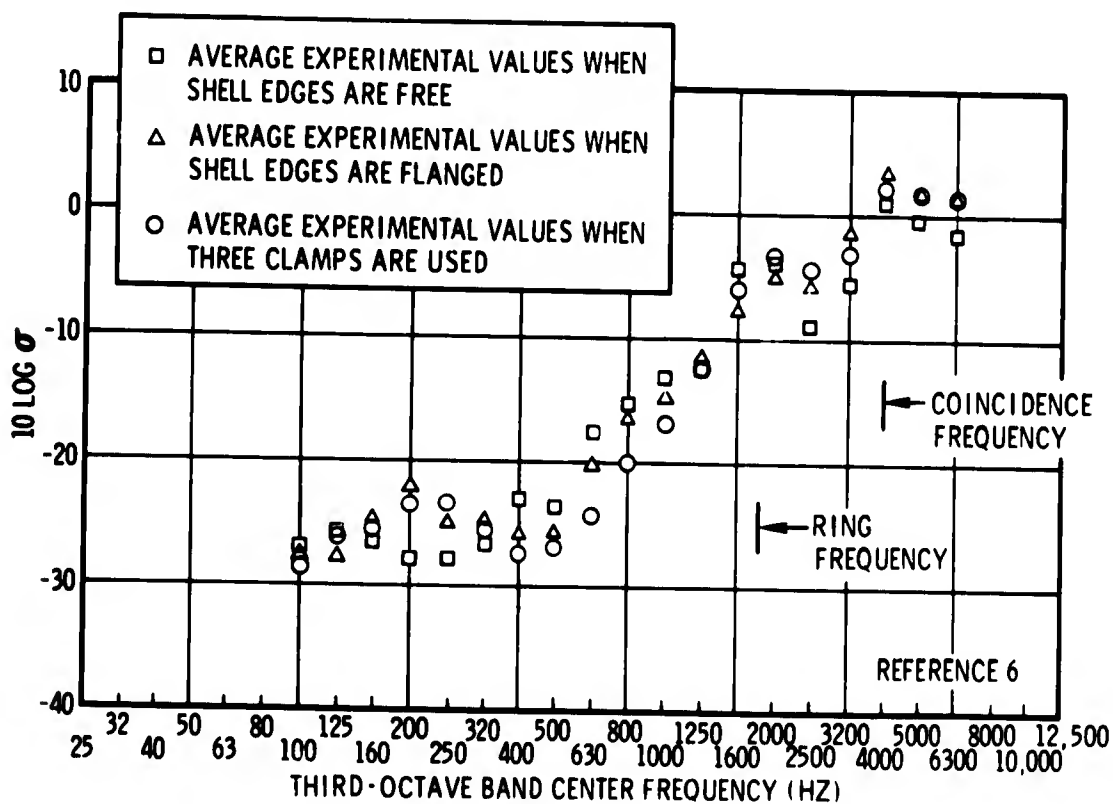


Fig. 7 - Radiation efficiency of cylindrical shell

TABLE 2
Constants for Mathematical Model

Section	Area (A)	Thickness		Freq (Hz)	A/t ²	A/t	At
		(t)	(t) ²				
1 & 3	172.5	0.31	0.096	1,025	1,795	557	53.5
2 & 4	70.5			4,250	733	227	21.8
5 & 7	107.0	0.16	0.026	1,065	4,180	670	17.1
6 & 8	43.5			4,425	1,700	272	6.95
9 & 11	108.5	0.16	0.026	1,100	4,240	678	17.35
10 & 12	44.5			4,550	1,740	278	7.13
13 & 15	250.5	0.16	0.026	1,165	9,800	1,770	40.0
14 & 16	102.0			4,820	4,000	638	16.3
17 & 19	757.0	0.125	0.013	1,530	57,400	6,150	94.6
18 & 20	309.0			6,370	23,300	2,460	38.5
21 & 23	269.0	0.125	0.013	2,225	21,500	2,150	33.7
22 & 24	109.5			9,250	8,250	875	13.7
25 & 27	254.0	0.090	0.008	5,000	31,400	2,820	22.9
26 & 28	103.0			21,000	12,700	1,145	9.27
29	733.0	0.25	0.063	NA	NA	2,940	183.2
30	13.5	0.09	0.008	NA	NA	150	1.21
31	497.0	0.125	0.013	NA	NA	4,000	62.0
32	213.0	0.08	0.0064	NA	NA	2,660	17.0
33	108.0	0.09	0.0081	NA	NA	1,200	9.7
34	573.0	0.09	0.0081	NA	NA	6,370	51.3
35	550.0	0.09	0.0081	NA	NA	6,120	49.5
36	450.0	0.08	0.0064	NA	NA	5,520	36.0
37	375.0	0.08	0.0064	NA	NA	4,630	30.0
38	298.0	0.08	0.0064	NA	NA	3,770	31.8
39	169.0	0.07	0.0049	NA	NA	2,420	11.9
40	138.0	0.07	0.0049	NA	NA	1,970	9.6
41	86.5	0.09	0.0081	NA	NA	950	7.7
42	65.3	0.07	0.0049	NA	NA	930	4.2
43	50.3	0.07	0.0049	NA	NA	720	3.5
44	37.0	0.07	0.0049	NA	NA	578	2.6
45	24.2	0.07	0.0049	NA	NA	346	1.7

TABLE 3
Frequency Dependent Constants
1250 Hz Data

Sec. No.	$\frac{f}{f_r}^*$	$(\frac{f}{f_r})^{2/3}$	σ	$\frac{A}{t^2} \cdot \sigma \cdot (\frac{f}{f_r})^{2/3}$	$\frac{A}{t} (\frac{f}{f_r})^{2/3}$
1 & 3	1.0	1.0	0.5	897.5	557
2 & 4	0.294	0.441	0.008	2.59	100
5 & 7	1.0	1.0	0.5	2,090	670
6 & 8	0.283	0.43	0.008	5.86	117
9 & 11	1.0	1.0	0.5	2,120	678
10 & 12	0.275	0.422	0.008	5.87	117
13 & 15	1.0	1.0	0.5	4,900	1770
14 & 16	0.26	0.4065	0.008	13	259
17 & 19	0.816	0.873	0.25	12,530	5370
18 & 20	0.196	0.338	0.004	31.5	832
21 & 23	0.561	0.67	0.063	905	1207
22 & 24	0.135	0.263	0.004	8.7	230
25 & 27	0.25	0.396	0.004	49.8	1117
26 & 28	0.06	0.152	0.0031	6.03	174
29	NA	NA	0.08	940	2940
30	NA	NA	0.02	33.2	150

*Values of f/f_r greater than unity are set equal to one.

TEST PROGRAM

In the first test of interest, the test specimen was suspended by bungee in the reverberation chamber, as shown in Fig. 4. In this case, the outer structure was excited uniformly, resulting in a case where the response is a strong function of damping and radiation resistance, and the effect of energy being transmitted along the structure is minimized.

Discussion of the second test of interest where only the aft closure was excited requires some description of the MDAC test facility used. This test was performed by using adjacent reverberation and anechoic chambers connected by a doorway, as shown in Fig. 8. A door was constructed with an elliptical opening. The first test performed using this configuration consisted of inserting the test specimen in the door so that only its base was exposed to the reverberation chamber, as shown in Fig. 9. The reverberation chamber was excited exposing the base to reverberant acoustical energy. The

transmission of energy along the specimen and, therefore, the energy distribution is controlled by the panel-to-panel coupling (ϵ) and damping while the effect of radiation efficiency is minimized.

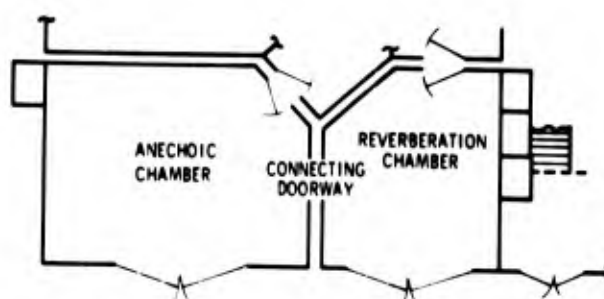


Fig. 8 - Test facility

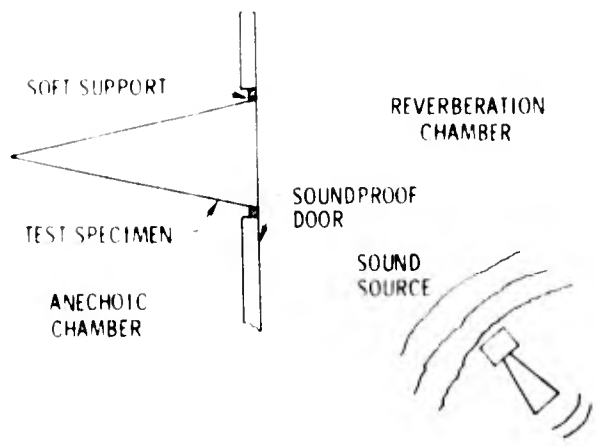


Fig. 9 - Reverberant acoustic excitation of base

The net result was three tests which were controlled by the three primary parameters. The first was a standard decay test to define damping as discussed in the previous section. The second was a test where the total structure was excited acoustically and was controlled by radiation efficiency and damping. The third was a test where the energy was introduced at the base, and the response was controlled by the coupling between sections and damping. Assuming the damping values were well chosen (damping, at best, is a difficult parameter to estimate or measure), then agreement between test and measurement would confirm not only the approach and model but also the constants used in that model.

The test specimen was instrumented as shown in Fig. 10, plus several transducers located on the Laser Triad Rate Gyro (LTRG). The transducers of primary interest were those along the specimen skin (4, 8, 11, 13 and 15) as well as

the inputs to the LTRG. In addition, accelerometers numbered 1, 2, and 3 were added to monitor response of the base and of heavily weighted skin; 6 and 9 to check symmetry of response; 5 and 12 to monitor response of the small radius of the ellipse; and 7, 10, 14 and 16 to monitor bulkhead response. The results of 1, 2 and 3 are of no direct interest here; 6 and 9 did show the expected symmetry; 5 and 12 were of secondary importance and were not considered in detail; and 7, 10, 14 and 16 showed that bulkhead response was overestimated. The ϕ_0 between the bulkheads and the outer structure was reduced to one-third the original value to lower the prediction responses.

The modal densities in the last two elliptical sections (Sections III and IV) were reduced to one-third and one-half their original values at 500 and 800 Hz, respectively. This was done to reduce the predicted response and thereby improve the agreement in the lower frequencies. This change was justified on the basis that the expression used could easily overestimate the modal densities in the low frequencies for the small panels considered.

At 500 Hz and 800 Hz, the vibration levels for the reverberation test were underestimated in Section II (see Fig. 10) and overestimated in Sections III and IV. To compensate for this, the radiation efficiency was multiplied by 4, 1/4, and 1/4 for the respective sections. At 1250 Hz, the area of underestimate had moved forward to Section III and the estimates were still high in IV. σ was multiplied by 4 in Section III and 1/4 in IV. At 2000 Hz, the σ was multiplied by 4 in Section IV to correct the underestimate and no corrections were added to the 3150 Hz model. These corrections did not completely eliminate the observed discrepancies but it was not felt that further alterations were justified.

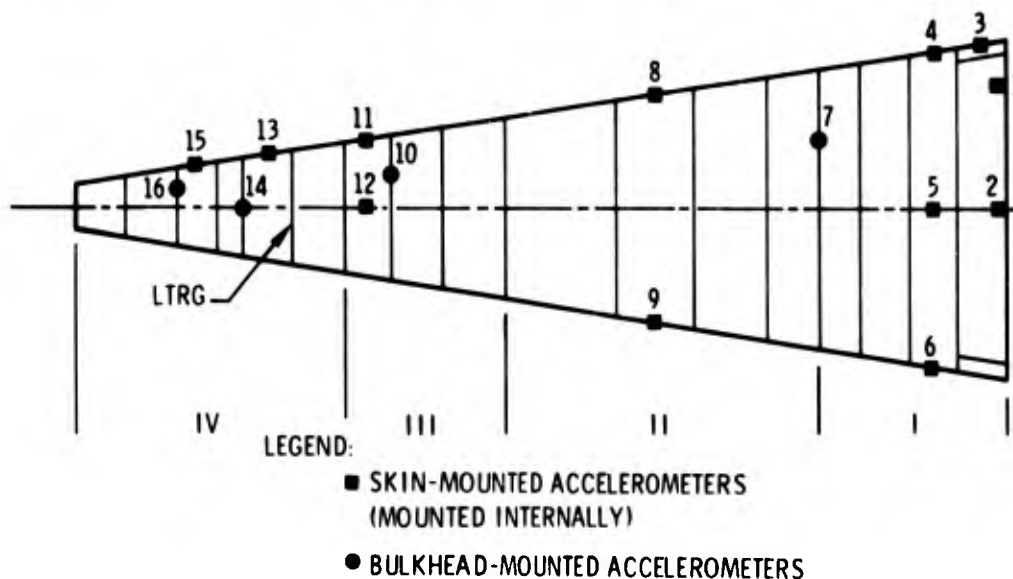


Fig. 10 - Accelerometer location

The comparison between the measured response and the predicted response using the two values of damping and the final values of the constants are given in Figs. 11 and 12. The curves labeled I, II, III and IV correspond with the areas indicated in Fig. 10.

The reverberant excitation case shows good agreement in areas I and II. In Section III a peak at 1250 Hz exists that is not predicted in the theory, but there appears to be a notch at this frequency for Section IV and the LTRG. The agreement between measured and predicted values at 2000 and 3150 Hz is quite acceptable for Section III and the LTRG, but the measurement exceeded the prediction for Section IV. It is pointed out that the LTRG is an extremely large component and could effect the levels in III and IV.

In evaluating these data, one must keep in mind that the intent is to evaluate an approach

and, therefore, some error in a parameter like damping is acceptable since it will be different in the flight model. If all of the predicted levels were raised slightly (lower damping), the agreement in Sections I and II would be quite good, and the average value of III, IV and the LTRG would be acceptable.

When just the base of the system is excited, the relative comparison becomes much more important than the absolute comparison. This is because the acoustic acceptance of the plate is not of concern since it in no way represents flight hardware. It is just a method of introducing energy into the aft portion of the vehicle. The data presented in Fig. 12 is normalized by the measurement made in Section I. The agreement in II is all that can be expected, and in III it is surprisingly good. In Section IV and on the LTRG, the environment is again overestimated at 1250 Hz and underestimated at 2000 Hz. The agreement is good at 3150 Hz.

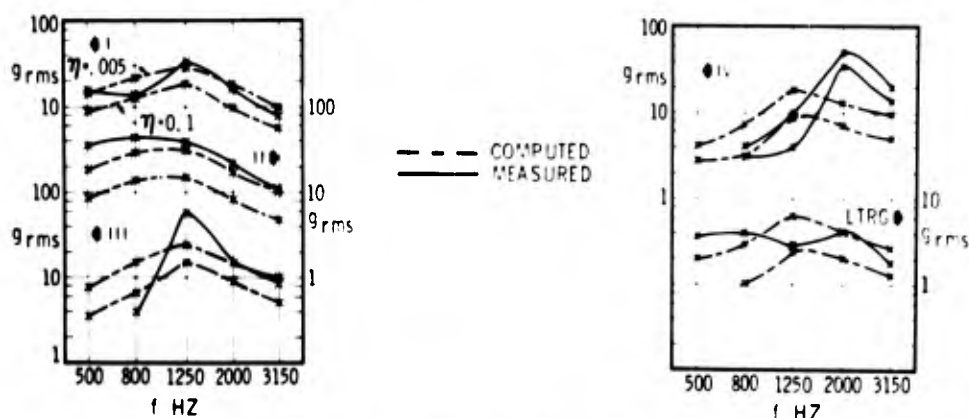


Fig. 11 - Comparison of predicted and measured response -- reverberant field excitation

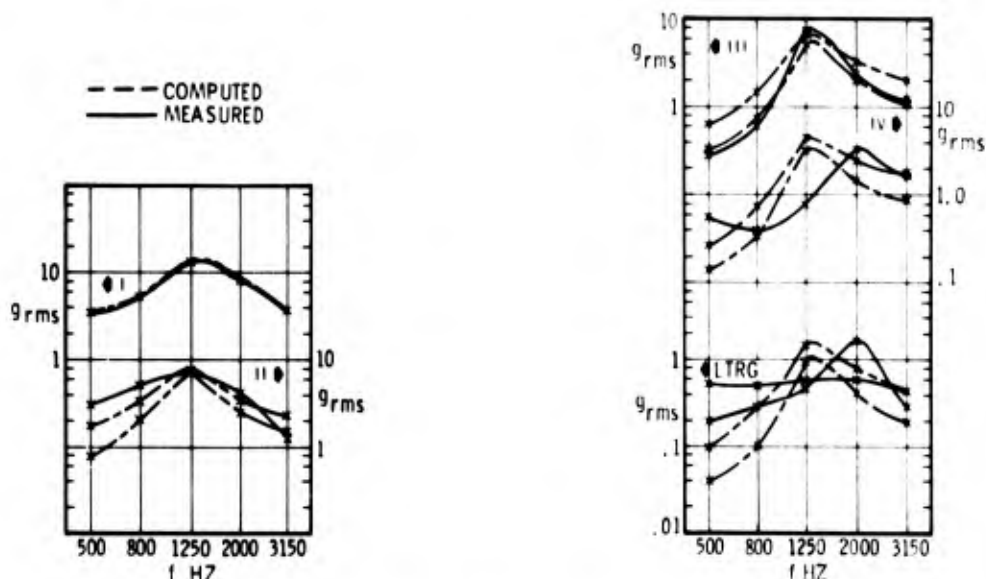


Fig. 12 - Comparison of predicted and measured response -- aft closure excitation

The last test of interest also made use of the two rooms separated by the door. The general setup is shown in Fig. 13, the details are shown in Fig. 14, and a photograph of the setup is shown in Fig. 15. In this case, the system is excited over 11 inches of one side of the vehicle in a manner similar to that which will exist due to the separated flow condition in flight. In comparing prediction to test

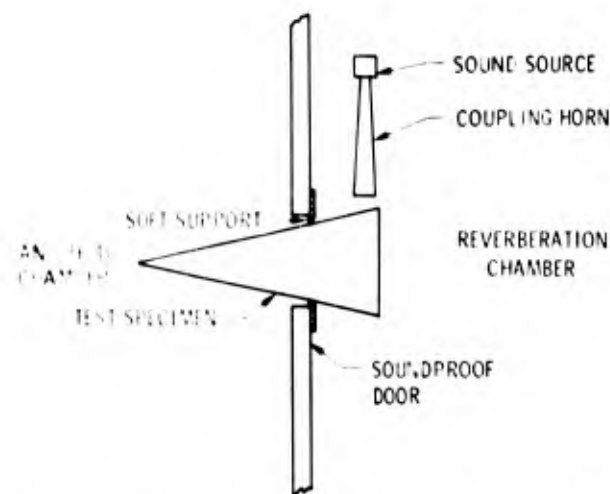


Fig. 13 - Direct impingement test configuration

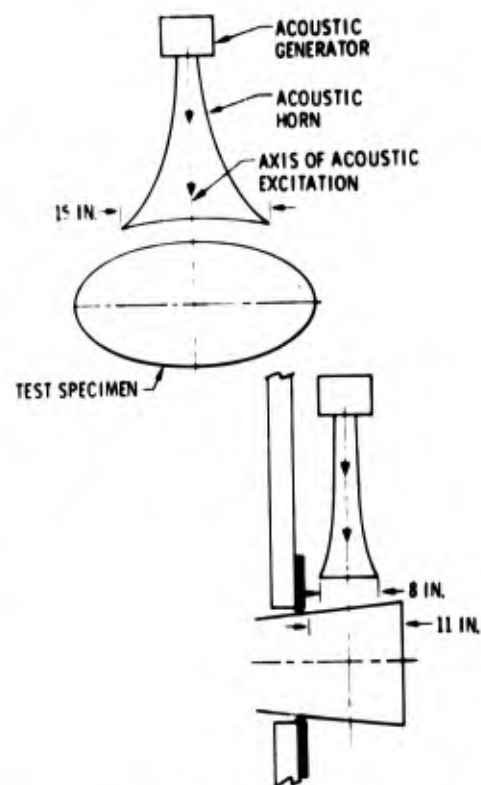


Fig. 14 - Configuration of acoustic generator/horn for direct impingement acoustical test

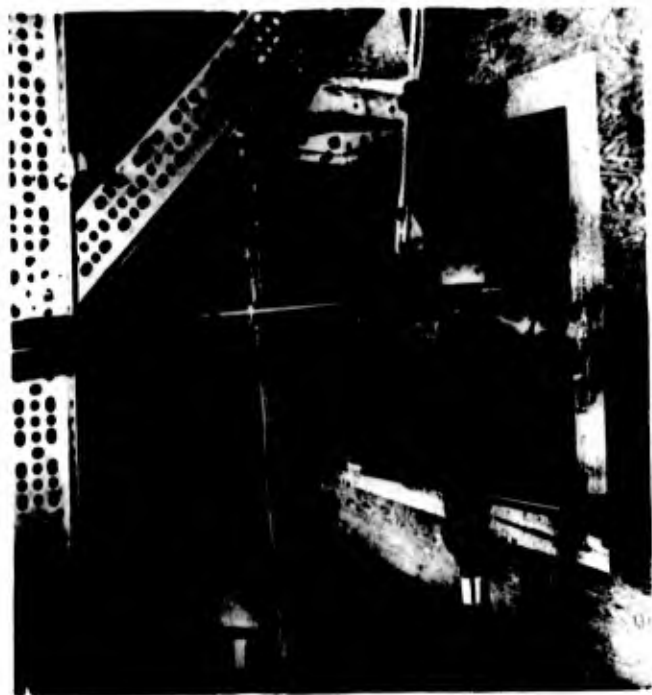


Fig. 15 - Direct impingement test configuration

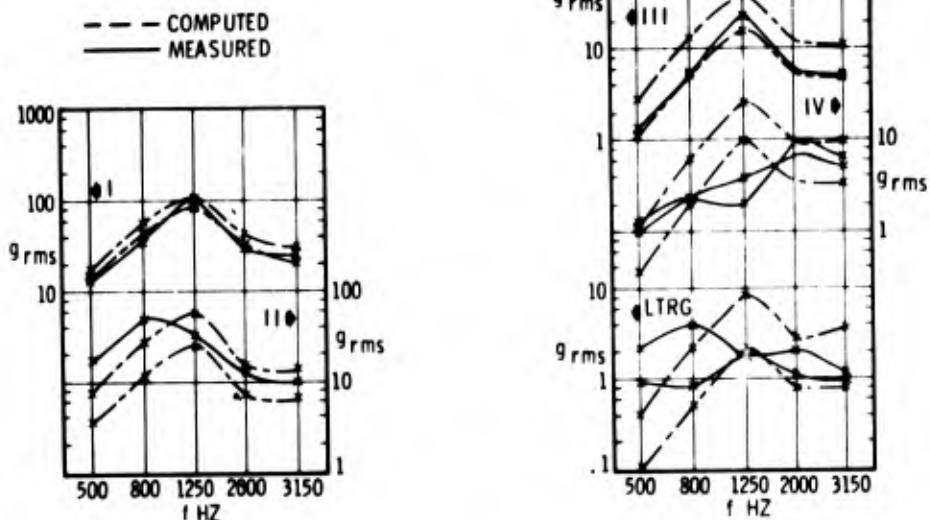


Fig. 16 - Comparison of predicted and measured response -- local excitation

(Fig. 16), the general observations are the same as those for the aft end reverberant excitation, except that the measured values are less than predicted at 2000 Hz on the LTRG and the same as the high band in Section IV. The apparent lack of damping observed in the reverberation case did not appear. This indicates that the overall radiation efficiency may have been underestimated.

FLIGHT CONFIGURATION

Modeling of the flight vehicle consists primarily of modifying the model of the test specimen. This modification consisted of updating skin thicknesses, modeling the base plate, adjusting the damping and incorporating the systems components.

The damping for the outer skin was obtained by performing "bop" tests on the elliptical specimen shown in Fig. 17 which has flight ablative. The resulting value of the damping parameter η was 0.02. The damping for the internal components is more difficult to define. The following values of damping were assigned based on engineering judgment.

The electronic components were assigned an η value of 0.1 (5 percent of critical damping). These components are densely packed and are potted so that a fairly high damping value is justified. The plumbing, fuel tanks and gas generators were assigned values of $\eta = 0.05$. This value for the fuel tanks and gas generator is probably low for the early portion of flight but will be more realistic towards the end of flight. The separated flow also maximizes late in flight. Damping values of bulkheads or frames not containing components were assumed to

be 0.05. Since the modal densities of these frames are small, their damping values will only have secondary effects.

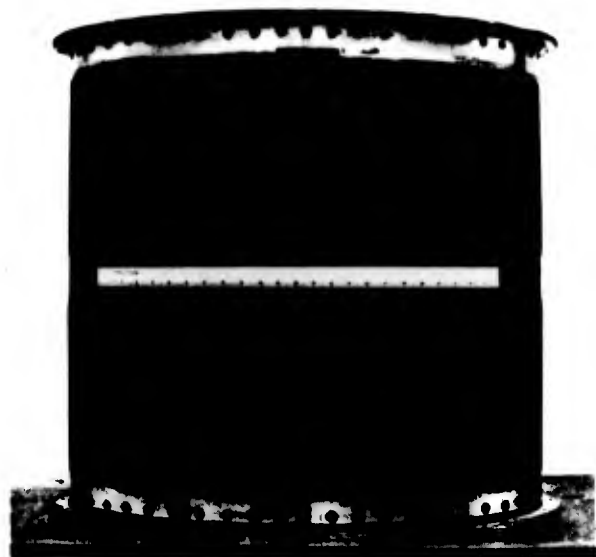


Fig. 17 - Elliptical cylinder with flight insulation

The modal density of the components is as critical as the damping. The majority of the components are made from investment castings with skin thicknesses on the order of one-eighth inch. It was assumed that the components would have modal densities equal to a one-eighth inch aluminum plate with the same surface area as the component.

The component modal densities and weights were added to the appropriate bulkheads in the model.

Flight Forcing Function

The sources of random vibration during flight are launch acoustics and flight aerodynamic noise. The launch acoustics are of short duration and were treated as a launch shock. The aerodynamic noise results from the turbulent boundary layer which excites the vehicle throughout flight and separated flow which exists during separation and maneuvers. The separated flow occurs only over a small portion of the vehicle, but the high fluctuating pressure levels (FPL's) result in it being a major source of vibration.

Aerodynamic noise resulting from the turbulent boundary layer was estimated by using available data. The RMS fluctuating pressure values reported by several investigators are presented on Fig. 18. The line on this figure was used in the UpSTAGE analysis.

Frequency spectra of the pressure fluctuations were normalized to a Strouhal number based on boundary layer momentum thickness (θ), local free stream velocity and frequency. Fig. 19 shows the normalized aerodynamic noise spectra. Fig. 20 presents the predicted environmental level at Station 97 for flight time of $t = 1.43$.

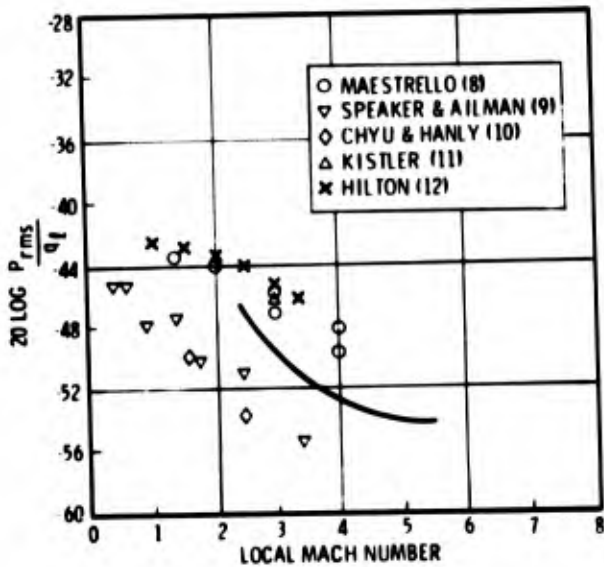


Fig. 18 - Ratio of fluctuating pressure to dynamic pressure as a function of mach number

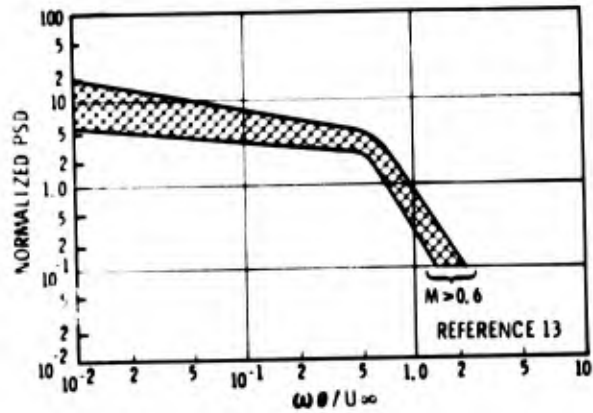


Fig. 19 - Nondimensional power spectra of the wall pressure fluctuations

The shift in the cutoff frequency as a function of θ (Fig. 19) will result in lowering the environment as the station number is reduced. To account for this, the environment was reduced 2 dB for Sections II and III, and 4 dB for Section IV.

The RMS value of the aerodynamic noise in the separated flow field is amplified by an amount dependent on the static pressure rise, as shown in Fig. 21. The variation of this amplification as a function of frequency is shown in Fig. 22. Using these two figures, the corresponding fluctuating pressure levels at $t = 1.43$ in the separated flow were obtained and are also shown in Fig. 20.

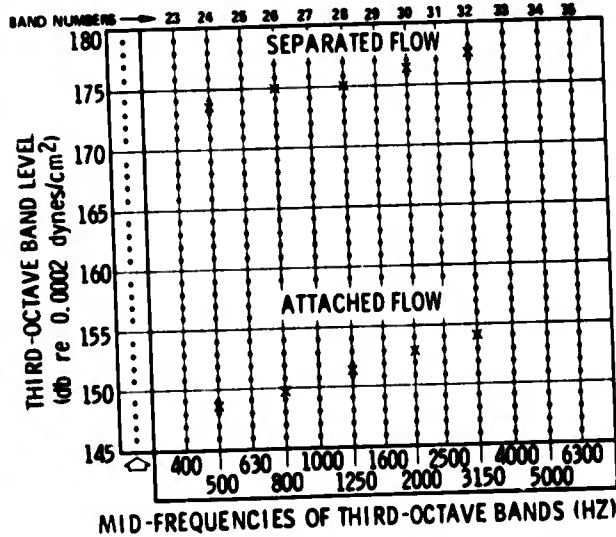


Fig. 20 - Third-octave band fluctuating pressure level at $t = 1.43$ seconds

Local Loading

It is assumed that the power introduced into a panel by an acoustic source is proportional to the area over which that acoustic field exists; that a given system (panel) can be divided into parts; and that the total power input into the system equals the sum of the power that would be introduced into the system if each section were excited separately. This simplifies the modeling required to introduce the local force and is consistent with the SEA as used here. The basic assumption is that the acoustic fields exciting the various local areas are statistically independent and/or the correlated area is small compared with the panel of interest. Close examination of this assumption may limit the minimum size of panels excited by acoustic energy that may be used. Detailed examination of this point was beyond the scope of this analysis.

The extension of the separated flow area forward of the injection centerline of the control gases is shown in Fig. 23 for the indicated flight times. The portion of the separated flow aft of -1 acts over a heavy manifold area of the skin and therefore can be neglected ($S = 1/t$). From -1 to -2 there is a skin doubler resulting in that area being half as effective in accepting energy as is free skin. The final area of concern is forward of -2. The effective length of these combined areas is assumed to be $l_e = .5 + l$ where l = length under the separated flow forward of -2. The power introduced into the structure is assumed to be proportional to this length.

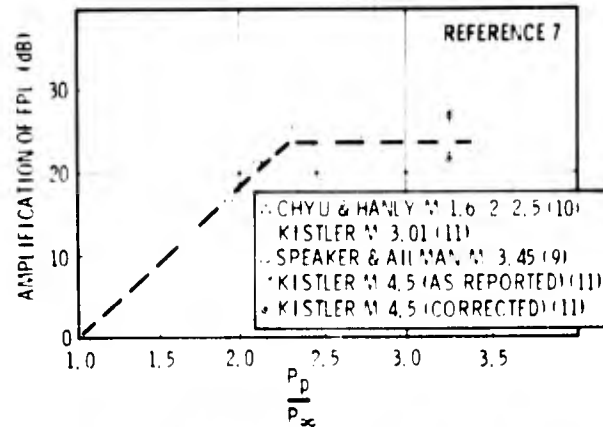


Fig. 21 - Separated flow FPL amplification versus static pressure ratio

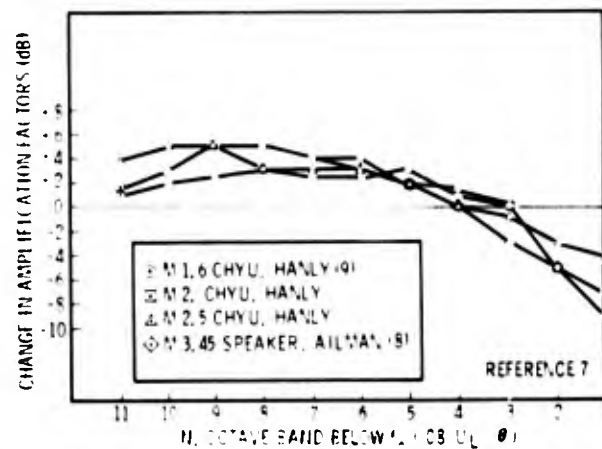


Fig. 22 - Change in amplification factors as a function of frequency

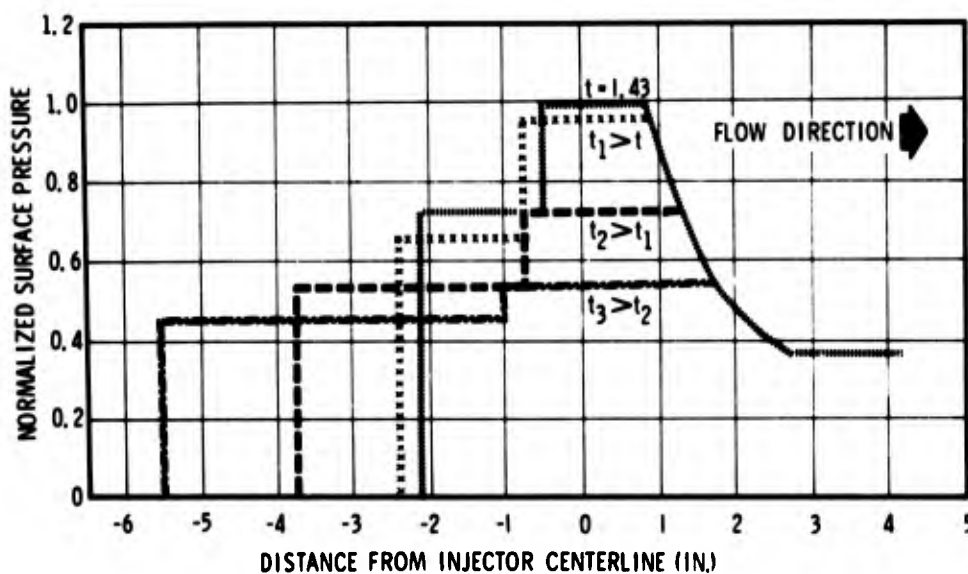
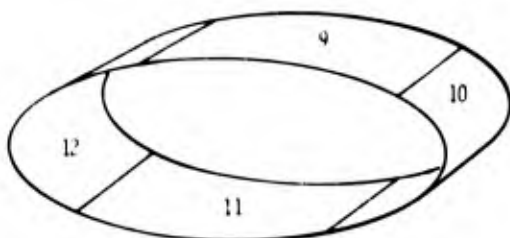


Fig. 23 - Pressure distribution -- control force

Only a portion of the system in the circumferential direction is excited by the separated flow. Consider the sketch shown below which shows the four panels which make up the circumference of the control gas exit station. Fourteen nozzles are located in both sections 9 and 11 to furnish pitch and roll control to the vehicle, and 4 nozzles are located in Stations 10 and 12 to furnish yaw control. Only 10 pitch control valves can be excited at one time.

The "worst case" environment condition occur when 10 pitch control valves are activated on one side in conjunction with the 4 yaw control valves on 10.



The vibratory energy is analytically introduced into the model through a 3-inch long panel. The effective length of the separated area on this panel is 0.7 inch at 1.43 seconds. The total power introduced through 9 and 10 at $t = 1.43$ must be proportional to the length of the separated flow times the fraction of the valves used. This gives

$$S_9 \langle \bar{p}_5^2 \rangle \frac{0.7 \text{ in.}}{3 \text{ in.}} \times \frac{10 \text{ nozzles}}{14 \text{ nozzles}} = 0.165 S_9 \langle \bar{p}_5^2 \rangle$$

$$S_{10} \langle \bar{p}_5^2 \rangle \frac{0.7 \text{ in.}}{3 \text{ in.}} = 0.234 S_{10} \langle \bar{p}_5^2 \rangle$$

$\langle \bar{p}_5^2 \rangle$ = mean squared FPL value in the separated flow region.

The response of the total system was then calculated by applying the attached boundary layer FPL's to the system and adding the resulting mean squared acceleration to that resulting from the local excitation. The environment predictions for later inflight times were obtained by scaling the calculated responses to both attached and separated flow at $t = 1.43$ seconds and adding the resulting mean squared values.

This approach did require some very specific assumptions concerning the excitation of structure by aerodynamic noise. It was assumed that the aerodynamic noise would excite the structure to the same levels as would reverberant acoustic energy, with one exception. The coincident effects have been eliminated from

the radiation efficiency term because of the high Mach number of interest. This does not imply that coincidence does not occur during flight, but that it would occur at a frequency above the range of interest.

Flight Predictions

The calculations for all of the flight predictions were put into power spectral density of acceleration (PSD) form by dividing the 1/3 octave mean squared values by Δf . The maximum PSD value for each section at 500, 800, 1250, 2000 and 3150 Hz are presented in Table 4.

The predicted environment for the majority of the equipment can be obtained directly from this table by identifying the section which contains the component of interest. The three general categories of interest are the densely packed electronics in the forward part of the vehicle, the two electronic packages at Station 88 and the valves located in the manifold area at Station 97. The predicted levels for these areas are presented in Figs. 24, 25 and 26.

The aft flight control accelerometers are also of interest and are located on the base plate close to the small radius, as shown in Fig. 27. The calculated response level of the base plate is controlled by the power flow from Sections 1 and/or 3, while the accelerometer environment will be controlled by the power flow from 2 or 4 depending on the side of interest. The accelerometer environment was obtained by

$$\bar{a}_{ac}^2 = \bar{a}_b^2 \times \frac{\bar{a}_2^2}{\bar{a}_1^2}$$

The resulting environment is presented in Fig. 28.

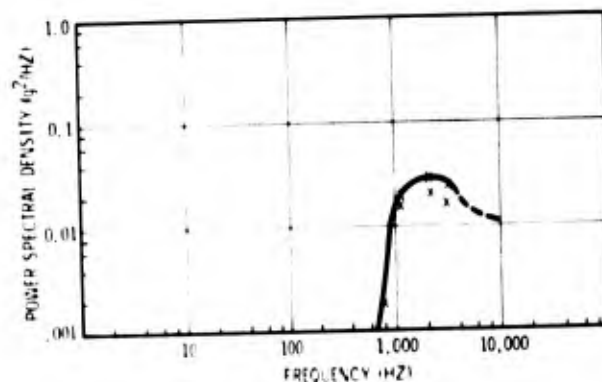


Fig. 24 - Envelope of forward electronic equipment environment

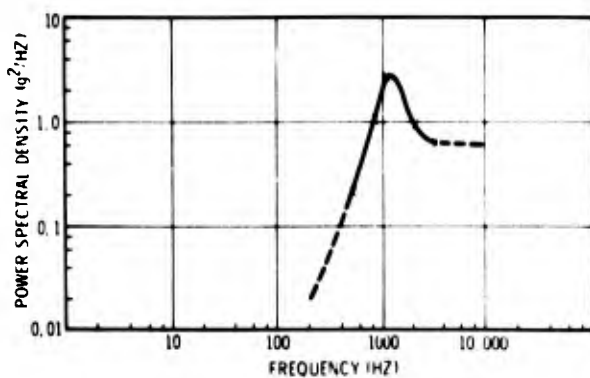


Fig. 25 - Envelope of aft electronic equipment environment

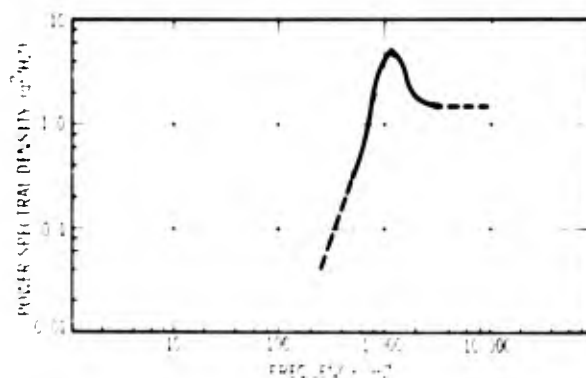


Fig. 28 - Envelope of control accelerometer environment

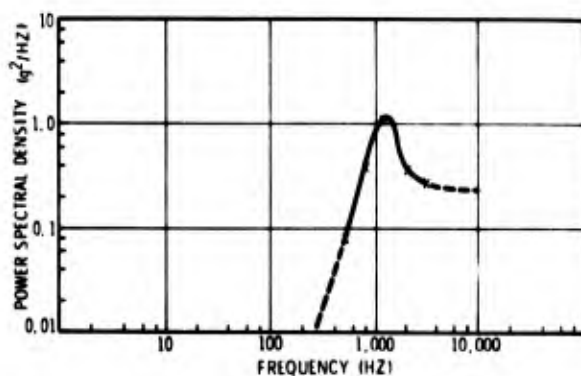


Fig. 26 - Envelope of manifold environment

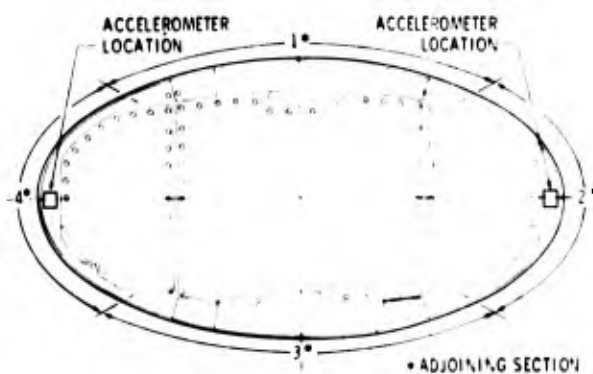


Fig. 27 - Base plate configuration

SUMMARY AND CONCLUSIONS

This document has presented a development of the method used to predict the flight environment for the UpSTAGE vehicle. This development included a rather extensive test program which verified the approach, model, and physical parameters for the load-carrying structure. The method was then extended to the flight configuration by using assumptions based on available data and experience.

The assumptions used to extend the model deal primarily with component modal density, damping and the efficiency of the boundary layer in exciting the structure. These assumptions can be evaluated by meaningful ground and flight tests.

The general conclusions are as follows:

- The method presented is logical and sound for environmental predictions.
- Additional experimental data are required before complete confidence can be placed in its results.

ACKNOWLEDGEMENT

The authors would like to express their appreciation to J. R. Donahue and R. M. Blythe who were responsible for performing the acoustical tests.

TABLE 4
Predicted UpSTAGE Environments
 g^2/Hz

Section	Frequency (Hz)				
	500	800	1250	2000	3150
1 & 3	.66	5.8	14.7	4.27	2.5
2 & 4	.09	2.5	6.5	7.26	1.74
5 & 7	3.24	11.2	27.3	7.73	4.35
6 & 8	.55	1.7	5.1	2.42	3.17
9 & 11	11.4	57.3	12.3	34.7	19.1
10 & 12	2.5	8.3	19.7	11.2	22.7
13 & 15	3.5	20.1	47.4	13.0	7.2
14 & 16	.67	3.98	10.5	4.4	4.5
17 & 19	.8	5.6	12.4	5.43	2.69
18 & 20	.24	1.67	3.8	2.16	1.51
21 & 23	.085	.85	5.02	4.78	2.23
22 & 24	.029	.23	1.8	1.61	.96
25 & 27	.02	.086	1.03	1.44	1.21
26 & 28	.012	.027	.316	.468	.41
29	.39	4.4	11.4	3.54	2.3
30	---	---	---	---	---
31	.21	1.25	2.69	.969	.57
32	.19	1.22	2.59	1.38	.66
33	.018	.155	1.02	.981	.52
34	.08	.90	1.14	.353	.27
35	.75	4.34	13.4	3.95	2.6
36	.66	4.36	8.7	4.25	2.1
37	.66	4.35	8.68	4.24	2.1
38	.041	.27	.54	.263	.132
39	.02	.19	1.17	1.13	.54
40	.003	.03	.19	.173	.083
41	---	---	.02	.03	.024
42	---	---	.023	.033	.028
43	---	.0035	.042	.059	.049
44	---	---	.0155	.022	.018
45	.0036	.014	.167	.238	.197

REFERENCES

1. E. E. Ungar, "Fundamentals of Statistical Energy Analysis of Vibrating Systems," AFFDL-TR-66-53, May 1966
2. J. E. Manning, R. H. Lyon, T. D. Scharton, "Transmission of Sound and Vibration to a Shroud-Enclosed Spacecraft," NASA CR-81688, October 1966, (N67 18035)
3. R. H. Lyon, et al., "Studies of Random Vibration of Coupled Structures in Electronic Equipment," ASD-TDR-63-205, Vol. I - November 1962, Vol. II - March 1964
4. P. M. Morse, "Vibration and Sound," Second Edition. McGraw-Hill Book Co., Inc., 1948
5. E. E. Ungar, N. Koronaios, and J. E. Manning, "Application of Statistical Energy Analysis to Vibration of Multi-panel Structures," AFFDL-TR-67-79, August 1967
6. R. H. Lyon and G. Maidanik, "Statistical Methods in Vibration Analysis," AIAA Journal, Vol. 2, pp. 1015-1024, June 1964
7. R. D. Hellweg, "Estimating Aerodynamic Noise Including Boundary Layer Injection Effects." Presented at National Aeronautics and Space Engineering Meeting - SAE, October 1970
8. L. Maestrello, "Radiation From and Panel Response to a Supersonic Turbulent Boundary Layer," J. of Sound and Vibration, Vol. 10, No. 2, pp. 261-295, September 1969
9. W. V. Speaker and C. M. Ailman, "Spectra and Space-Time Correlations of the Fluctuating Pressures at a Wall Beneath a Supersonic Turbulent Boundary Layer Perturbed by Step and Shock Waves," NASA CR-486, May 1966
10. W. J. Chyu and R. D. Hanly, "Power and Cross-Spectra and Space-Time Correlations of Surface Fluctuating Pressure at Mach Numbers Between 1.6 and 2.5," AIAA paper 68-77, January 1968
11. A. L. Kistler, "Fluctuating Wall Pressure Under a Separated Supersonic Flow," JASA, Vol. 36, No. 3, pp. 543-550, March 1964
12. D. A. Hilton, "Scout-Vehicle Aerodynamic-Noise Measurements," SOUND, Vol. 2, No. 5, pp. 28-31, September-October 1963
13. C. M. Ailman, "On Predicting Fluctuating Pressures at a Wall Beneath a Turbulent Boundary Layer." Presented to Acoustical Society of America, New York, New York, April 1967. Published in Douglas Paper No. 4331, McDonnell Douglas Astronautics Company-West.

DISCUSSION

Mr. Kana (Southwest Research Institute): I am curious as to how you arrived at the form of the excitation for our system. Did you have flight data to obtain the spatial distribution,--and if so, it was significantly different from the apparent symmetrical and reverberant form that you had?

Mr. Hines: We assumed that we had the normal boundary layer type excitation of the major part of the vehicle, that the reverberant field in the boundary layer would have the same efficiency in exciting the vehicle. In the portion where we had the step function, or the separated flow, wind tunnel tests, for the purpose of obtaining static data rather than fluctuating pressure data, indicated that the flow is very similar to what you would see when you have a step, so we used the fluctuating pressure levels from the step data. Again we had to assume it had the same efficiency as the excitation that we could produce in the laboratory. Obviously, to check this we need some flight data. There are five vehicles and we do have four vibration measurements per vehicle so we will be able to confirm or disprove this eventually but we have not done it yet.

Mr. Unger, Bolt Beranek & Newman: You said that you had analyzed something like 45 different lumps and to use all these lumps you need to know the power flow coupling coefficients between all these lumps. How did you obtain these?

Mr. Hines: We used what I think was some of your data. At least it was BB&N data where you had the cylinder which was divided into three or four sections separated by stringers. As a first guess we took that as the coupling factor, and one of the primary reasons for running the experiment was to determine how good these coupling factors were. I have to admit that either we were pretty lucky or you had some pretty good coupling factors because the agreement was quite good.

Mr. Unger: I clearly cannot quarrel with an answer like that. But I have a real nasty question, if you don't mind? And that is: you had the real vehicle, or you had a good model, and I think you really wanted to find the response of this model to a certain distribution of environments. Why did you not just measure what you wanted to know rather than going through this analysis?

Mr. Hines: We had a real vehicle up to a point. This analysis was performed early in the development. The skin gauges, although they were close, did change as we did the loads analysis. We did not have any components in it. We chose not to dummy up the weight in the component, because I felt that we would be forced to make a correction for the dummy components and then we would have to correct somehow for the real component. Basically

we used the statistical energy approach to scale the experimental data instead of taking that data directly. We used the experimental data to confirm the model and turned around and used the model to predict the results.

Mr. Hou (Bellcom): I can see your testing confirmed your predictions. But how did you arrive at your predictions?

Mr. Hines: We started out with a two degree of freedom system, or two systems, and expanded this to the 45 systems that are used. We calculated the modal densities, and coupling factors, etc., and then we used a matrix subtraction technique to solve the 45 degree-of-freedom or 45 panel system.

ON THE REDUCTION AND PREVENTION OF THE FLUID-INDUCED
VIBRATIONS OF CIRCULAR CYLINDERS OF FINITE LENGTH

Dirse W. Sallet
Department of Mechanical Engineering
University of Maryland
College Park, Maryland

and

U.S. Naval Ordnance Laboratory
White Oak, Silver Spring, Maryland

The self excited vibrations which elastically suspended circular cylinders will exhibit when exposed to uniform viscous fluid flow have received ample attention by various investigators in the past decade. Usually such flutter motions are highly detrimental to the proper functioning of the particular system or devices for a variety of reasons such as fatigue failures, noise production and intolerable secondary motions. This report discusses a method which prevents the unsteady pressure distribution around the cylinder and thereby eliminates the fluid induced vibrations.

INTRODUCTION

When a circular cylinder is exposed to cross flow of a viscous fluid such as air or water, vortex shedding will occur once the Reynolds number based on the cylinder diameter and the approach velocity exceeds the value of 50. The vortices are shed in an alternating fashion. The relation between the frequency of the vortex shedding f , the fluid velocity U and the diameter of the cylinder D is

$$f = S \frac{U}{D} \quad (1)$$

The constant of proportionality S , the so-called Strouhal number is a function of the Reynolds number. In the range $2000 \leq Re \leq 100,000$, S lies between 0.18 and 0.21. A summary of the experimentally determined values of S in the various Reynolds number ranges is given in reference 1. Due to the vortex shedding an alternating pressure distribution acts on the surface of the cylinder, giving rise to periodically varying lift forces (ref. 2). These lift forces cause the fluid-induced vibrations which have been observed on submarine periscopes, submerged towed blunt bodies with length to width ratios larger than one (and equivalently, on similar, submerged moored bodies when currents exist) and on cables in fluid flow (cable strumming). The magnitude of the periodical lift forces may be as large as the drag force. It is therefore of importance to neutralize these alternating lift forces. This may be accomplished in three, basically different ways: One, purely mechanically, by detuning or installation of proper

damping devices. Detuning is accomplished by insuring that the natural frequencies of the vibrating system (the system which is prone to flutter) do not coincide or come within a certain limit range of the vortex shedding frequency. As is easily recognized from reference 1, for prevention of flutter in cases where the vibrating body has approximately the same average density as the flowing medium to which it is exposed, it is best to insure that the natural frequencies of the vibrating system are well below the vortex shedding frequency. The installation of proper damping devices is not always technically feasible or may create undesirable side effects, such as noise. Two, purely fluid mechanically, by partial or total prevention of the uniform vortex growth in the wake of the body. Three, again purely fluid mechanically, by the prevention of alternating vortex shedding. The last two methods are currently being investigated by the author. This report will discuss method three, the prevention of alternating vortex shedding. The initial theoretical considerations were already reported in reference 3 but will be here repeated for completeness sake.

POTENTIAL FLOW MODEL

For flow velocities for which the Reynolds number is smaller than 50, two symmetrical vortices will form behind the cylinder; these vortices will not shed as long as the Reynolds number stays below 50. A simulation of flow around a cylinder with two symmetrical vortices behind the cylinder is accomplished as follows:

Let the complex potential for two-dimensional flow be

$$w(z) = \varphi(x, y) + i\psi(x, y) \quad (2)$$

Then the complex velocity is

$$\frac{dw}{dz} = u - iv \quad (3)$$

where

$$u = \frac{\partial \varphi}{\partial x} = \frac{\partial \psi}{\partial y} \quad (4)$$

and

$$v = \frac{\partial \varphi}{\partial y} = -\frac{\partial \psi}{\partial x} \quad (5)$$

A closed circular stream line, with a radius equal to unity, representing the cylinder in uniform flow is formed by the complex potential

$$w_c = U \left(z + \frac{1}{z} \right) \quad (6)$$

while the potential of vortex 1 and vortex 2 is

$$w_1 = + i K \log (z - z_1) \quad (7)$$

$$w_2 = - i K \log (z - z_2) \quad (8)$$

To retain the unit circle as a stream line (see fig. 1) when adding equations (6), (7) and (8), the images of vortices 1 and 2 (with respect to the circle)

$$w_{11} = + i K \log (z - z_{11}) \quad (9)$$

$$w_{22} = - i K \log (z - z_{22}) \quad (10)$$

must be included (Thomson's theorem). Summing equations (6) through (10) yields

$$w = U \left(z + \frac{1}{z} \right) + i K \log \frac{(z - z_1)(z - z_{11})}{(z - z_2)(z - z_{22})} \quad (11)$$

By choosing a cylinder with a unit radius all distances are expressed in radii.

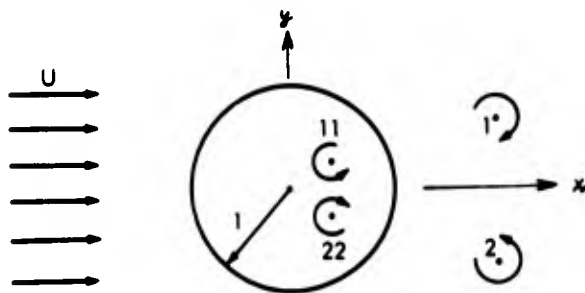


Fig. 1 Nomenclature of Vortices

According to Thomson's principle

$$z_{11} = \frac{1}{z_1} \quad (12)$$

and

$$z_{22} = \frac{1}{z_2} \quad (13)$$

so that

$$x_{11,22} = \frac{x_{1,2}}{\frac{x_{1,2}^2}{2} + y_{1,2}^2} \quad (14)$$

and

$$y_{11,22} = \frac{y_{1,2}}{\frac{x_{1,2}^2}{2} + y_{1,2}^2} \quad (15)$$

By setting the propagation velocities of the vortices 1 and 2 equal to zero, Föppl (ref. 4) obtained

$$\pm 2y_{1,2} = r_{1,2} - \frac{1}{r_{1,2}} \quad (16)$$

and

$$K = 2 \cdot U y_{1,2} \left(1 - \frac{1}{r_{1,2}^4} \right) \quad (17)$$

where

$$r_{1,2} = \sqrt{x_{1,2}^2 + y_{1,2}^2} \quad (18)$$

and

$$r_1 = r_2$$

since x_1 equals x_2 and y_1 equals $-y_2$ for the here assumed symmetrical case.

Equation (16) gives the loci at which the two vortices must be, if they are stationary with respect to the cylinder (see fig. 2).

Equation (17) correlates the strength K of such a stationary vortex with its position behind the circular cylinder and the free stream velocity U . For instance, at constant free stream velocity the vortex strength increases as the vortex pair moves away from the cylinder on the Föppl path.

The flow pattern obtained from the mathematical model, namely equation (11) is shown in figure 3.

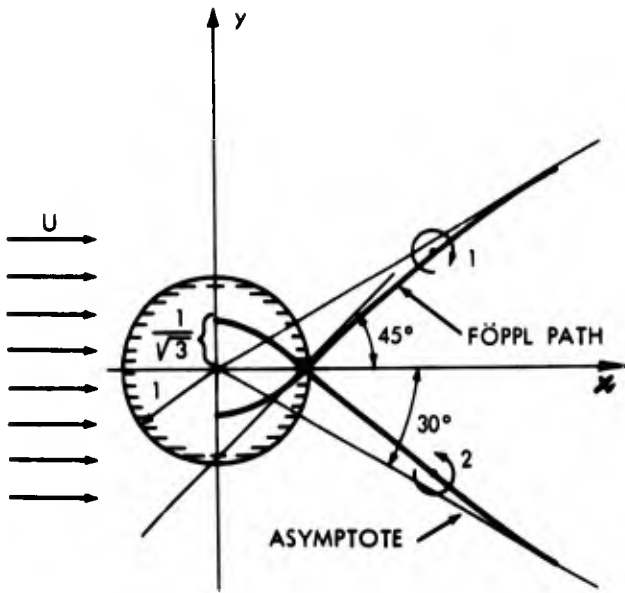


Fig. 2 Location of Vortices

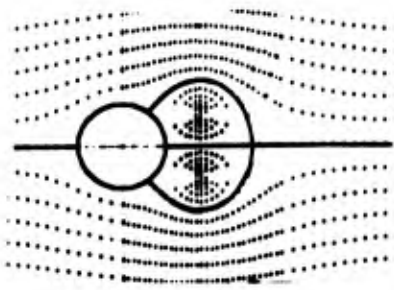


Fig. 3 Stream Lines for Potential Flow

Depending upon the choice of the vortex strength or vortex position (which in turn determines the vortex position or the vortex strength respectively, according to equations (16) and (7)) the potential flow pattern can be made to agree with actual observed flow pattern quite well, e.g. see reference 5.

FÖPPL STABILITY ANALYSIS

Since it is desired to keep the vortices from shedding it is important to determine if the vortices on the Föppl path, which are now at rest with respect to the cylinder, are in positions of equilibrium. To determine stability vortices 1 and 2 are displaced by a small distance from their position on the Föppl path; a return to their original location or a closed vortex path around its original position means that this position is one of equilibrium. For a small symmetrical disturbance of the vortices (the x - axis being the axis of symmetry) Föppl (ref. 4) obtained

$$\frac{d^2 \alpha}{dt^2} + (Y - A) \frac{d\alpha}{dt} + (BX - AY) \alpha = 0 \quad (19)$$

after replacing u by $\frac{dx}{dt}$, v by $\frac{dy}{dt}$, x by $x + \alpha$ and y by $y + \beta$ in the equations representing the propagation velocities of the vortices.

Here

$$A = \frac{-2U}{r} \times (4y^2 + 1) \quad (20)$$

$$B = \frac{2U}{r^5} \left(r^4 + 2r^2 + \frac{2y^2}{r^2} \right) \quad (21)$$

$$X = 8x^2 y \frac{U}{r^6 (r^4 - 1)} \quad (22)$$

and

$$Y = \frac{2xU}{r^4} \left(1 + \frac{4y^2}{r^2 (r^4 - 1)} \right) \quad (23)$$

The indices on x , y and r have been omitted. The general solution of equation (19) is

$$\alpha = C_1 \exp(\lambda_1 t) + C_2 \exp(\lambda_2 t) \quad (24)$$

where

$$\lambda_{1,2} = -\frac{Y-A}{2} \pm \frac{1}{2} \sqrt{(Y-A)^2 - 4(BX-AY)} \quad (25)$$

Stability is therefore proven, since

$$Y > A$$

$$\text{and} \quad (26)$$

$$(BX - AY) > 0$$

A similar stability investigation, for the case for which the symmetry of the vortices with respect to the x - axis is not preserved, yields instability of the displaced vortices. The stability problem and in addition the motion of the vortices was more completely discussed by Howland (ref. 6) in 1925, Walton (ref. 7) in 1928 and Vibrans (ref. 8) in 1962.

The above considerations show that a pair of vortices may be at rest behind a circular cylinder in uniform flow. If this is the case, they will position themselves according to equations (16) and (17), where the latter equation relates position with vortex strength and free stream velocity. When a small disturbance acts upon these vortices, the vortices will move on closed paths around their original position on the Föppl path, if the disturbance is of such a manner that it results in a displacement of the vortices which is symmetrical with respect to the x - axis. A disturbance producing

an unsymmetrical displacement with respect to the x -axis results in instability of the vortices. The typically staggered Kármán vortex street is usually formed in this case.

SPLITTER PLATE

The method by which the periodical vortex shedding behind a circular may be inhibited is now quite apparent. An infinitely thin plane plate is extended along the x -axis and perpendicular to the x - y plane. The sectional view of the cylinder and the plate is the same as shown in figure 2, except that the x -axis now represents the cross section of a rigid wall. Due to the image effect of the wall either of the vortices 1 or 2 only "sees" its own image, and not the other real vortex 2 or 1 respectively. This image vortex is naturally always symmetrical with respect to the image plane, in this case a plane along the x -axis and perpendicular to the x - y plane. Symmetry of the vortices 1 and 2 with respect to the x -axis is therefore always assured, and consequently, for the potential flow model, the vortices will not shed.

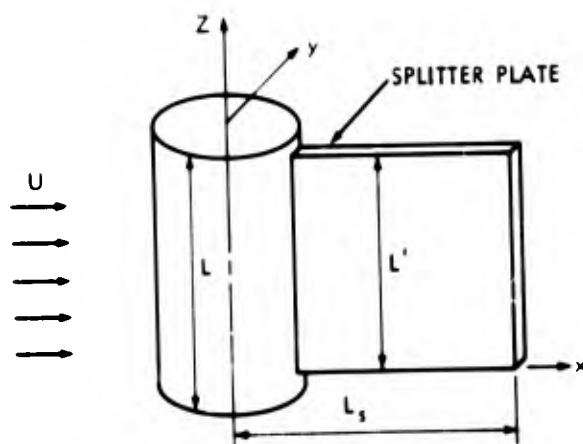


Fig. 4 Splitter Plate

The technical realization of the image plane is shown in figure 4. Naturally the splitter plate will have a finite thickness, a finite length ($L_s = l$) along the x -axis and a finite length L' along the cylinder. For practical design purposes the optimum lengths ($L_s = l$) and L' are of interest, the optimum lengths are the minimum dimensions of the splitter which will inhibit the fluid induced motions to the desired degree. These optimum dimensions will of course depend upon the design requirements. Methods of deducing the lengths L_s and L' by making plausible assumptions regarding the viscous fluid flow pattern are discussed in reference 3. It should be pointed out, that due to the down wash at the ends of the cylinder, L' can be smaller than L . For a length to

diameter ratio of 5.15 experiments showed that $L' = 0.9L$ is sufficient as long as the Reynolds number is less than the critical (see figures 5 and 6). Experimentally it was also determined that when L_s equals to 7 cylinder radii, i.e. when the splitter plate itself is 3 cylinder diameters long, the usual flutter due to vortex shedding was virtually non-existent. Preliminary calculations of the pressure gradients in the y -direction at $x/D = 1$, $x/D = 2$, $x/D = 3$ and $x/D = 4$ indicate that the splitter plate need not be continuous from $x/D = 1$ to $x/D = 3$. It seems to be more important that the plate exists in the neighborhood of $x/D = 3$.

Figure 5 shows the amplitudes of fluid induced vibrations of a bare cylinder and the reduction of these amplitudes due to the splitter plate. The cylinder had the above stated L/D ratio and was 1.75 ft. in diameter. The different amplitude ranges are due to a change in the natural frequency of the elastically held cylinder. The splitter plate prevented the vibrations to the same degree, regardless of the natural frequency of the system. The density ratio for these cases was $\rho_R = 1.78$.

Figure 6 shows just like figure 5 the amplitudes of the fluid induced vibrations of a cylinder with and without the splitter plate. The diameter and the L/D ratio of the cylinder are the same as for the experiments presented in figure 5. However the density ratio was in this case $\rho_R = 1.91$, resulting in a very wide amplitude range. The vibrational system was tested over the shown Reynolds number range with the three different natural frequencies, namely 0.047 cps, 0.037 cps, and 0.032 cps. The amplitude response did not change significantly when the vibrational system was changed to have the above natural frequencies. Again the splitter plate eliminated the flutter vibrations to the same degree, regardless of the natural frequency of the system.

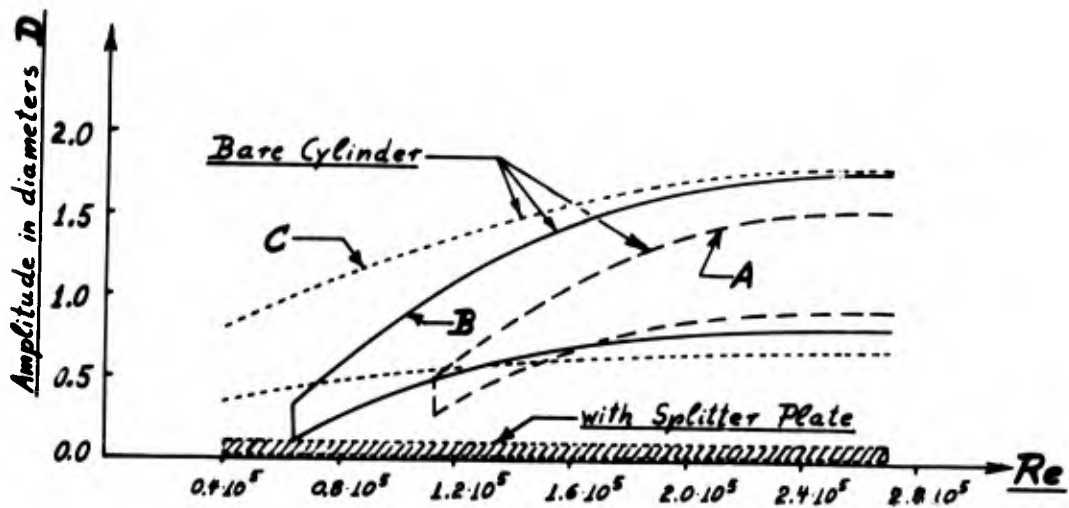


Fig. 5: Amplitude vs Reynolds Number

$f_{nat.A} = 0.081$ cps, $f_{nat.B} = 0.062$ cps, $f_{nat.C} = 0.052$ cps

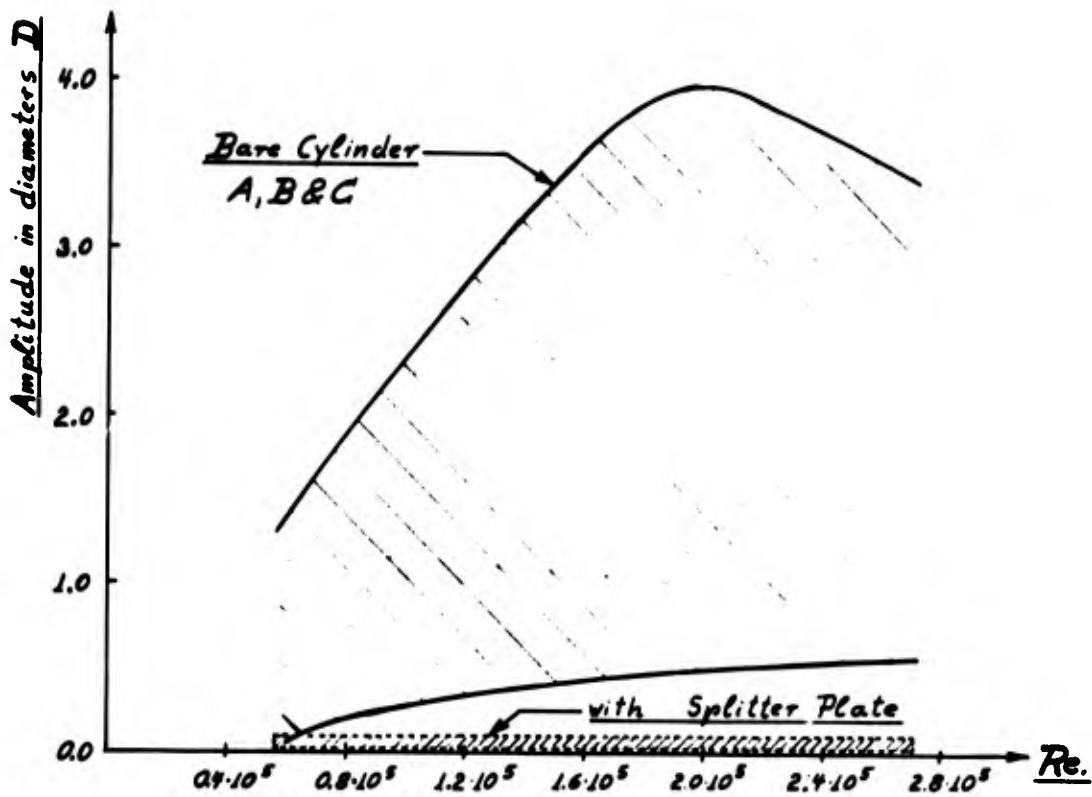


Fig. 6: Amplitude vs Reynolds Number

$f_{nat.A} = 0.047$ cps, $f_{nat.B} = 0.037$ cps, $f_{nat.C} = 0.032$ cps

SYMBOLS

D	diameter of cylinder
f	frequency of vortex shedding
L	length of cylinder
L ¹	height of splitter plate
L _S -l	length of splitter plate in cylinder radii
S	Strouhal number based on the diameter D and the velocity U
u	velocity component in x-direction
U	approach velocity
v	velocity component in y-direction
w	complex potential
x _n	x-coordinate of vortex n
y _n	y-coordinate of vortex n
z	complex function $z(x,y) = x + iy$ where $i = \sqrt{-1}$
\bar{z}	conjugate of z
K	strength of vortex
ρ	density of fluid
ρ_c	average density of cylinder
ρ_R	$\rho_R = \frac{\rho + \rho_c}{2}$
ϕ	velocity potential
ψ	stream function

LITERATURE

1. D.W. Sallet, "On the Self Excited Vibrations of a Circular Cylinder in Uniform Flow", The Shock and Vibration Bulletin, Bulletin 40, Part 3, December 1969, pp. 303-309.
2. H. Drescher, "Messung der auf querangeströmte Zylinder ausgeübten zeitlich verändernden Drücke," Zeitschrift für Flugwissenschaften, Vol. 4, No. 2, 1956, pp. 17-21.
3. D.W. Sallet, "A Method of Stabilizing Cylinders in Fluid Flow", Journal of Hydrodynamics, Vol. 4, No. 1, January 1970, pp. 40-45.
4. L. Föppl, "Wirbelbewegung hinter einem Kreiszylinder," Sitzungsberichte der

mathematisch-physikalischen Klasse der Königlich Bayerischen Akademie der Wissenschaften, München, 1913, pp. 1-17.

5. O. Tietjens, Hydro-und Aeromechanik, Vol. II, Verlag Julius Springer, Berlin, 1931, Tafel 3, Abb. 5.
6. R.G.J. Howland, "Vortex Motion Behind a Circular Cylinder", The Journal of the Royal Aeronautical Society, Vol. 29, 1925, pp. 189-195.
7. E.T.S. Walton, "On the Motion of Vortices Near a Circular Cylinder in a Stream of Liquid", Proceedings of the Royal Irish Academy, Vol. 381 Sec. A, No. 3, 1928, pp. 29-39.
8. G. Vibrans, "Motion of a Pair of Vortices Behind a Cylinder", NWL Report No. 1794, November 1962.

DISCUSSION

Mr. Dodge (Southwest Research Institute): If I followed your presentation correctly, the main point which you wanted to make was that this potential flow analysis enabled you to calculate the length of the splitter plate. Most of us realize that a splitter plate will eliminate vibration? Did you vary the length of the splitter plate to see if it agreed with your calculations?

Mr. Sallet: Yes, I did. And roughly they agreed. It depends on how one relates the potential flow to the actual flow parameters. In the presentation I pointed out the weakness, that it is very bad to have a potential flow analysis for a real flow, particularly if you use low Reynolds numbers. The analysis gives an insight as to why the vortices were not shed. In my paper I also stated that you do not have to have the plate right next to the cylinder and that the plate is more important further downstream. I have not made an analysis of that.

Mr. Callahan (Black and Veatch): We had a similar problem in air. We were called to consult with the Air Force on an antenna, at Thule, that had some cylinders that were supported both at the top and the bottom, that had been failing regularly for three or four years. Our investigation indicated that we were having the same phenomena in air for columns anchored at both the top and the bottom. Of some hundred columns only about five failed and we noticed that the columns that were loaded axially, either in compression or in tension, did not fail. But the welds in the unloaded columns were cracking at the end of the structures. Do you care to comment from your studies?

Mr. Sallet: Yes. I must warn you to apply wind tunnel data to data that should hold up in water and vice versa, in this particular type of problem. When I first looked in to that I said it is very easy to silence or reduce the vibrations. I looked at some of the wind tunnel results. That does not work in

water, particularly if the average density of your vibrating body, or your vibrating mass, is roughly equal to the density of the fluid, which is very often the case. We have an amplitude which is a function of the approach velocity or the Reynolds number, if the density ratios are very different, then the vibration problem is similar to a one degree of freedom system where the critical frequency or the Strouhal frequency is suddenly excited. If this frequency is excited due to having this critical approach velocity you obtain a critical frequency. If one has a system where the density is similar to, or approaches a density of the approach fluid the amplitude versus velocity ranges are similar to a very broad -- excitation spectrum, and that is where you run into difficulties. We have something which is not quite completely explained. I am working on it, many people much smarter than I have been working on it, and they have not explained it either.

Mr. Galef (TRW Systems): I would like to offer a few practical comments based on some experience designing risers for use in Cook Inlet where we have six knot currents and big waves. Unfortunately, the currents are not kind enough to come always from the same direction. If the splitter plate were attached to a riser it would act as an airfoil. This will have a lift coefficient of 2π times the angle of attack and the riser will break off very soon. Of course, one might argue that it will stall before it breaks and that might be true, but this is much worse. Because if the stall condition occurs, a galloping, which is a special form of stall flutter, occurs and the riser will break. I just do not think you can do this sort of thing.

Mr. Sallet: The problem is purely an engineering problem. Obviously, one has to install the plate in such a fashion that it will swing around so that these lift forces do not occur. I have discussed a fluid mechanics problem, there are many ways to solve it.

BLANK PAGE

EFFECTS OF LOOSENESS ON DYNAMIC BEHAVIOR

R. L. Beckett, F. C. Pan
U. S. Army Weapons Command
Rock Island, Illinois

and

D. D. Penrod
The University of Iowa
Iowa City, Iowa

The response of a mechanical assembly in a vibration environment is strongly dependent upon the tolerance between parts. An increase in the looseness in an assembly may increase the amplitude of the response which can cause premature damage or failure. Of particular concern is the packaging of electronic components and fatigue of mechanical parts. This paper gives a numerical solution for the motion of a mass that is forced to vibrate between two springs which allow some free travel at the center. Viscuous damping is considered. Results are presented in the form of amplification curves which are plotted against a dimensionless excitation frequency.

INTRODUCTION

Acceptance tests for assemblies and subassemblies of complex systems often require forced vibration over a wide spectrum of frequencies. In the design of these assemblies it is helpful to predict the response analytically so that harmful effects can be minimized. In many instances tolerances occur between mating parts and this complicates the analysis by causing the response to be nonlinear.

It is also known that the service life of an assembly that is subject to a dynamic environment is adversely affected by tolerance buildup between parts [1]. Tests have shown that failures of assemblies are almost always preceded by an increase in the looseness between parts of the assembly.

This paper investigates the effect of looseness (tolerance) on the response of a simple spring mass system that is subject to a vibration environment. Also included is an evaluation of the effect on the behavior of viscous damping which is sometimes present in a loose assembly--particularly those where some isolation from the environment may be sought.

Numerical methods are used to solve the nonlinear problem on a digital computer and for comparison these same results are also obtained using an analog computer. Results are obtained which show the response for different system parameters, different excitation frequencies and different initial conditions since it is shown that the nonlinear response can be dependent on initial conditions. Results are presented in graphical form.

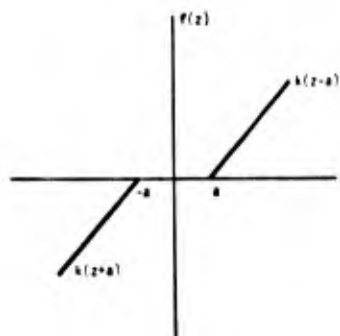
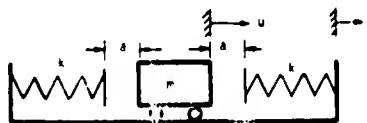


Fig. 1 - Spring Mass System

EQUATIONS OF BEHAVIOR

Figure 1 shows the problem that is considered. The mass m oscillates between the two springs with spring constant k . The tolerance in the system is represented by the two gaps of length a . The support is subjected to an excitation represented by x and the mass motion is defined by u . A representative spring force is graphed against the relative displacement $z(z = u - x)$ in the figure. Viscous or coulomb damping may be included. The equation of motion

for the mass is written

$$m\ddot{u} = -f - F \quad (1)$$

where f is the spring force and F is the dissipation force.

$$f = 0 \quad |z| \leq a \quad (2)$$

and it will depend upon the characteristics and deformation of the spring when $|z| > a$. The force F may represent any kind of dissipation force.

SOLUTION OF EQUATIONS

The behavior is evaluated by two different methods. The first method requires that the springs be linear and equal, no damping, the excitation be harmonic and the response of the mass is suitably represented by a sine function. In the second method used, the equations of behavior are solved numerically and the springs may be unequal and nonlinear, damping may exist and there is no requirement on the form of the response. The second method will, of course, handle many more cases; but, the former will give very good estimations of the response even for systems with substantial nonlinearity provided the conditions cited above hold. Computation time for the first method is considerably less although this was not an important consideration when the work was done on a high speed third generation computer system.

If F is assumed to be zero and if the springs are linear and symmetrical then Eq. (1) can be written

$$m\ddot{u} = -f(u-x) \quad (3)$$

where

$$\begin{aligned} f &= 0 & |u-x| &\leq a \\ f &= k(u-x-a) & u-x &> a \\ f &= k(u-x+a) & u-x &< -a \end{aligned} \quad (4)$$

Equation (3) can be solved explicitly for the period T when x is harmonic and the response u is assumed to be harmonic [2].

$$\frac{T}{4} = \int_{-u}^u \frac{du}{\sqrt{\frac{2}{m} \int_u^{-u} -f(u-x) du}} \quad (5)$$

where u is the amplitude of motion of the mass. The integration in Eq. (5) is carried out for f as defined in Eq. (4) and for

$$x = \pm \frac{x_0}{u} \quad (6)$$

The plus and minus signs give respectively the in-phase and out-of-phase response of the system. For the former

$$\frac{T}{4} = \sqrt{\frac{m}{k}} \frac{1}{\sqrt{1 - \frac{x_0}{u_0}}} \left(\frac{a}{u_0 - x_0 - a} + \frac{\pi}{2} \right) \quad (7)$$

For the latter

$$\frac{T}{4} = \sqrt{\frac{m}{k}} \frac{1}{\sqrt{1 + \frac{x_0}{u_0}}} \left(\frac{a}{u_0 + x_0 - a} + \frac{\pi}{2} \right) \quad (8)$$

If T is replaced by its equivalent in terms of frequency then Eq. (7) (or Eq. (8)) is a relationship between frequency, level of input represented by x_0 and the amplitude of the output u_0 .

Good approximation can also be obtained by solving the following equivalent system based on the method of slowly changing amplitudes (van der Pol method).

$$m\ddot{z} + kz + g(z) = m\omega^2 x_0 \sin \omega t \quad (9)$$

$$\begin{aligned} g(z) &= -ka & z &\geq a \\ g(z) &= -kz & |z| &\leq a \\ g(z) &= ka & z &\leq -a \end{aligned} \quad (10)$$

Indeed, one term approximation has been shown to be sufficient if the condition $|a/z_0| \ll 1$ holds.

The second method of solution used for Eq. (1) is based on numerically integrating the equation. The general objective in the numerical integration will be to generate a periodic solution under given conditions of excitation.

The equation is integrated by using a standard Runge-Kutta method. In order to find the steady state response two techniques are employed. In one sufficient damping is introduced to dissipate any transients after a number of cycles and the other uses a shooting technique where initial conditions are systematically refined to give a pure periodic or steady state response.

In the first technique, referred to here as the damped-out method, arbitrary initial conditions are assumed and the integration carried out until the response is clearly identified to be periodic. This is accomplished by recording conditions at intervals T which is the period of the excitation. When it is observed that conditions exactly repeat after some multiple of the interval T , then it is assumed that a steady state condition is reached.

The shooting method assumes that periodic motion occurs with period equal to T . Starting conditions for the response are systematically varied until the solution after a time T exactly equals the starting conditions. Refinement of the starting conditions is done by using Newton's method.

In Eq. (1) let $z = u - x$, then

$$\ddot{z} = -\frac{1}{m}f - \frac{1}{m}F - \ddot{x} \quad (11)$$

Equation (11) is replaced by two first order equations

$$\begin{aligned} \dot{z} &= \dot{y} \\ \dot{y} &= -\frac{1}{m}f - \frac{1}{m}F - \ddot{x} \end{aligned} \quad (12)$$

The excitation x is assumed known and for any problem the spring force f and dissipation force F will be known. Starting values for the position u and the velocity \dot{u} of the mass permit the numerical solution of Eqs. (12).

The shooting technique is based upon selecting starting values for u and \dot{u} , such that after a period of time T the system returns to precisely the starting conditions, (Fig. 2), i.e.,

$$\begin{aligned} u(T) &= u_0 \\ \dot{u}(T) &= \dot{u}_0 \end{aligned} \quad (13)$$

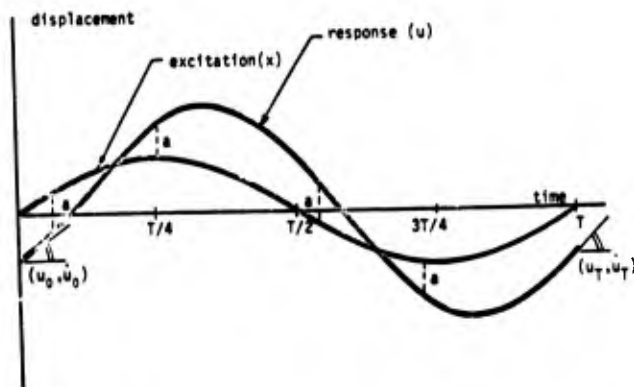


Fig. 2 - Excitation and Response

The Newton Raphson technique is used for finding a solution of Eq. (12) that will satisfy Eq. (13). Starting conditions u_0 and \dot{u}_0 are assumed and the integration of Eq. (12) is carried out. In general, the condition in Eq. (13) is not satisfied, and in order to satisfy this condition the starting values are corrected as follows.

It is assumed that $u(T)$ and $\dot{u}(T)$, denoted by u_T and \dot{u}_T , have appropriate continuity with respect to u_0 and \dot{u}_0 so that the Taylor expansions in Eq. (14) and (15) will hold.

$$\begin{aligned} u_T(u_0 + \Delta u_0, \dot{u}_0 + \Delta \dot{u}_0) &= u_T(u_0, \dot{u}_0) + \frac{\partial u_T}{\partial u} \bigg|_0 \Delta u_0 \\ &+ \frac{\partial u_T}{\partial \dot{u}} \bigg|_0 \Delta \dot{u}_0 + \dots \end{aligned} \quad (14)$$

$$\begin{aligned} \dot{u}_T(u + \dot{u}, \dot{u} + \dot{\dot{u}}) &= \dot{u}_T(u, \dot{u}) + \frac{\partial \dot{u}_T}{\partial u} \Delta u \\ &+ \frac{\partial \dot{u}_T}{\partial \dot{u}} \Delta \dot{u} \end{aligned} \quad (15)$$

where the subscripts indicate time. From Eqs. (14) and (15) values for \dot{u}_T and $\dot{\dot{u}}_T$ are sought that will make u_T and \dot{u}_T equal to the starting values, i.e.,

$$u_T(u + \dot{u}, \dot{u} + \dot{\dot{u}}) - (u + \dot{u}) = 0 \quad (16)$$

$$\dot{u}_T(u + \dot{u}, \dot{u} + \dot{\dot{u}}) - (\dot{u} + \dot{\dot{u}}) = 0 \quad (17)$$

Substituting for u_T and \dot{u}_T in Eqs. (14) and (15) gives two simultaneous equations in the correction terms Δu and $\Delta \dot{u}$.

$$\left(1 - \frac{\partial u_T}{\partial u}\right) \Delta u - \frac{\partial u_T}{\partial \dot{u}} \Delta \dot{u} = u_T(u, \dot{u}) - u \quad (18)$$

$$-\frac{\partial \dot{u}_T}{\partial u} \Delta u + \left(1 - \frac{\partial \dot{u}_T}{\partial \dot{u}}\right) \Delta \dot{u} = \dot{u}_T(u, \dot{u}) - \dot{u} \quad (19)$$

The right hand side of Eqs. (18) and (19) is the difference between u (or \dot{u}) at time T as found from the solution of Eqs. (12) and the starting values. The derivative terms in the coefficients are evaluated numerically by making individual variations in u and \dot{u} . Thus,

$$\frac{\partial u_T}{\partial u} = \frac{u_T(u_0 + \Delta u, \dot{u}_0) - u_T(u_0, \dot{u}_0)}{\Delta u} \quad (20)$$

$u_T(u_0 + \Delta u, \dot{u}_0)$ is found by making a small change in u_0 , i.e., Δu_0 , and then computing u_T from Eqs. (12).

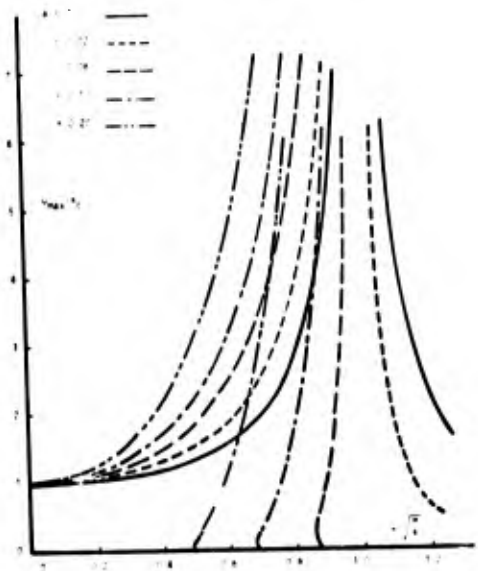


Fig. 3 - Amplification Factor vs Frequency Ratio

RESULTS

Numerical results are obtained by solving Eqs. (12) using both the digital and analog

in order to investigate the effect of the excitation frequency on the response of the system. The excitation frequency is varied from 0.4 to 1.0. The excitation amplitude is fixed at 1.0. The excitation frequency is varied from 0.4 to 1.0. The excitation amplitude is fixed at 1.0. The excitation frequency is varied from 0.4 to 1.0. The excitation amplitude is fixed at 1.0.

holder. A value of 1.0 is used for γ . These values have been chosen so that they represent a real engineering problem.

Of greatest interest in this study is the effect of the looseness on the response of the system. Accordingly the response of the system for different values of the tolerance gap and for different excitation frequencies is determined. The effect of dissipation is also of interest particularly as it might influence the nonlinear response. In order to find the general influence of damping a linear damping term $c\dot{u}$ is used for F in the equation of behavior.

Figure 2 shows a sample excitation and response curve. The excitation is harmonic throughout the study. The response may be harmonic or it may have both harmonic and subharmonic components that occur because of the nonlinearity of the spring force.

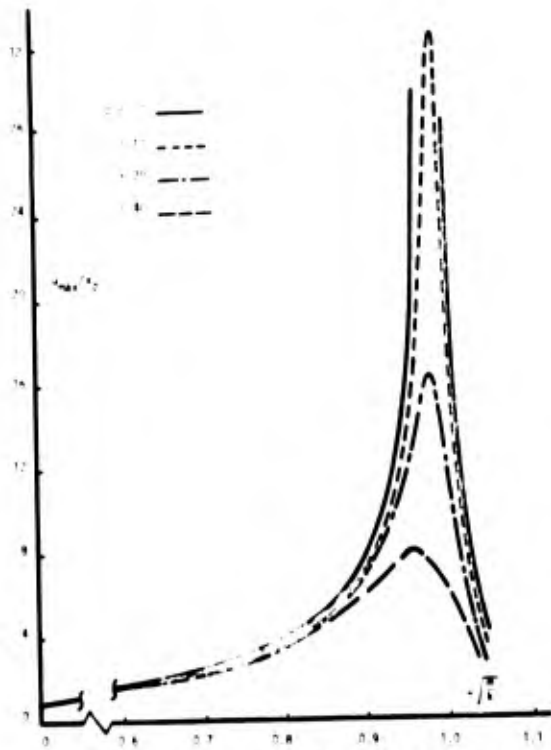


Fig. 4 - Effect of Damping for Small Gap($a=0.02''$)

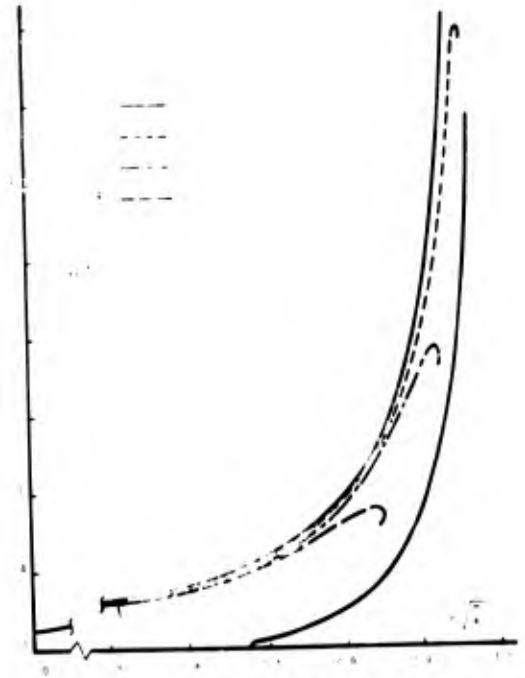


Fig. 5 - Effect of Damping for Large Gap($a=0.10''$)

Figure 3 shows the amplification factor u_{max}/x_0 , as a function of the ratio of the excitation to the natural frequency of the linear system ω/ω_n ($\omega_n = \sqrt{k/m}$) for different values of looseness. The effect of increased looseness is to increase the amplification factor for the in-phase motion, i.e., $\omega/\omega_n < 1$. Whereas the amplitude of the oscillation goes virtually to zero for the out-of-phase response, $\omega/\omega_n > 1$. The amplification curves show that for a gap of 0.20" and a frequency ratio of 0.6 the amplitude of the response can exceed three times the amplitude for the linear case.

Figures 4 and 5 show the amplification factor for different values of the velocity damping coefficient. Figure 4 is an almost linear case, i.e., small gap, while Fig. 5 with a gap of 0.10" shows strong nonlinear behavior. Comparison of Fig. 3 and 5 show that the effect of damping for the nonlinear case is to reduce the amplitude of the response in much the same way as for the linear case.

In order to determine the actual content of the response curves, they were found by both the digital (damped-out) and analog methods of solution. The two solutions proved to be equal thus giving additional validity to the numerical results. An interesting result of the study is that for certain conditions the solution is not unique. This is demonstrated in Figs. 6 through 9. Figs. 6 and 7 show the response for the same system with an input of 1g at frequency $\omega = 0.441/\sqrt{k/m}$. Only the initial conditions on u_0 and \dot{u}_0 are changed. In Fig. 6 the response contains one or more subharmonics with frequency equal to $n\omega/3$. This is determined by the period of the response which is $3T$. In Fig. 7, the

response is pure harmonic as can be verified by the period and the form of the curve.

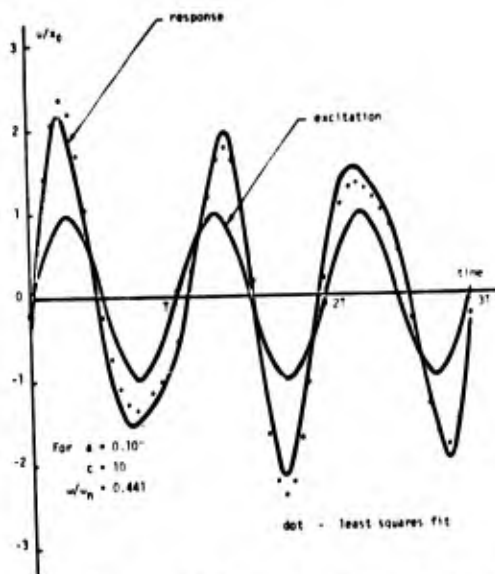


Fig. 6 - Excitation and Response Curve for 1/3 Subharmonic

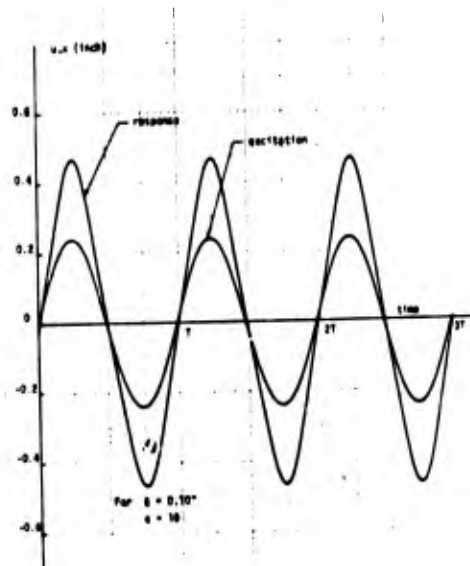


Fig. 7 - Harmonic Response ($\omega/\omega_n = 0.441$)

The two different forms of the response can be obtained by varying the initial conditions. However, the harmonic response is quite sensitive to the initial conditions and can be obtained only when the starting conditions are carefully chosen to nearly duplicate the steady state harmonic conditions.

Figures 8 and 9 show the response for the same system used for Figs. 6 and 7 except that the excitation frequency is raised to $\omega = 0.496\omega_n$. The third subharmonic disappears and for non-linear response a second order subharmonic

occurs. This is verified in Fig. 8 where the motion clearly repeats after $2T$. Figure 9 shows the pure harmonic response for precisely the same system.

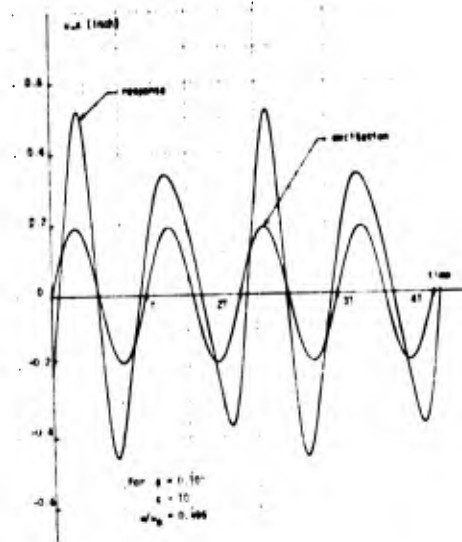


Fig. 8 - Excitation and Response Curve for 1/2 Subharmonic

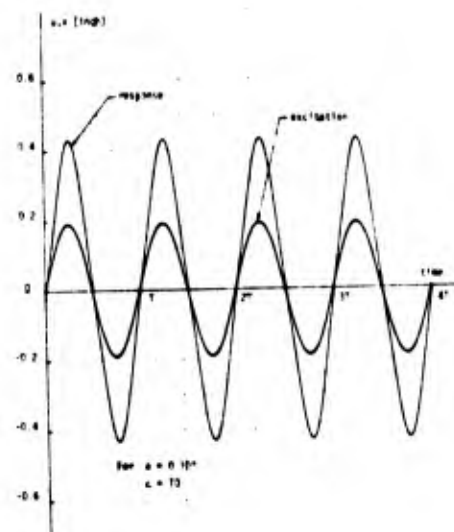


Fig. 9 - Harmonic Response ($\omega/\omega_n = 0.496$)

Results for frequencies over the spectrum from near zero to a value of $\omega/\omega_n = \sqrt{k/m}$ of roughly 1.2 were run for the system with a gap of $0.10''$. For very low frequencies of excitation the response curves were dominated by the pure harmonic term. The contribution due to subharmonics was trivial. Subharmonic response becomes obvious as ω increases. For a value of $\omega = 0.441\omega_n$ the subharmonic of 1/3 order becomes quite prominent and at $\omega = 0.50\omega_n$ the subharmonic of 1/2 order is most prominent. For a greater

than about 0.02 in no subharmonics are detected. It is interesting to observe that several order subharmonics will occur as the frequency is varied over the range $0.3 \omega_n$ to $0.5 \omega_n$. For example, one fourth and one fifth order subharmonics can be detected at selected frequencies as well as the two illustrated in the figures.

Occurrence of the subharmonics depends upon the degree of the nonlinearity. By reducing the gap to less than about 0.04 in the subharmonics can no longer be detected and in this range a linear approximation to the solution of the problem is satisfactory. For gap size greater than 0.04 in the subharmonics described above will occur; they become more pronounced as the gap increases.

Figure 10 shows the effect of looseness on the amplification factor for different frequencies of the shaking force. Sufficient damping ($c=10$) is included to damp out transients after about 60 to 70 cycles.

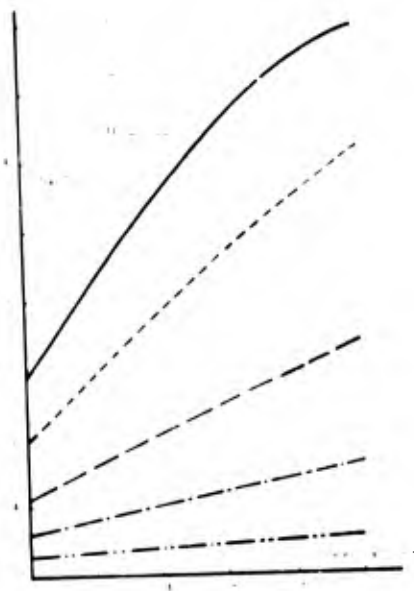


Fig. 10 - Effect of Looseness ($c=10$)

DISCUSSION

The general problem of the effect of looseness on dynamic behavior occurs frequently and of greatest concern is the contribution of looseness to potential failure of the system. Accordingly the most important contribution of this paper is an evaluation of the effect of looseness on the amplification factor under forced vibration. Figures 3 and 10 show that the amplification factor can be as much as three times the linear case when the gap between the spring is 0.10 in . Figure 3 shows that the amplification factor continues to increase rather dramatically as the looseness increases. This would verify that once a failure starts to occur in a dynamic environment it will proceed very

rapidly.

In a problem of packaging a cryogenic tank weighing some 1400 lbs in a flexible cage, with an equivalent spring constant of about 30,000 lb/in, gaps of 0.10 in in the support structure were normal. Thus the response curves given here are typical of the behavior of this system.

There was no opportunity to measure directly the response of the tank under a forced vibration acceptance test, but some failures which occurred indicated that forces in the range predicted by the amplification factor probably were reached.

Subharmonic response was expected for the nonlinear problem but the existence of all orders of the subharmonic is surprising. The preference of a particular subharmonic for a fairly narrow range of the excitation frequency was unexpected. In some cases the subharmonic is a substantial part of total response. To verify this a least squares analysis of the response curves has been carried out by assuming the curve is the sum of harmonic and subharmonic parts.

$$u(t) = A_0 \sin(\omega t + \phi_0) + \sum_{n=1}^{\infty} A_n \sin\left(\frac{n\omega t}{m} + \phi_n\right) \quad (22)$$

where m is the order of the subharmonic determined by the technique described earlier. A_0 and ϕ_0 are the amplitude and phase angle of the harmonic part, while A_n and ϕ_n ($n \neq m$) represent the amplitude and phase shift of the subharmonics. The maximum amplitude of a subharmonic is observed to be almost one-half the amplitude of the harmonic term. Thus the subharmonics are important in evaluating the total amplitude of the response.

A definition of looseness would be helpful in a discussion of results. Here for the lack of a definition the actual dimension of the gap is used. A better measure might be a ratio of the gap to the amplitude of the forced response of the mass. A study to find a significant measure for looseness is underway.

The effect of the velocity damping assumed here is to reduce the amplitude of the response and to change the phase angle in much the same way as happens in the linear case. Thus the introduction of light damping to eliminate the transients after several cycles in both the damped-out and analog methods appears justified for finding the steady state response.

REFERENCES

1. K. Rim and C. Louis, "Investigation of the Effect of Looseness of Imperfect Points on Structural Integrity," Fall Meeting of SESA, October 1969.
2. J. P. Den Hartog, Mechanical Vibration, pp. 351-361. McGraw-Hill, New York, 1956.

DISCUSSION

Mr. Fox (Barry Controls): Did you attempt to look at the effect of a nonrigid mass on the system, or do you think that would be a consideration in your system?

Mr. Beckett: No, the only problem we tried to solve was a very simplistic one. I realize that the spring impact will probably change the response of the system, however, I do not know how much.

Mr. Prouse (Battelle Memorial Institute): Have you looked at some of the stability analysis that has been performed on what is known as an acceleration damper or a mass damper? A mass is in a rigid, or in a more or less rigid, container but it has freeplay and the spring stiffness is derived from the coefficient of restitution of the elastic impact. There has been a considerable amount of stability analysis which I think you would be very interested in studying,

at least it is similar to some of your stiff spring type of approaches.

Mr. Beckett: We did not attempt to use any of those results. And I think you are right that this approach could be directly applicable.

Mr. Ungar (Bolt Beranek & Newman): I noticed in some of your slides that there was a possibility of two amplitudes occurring at the same frequency. Is this a sort of classical thing that you would expect in some nonlinear systems? As I recall this has been described by Stoker maybe 20 years ago. I just wonder how your computer solutions checked with the classical solutions?

Mr. Beckett: They checked very well for small values of "a". The quasi-linear solutions checked extremely well. For large values of the gap though they did not check very well at all.

BLANK PAGE

DYNAMIC DEFLECTIONS OF MULTIPLE-SPAN GUIDEWAYS
UNDER HIGH SPEED, AIR CUSHION VEHICLES

James F. Wilson
Duke University
Durham, North Carolina

Series solutions are presented for dynamic responses of elevated guideways to high speed vehicles. The guideways are modeled as identical, end to end Bernoulli-Euler beams, each simply supported at the ends. Influence functions are presented for the deflections resulting from a point force traversing a span with any number of internal rigid props, with explicit results for the single-span, two-span (one prop) and three-span (two prop) cases. Superposition of influence functions is used to obtain responses for the multiple loading of traversing air cushion vehicles. Numerical results include peak deflections and bending moments of simple spans in response to a variety of loadings. Ratios of maximum dynamic to maximum static deflections and bending moments at midspan approach 2.0 for long, continuous loadings, but are as high as 3.2 for certain segmented loadings which overlap two spans at once. Parametric studies show that, for a given span, the vehicle speeds at which these peak responses occur are always quite different than the critical speed for a point load.

INTRODUCTION

It is well known that a simple, elevated span can undergo higher maximum deflections and bending moments as the speed of the vehicle traversing the span increases. A reasonably complete historical review of this subject is given by Wilson [1], who further considered the dynamic response of simply supported spans to traveling constant pressure segments of up to one span in length. More recently, Wilson and Biggers [2] studied the dynamic response of simple, linearly damped spans subjected long pressure segments traveling at constant speed and concluded that the maximum ratios of dynamic to static span deflection approach 2.0. Under certain conditions, these maximum dynamic deflections did not occur until most of the pressure had passed over the span--when the span was vibrating freely. These results, and those which follow for the multiple span cases, are applicable to the design of guideway spans for tracked air cushion vehicles provided that the total weight of the vehicles between two consecutive span supports is always much smaller than the total weight of that span section. However, if the vehicle suspension system is somehow controlled so that the vehicle mass times its

vertical acceleration during traverse is always much smaller than the vehicle weight, the span loading is nearly constant, and the results which follow are also approximately valid for high ratios of vehicle to span weight.

Practically, it is necessary to keep vertical vehicle acceleration below 0.04 g's for the safety and comfort of the passengers [3]. With this criterion in mind, much work is presently being done on the coupling effects between guideways and traversing vehicles modeled as various types of linear spring-mass systems [4-6]. In the final design stages of a guideway for a high speed tracked air cushion vehicle, it would be best to check the guideway deflections and moments obtained from some of these complex models before making the assumption inherent in the results which follow here--the assumption of non-fluctuating pressure loading.

FREE VIBRATIONS OF CONTINUOUS SPAN GUIDEWAYS

With the assumptions of classical beam theory, the governing differential equation of motion for a span of uniform properties, subjected to an external transverse force $f = f(x,t)$ per unit

length of span is [7]

$$EI \frac{\partial^4 Y}{\partial x^4} + \rho A \frac{\partial^2 Y}{\partial t^2} = f(x, t) \quad (1)$$

where EI is the stiffness; ρ and A are the mass density and the cross sectional area of the beam, respectively; (x, y) are the coordinates of the neutral axis of the span as shown in Figure 1, and t is time. It is assumed that the span is

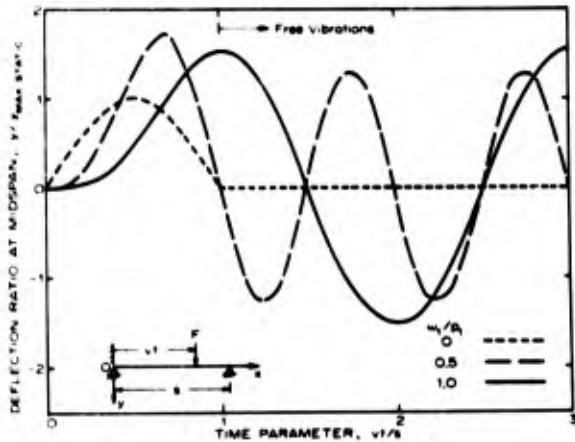


Fig. 1 - Typical deflection influence functions for a single span guideway

elevated. End tensions are neglected since it has been shown that longitudinal span tensions of practical magnitudes have small effect on the natural vibration frequencies of simple spans [1].

The controlling variable in the calculation of span frequency is the span length, s . For free vibrations of the simple span described by Equation (1), where $f = 0$ and the deflections and bending moments at the ends $x = (0, s)$ are zero, the frequencies are given by [7]

$$p_r = \frac{r^2 \pi^2}{s^2} \sqrt{\frac{EI}{\rho A}}, \quad r = 1, 2, \dots \quad (2)$$

For any consistent set of units for the span parameters, p_r has units of radians per unit time. For a span of the same length s and with the same simple support conditions at each end, the addition of one or more prop supports between the ends will increase the vibration frequencies, designated as Λ_m . It is assumed that these intermediate props are rigid, allowing for no vertical deflection at their points of contact, and that the bending moments are equal across them, so that span continuity is preserved. A general method for

calculating Λ_m is presented by Saibel [8] for arbitrarily spaced props and by Miles [9] for evenly spaced props. Numerical results for the latter case are also presented by Ayre and Jacobsen [10] for uniform spans of total length s in the form

$$\Lambda_m = \alpha_m^2 \frac{K^2 \pi^2}{s^2} \sqrt{\frac{EI}{\rho A}}, \quad m = 1, 2, \dots \quad (3)$$

where K is the number of span sections ($K-1$ is the number of internal props), and α_m is a constant depending both on K and the mode number m . Numerical values of α_m as a function of K and m for the continuous span with the ends simply supported are given in Table 1. It is noted that Equation (1) is a special case of Equation (3), since for $K = 1$ there are no internal props, $\alpha_m = r$, and $p_r = \Lambda_r$. Further, for the two span case, $K = 2$, and the odd numbered natural frequencies $\Lambda_{(2n-1)}$ ($n = 1, 2, \dots$) coincide with the corresponding even numbered natural frequencies of the simple beam p_{2n} ($n = 1, 2, \dots$), or

$$\Lambda_{2n-1} = p_{2n}, \quad K = 2, \quad n = 1, 2, \dots \quad (4)$$

Also, for the three span case (two evenly spaced props) coincident frequencies are:

$$\Lambda_{3n-2} = p_{3n}, \quad K = 3, \quad n = 1, 2, \dots \quad (5)$$

Similar frequency relations can be deduced for higher values of K . The results expressed by Equations (4) and (5) will be used presently.

In free vibration, the mode shapes of a simple span ($K=1$) are

$$\phi_m(x) = \sqrt{\frac{2}{s\rho A}} \sin \frac{m\pi x}{s}, \quad m = 1, 2, \dots \quad (6)$$

where there is a corresponding frequency p_m given by Equation (2) for each mode shape. The eigenfunctions $\phi_m(x)$ form a complete set and satisfy the following properties

$$\int_0^s \rho A \phi_m(x) \phi_n(x) dx = 0, \quad m \neq n$$

$$\int_0^s \rho A \phi_m^2(x) dx = 1 \quad (7)$$

From the work of Lee [11] and Sabel and Lee [12], the general solution for free vibrations of continuous spans with $N(K-1)$ rigid props at distances c_i ($i = 1, 2, \dots, N$) from the left support, for time $t \geq t_0$, is implied to have the form

$$\begin{aligned} \hat{y}(x, t) = & \left\{ \sum_{(m,j)} B_{jm} \phi_j(x) \right. \\ & - \sum_{m=1}^{\infty} \sum_{r=1}^N \hat{R}_{mi} \frac{\phi_r(c_i) \cdot \phi_r(x)}{p_r^2 - \Lambda_m^2} \left. \right\} \\ & \cdot \sin \Lambda_m(t - t_0) + \left\{ \sum_{(m,j)} B'_{jm} \phi_j(x) \right. \\ & - \sum_{m=1}^{\infty} \sum_{r=1}^N \hat{R}'_{mi} \frac{\phi_r(c_i) \cdot \phi_r(x)}{p_r^2 - \Lambda_m^2} \left. \right\} \\ & \cdot \cos \Lambda_m(t - t_0) \end{aligned} \quad (8)$$

where $\phi_m(x)$ is given by Equation (6) when the ends at $x = 0, s$ are simply supported. The symbol j affixed to the r summations means that the values for which $r = j$ where $p_j = \Lambda_m$ are excluded in those sums. The symbol (m, j) on the sums involving the B_{jm} and B'_{jm} coefficients means that the sums are over only those modes whose frequencies are identical to those of the simple span, or for $\Lambda_m = p_j$. An example of the latter coincidence condition occurs in the three span case with two evenly spaced props, where, as indicated in Equation (5), the ordered pairs $(m, j) = (1, 3); (4, 6); (7, 9); \dots$. If the internal props are placed so that no mode shape of the multiple span coincides with any of those of the simple span, then all of the coefficients B'_{jm} and B_{jm} are zero. When these constants exist, they are calculated using Fourier analysis, where the initial conditions at time $t = t_0$, are expanded in a Fourier sine series and the properties of Equation (7) are used. The results are

$$B'_{jm} = \rho A \int_0^s y(x, t_0) \cdot \phi_j(x) dx \quad (9a)$$

$$B_{jm} = \frac{\rho A}{\Lambda_m} \int_0^s \frac{\partial y(x, t_0)}{\partial t} \cdot \phi_j(x) dx \quad (9b)$$

where $y(x, t_0)$ and $\partial y(x, t_0)/\partial t$, the vertical displacement and velocity, respectively, of each material point on the

span, must be specified at time $t = t_0$ to have free vibrations. With the same technique, it is readily shown that the sets of equations which give the constants \hat{R}'_{mi} and \hat{R}_{mi} are

$$\begin{aligned} & - \sum_{m=1}^{\infty} \sum_{i=1}^N \hat{R}_{mi} \frac{\phi_r(c_i)}{p_r^2 - \Lambda_m^2} \\ & = \rho A \int_0^s y(x, t_0) \phi_r(x) dx \end{aligned} \quad (10a)$$

$$\begin{aligned} & - \sum_{m=1}^{\infty} \sum_{i=1}^N \hat{R}'_{mi} \frac{\Lambda_m \cdot \phi_r(c_i)}{p_r^2 - \Lambda_m^2} \\ & = \rho A \int_0^s \frac{\partial y(x, t_0)}{\partial t} \phi_r(x) dx \end{aligned} \quad (10b)$$

where $r = 1, 2, \dots$ with $r = j$ omitted. By truncating the series to include only a finite number of modes m , values of \hat{R}_{mi} and \hat{R}'_{mi} can be found by solving each set of simultaneous equations, since the right sides of Equations (10) can be calculated for known initial conditions.

FORCED VIBRATIONS FOR A MOVING POINT LOAD

References [11] and [12] give the particular solution $y = y_p$ to Equation (1) for a point force F moving at constant speed v over a continuous span. That is

$$y_p(x, t) = \frac{2F}{s} \sum_{k=1}^{\infty} \sin \omega_k t \cdot \sum_{r=1}^{\infty} \frac{S_{rk} \cdot \phi_r(x)}{p_r^2 - \omega_k^2} \quad (11)$$

where the passage frequencies ω_k are never equal to any of the frequencies p_r . These passage frequencies are defined by

$$\omega_k = \frac{k - v}{s} \quad (12)$$

and S_{rk} is given by

$$\begin{aligned} S_{rk} = & \int_0^s \left(\phi_r(a) \sin \frac{k - a}{s} \right. \\ & - \sum_{i=1}^N \phi_r(c_i) \bar{R}_{ki} \sin \frac{k - a}{s} \left. \right) da \end{aligned} \quad (13)$$

where

$$\bar{R}_{k1} = \frac{1}{p_r^2 - \omega_k^2} \quad (14)$$

and Δ_{ii} is the determinant

$$\left| \sum_{r=1}^N \frac{\phi_r(c_s) \phi_r(c_t)}{p_r^2 - \omega_k^2} \right|; s, t = 1, 2, \dots, N.$$

The value of Δ_{ii} is the same as Δ_{ii} except that the i -th column is replaced by

$$\sum_{r=1}^N \frac{\phi_r(c_s) \phi_r(a)}{p_r^2 - \omega_k^2}, \quad s = 1, 2, \dots, N$$

The total solution for span deflection where $\Delta_m = p_j \neq \omega_k$ becomes

$$y(x, t) = y_p(x, t) + \hat{y}(x, t) \quad (15)$$

where y_p and \hat{y} are given by Equations (11) and (8), respectively. Suppose that the continuous span has zero deflection and zero velocity at time $t = 0$, just before the point load begins its traverse. From Equations (9a) and (10a), using (15), (8) and (11), it can be deduced that $B'_{jm} = \hat{R}'_{mi} = 0$, so that the solution is

$$\begin{aligned} y(x, t) = & \frac{2F}{s} \left\{ \sum_{k=1}^{\infty} \sin \omega_k t \cdot \sum_{r=1}^N \frac{S_{rk} \phi_r(x)}{p_r^2 - \omega_k^2} \right. \\ & - \sum_{(m, j)} \sum_{k=1}^{\infty} \left(\frac{\omega_k}{\Lambda_m} \right) \frac{S_{jk} \phi_j(x)}{p_j^2 - \omega_k^2} \sin \Lambda_m t \Big\} \\ & - \sum_{m=1}^{\infty} \sum_{r=1}^N \sum_{i=1}^N R_{mi} \frac{\phi_r(c_i) \phi_r(x)}{p_r^2 - \Lambda_m^2} \sin \Lambda_m t \end{aligned} \quad (16)$$

Here, the symbol (\wedge) has been deleted from the constants R_{mi} in order to avoid confusion later. Thus, R_{mi} can be calculated from the following simultaneous restraint equations, deduced from Equations (16) and (10b). The series in m is truncated at M terms and the number of consecutive equations r is also equal to M .

$$\begin{aligned} & \sum_{m=1}^M \sum_{r=1}^N \left(\frac{\Lambda_m}{p_r} \right) \frac{R_{mi} \phi_r(c_i)}{p_r^2 - \Lambda_m^2} \\ & = \frac{2F}{s} \cdot \sum_{k=1}^{\infty} \left(\frac{\omega_k}{p_r} \right) \frac{S_{rk}}{p_r^2 - \omega_k^2} \end{aligned} \quad (17)$$

It is noted that $r = 1, 2, \dots$ where integers $r = j$ are omitted. Equations (16) and (17) have been derived by Lee [11], page 75, and are restricted to cases where $m = p_j \neq \omega_k$. The general solution for resonance in which $\Delta_m = p_j = \omega_k$ has yet to be solved in closed form for multiple spans. This latter condition occurs in typical spans for vehicle velocities between 100 and 300 mph. The significance of this resonance will be discussed in the section on Numerical Results for the special cases below.

Case 1. Single Span with Simple End Supports

For a single, simple span, $\phi_m(x)$ is given by Equation (6), $\Delta_m = p_m$ for no intermediate supports, and Equation (16), with (13) and (14) reduces to

$$\begin{aligned} y(x, t) = & \frac{2Fs}{\pi^4 EI} \left\{ \sum_{k=1}^{\infty} \frac{\sin \frac{k\pi x}{s}}{k^4 \left[1 - \frac{\omega_k^2}{p_k^2} \right]} \right. \\ & \cdot \left[\sin \omega_k t - \frac{\omega_k}{p_k} \sin p_k t \right] \Big\} \end{aligned} \quad (18)$$

where $\omega_k \neq p_k$. This result agrees with Timoshenko's [7]. At resonance, when $\omega_k = p_k$, let $y = y_R$. It is seen that Equation (18) is an indeterminate form (0/0) which can be evaluated in the limit as $\omega_k \rightarrow p_k$ using L'Hospital's rule. The result is

$$\begin{aligned} y_R(x, t) = & \frac{Fs^3}{\pi^4 EI} \sum_{k=1}^{\infty} \frac{1}{k^4} \left(\sin p_k t - p_k t \cos p_k t \right) \\ & \cdot \sin \frac{k\pi x}{s} \end{aligned} \quad (19)$$

where $\omega_k = p_k$.

Equations (18) and (19) are valid only while F is on the span, in the time interval $0 \leq t \leq s/v$. At time $t_0 = s/v$, the simple span begins free vibrations. For $t > t_0$, span deflections are given by Equation (8) where $\Lambda_m = p_j$, $j = m = 1, 2, 3, \dots$, and the terms involving \hat{R}_{mi} and R'_{mi} do not exist since the integers r do not exist. When the coefficients B_{jm} and B'_{jm} are evaluated from Equations (9), with the initial conditions from Equation (19), the result is

$$\hat{y}(x, t) = \frac{2Fs^3}{\pi^4 EI} \sum_{k=1}^{\infty} \frac{1}{k^4} \cdot \left(\frac{\omega_k}{p_k} \right) \cdot [C_k \sin p_k (t-s/v) - D_k \cos p_k (t-s/v)] \cdot \sin \frac{k\pi x}{s} \quad (20)$$

where

$$C_k = \frac{(-1)^k - \cos(p_k s/v)}{1 - \frac{\omega_k^2}{p_k^2}}$$

$$D_k = \frac{\sin(p_k s/v)}{1 - \frac{\omega_k^2}{p_k^2}}$$

where $t \geq s/v$ and $\omega_k \neq p_k$.

At resonance, this same procedure is used to determine the free vibrations, except that the initial conditions used to calculate B_{jm} and B'_{jm} are those of Equation (19), evaluated at $t = t_0 = s/v$. The result is

$$\hat{y}_R(x, t) = \frac{Fs^3}{\pi^4 EI} \sum_{k=1}^{\infty} \frac{1}{k^4} \left[\hat{C}_k \sin p_k (t-s/v) + \hat{D}_k \cos p_k (t-s/v) \right] \sin \frac{k\pi x}{s} \quad (21)$$

where

$$\hat{C}_k = p_k \frac{s}{v} \sin(p_k s/v)$$

$$\hat{D}_k = \sin(p_k s/v) - p_k \frac{s}{v} \cos(p_k s/v)$$

where $t \geq s/v$ and $\omega_k = p_k$.

Case 2. Double Span with Simple End Supports

For the two span case with simple end supports and with a central rigid prop, the natural frequencies Λ_m are given by Equations (3) and (4), with the help of Equation (2) and Table 1. With Equation (6), S_{rk} and R_{ki} are first calculated from Equations (13) and (14), respectively, where $i = N = 1$. Equations (16) with the series in m truncated at M terms, then reduces to

$$y(x, t) = \frac{2Fs^3}{\pi^4 EI} \sum_{m=1}^M \left(Q_m^{(1)} - Q_m^{(2)} - Q_m^{(3)} - Q_m^{(4)} \right) \quad (22)$$

Λ_m	1	2	3	4	5	6
1	1.00	1.00	1.00	1.00	1.00	1.00
2	2.00	1.25	1.13	1.08	1.05	1.04
3	3.00	2.00	1.37	1.25	1.18	1.13
4	4.00	2.25	2.00	1.42	1.32	1.25
5	5.00	3.00	2.13	2.00	1.45	1.37
6	6.00	3.25	2.37	2.08	2.00	1.46
7	7.00	4.00	3.00	2.25	2.05	2.00
8	8.00	4.25	3.13	2.48	2.18	2.04
9	9.00	5.00	3.37	3.00	2.32	2.13
10	10.00	5.25	4.00	3.08	2.45	2.25

TABLE 1
Numerical values of Λ_m in Equation (3), where K is the number of span sections and m is mode number. Both extreme ends are simply supported. Ayre and Jacobson [3].

where

$$Q_m^{(1)} = \frac{\sin \Lambda_m t}{m^4 \left(1 - \frac{\omega_m^2}{p_m^2} \right)} \sin(m\pi x/s)$$

$$Q_m^{(2)} = \frac{(-1)^{m+1} \sin(\omega_{2m-1} t)}{(2m-1)^4 \left(1 - \frac{\omega_{2m-1}^2}{p_{2m-1}^2} \right)}$$

$$\sum_{\ell=1}^{\infty} \frac{(-1)^{\ell+1} \sin[(2\ell-1)\pi x/s]}{(2\ell-1)^4 \left(1 - \frac{\omega_{2\ell-1}^2}{p_{2\ell-1}^2} \right)}$$

$$\cdot \frac{\sum_{\ell=1}^{\infty} (2\ell-1)^{-4} \left(1 - \frac{\omega_{2\ell-1}^2}{p_{2\ell-1}^2} \right)^{-1}}{\sum_{\ell=1}^{\infty} (2\ell-1)^{-4} \left(1 - \frac{\omega_{2\ell-1}^2}{p_{2\ell-1}^2} \right)^{-1}}$$

$$Q_m^{(3)} = \left(\frac{\omega_{2m}}{\Lambda_{2m-1}} \right) \frac{\sin(\Lambda_{2m-1} t)}{(2m)^4 \left(1 - \frac{\omega_{2m}^2}{p_{2m}^2} \right)} \sin(2m\pi x/s)$$

$$Q_m^{(4)} = \left(\frac{R_{m1}}{F} \right) \sin(\Lambda_m t)$$

$$\cdot \sum_{\ell=1}^{\infty} \frac{(-1)^{\ell+1} \sin[(2\ell-1)\pi x/s]}{(2\ell-1)^4 \left(1 - \frac{\Lambda_m^2}{p_{2\ell-1}^2} \right)^2}$$

The constants $\{R_{m1}/F\}$ from Equation (17) are given by the set of simultaneous equations

$$\sum_{m=1}^M \left(\frac{\Lambda_m}{P_{2n-1}} \right) \left(\frac{R_{m1}/F}{1 - \frac{\Lambda_m^2}{P_{2n-1}^2}} \right) = \left(\frac{\omega_{2n-1}}{P_{2n-1}} \right) \frac{(-1)^{n+1}}{\left(1 - \frac{\omega_{2n-1}^2}{P_{2n-1}^2} \right)}$$

$$- \sum_{k=1}^{\infty} \left(\frac{\omega_{2k-1}}{P_{2n-1}} \right) \frac{(-1)^{k+1}}{(2k-1)^4}$$

$$\cdot \frac{\left[\sum_{\ell=1}^{\infty} (2\ell-1)^{-4} \left(1 - \frac{\omega_{2\ell-1}^2}{P_{2\ell-1}^2} \right)^{-1} \right]}{\left(1 - \frac{\omega_{2k-1}^2}{P_{2k-1}^2} \right) \left(1 - \frac{\omega_{2n-1}^2}{P_{2n-1}^2} \right)} \quad (23)$$

where $n = 1, 2, 3, \dots, M$. The above results have also been given by Lee [11] and by Ayre, et al. [13] in different mathematical form and in terms of bending stresses rather than deflections.

At time $t = t_0 = s/v$, the force reaches the right end of the double span and the free vibration deflections are described by Equation (8) where $i = N = 1$. The constants B_{jm} , B'_{jm} , \hat{R}_{m1} , \hat{R}'_{m1} are calculated from Equations (9) and (10) using the initial conditions derived from Equation (22). In this case, the ordered pairs (m, j) are $(1, 2)$; $(3, 4)$; $(5, 6)$; ... so that only the coefficients $B_{(2n, n-1)}$ and $B'_{(2n, n-1)}$ are nonzero for all positive integers n ; the coefficients \hat{R}_{m1} and \hat{R}'_{m1} exist for all $m = 1, 2, \dots$, but are based on $r = 1, 3, 5, \dots$ only when evaluating them by Equations (10). After lengthy calculations, the results are

$$\hat{y}(x, t) = \hat{y}_B + \hat{y}_C \quad (24)$$

where

$$\hat{y}_B = \frac{2Fs^3}{\pi^4 EI} \sum_{n=1}^{\infty} \left\{ \frac{\omega_{2n}}{\Lambda_{2n-1}} \left[\cos(\omega_{2n}s/v) - \cos(\Lambda_{2n-1}s/v) \right] \cdot \sin[\Lambda_{2n-1}(t-s/v)] \right.$$

$$+ \left[\sin(\omega_{2n}s/v) - \left(\frac{\omega_{2n}}{\Lambda_{2n-1}} \right) \sin(\Lambda_{2n-1}s/v) \right] \cdot \cos[\Lambda_{2n-1}(t-s/v)] \left. \right\} \frac{\sin(2n\pi x/s)}{(2n)^4 \left(1 - \frac{\omega_{2n}^2}{P_{2n}^2} \right)}$$

$$(25)$$

$$\hat{y}_C = \frac{-2Fs^3}{\pi^4 EI} \sum_{m=1}^M \sum_{\ell=1}^{\infty} \frac{(-1)^{\ell+1} \sin[(2\ell-1)\pi x/s]}{(2\ell-1)^4 \left(1 - \frac{\Lambda_m^2}{P_{2\ell-1}^2} \right)}$$

$$\cdot \left[\left(\frac{\hat{R}'_{m1}}{F} \right) \cos \Lambda_m(t-s/v) + \left(\frac{\hat{R}_{m1}}{F} \right) \sin \Lambda_m(t-s/v) \right] \quad (26)$$

The values of (\hat{R}_{m1}/F) and (\hat{R}'_{m1}/F) are each calculated from the following M simultaneous equations, where $r = 1, 3, 5, \dots$, and where values of (R_{m1}/F) are calculated from Equation (23).

$$- \sum_{m=1}^M \left(\frac{\hat{R}'_{m1}}{F} \right) \frac{\sin(r\pi/2)}{\left(1 - \frac{\Lambda_m^2}{P_r^2} \right)} = \frac{\sin(\omega_r s/v)}{\left(1 - \frac{\omega_r^2}{P_r^2} \right)}$$

$$- \sum_{m=1}^M \frac{(-1)^{m+1} \sin(\omega_{2m-1}s/v)}{(2m-1)^4 \left(1 - \frac{\omega_{2m-1}^2}{P_{2m-1}^2} \right)}$$

$$\cdot \frac{\sin(r\pi/2)}{\left(1 - \frac{\omega_{2m-1}^2}{P_r^2} \right) \cdot \sum_{\ell=1}^{\infty} \frac{1}{(2\ell-1)^4 \left(1 - \frac{\omega_{2\ell-1}^2}{P_{2\ell-1}^2} \right)}}$$

$$- \sum_{m=1}^M \left(\frac{\hat{R}_{m1}}{F} \right) \sin(\Lambda_m s/v) \cdot \frac{\sin(r\pi/2)}{\left(1 - \frac{\Lambda_m^2}{P_r^2} \right)} \quad (27)$$

and

$$- \sum_{m=1}^M \left(\frac{\Lambda_m}{P_r} \right) \left(\frac{\hat{R}_{m1}}{F} \right) \frac{\sin(r\pi/2)}{\left(1 - \frac{\Lambda_m^2}{P_r^2} \right)} = \left(\frac{\omega_r}{P_r} \right) \frac{\cos(\omega_r s/v)}{\left(1 - \frac{\omega_r^2}{P_r^2} \right)}$$

$$- \sum_{m=1}^M \left(\frac{\omega_{2m-1}}{P_r} \right) \frac{(-1)^{m+1} \cos(\omega_{2m-1}s/v)}{(2m-1)^4 \left(1 - \frac{\omega_{2m-1}^2}{P_{2m-1}^2} \right)}$$

$$\cdot \frac{\sin(r\pi/2)}{\left(1 - \frac{\omega_{2m-1}^2}{P_{2m-1}^2} \right) \cdot \sum_{\ell=1}^{\infty} \frac{1}{(2\ell-1)^4 \left(1 - \frac{\omega_{2\ell-1}^2}{P_{2\ell-1}^2} \right)}}$$

equation continued on next page

$$= \sum_{m=1}^{\infty} \left(\frac{R_{m1}}{F} \right) \cdot \left(\frac{\Lambda_m}{P_r} \right) \cos(\Lambda_m s/v) \cdot \frac{\sin(r\pi/2)}{\left(1 - \frac{\Lambda_m^2}{P_r^2} \right)} \quad (28)$$

Case 3. Triple Span with Simple End Supports

For the three span case with simple end supports and with a rigid prop at $x = c_1 = s/3$ and at $x = c_2 = 2s/3$, the natural frequencies Λ_m are given by Equations (3) and (5) with the help of Equation (2) and Table 1. With Equation (6), S_{rk} and R_{ki} are first calculated from Equations (13) and (14), respectively, where $N = 2$ is the maximum value of i . Equations (16), with the series in m truncated at M terms then reduces

$$y(x,t) = \frac{2Fs^3}{\pi^4 EI} \sum_{m=1}^M \left(Q_m^{(1)} - Q_m^{(2)} - Q_m^{(3)} - Q_m^{(4)} \right) \quad (29)$$

where

$$Q_m^{(1)} = \frac{\sin \omega_m t}{m^4 \left(1 - \frac{\omega_m^2}{P_m^2} \right)} \sin(m\pi x/s)$$

(All values of $m = 1, 2, \dots, M$ included in $Q_m^{(1)}$)

$$Q_m^{(2)} = \sum_{\ell=1}^{\infty} j \frac{\left[\delta_m \sin(\ell\pi/3) + \epsilon_m \sin(2\ell\pi/3) \right]}{\ell^4 m^4 \left(1 - \frac{\omega_m^2}{P_{\ell}^2} \right) \left(1 - \frac{\omega_m^2}{P_m^2} \right)} \cdot \frac{\sin(\ell\pi x/s)}{\left(\alpha_m \gamma_m - \beta_m^2 \right)} \sin \omega_m t$$

(Values of $m, \ell = 3, 6, 9, \dots$ are excluded in $Q_m^{(2)}$)

$$Q_m^{(3)} = \left(\frac{\omega_{3m}}{\Lambda_{3m-2}} \right) \frac{\sin(\Lambda_{3m-2} t)}{(3m)^4} \cdot \frac{\sin(3m\pi x/s)}{\left(1 - \frac{\Lambda_{3m}^2}{P_{3m}^2} \right)}$$

(All values of $m = 1, 2, \dots, M$ included in $Q_m^{(3)}$)

$$Q_m^{(4)} = \sin \omega_m t \sum_{r=1}^{\infty} j G_{rm} \frac{\sin(r\pi x/s)}{r^4 \left(1 - \frac{\Lambda_m^2}{P_r^2} \right)}$$

(All values of $\ell = 3, 6, 9, \dots$ are excluded in $Q_m^{(4)}$)

The constants G_{rm} are given by

$$G_{rm} = \left(\frac{R_{m1}}{F} \right) \sin(r\pi/3) + \left(\frac{R_{m2}}{F} \right) \sin(2r\pi/3) \quad (30)$$

and by 2M equations in r of the form

$$\sum_{m=1}^{\infty} \left(\frac{\Lambda_m}{P_r} \right) \frac{G_{rm}}{\left(1 - \frac{\Lambda_m^2}{P_r^2} \right)} = \left(\frac{\omega_r}{P_r} \right) \frac{1}{\left(1 - \frac{\omega_r^2}{P_r^2} \right)} - \sum_{k=1}^{\infty} \frac{\left(\omega_k/P_r \right) \left[\delta_k \sin(r\pi/3) + \epsilon_k \sin(2r\pi/3) \right]}{k^4 \left(1 - \frac{\omega_k^2}{P_r^2} \right) \left(\alpha_k \gamma_k - \beta_k^2 \right)} \quad (31)$$

where $r \neq 3, 6, 9, \dots$. The additional coefficients where $k, \ell \neq 3, 6, 9, \dots$ are

$$\alpha_k = \sum_{\ell=1}^{\infty} j \frac{\sin^2(\ell\pi/3)}{\ell^4 \left(1 - \frac{\omega_k^2}{P_{\ell}^2} \right)} \quad (32a)$$

$$\epsilon_k = \sum_{\ell=1}^{\infty} j \frac{\sin(\ell\pi/3) \cdot \sin(2\ell\pi/3)}{\ell^4 \left(1 - \frac{\omega_k^2}{P_{\ell}^2} \right)} \quad (32b)$$

$$\gamma_k = \sum_{\ell=1}^{\infty} j \frac{\sin^2(2\ell\pi/3)}{\ell^4 \left(1 - \frac{\omega_k^2}{P_{\ell}^2} \right)} \quad (32c)$$

$$\delta_k = \gamma_k \sin(k\pi/3) - \epsilon_k \sin(2k\pi/3) \quad (32d)$$

$$\epsilon_k = \alpha_k \sin(2k\pi/3) - \delta_k \sin(k\pi/3) \quad (32e)$$

For free vibrations, the coefficients of Equation (8) are evaluated from Equations (9) and (10) as previously, except that the conditions at $t_0 = s/v$ are based on Equation (29). In this case, the ordered pairs (m, j) are (1,3); (4,6); (7,9); The results are

$$\hat{y}(x,t) = \hat{y}_B + \hat{y}_C \quad (33)$$

where

$$Y_B = \frac{2Fs}{EI} \sum_{m=1}^M \left\{ B_m \sin \left[\lambda_m (t-s/v) \right] + B'_m \cos \left[\lambda_m (t-s/v) \right] \right\} \frac{\sin(3m\pi x/s)}{(3m)^2 \left(1 - \frac{\lambda_m^2}{p_r^2} \right)} \quad (34)$$

where

$$B_m = \frac{\lambda_m}{\lambda_{m-2}} \left[\cos \left(\lambda_{m-2} s/v \right) - \cos \left(\lambda_{m-1} s/v \right) \right]$$

$$B'_m = \sin \left(\lambda_{m-2} s/v \right) - \frac{\lambda_m}{\lambda_{m-2}} \sin \left(\lambda_{m-1} s/v \right)$$

and where

$$\dot{Y}_C = - \frac{2Fs}{EI} \sum_{m=1}^M \sum_{\ell=1}^M \left\{ E_{\ell m} \sin \left[\lambda_m (t-s/v) \right] + E'_{\ell m} \cos \left[\lambda_m (t-s/v) \right] \right\} \frac{\sin(\ell\pi x/s)}{\ell^2 \left(1 - \frac{\lambda_m^2}{p_\ell^2} \right)} \quad (35)$$

where

$$E_{\ell m} = \left(\frac{\hat{R}_{m1}}{F} \right) \sin(\ell\pi/3) + \left(\frac{\hat{R}_{m2}}{F} \right) \sin(2\ell\pi/3)$$

$$E'_{\ell m} = \left(\frac{\hat{R}'_{m1}}{F} \right) \sin(\ell\pi/3) + \left(\frac{\hat{R}'_{m2}}{F} \right) \sin(2\ell\pi/3)$$

The values of (\hat{R}'_{m1}/F) and (\hat{R}'_{m2}/F) are calculated from $E'_{\ell m}$ above and $2M$ of the following simultaneous equations, where $r \neq 3, 6, 9, \dots$

$$\begin{aligned} & - \sum_{m=1}^M \frac{E_{\ell m}}{\left(1 - \frac{\lambda_m^2}{p_r^2} \right)} = \frac{\sin(\omega_r s/v)}{\left(1 - \frac{\omega_r^2}{p_r^2} \right)} \\ & - \sum_{m=1}^M \frac{\sin(\omega_m s/v)}{m^2 \left(1 - \frac{\omega_m^2}{p_r^2} \right) \left(1 - \frac{\omega_m^2}{p_m^2} \right)} \\ & \quad \cdot \frac{[\delta_m \sin(r\pi/3) + \epsilon_m \sin(2r\pi/3)]}{(\alpha_m \gamma_m - \beta_m^2)} \end{aligned}$$

equation continued at top of page

$$\begin{aligned} & \sum_{m=1}^M \sin(\lambda_m s/v) \\ & \cdot \frac{\left[\left(\frac{P_{m1}}{F} \right) \sin(r\pi/3) + \left(\frac{R_{m2}}{F} \right) \sin(2r\pi/3) \right]}{\left(1 - \frac{\lambda_m^2}{p_r^2} \right)} \end{aligned} \quad (36)$$

Finally, the values of (\hat{R}_{m1}/F) and (\hat{R}_{m2}/F) are calculated from $E_{\ell m}$ above and $2M$ of the following simultaneous equations where $r \neq 3, 6, 9, \dots$

$$\begin{aligned} & - \sum_{m=1}^M \left(\frac{\lambda_m}{p_r} \right) \frac{E_{\ell m}}{\left(1 - \frac{\lambda_m^2}{p_r^2} \right)} = \left(\frac{\omega_r}{p_r} \right) \frac{\cos(\omega_r s/v)}{\left(1 - \frac{\omega_r^2}{p_r^2} \right)} \\ & - \sum_{m=1}^M \left(\frac{\omega_m}{p_r} \right) \frac{\cos(\omega_m s/v)}{m^2 \left(1 - \frac{\omega_m^2}{p_r^2} \right) \left(1 - \frac{\omega_m^2}{p_m^2} \right)} \\ & \quad \cdot \frac{[\delta_m \sin(r\pi/3) + \epsilon_m \sin(2r\pi/3)]}{(\alpha_m \gamma_m - \beta_m^2)} \\ & - \sum_{m=1}^M \left(\frac{\lambda_m}{p_r} \right) \cos(\lambda_m s/v) \\ & \quad \cdot \frac{\left[\left(\frac{R_{m1}}{F} \right) \sin(r\pi/3) + \left(\frac{R_{m2}}{F} \right) \sin(2r\pi/3) \right]}{\left(1 - \frac{\lambda_m^2}{p_r^2} \right)} \end{aligned} \quad (37)$$

It is seen that such calculations are more lengthy as the number of props increase. However, the series involved are rapidly convergent because of the factor m^4 in the denominators of these sums. Sets of simultaneous equations for the unknown constants are easily solved on the digital computer so that numerical values for y can be obtained to any reasonable degree of accuracy desired.

STATIC DEFLECTIONS FOR A MOVING POINT LOAD

The static deflection of a point force F at a distance vt from the left support of a continuous span, which has N rigid, internal props at distances c_1, c_2, c_3, \dots from that support, can be found from elementary beam theory [14]. The $(N+2)$ reaction forces R_i are labeled

R_0, R_1, \dots , starting at the left support. The static equilibrium conditions are

$$\sum_{i=0}^{N+1} R_i = F \quad (38)$$

$$s R_{N+1} + \sum_{i=1}^N c_i R_i = vtF \quad (39)$$

Using double integration and the Macauley bracket method, the static deflection for the span simply supported at each end is

$$y(x,t) = \frac{-1}{6EI} \cdot \left\{ R_0 x^3 + \sum_{i=1}^N R_i \langle x - c_i \rangle^3 - F \langle x - vt \rangle^3 + Dx \right\} \quad (40)$$

where $vt < s$ and where Macauley's bracket convention is used. That is, if C is a real number

$$\begin{aligned} \langle C \rangle^3 &= 0 & \text{if } C \leq 0 \\ \langle C \rangle^3 &= C^3 & \text{if } C > 0 \end{aligned}$$

To explicitly evaluate the $N+3$ unknowns ($N+2$ reactions and one integration constant D), Equations (28) and (39) are solved simultaneously with the $(N+1)$ constraint equations

$$\begin{aligned} y(c_i, t) &= 0, \quad i = 1, 2, \dots, N \\ y(s, t) &= 0 \end{aligned} \quad (41)$$

Static deflections will be used as the reference values in dynamic calculations.

BENDING MOMENTS, STRESSES, AND LOAD ACCELERATIONS

Once the span deflection has been determined, either static or dynamic, the bending moment $M(x, t)$ can be calculated from

$$M(x, t) = -EI \frac{\partial^2 y(x, t)}{\partial x^2} \quad (42)$$

where $\hat{y}(x, t)$ replaces $y(x, t)$ if the moments for free vibration are required. The maximum flexural stress in any case is found by dividing $M(x, t)$ by the section modulus of the span.

As the point force travels at constant speed v along the span, the total velocity of F is directed tangent to the trajectory of the span at any instant. Although the magnitude of this velocity is constant, its direction is not, since the span does not remain horizontal. For this reason, the total vertical

acceleration of the force F , as shown in Ref. [1], is

$$\frac{d^2 y}{dt^2} = \frac{\partial^2 y}{\partial t^2} + 2v \frac{\partial^2 y}{\partial x \partial t} + v^2 \frac{\partial^2 y}{\partial x^2} \quad (43)$$

which can be evaluated directly when the deflections at the location of F are known. It is necessary to consider these "heave" accelerations when designing vehicle suspension systems for passenger comfort.

RESPONSE TO PRESSURE LOADS BY SUPERPOSITION

The continuous pressure loads of air cushion vehicles traversing multiple spans can be approximated by a series of point loads F_1, F_2, \dots moving in tandem, which are spaced Δx apart. It is assumed that these loads may have different prescribed magnitudes (some may be zero) but that they are time-invariant. Consider time $t = t_n$ where

$$t_n = n \frac{\Delta x}{v} \quad (44)$$

and designate the deflection due to a unit load at position $n\Delta x$ as $y(x, t_n)$. At time $t = t_1$, let F_1 , the first load of the tandem, be at position $x = \Delta x$ and the span deflection at all x due to F_1 will then be $F_1 y(x, t_1)$. At time t_2 , load F_1 will be at position $x = 2\Delta x$ and its contribution to the span deflection will be $F_1 y(x, t_2)$. Also, F_2 will be at position $x = \Delta x$ and will cause a deflection $F_2 y(x, t_2)$. By superposition, the deflection due to both F_1 and F_2 at time $t = t_2$ are additive, and this sum is designated as $Y(x, t_2)$, where

$$Y(x, t_2) = F_1 \cdot y(x, t_2) + F_2 \cdot y(x, t_1)$$

It is thus easily deduced that the total span deflection at any time $t = t_n$ is given by

$$Y(x, t_n) = \sum_{j=1}^n F_j \cdot y(x, t_{n+1-j}) \quad (45)$$

where the value of $y(x, t_{n+1-j})$ is the value derived for the unit point load in forced vibrations if $t_{n+1-j} \leq s/v$. However, if $t_{n+1-j} \geq s/v$, the value of y derived for free vibrations where the unit load has left the span, must be used, or $y(x, t_{n+1-j}) = y(x, t_{n+1-j})$. With these restrictions, Equation (45) can be used in conjunction with the previous results to obtain the dynamic response to multiple loads of fixed magnitude

traversing a multiple span at constant velocity, where the length of the loading compared to the span length s is unrestricted. The numerical results which follow illustrate these ideas.

NUMERICAL EXAMPLES FOR SEGMENTED PRESSURES TRAVERSING SINGLE SPANS

Fortran IV computer programs were written and an IBM-360/75 digital computer was utilized to study the dynamic deflections and bending moments of single, double, and triple-span guideways for multiple, constant velocity loadings. Extensive numerical results are presently available for the single span guideway and those results will now be summarized. The critical section of this guideway is in the neighborhood of the midspan. For several types of moving loads, it was found that the maximum values of deflection and bending moment actually occurred at various distances up to about $1/30$ the span length from the center, but that those off center values never exceeded 2% of those at midspan. For design purposes, then it appears that a knowledge of midspan values are sufficient.

In the numerical procedure, the dynamic response to the point force, or influence function, is first calculated. Some typical influence functions at midspan, based on Equations (18-22) and five modes ($k=5$), are shown in Figure 1 for fixed ratios of the first passage frequency to the fundamental span frequency, ω_1/p_1 . For a fixed traverse velocity over a given span, this ratio is fixed. These curves depict the variation of the midspan deflection with time. For $\omega_1/p_1 = 0$, the static response corresponding to "crawl" velocity is shown, where the free vibrations are zero. The maximum dynamic deflection occurs for $\omega_1/p_1 = 0.5$, while the force is on the span; but the span undergoes free vibrations of smaller amplitude. At resonance, $\omega_1/p_1 = 1$ and the maximum deflections are the same during passage and during free vibrations. For all values of $\omega_1/p_1 > 1$, the deflection amplitudes, both in forced and free vibrations, are less than those of Figure 1. The bending moment curves show similar behavior.

In Figure 2, the maximum values of deflection and bending moment at midspan are shown in terms of the parameter ω_1/p_1 . It is not difficult to show that both curves approach zero as ω_1/p_1 approaches large numbers. For the typical span reported in [1] whose natural frequency is 2.25 cycles per second ($p_1 = 14.1$ radians/sec), where the length s is 75 ft., the absolute maximum amplification of deflection and bending moment

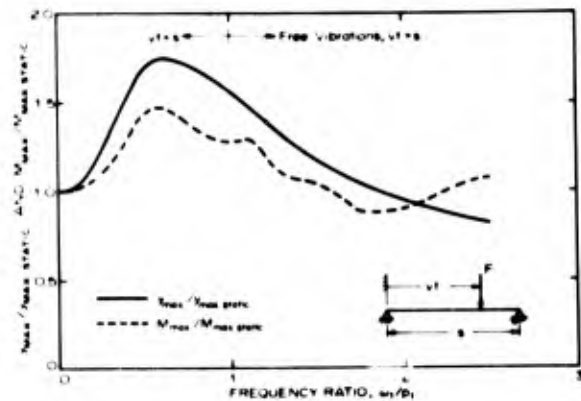


Figure 2 - Maximum values of deflection and bending moment at midspan for a single span guideway in response to a force traversing at constant speed.

with respect to their maximum static values are 1.71 and 1.41, respectively, corresponding to $\omega_1/p_1 = 0.5$, or a passage velocity of 115 mph. The maximum static values of deflection and bending moment, based on a point load at midspan are respectively

$$Y_{\max}^{\text{static}} = \frac{F s^3}{48EI} = Y_0 \quad (46)$$

$$M_{\max}^{\text{static}} = \frac{F s}{4} = M_0 \quad (47)$$

The span response to vehicle loading cases A through F, shown in Table 2, were next solved by superposition of the point load influence functions, as explained previously. In all cases, the uniformly distributed loads were approximated by point loads of equal magnitude, at spacings of 0.02s to 0.04s. For these spacings, the dynamic maximum deflections were within 9% of those calculated from the closed form solutions of the uniformly loaded case of Ref. [1]. The static deflections agreed to within 1% for these spacings. For ease of reference, the maximum static values for deflections and bending moments for the six loading cases considered are listed in Table 2, all based on the point load reference values Y_0 and M_0 of Equations (46) and (47). The total load was taken to be the same for all cases, even though, for cases E and F, a part of this load is off the reference span.

Figure 3 shows the results for a vehicle which is two-thirds the length of the span. When the load is uniform under the whole length of the vehicle, case A, the curves for deflection and moment are nearly coincident and have only one peak. This peak occurs for $\omega_1/p_1 = 0.8$, where the deflection amplification is 1.64. This represents a shift to the right in the deflection vs

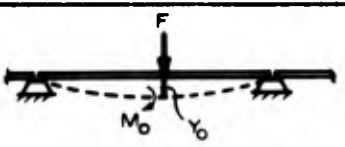
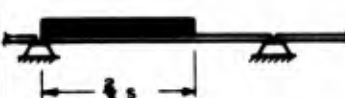

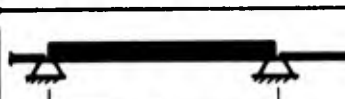


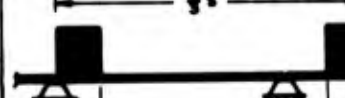
Type of Loading	$\frac{Y_{\max \text{ static}}}{Y_0}$	$\frac{M_{\max \text{ static}}}{M_0}$
	1	1
A 	0.808	0.606
B 	0.723	0.530
C 	0.615	0.492
D 	0.522	0.484
E 	0.463	0.372
F 	0.522	0.484

TABLE 2
Maximum static deflections and bending moments at midspan of a single span guideway, where the total load F is the same in each case

ω_1/p_1 curve when compared to Figure 2 for the point load case. When the load is segmented as in case B, however, two peaks occur in both the deflection and moment curves. These peak amplification factors, and the corresponding values of ω_1/p_1 are summarized in Table 3 for all cases (A-F).

Several trends are apparent when the results of Figures 3, 4, and 5, or Table 3 are compared.

- (a) For increasing lengths of non-segmented, uniform loadings A, C and E the frequency ratios ω_1/p_1 at which the peak amplifications occur increase from 0.8 to 1.25 and the amplifications increase from 1.64 to 1.9. These results are

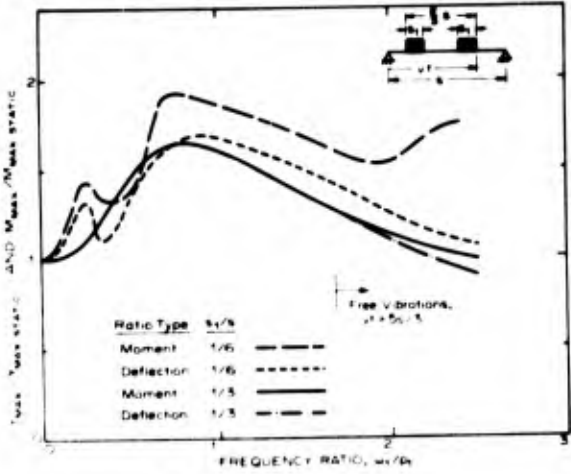


Figure 3 - Maximum deflections and bending moments for a single span guideway where the vehicle length is two-thirds the span length

LOAD TYPE	$\frac{Y_{\text{peak}}}{Y_{\max \text{ static}}}$	$\frac{\omega_1}{p_1}$ at Y_{peak}	$\frac{M_{\text{peak}}}{M_{\max \text{ static}}}$	$\frac{\omega_1}{p_1}$ at M_{peak}
POINT FORCE (Fig. 2)	1.71	0.50	1.41	0.50
A (Fig. 3)	1.64	0.80	1.65	0.80
B (Fig. 3)	1.32	0.25	1.43	0.25
C (Fig. 4)	1.70	0.90	1.93	0.75
D (Fig. 4)	1.73	1.00	1.78	1.00
E (Fig. 5)	2.31	0.50	1.98	0.50
F (Fig. 5)	1.53	0.90	1.44	0.80
			1.48	1.20
			1.60*	2.15
	1.85	1.25	1.91	1.25
	3.20	1.63	2.78	1.63
			1.20	1.78

TABLE 3
Peak values of dynamic deflections and bending moments at midspan of a single span guideway. (*) denotes free vibration

consistent with those of Ref. [2] where, for uniformly loaded trains of air cushion vehicles longer than the span length, the non-damped deflection amplifications approached 2.0.

- (b) The amplification of deflections and bending moments are nearly identical at corresponding values of ω_1/p_1 for non-segmented loadings.
- (c) For segmented loadings B, D and F where the loaded segments are all

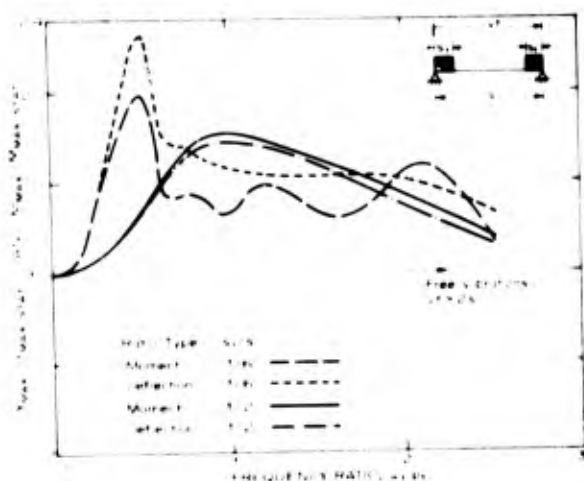


Figure 4 - Maximum deflections and bending moments at midspan for a single span guideway where the vehicle length is equal to the span length

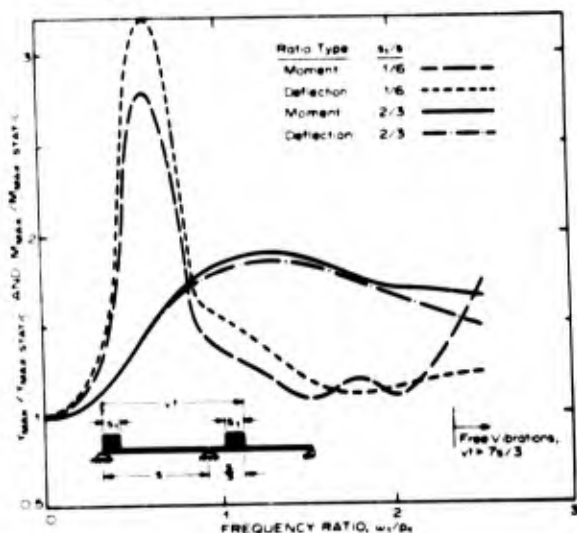


Figure 5 - Maximum deflections and bending moments at midspan where the vehicle length is four-thirds the span length

one-sixth the span length, the amplifications, which approach 3.2, increase as the segments are separated. Although there may be more than one peak value of amplification, the highest of these peaks occur for $\omega_1/p_1 < 1$.

- (d) Although these amplification factors seem high, it is recalled that they are values relative to the maximum values for the corresponding distributed static loads. As shown in Table 2, the actual deflections and moments due to a distributed load may be one-half that of the same concentrated point load.

On this basis, then, maximum dynamic deflections for segmented pressure loads may still be less than twice those for the same static point load.

- (e) The extreme amplification peaks occur in the range $0.5 < [\omega_1/p_1] < 1.5$, which corresponds to vehicle cruising speeds of 100 to 300 mph and span frequencies of about 2 cps. Thus, guideways should be designed for these extreme peaks. However, since vehicles with non-segmented pressure distributions give lower peaks, cost savings on guideway construction might be effected by considering vehicles of types A, C and E rather than the segmented types B, D and F.
- (f) For distributed loads, the extreme peaks for deflection and bending moment all occur while the tail end of the load is leaving the span. The maximum peaks were found to be less during free vibration.

In reaching its cruising speed, an air cushion vehicle needs to accelerate along the span. For passenger comfort, this horizontal acceleration, \ddot{x} , should probably not exceed $0.04 g$'s ($g = 32.2 \text{ ft/sec}^2$) as discussed in [3]. To determine the effects of horizontal vehicle acceleration on guideway deflections, numerical results were obtained using the theory developed in [1]. The following results are based on a vehicle modeled as one with a continuous pressure covering $0.427s$; for values of \ddot{x} in the range $0 \leq \ddot{x} \leq 1.0g$; and for frequency ratios in the range $0 < \omega_1/p_1 < 1.75$. Here, ω_1 is based on the initial vehicle as it enters a simply supported span.

- (a) In the frequency range $0 < \omega_1/p_1 < 0.5$, there is a maximum decrease in the ratio of dynamic to static deflection of 16% for $\ddot{x} = 1.0g$.
- (b) In the frequency range of interest for high speed vehicles, $0.5 \leq \omega_1/p_1 \leq 1.75$, there is a maximum decrease in the ratio of dynamic to static deflection of 2% for $\ddot{x} = 1.0g$.
- (c) For \ddot{x} in the range $0 < \ddot{x} < 1.0g$, the percent decrease in dynamic deflections were always less than those reported above.

It is concluded that, for horizontal vehicle accelerations of less than $1.0g$, guideway design based on the assumption of constant vehicle speed, is quite appropriate.

THE TWO-SPAN CASE

Ayre, et al. [13] report both experimental and theoretical results for the response to a moving point force of the two-span case with a central, rigid prop. The experimental results have been replotted in Figure 6, where the maximum

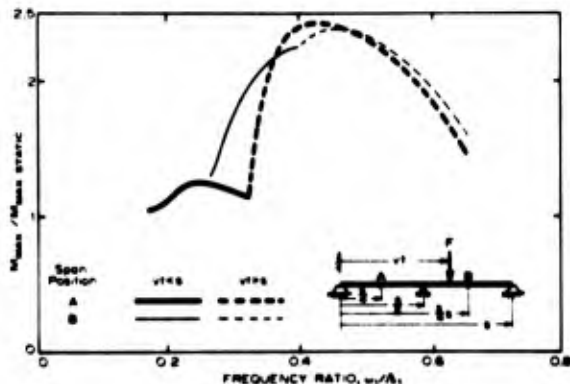


Figure 6 - Maximum experimental values of bending moment at the quarter and three-quarter points of a two-span guideway in response to a point force traversing at constant speed. Ayre, et al. [13]

bending moments are shown as a function of the frequency ratio ω_1/λ_1 at the critical points, the quarter and three-quarter span positions, where λ_1 is the fundamental span frequency. The maximum static bending moment at either position is easily shown to be

$$M_{\max} = 1.024 \frac{F s}{\pi^2} \quad (48)$$

static

Unlike the analogous dashed curve of Figure 2 for the single span, the peak responses at both critical points occur after the load has left the span, or during free vibrations. The theory developed above is presently being compared with these experimental curves and results similar to those in Figures 3-5 will soon be available. Preliminary results for the influence functions give peak amplifications near 3.0, which are higher than the peak experimental values of 2.4 shown in Figure 6. Whether the experimental influence functions, which include the effects of free vibration damping, or the theoretical influence functions, Equations (22-28), which do not include damping, should be used to derive the response of multiple spans to multiple loads, is presently being evaluated.

ACKNOWLEDGEMENTS

This research was sponsored by a NASA Sustaining Grant to Duke University under contract number NGL 34-001-005 and also by the U.S. Department of Transportation under contract number DOT-FR-00037.

REFERENCES

1. J.F. Wilson, "Dynamic Response of Beams to Moving Pressure Loads As Related to Tracked Air Cushion Vehicles," Shock and Vibration Bulletin, Vol. 40, Part 4, pp. 47-62, December 1969.
2. J.F. Wilson and S.B. Biggers, "Dynamic Interactions Between Long, High Speed Trains of Air Cushion Vehicles and Their Guideways," to be published in Journal for Engineering and Industry, ASME, 1971.
3. Quarterly Report of the Railway Technical Research Institute, Japanese National Railways, August, 1964.
4. S.B. Biggers, "Dynamic Interactions of Multiple, High Speed Air Cushion Vehicles with Their Guideways - A Parametric Study," Ph.D. dissertation, Duke University, 1970.
5. A. Kaplan; N. Lipner; F.B. Roberts; R.O. Strom, "Train Elevated Guideway Interactions," Report No. FRA-RT-70-23, TRW Systems Group, Feb. 1970.
6. N. Lipner; D.A. Evensen; A. Kaplan, "Dynamic Response of Continuous Beam Elevated Guideways," Draft Report No. 06818-6046-RO-00, Vols. I and II, TRW Systems Group, June, 1970.
7. S. Timoshenko and D.H. Young, Vibration Problems in Engineering, D. Van Nostrand, Inc., N.Y., 1955.
8. E. Saibel, "Vibration Frequencies of Continuous Beams," Journal of the Aeronautical Sciences, Vol. 11, pp. 88-90, 1944.
9. J.W. Miles, "Vibrations of Beams on Many Supports," Journal of the Engineering Mechanics Division, ASCE, Vol. 82, pp. 1-9, Jan. 1956.
10. R.S. Ayre and L.S. Jacobsen, "Natural Frequencies of Continuous Beams of Uniform Span Length," Journal of Applied Mechanics, Vol. 17, pp. 391-395, Dec. 1950.

11. W.F.Z. Lee, "On the Free and Forced Vibrations of Continuous Beams and Plates," Doctor of Science Dissertation, Carnegie-Mellon-University, 1952.
12. E. Sattel and W.F.Z. Lee, "Vibrations of a Continuous Beam Under a Constant Moving Force," Journal of the Franklin, pp. 499-516, Dec. 1952.
13. R.S. Ayre; G. Ford, and L.S. Jacobsen, "Transverse Vibration of a Two-Span Beam Under Action of a Moving Constant Force," Journal of Applied Mechanics, ASME, Vol. 17, pp. 1-12, March 1950.
14. S.H. Crandall and N.C. Dahl, editors, "An Introduction to the Mechanics of Solids," Ch. 8, McGraw-Hill Book Co., Inc., 1959.

DISCUSSION

Mr. Nicholas (Air Force Materials Laboratory): In your analysis, did you consider any interaction between the vehicle and the bridge, or did you consider the loading to be constant?

Mr. Wilson: Yes. In this particular paper the loading was considered constant or zero. Since then we have considered the Richardson model, which is spring-mass, spring-mass with damping in between on top of these pressure segments, and some very interesting results have been found.

Mr. Nicholas: You included a term in the differential equation which considers the axial tension in the beam. Were you considering these to be pinned-pinned beams or simply supported on rollers?

Mr. Wilson: The civil engineers who work on these simple spans tell me that it is best to consider these bridges as simple spans with no end tension and without any foundation effects. I included that k too. I made some studies of the relative frequencies of the beam as the end tension is applied, however, for these results the end tension was zero. It turns out for practical cases, if some end tension is placed on the beams it does not change the frequency very much. If too much tension is applied the beams will fail, because concrete can not take tension. This is how I rationalized taking the end tension to be zero. So, in essence, the answer to the question is that they are simply supported on rollers.

ANALYSIS OF THE MOTION OF A LONG WIRE TOWED FROM AN ORBITING AIRCRAFT*

S. A. CHAI
Department of Engineering Mechanics
USAF Academy, Colorado

A lumped mass model of a long trailing wire antenna is presented and Lagrange's equations of motion derived. These equations were solved numerically for the case of vertical aircraft oscillations in a constant radius and altitude orbit. A slack condition was found at the drogue for certain magnitude oscillations. The equations were also solved for the case of aircraft transition from orbit to straight and level flight. Both tension at the aircraft and instantaneous positions of the cable are presented.

INTRODUCTION

Previous studies by the Cornell Aeronautical Laboratory and the Naval Air Development Center [1,2] have generated the steady state shape of a long wire towed from an orbiting aircraft. The parameters used in those studies and this paper are appropriate for the VLF antenna used by the TACAMO system. Cornell and NADC used a partial differential approach and a finite differences solution scheme to calculate the steady state shape. Their studies did not include any transient motions. The present study has extended the investigations of the TACAMO cable to include the effect of aircraft oscillations on cable motion.

The previous studies assumed an inextensible cable attached to an aircraft flying in a constant altitude, speed and radius orbit. A conical drogue was assumed to be attached at the lower end of the cable. The partial differential equations were derived by assuming static equilibrium for a mass element.

The present study has extended the investigations of the TACAMO cable to include the effect of aircraft oscillations and wind shear on cable motion. To overcome the difficulties associated with a numerical solution of a system of partial differential equations having time dependent boundary conditions (due to the drogue end of the cable), a lumped mass model of the cable was developed and ordinary differential equations derived via the Lagrangian for the system. The discrete mass approach is equivalent to the continuous or distributed mass approach in the limit as the number of mass points approach infinity. However, good accuracy can be achieved with a few mass points [3].

The results are presented below for the case of an aircraft undergoing severe vertical oscillations and the case of an orbiting aircraft transitioning to straight and level flight with the cable deployed. The analysis for the wind shear problem is described but no results are available. The analysis has also been extended to studies which include the effects of a nuclear blast passing over the cable but the results are not included because of security restrictions.

The results presented are merely examples of the types of computer experiments which can easily be conducted using the present analysis. Many interesting operational cases remain to be studied.

DERIVATION OF EQUATIONS OF MOTION

The TACAMO cable is divided into n mass points connected by straight, linear elastic, massless spring segments. The spring segments must be included to allow for both transverse and axial wave propagation in the cable. Each mass point has three degrees of freedom and is located in the x, y, z coordinate system shown in Fig. 1.

The equations of motion can be derived by treating the aerodynamic forces and using Lagrange's equation. The kinetic energy of the cable system is given by

$$T = \sum_{i=1}^n \frac{m_i}{2} (\dot{x}_i^2 + \dot{y}_i^2 + \dot{z}_i^2) \quad (1)$$

* This research supported by the Naval Electronic Systems Command through Office of Naval Research Contract No. N00014-66-C-0357, Task No. NR321-013.

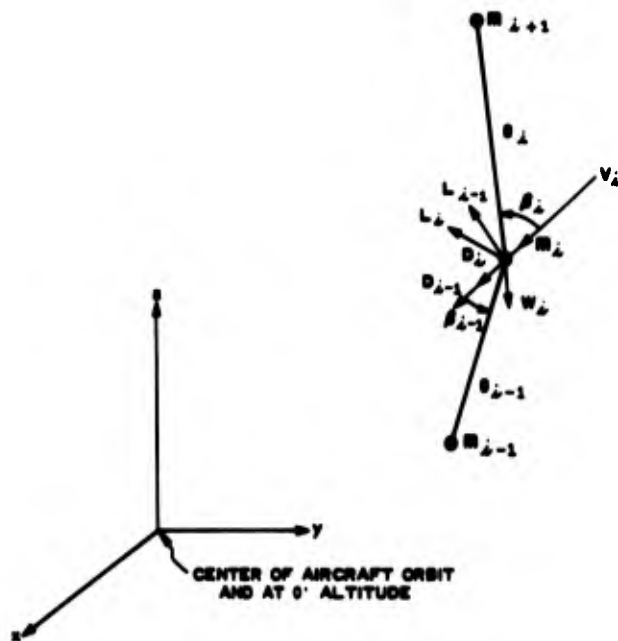


Figure 1
Coordinate System For i^{th} Mass Point

The potential energy is given by

$$V = \sum_{i=1}^n \frac{k_i}{2} (e_i - s_i)^2 + \sum_{i=1}^n m_i g z_i \quad (2)$$

where

- e_i = stretched spring length
- $g = 32.2 \text{ ft/sec}^2$
- k_i = springs constant =
 $= \frac{(\text{crosssectional area} \times \text{elastic modulus})}{s_i}$
- m_i = mass of i^{th} element
- s_i = unstretched spring length.

For any given mass point, i , the two connecting segment lengths e_i and e_{i+1} are given by

$$e_i = \left[(x_{i+1} - x_i)^2 + (y_{i+1} - y_i)^2 + (z_{i+1} - z_i)^2 \right]^{1/2} \quad (3)$$

and

$$e_{i-1} = \left[(x_i - x_{i-1})^2 + (y_i - y_{i-1})^2 + (z_i - z_{i-1})^2 \right]^{1/2} \quad (4)$$

The Langrangian is given by $L = T - V$ and Lagrange's equations of motion are

$$\frac{d}{dt} \left[\frac{\partial L}{\partial \dot{q}_i} \right] - \frac{\partial L}{\partial q_i} = Q_i \quad i=1,2,\dots,n \quad (5)$$

where the q_i are the generalized coordinates namely x_i, y_i, z_i and the Q_i are the generalized forces arising from the lift and drag on the i^{th} cable segment.

The deviations indicated in equation (5) are as follows

$$\frac{d}{dt} \left[\frac{\partial L}{\partial \dot{q}_i} \right] = \begin{cases} m_i \ddot{x}_i \\ m_i \ddot{y}_i \\ m_i \ddot{z}_i \end{cases} \quad i=1,2,\dots,n \quad (6)$$

and

$$\frac{\partial L}{\partial q_i} = \begin{cases} -k_i(e_i - s_i) \frac{\partial e_i}{\partial x_i} \\ -k_{i-1}(e_{i-1} - s_{i-1}) \frac{\partial e_{i-1}}{\partial x_i} \\ -k_i(e_i - s_i) \frac{\partial e_i}{\partial y_i} \\ -k_{i-1}(e_{i-1} - s_{i-1}) \frac{\partial e_{i-1}}{\partial y_i} \\ -k_i(e_i - s_i) \frac{\partial e_i}{\partial z_i} \\ -k_{i-1}(e_{i-1} - s_{i-1}) \frac{\partial e_{i-1}}{\partial z_i} - m_i g. \end{cases} \quad (7)$$

In addition

$$\frac{\partial e_i}{\partial q_i} = -\frac{(q_{i+1} - q_i)}{e_i} \text{ and } \frac{\partial e_{i-1}}{\partial q_i} = \frac{(q_i - q_{i-1})}{e_{i-1}}$$

where again the q_i 's are x_i , y_i , or z_i .

The last step is to calculate the Q_i forces due to lift and drag on each cable segment. The wind velocity vector, \bar{V}_i is due to the cable motion and any prevailing wind and can be expressed as

$$\bar{V}_i = -\dot{x}_i \hat{i} - \dot{y}_i \hat{j} - \dot{z}_i \hat{k} + \bar{V}_{ip} \quad (8)$$

where \bar{V}_{ip} is due to a prevailing wind at the i th mass point. This could also be due to a nuclear blast. The vectors along the e_i segment can be expressed as

$$\bar{e}_i = (x_{i+1} - x_i) \hat{i} + (y_{i+1} - y_i) \hat{j} + (z_{i+1} - z_i) \hat{k} \quad (9)$$

and a similar expression for \bar{e}_{i-1} . From the dot product, the angles of attack, β_i and β_{i-1} can be found to be given by

$$\beta_i = \cos^{-1} \left[\frac{-\bar{V}_i \cdot \bar{e}_i}{|\bar{V}_i| |\bar{e}_i|} \right] \quad (10)$$

and

$$\beta_{i-1} = \cos^{-1} \left[\frac{-\bar{V}_i \cdot \bar{e}_{i-1}}{|\bar{V}_i| |\bar{e}_{i-1}|} \right] \quad (11)$$

From the cross-products, one can find the vectors in the direction of lift (i.e., perpendicular to \bar{V}_i and in the plane formed by \bar{V}_i and \bar{e}_i or \bar{e}_{i-1}). Letting \hat{n}_i and \hat{n}_{i-1} be unit vectors in the lift direction, we get

$$\hat{n}_i = \frac{(\bar{V}_i \times \bar{e}_i) \times \bar{V}_i}{|(\bar{V}_i \times \bar{e}_i) \times \bar{V}_i|} \quad (12)$$

and

$$\hat{n}_{i-1} = \frac{(\bar{V}_i \times \bar{e}_{i-1}) \times \bar{V}_i}{|(\bar{V}_i \times \bar{e}_{i-1}) \times \bar{V}_i|} \quad (13)$$

the unit vectors in the drag direction are simply given by

$$\hat{\xi}_i = \hat{\xi}_{i-1} = \frac{\bar{V}_i}{|\bar{V}_i|}$$

the magnitude of the lift at mass point i is given by

$$L_i = \frac{1}{2} \rho |\bar{V}_i|^2 C_{L_i}$$

and

$$L_{i-1} = \frac{1}{2} \rho |\bar{V}_i|^2 C_{L_{i-1}}$$

where C_{L_i} and $C_{L_{i-1}}$ are functions of β_i and β_{i-1} respectively. The drag forces are similar except they are functions of C_{D_i} and $C_{D_{i-1}}$. Everything needed to write the equations of motion is now known.

The equations of motion are as follows:

$$\begin{aligned} m_i \ddot{x}_i &= k_i(1 - s_i/e_i)(x_{i+1} - x_i) \\ &\quad - k_{i-1}(1 - s_{i-1}/e_{i-1})(x_i - x_{i-1}) \\ &\quad + L_i \eta_{x_i} + L_{i-1} \eta_{x_{i-1}} + (D_i + D_{i-1}) \xi_{x_i} \end{aligned} \quad (14)$$

$$\begin{aligned} m_i \ddot{y}_i &= k_i(1 - s_i/e_i)(y_{i+1} - y_i) \\ &\quad - k_{i-1}(1 - s_{i-1}/e_{i-1})(y_i - y_{i-1}) \\ &\quad + L_i \eta_{y_i} + L_{i-1} \eta_{y_{i-1}} + (D_i + D_{i-1}) \xi_{y_i} \end{aligned} \quad (15)$$

$$\begin{aligned} m_i \ddot{z}_i &= k_i(1 - s_i/e_i)(z_{i+1} - z_i) \\ &\quad - k_{i-1}(1 - s_{i-1}/e_{i-1})(z_i - z_{i-1}) \\ &\quad - m_i g + L_i \eta_{z_i} + L_{i-1} \eta_{z_{i-1}} \\ &\quad + (D_i + D_{i-1}) \xi_{z_i} \end{aligned} \quad (16)$$

$$i = 1, 2, \dots, n.$$

In the above equations, $\eta_{x,y,z}$ and $\xi_{x,y,z}$ are the direction cosines of the vectors \hat{n} and $\hat{\xi}$

respectively.

STEADY STATE SHAPE ANALYSIS

The initial conditions for equations (14), (15) and (16) are the coordinates for the steady state shape corresponding to the nominal flight path being studied. One way to calculate these coordinates is to solve equations (14) - (16) with all acceleration terms zero and appropriate velocity terms. However, this is not practical and an easier method exists.

If one assumes that the angular rate of the orbit is known and that the radius and altitude for the drogue are also known, then the forces acting on the drogue can be calculated. For example; if a sphere is assumed (for simplicity) the lift is zero and the drag may be calculated using a standard drag coefficient for the size sphere equivalent to the actual drogue. Since it must be in static equilibrium, the force in the attached cable segment and its direction can easily be calculated. The force determines the amount of stretching for the first segment of cable which in turn allows the x , y , z coordinates of the next mass point to be calculated. If one then imposes static equilibrium on that mass point, the three components of force are determined for the next cable segment which in turn defines the next mass point's location. Calculations then continue on to the aircraft. In other words, one assumes the location of the drogue and calculates where the aircraft is. In most practical cases, the location of the aircraft is known and the drogue location is unknown. Hence, it is necessary to iterate until the desired aircraft position is obtained.

COMPUTER CONSIDERATIONS

The equations derived above can be numerically integrated for specific initial conditions. In the present study, the equations were integrated using a fourth order Runge-Kutta technique on a CDC 6400 computer. The x_i , y_i and z_i 's are placed in a single subscripted array with x_i , y_i and z_i being the aircraft location at any instant in time. These variables are calculated by a subroutine which defines the aircraft flight path as a function of time. This allows one to "fly" the airplane around as desired.

The subscripted coordinate array and the corresponding velocity array (i.e., \dot{x}_i 's, \dot{y}_i 's and \dot{z}_i 's) are then operated on by the Runge-Kutta subroutine. The subroutine must be modified to skip over the x_i , y_i , z_i entries in the subscripted arrays since they are not governed by equations of motion.

The computer program requires about 0.15 sec/step for 15 mass points or about .01 sec/step/mass point. For example, the plots shown

in this report used 270 sec. of central processor time for 64 sec. of aircraft "flight" time yielding a 4.2:1 ratio. Because of the computer time involved, it is advantageous to write the input data, instantaneous time, positions and velocity on magnetic tape for later processing. This allows various aspects of each "flight" to be examined as desired at a future date. By storing basic data on magnetic tape, one is not required to foresee all possible quantities of interest such as shape, tension, frequencies, verticality, etc., at run time.

RESULT OF AIRCRAFT OSCILLATIONS

The results that follow pertain to a system like TACAMO. The drogue in the present study has been assumed to be a mass point weighing 100 lb., having zero lift and a drag coefficient of 0.6. The drag term is given by

$$D_{\text{CONE}} = \frac{1}{2} \rho V^2 (0.6)S$$

where $S = \pi R_{\text{base}}^2 = 3.6 \text{ ft}^2$. The density for all calculations was that for a standard atmosphere at altitude.

For the cable, a length of 24,600 ft., a Young's Modulus of 10.2×10^6 psi based on overall diameter, a diameter of 0.21 in., and a density based on overall diameter of 455.5 lb/ft³ was assumed. The aerodynamic coefficients were assumed to be

$$C_L = 0.4 \sin^2 (2.08)$$

and

$$C_D = 0.01 + 1.2 \sin^2 (3)$$

These coefficients were obtained experimentally and have later shown to be inferior to the cross-flow model presented later. However, the types of results obtained are valid for a long wire system.

In the present study the aircraft was allowed to fly in the same orbit which was used for the equilibrium cable shape calculations but its altitude was varied sinusoidally. The different cases presented show the effects of amplitude, frequency and airspeed on the cable tension at the aircraft and the drogue.

Case I

For this case, 15 mass points were used (this number gave 10% difference between the static results in [2] and the present results). The aircraft was oscillating vertically ± 4 ft (1H) at 0.5 cy/sec. The equilibrium tension was 2,974 lb. at the aircraft. The aircraft was flying a 2,920 ft. radius orbit at 106 KTAS. As seen in Figure 2, the maximum tension at the aircraft is about 4,140 lb. This is below the 4,840 lb. ultimate strength of the TACAMO cable.

Note that there is almost 2700 lb. variation in tension at the maximums.

It is interesting to note the buildup in tension over the first nine cycles. The initial three are essentially constant and then an increase occurs. The time associated with these "flat" spots corresponds to the time required for a stress wave to proceed down to the drogue and return. The longitudinal wave speed in a solid is given by

$$V_S = \frac{E}{\rho} = 10,220 \text{ ft/sec}$$

where ρ = mass/unit length and E = Young's Modulus. A stress wave initiated at the aircraft should take 2.4 sec to propagate down to the drogue. However, the stress wave appears to have returned after about 4 sec which indicated a wave speed of 12,300 ft/sec. This difference is caused by lumped mass approximation and relatively few number of mass points taken and may also be affected in a minor way by the aerodynamic resistance along the cable.

Case II

In Case I, no provision was made for the possibility of the cable going slack. If it were to attempt to go slack, the analysis presented in Section 1.2 would compute a compressive force in the cable segment; this is, of course, impossible since everyone knows "you can't push on a rope". To allow for this condition, the computer program was modified to let the force in any given segment equal zero if it tried to undergo compression. Figure 3 shows a plot of the tension at the drogue with the modification included. Note that the drogue is undisturbed for approximately 2.1 sec which is close to that predicted above. Note also that after the first impulse of about 200 lb., the cable force at the drogue attempts to go compressive. This indicates that the results plotted in Figure 2 were not valid and the allowance for slack cable must be made.

In Figure 4, the tension at the aircraft is plotted again allowing for slack cable. A comparison of Figures 2 and 4 reveals that the tension is unchanged for the first few seconds until the effect of the slack cable at the drogue has propagated back up to the aircraft. One can also see that the peak tension at the aircraft is approximately 350 lb. less when slack cable is allowed and the peak to peak values are also less. The periodicity observed in Figure 2 is destroyed by the discontinuous load-deflection relation for Figure 4 and the remainder of the analysis.

Figure 5 shows the drogue altitude as a function of time. It is interesting to note that the drogue starts at 100 ft. equilibrium altitude but as it oscillates it "pumps" itself up to an average altitude of about 115 ft. The peaks in Figure 5 fall between the spikes in Figure 3 as would be expected. The ratio

of the first tension pulse at the aircraft and that at the drogue is 300:188 or the wave dies out as it propagates.

Case III

In Figure 6, the aircraft is still in a 2,920 ft. radius orbit at 106 KTAS but the aircraft is now oscillating at 1.0 cps. The peak tension in this case is 4750 lb. which is very near the 4,840 lb. ultimate strength of the cable. At approximately 24 sec., a very strong wave arrives at the aircraft and the tension almost goes to zero.

Figure 7 shows the corresponding tension at the drogue. The tensions are quite severe, reaching levels of several thousand pounds at several instances. These are an order of magnitude higher than the steady state values. The ratio of the initial tension pulse at the aircraft to that at the drogue is 526:185 or the initial pulse the drogue feels is about the same as for Case II but the aircraft pulse is 2/3 higher.

Figure 8 shows the drogue altitude as a function of time. The drogue reaches an average altitude of about 155 ft. This is 40 ft higher than for Case II at 0.5 cps.

Case IV

In this case, the aircraft is in a 4,367 ft. radius orbit at 155 KTAS. The tensions shown in Figure 9 are generally not any higher at the aircraft, however, there is a single spike at about 62 sec. which exceeds the ultimate strength of the cable. In Figure 10, one can see that the tensions at the drogue are not significantly different from those in Case III.

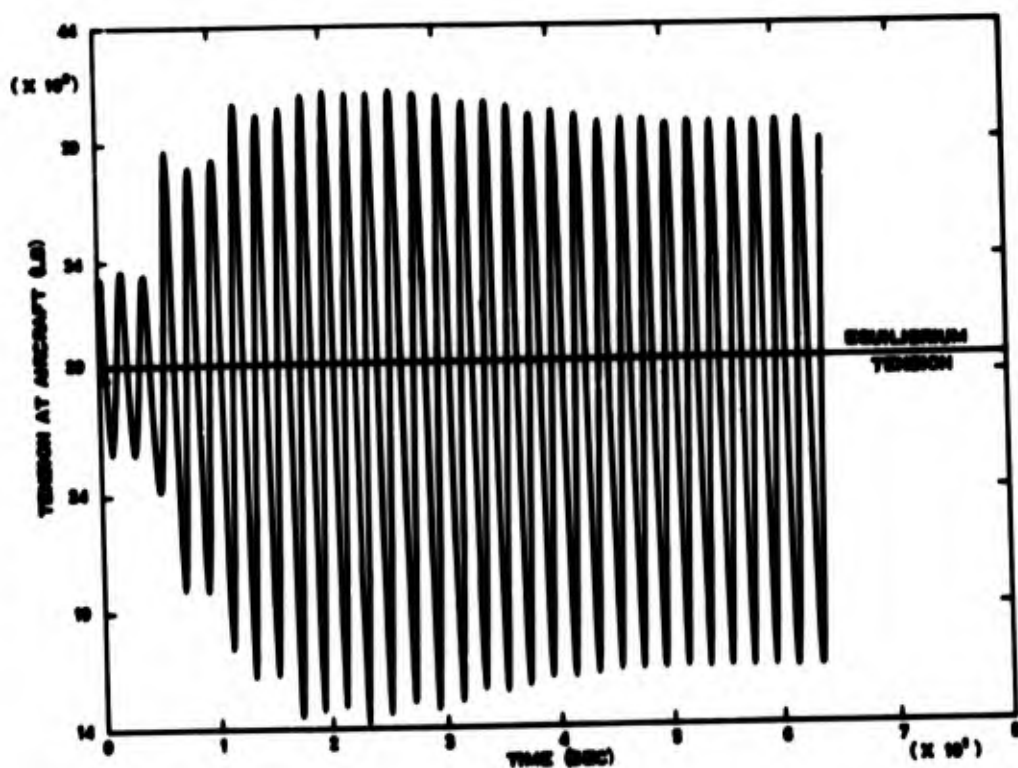
Case V

In this case, also, the aircraft is in a 4,367 ft. radius orbit at 155 KTAS. With the reduced amplitude of aircraft oscillations and slower frequency, the tension changes in Figure 11 are not significant. Note also that the tension at the drogue in Figure 12 never reaches zero and the tensions in the cable reach a steady state value after about 35 sec of disturbance. There is no mechanical damping in the system but adequate damping exists from aerodynamic effects to cause transient motions to die out.

RESULTS OF AIRCRAFT TRANSITION FROM ORBIT

For the following calculations, the cable was 29,000 ft and cross-flow aerodynamic coefficients for the cable were used (see Reference [2]) with

$$C_L = 1.03 \sin^2 \alpha \cos \beta \quad C_D = .022 + 1.03 \sin^2 \alpha$$



(U) Figure 2

TENSION AT AIRCRAFT (DELH = 4 ft., OMEGA = .5 Cy/Sec)(U)

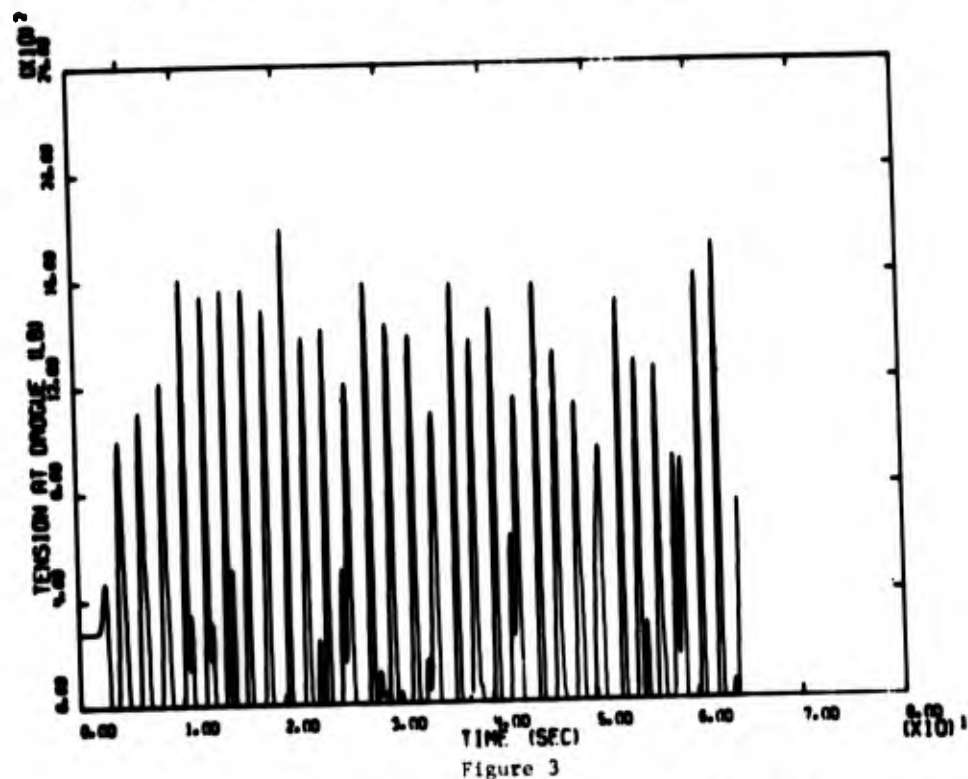


Figure 3

TENSION AT DROGUE (DELH = 4 ft., OMEGA = .5 Cy/Sec)

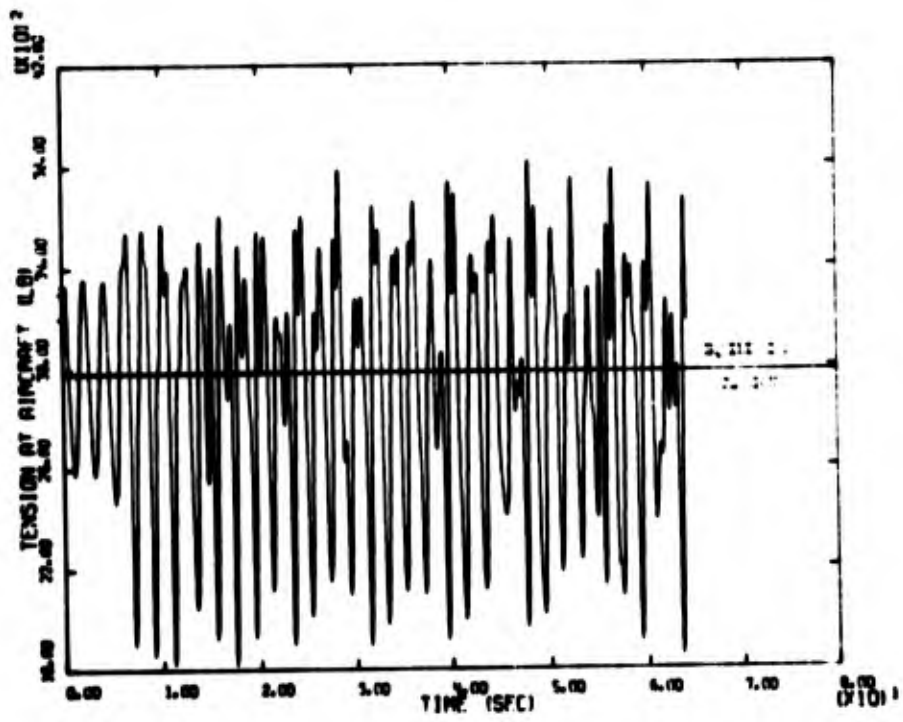


Figure 4

TENSION AT AIRCRAFT (DELH = 4 ft., OMEGA = .5 Cy/Sec)

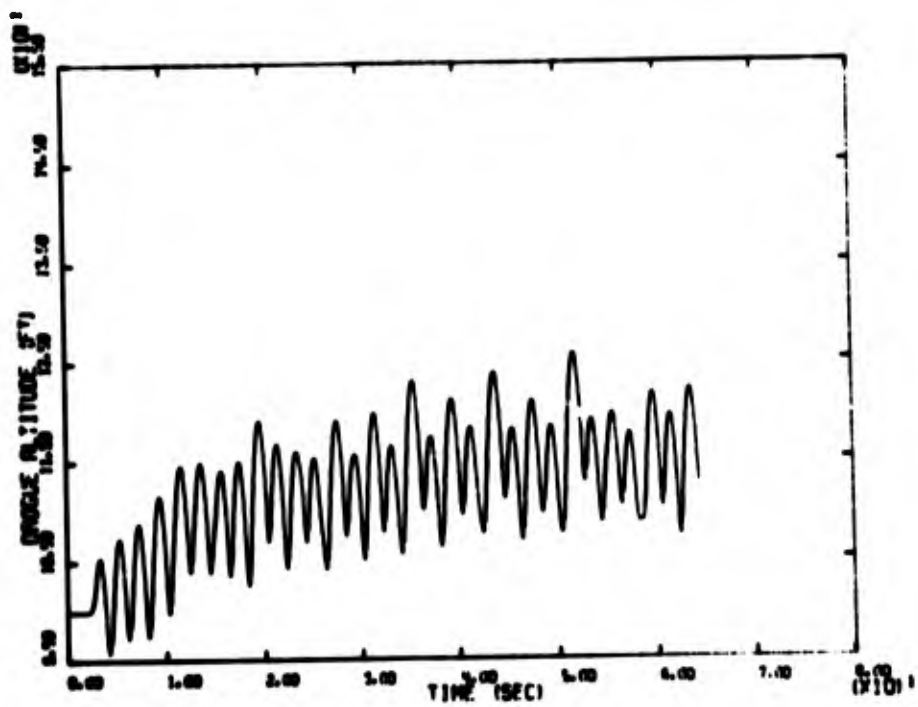


Figure 5

DROGUE ALTITUDE (DELH = 4 ft., OMEGA = .5 Cy/Sec)

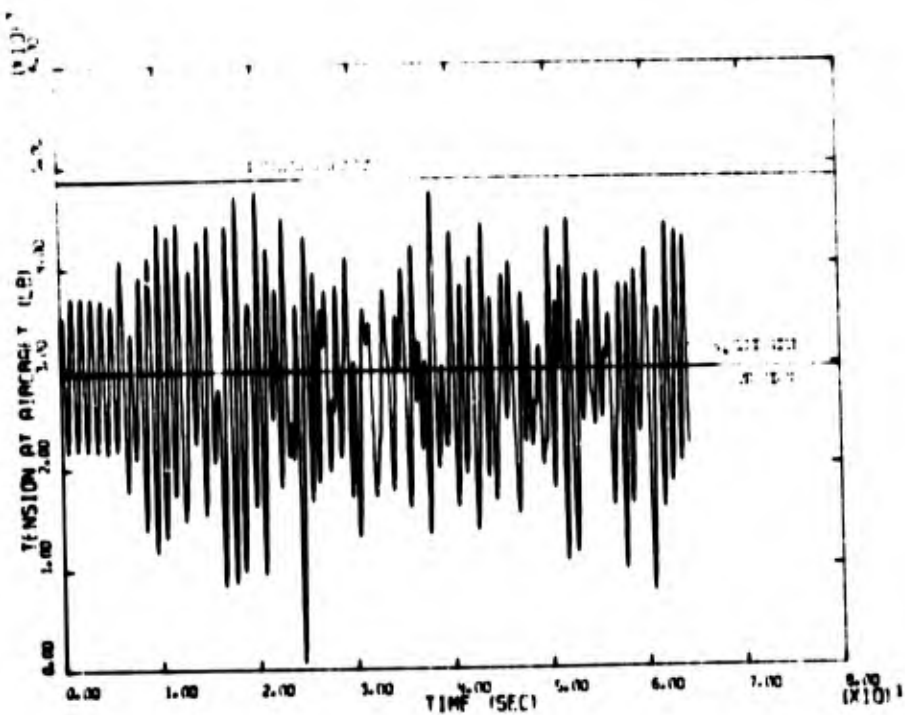


Figure 6

TENSION AT AIRCRAFT (DELH = 4 ft., OMEGA = 1.0 Cy/Sec)

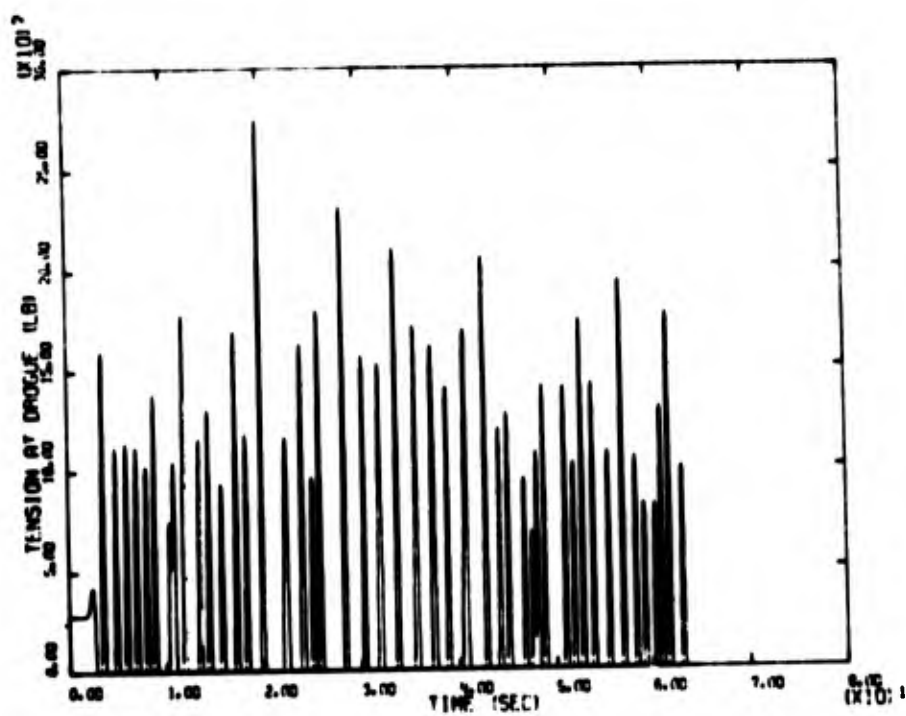


Figure 7

TENSION AT DROGUE (DELH = 4 ft., OMEGA = 1.0 Cy/Sec)

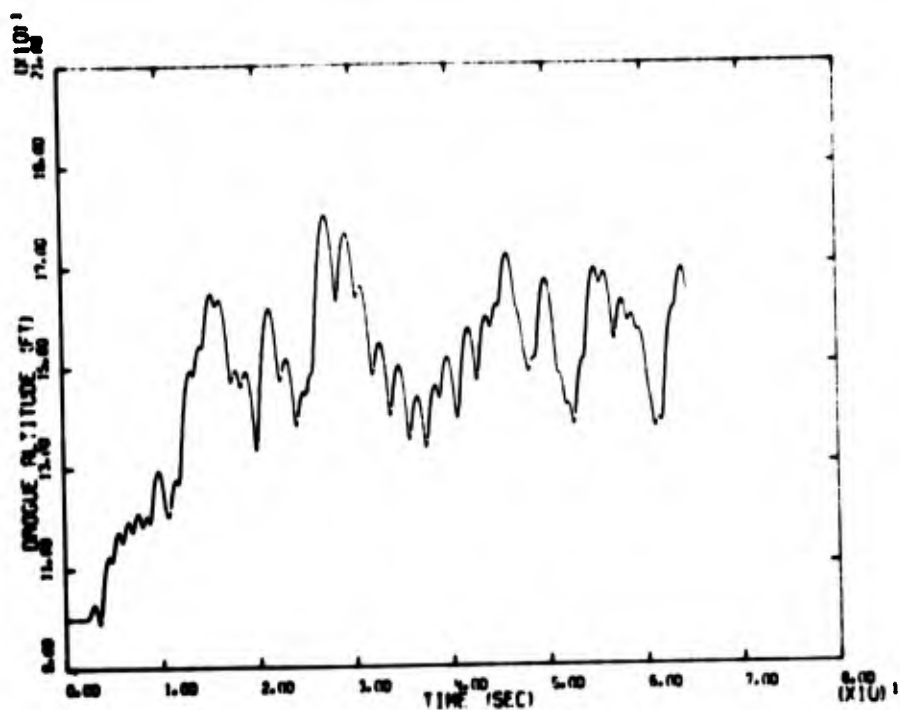


Figure 8

DROGUE ALTITUDE (DELH = 4 ft., OMEGA = 1.0 Cy/Sec)

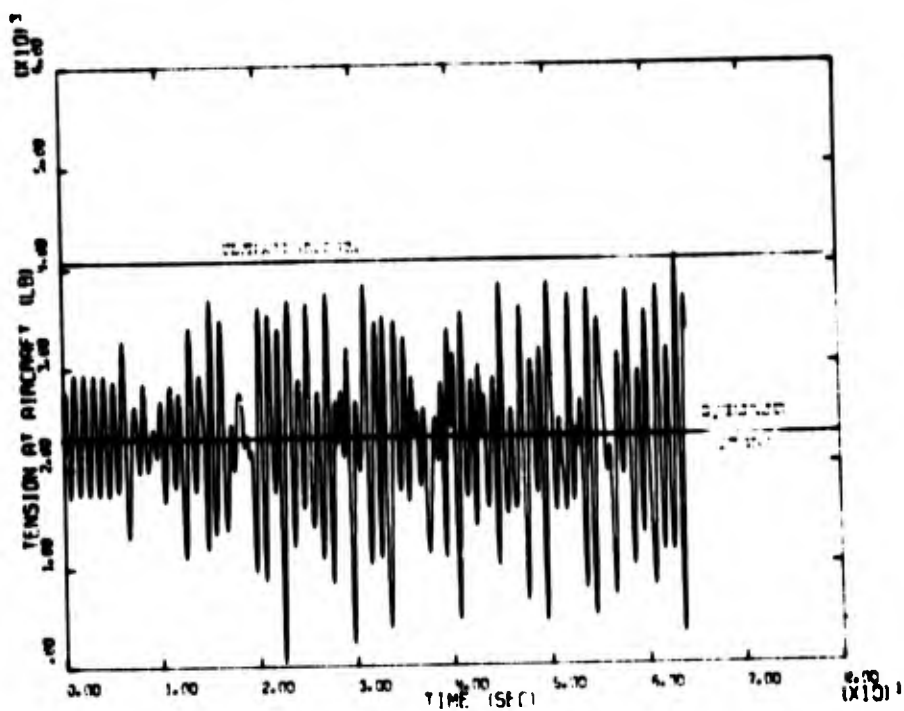


Figure 9

TENSION AT AIRCRAFT (DELH = 4 ft., OMEGA = 1.0 Cy/Sec)

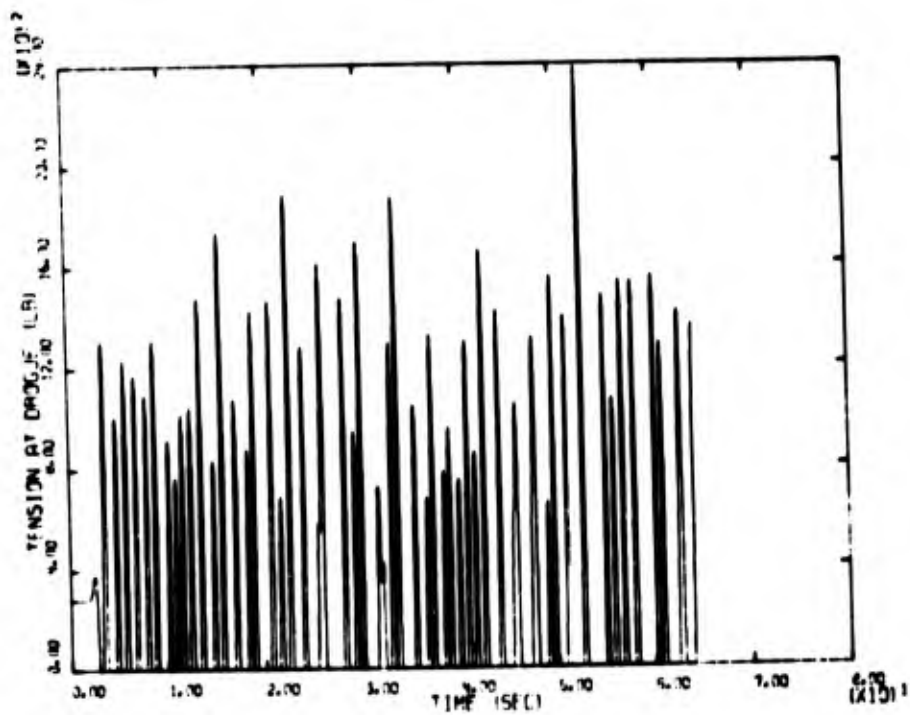


Figure 10

TENSION AT DROGUE (DELH = 4 ft., OMEGA = 1.0 Cy/Sec)

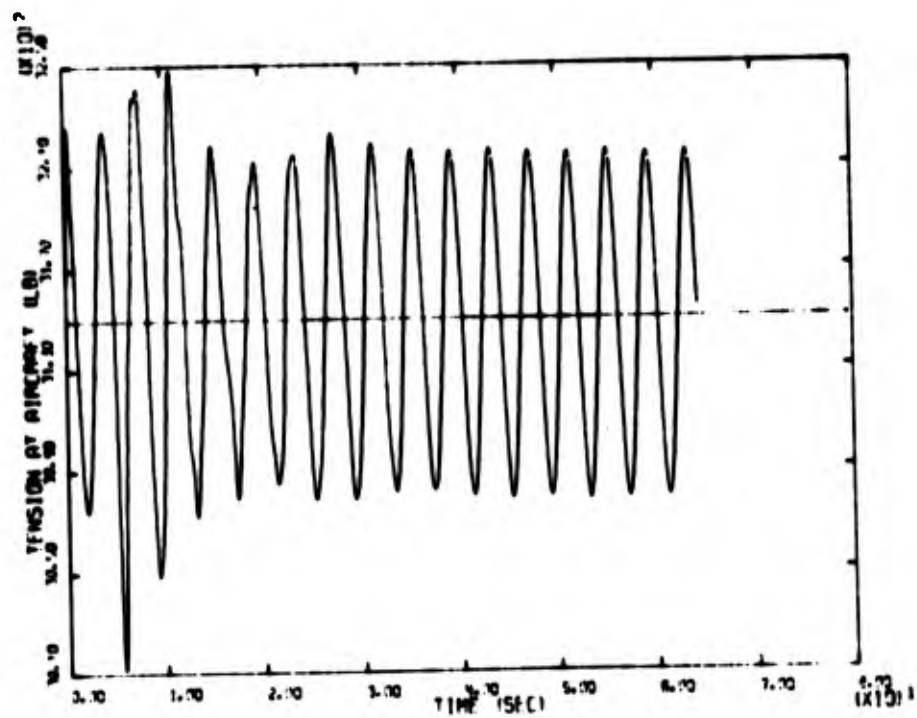


Figure 11

TENSION AT AIRCRAFT (DELH = 2 ft., OMEGA = .25 Cy/Sec)

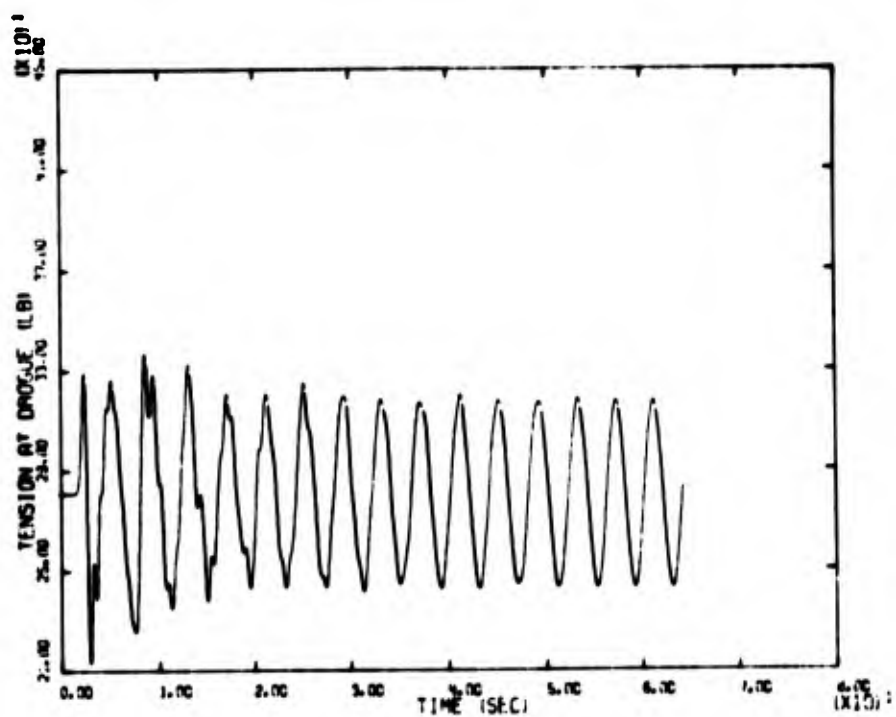


Figure 12
TENSION AT DROGUE (DELH = 2 ft., OMEGA = .25 Cy/Sec)

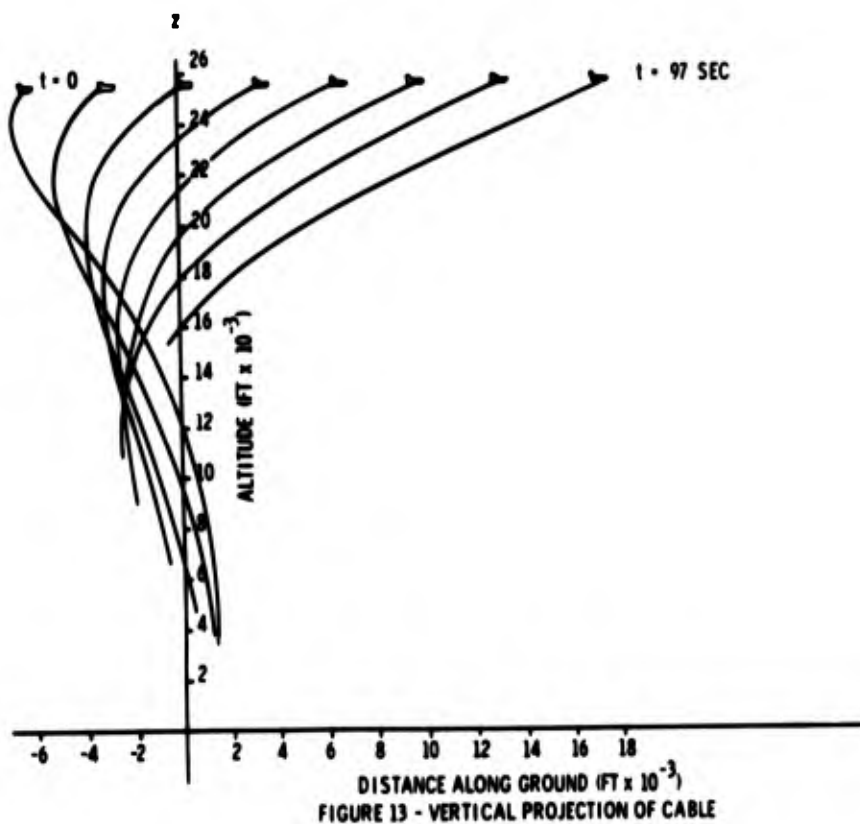


FIGURE 13 - VERTICAL PROJECTION OF CABLE

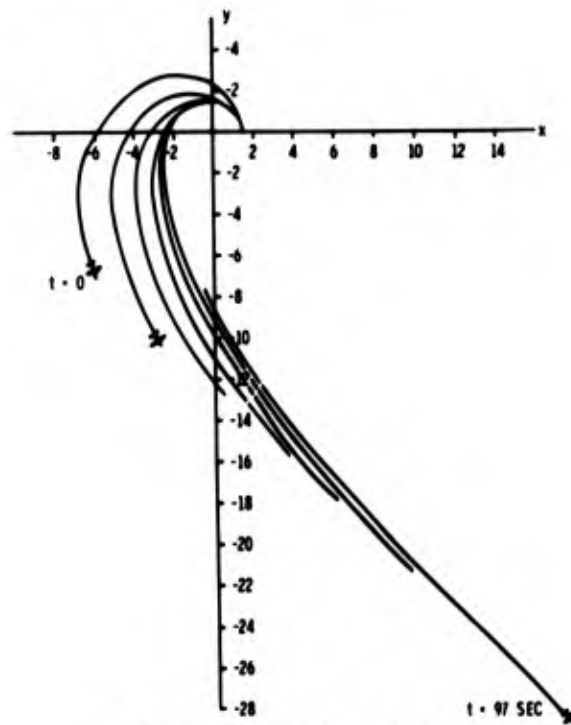


FIGURE 14 - GROUND PROJECTION OF CABLE

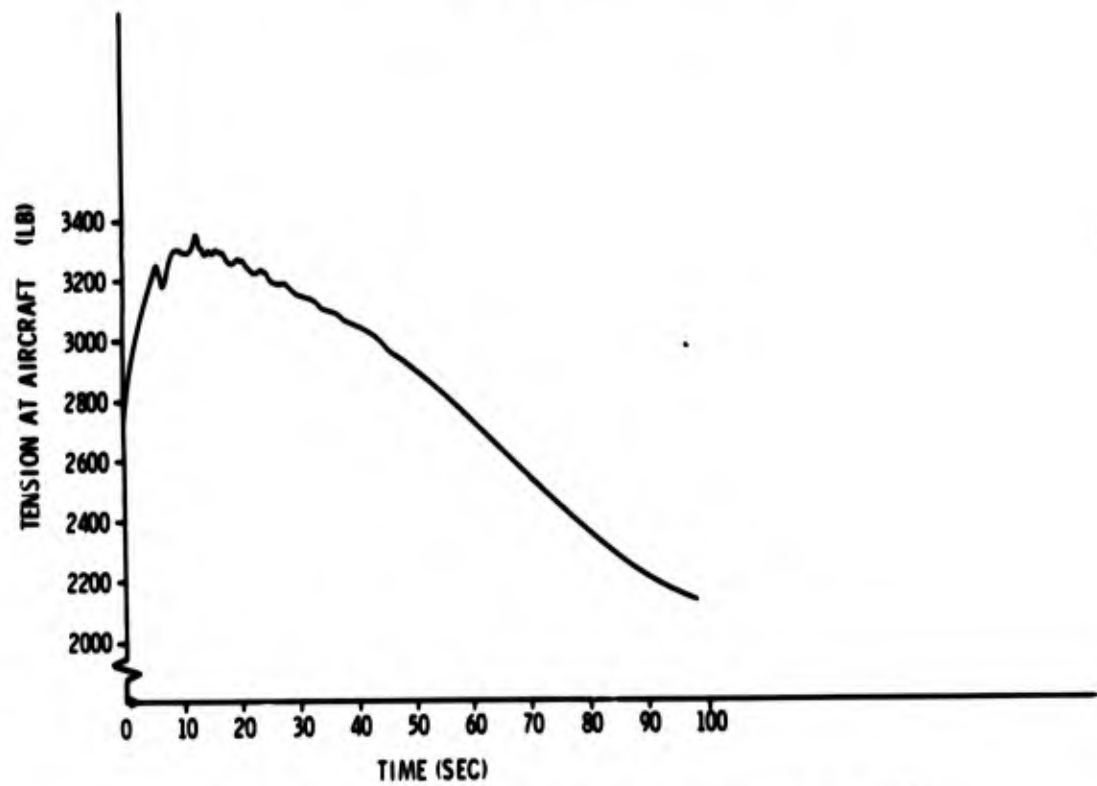


FIGURE 15- TENSION AT AIRCRAFT FOR TRANSITION FROM ORBIT

The aircraft at $t = 0$ was flying in a constant radius of altitude orbit. At $t = 0$ the aircraft begins a straight and level flight path which is tangent to its original orbit. Figure 13 shows a vertical projection of the cable for several instances of time as the aircraft flies straight and level from orbit. At $t = 0$, the cable is shown in a steady state configuration. Figure 14 shows a horizontal or ground projection of the cable for several instances of time from $t = 0$ to $t = 97$ sec. These two figures show how the cable progresses from its orbiting configuration to a straight and level trailing position. Figure 15 shows the tension at the aircraft. It begins at 2660 lbs and increases during transition to approximately 3350 lb. Aerodynamic damping eventually damps out the transient disturbances and drops toward its straight and level value which is less than the orbital value of tension.

CONCLUSIONS

- (1) The analysis has been developed which allows one to calculate the motion of a cable towed behind an orbiting aircraft which is following any prescribed flight path.
- (2) Fifteen (15) mass points may be successfully used to study a system such as TACAMO.

- (3) The effects of slack cable must be included in most analysis.
- (4) The tension at the drogue can be considerably higher than the equilibrium tension when the aircraft oscillates vertically.
- (5) Tension in the cable during transition from orbit can be considerable, even for a smooth transition from orbit.

REFERENCES

1. James Kline, "Final Report of Concepts For Airborne and Tethered VLF Antenna-Supporting Aerial Vehicles," (U), CM-2520-B-2, Jan. 1968, Cornell Aeronautical Laboratory, Inc., Buffalo, N.Y.
2. "Mathematical Model For Long Cable Towed By Orbiting Aircraft," Final Report, Air Task A05-533-438/2021/15080000, Report No. NADC-AM-6849, 12 June 1969, U. S. Naval Air Development Center, Johnsville, Warminster, Penna.
3. S.A. Crist, "Motion and Stability Of A Spinning Cable Connected System in Orbit," The University of Michigan Radio Astronomy Observatory, Report 67-7, Sponsored by National Aeronautics and Space Administration Grant NGR-23-005-131, June 1967.

BLANK PAGE

A POSTSHOT STUDY OF THE DYNAMIC RESPONSE
OF THE LASL MOBILE TOWER DURING THE PLIERS EVENT*

R. E. Bachman, E. F. Smith
Holmes & Narver, Inc.
Las Vegas, Nevada

and

R. P. Kennedy
Holmes & Narver, Inc.
Los Angeles, California

The LASL Mobile Tower, an eight-story steel space truss structure with a combined dead load of approximately 495 kips, was positioned at surface zero during the Pliers underground nuclear event. Accelerometers measured a vertical ground shock exceeding 4 g's and subsequent tower responses exceeding 10 g's. Measured relative displacements at points on the tower were compared with those computed analytically using the measured ground shock as the input motion. The non-linear effect of tower jumping was included in the analysis. Comparisons indicated that the time history response of tower structures could be accurately predicted provided the input motion time history can be reliably predetermined. The data reduction and dynamic analysis performed by Holmes & Narver, Inc. are described.

INTRODUCTION

In conducting certain underground experiments with nuclear devices, it is necessary to "view" the initial radioactive particles produced by the event without leakage of significant doses of radiation into the atmosphere. One method of achieving this goal is with a line-of-sight (LOS) pipe which extends vertically from the buried device to the ground's surface (surface zero). The LOS pipe contains various mechanical closure devices which permit only the initial particle stream to reach the surface.

For most vertical LOS pipe events, a multi-story tower is positioned at surface zero to support experiment packages, instruments, and equipment during the event. As the prime architect-engineer contractor at the Atomic Energy Commission's (AEC) Nevada Test Site (NTS), Holmes & Narver, Inc. (H&N) is responsible for the design and field inspection of all major structures constructed at the NTS, including these towers. In Yucca Flat, where a majority of the events of this type are conducted, a large subsidence crater will normally form at surface zero within 60 minutes after detonation. Therefore, key experiment packages which need to be recovered intact are usually placed on sleds and winched clear of the anticipated cratering area, starting approximately

one minute after the detonation. The tower and remaining experiment packages have in the past been considered expendable.

Los Alamos Scientific Laboratory (LASL) conducted the Pliers underground nuclear event in Yucca Flat on August 27, 1969. A vertical LOS pipe extended from the device to surface zero. A diagnostic tower (LASL Mobile Tower) was positioned at surface zero during the event. The nuclear device was detonated at a depth of burial of 754 feet, and it had a yield of less than 20 kilotons. An interpretation of the boring logs and core samples taken in the vicinity of surface zero indicated that the site geology is comprised of alluvium to a depth 1,900 feet; tuff from 1,900 feet to 3,500 feet; and paleozoic rock at depths greater than 3,500 feet.

A GENERAL DESCRIPTION OF THE TOWER

The LASL Mobile Tower was originally designed as an expendable facility but was modified prior to the Pliers event to be recovered intact in a manner similar to the recovery of key experiment packages in previous events. The modified design made maximum use of materials and structural sections from the original design and, therefore, some elements were knowingly over-sized for anticipated loads.

* Some of the material in this paper originally appeared in Reference 1.

A pre-shot photograph of the tower is presented in Figure 1.

The tower is basically a single-panel, eight-story, bolted-steel space truss structure, 105-feet tall. The upper 75 feet of the tower consists of interchangeable modules, each 25 feet in height. The tower is enclosed by plywood sheeting with outside stairs leading to each working platform. A conceptual view of the tower is shown in Figure 2 and an elevation view of the tower, with approximate locations and weights of the experiment packages, is shown in Figure 3. The tower height is intersected at 12.5-foot intervals by working platforms. The nominal plan dimensions of each platform are 20 feet by 20 feet. Each platform is composed of 1/4-inch thick steel plate decking and has a center opening of 6 feet by 6 feet. The decking is supported by a grid of steel structural shapes. Typical platform framing is presented in Figure 5.

The experiment packages were quite heavy (see Figure 3); all weighed in excess of 40 kips. In general, the packages were positioned at the center opening. The total dead load weight of the tower, including all equipment and experiment packages, was estimated to be 495 kips.

Based on experience from previous events conducted in Yucca Flat, a subsidence crater approximately 350 feet in diameter was expected to form at surface zero within 60 minutes after detonation. Therefore, a recovery system (Figure 2) was designed by LASL to enable the tower to be moved laterally a distance of 400 feet. Mobility of the tower was achieved primarily by placing it on two large girders that rest on four bogies (crane wheel assemblies). These bogies, in turn, rested on two pair of rails that led from surface zero to a recovery pad 400 feet to the northwest. Four truss outriggers extended from the lower part of the tower to provide additional lateral stability during the movement of the tower, if required. At surface zero, the rails were embedded in a 32-foot square by 4-foot thick reinforced concrete emplacement pad. The upper end of the emplacement hole casing was embedded in the center of the concrete pad. The casing extended downward to the point of detonation and thus the pad received input motion from both the free surface and the casing.

Based on experience from previous tests, the tower was expected to experience a severe vertical ground shock accompanied by some lateral motion. A time-dependent pre-shot analysis performed using the in-house computer program IDYNE (Reference 2), and utilizing ground motion data from a similar event, indicated the tower would "jump." Therefore, tie bars were designed to limit vertical jumping and thereby help prevent derailment of the bogie wheels. The tie bars were secured at the outside corners of the pad with explosive

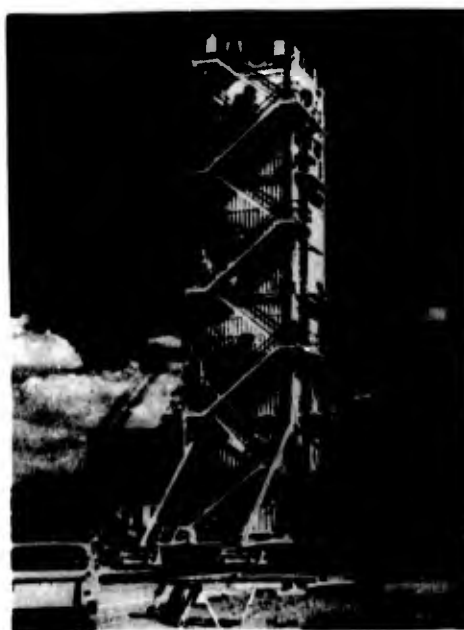


Fig. 1 - Preshot view of LASL Mobile Tower positioned at surface zero

pins and were attached to the tower columns near the second floor level. (The explosive pins were triggered just after detonation to uncouple the tower from the pad.) The bogie wheels were double-flanged such that the tower would have to experience a vertical separation of approximately 3/4-inch from the pad before it could derail laterally.

The tower remained vertically coupled to the emplacement pad at all times during the ground shock. During the compression mode of the tower response, coupling was directly through the bogies into the tower columns. During the tension mode (jumping) of response, coupling was through the tie bars into the columns.

After the device was detonated, the key experiment packages were retrieved on sleds starting approximately one minute after detonation. Sleds were still used to recover the key experiment packages since the recovery system and overall design concept had not proven too successful in prior events. Recovery of the tower was accomplished by winching it to the recovery pad (400 feet from surface zero) beginning about three minutes after detonation. The entire winching operation was completed successfully approximately five minutes after detonation. The subsidence crater formed 20 minutes after detonation.

A time-sequence of aerial photographs were taken of the tower during and immediately following detonation. These are presented in Figures 6 through 12.

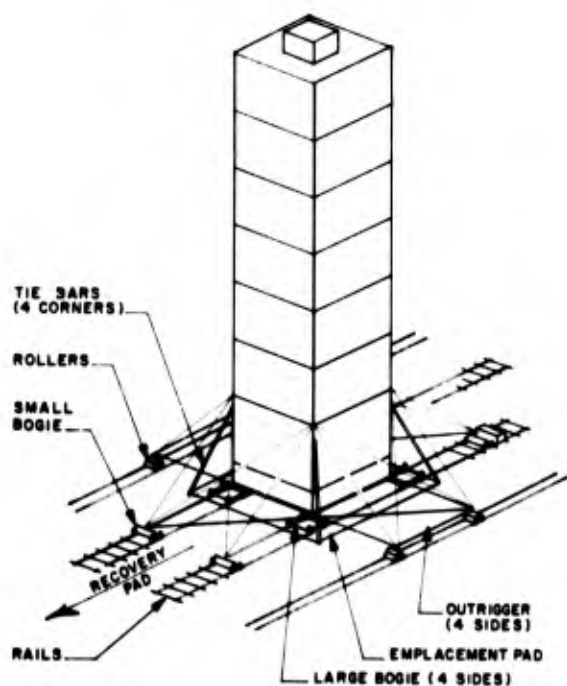


FIGURE 2
CONCEPTUAL VIEW OF LASL MOBILE TOWER
JUST PRIOR TO DETONATION

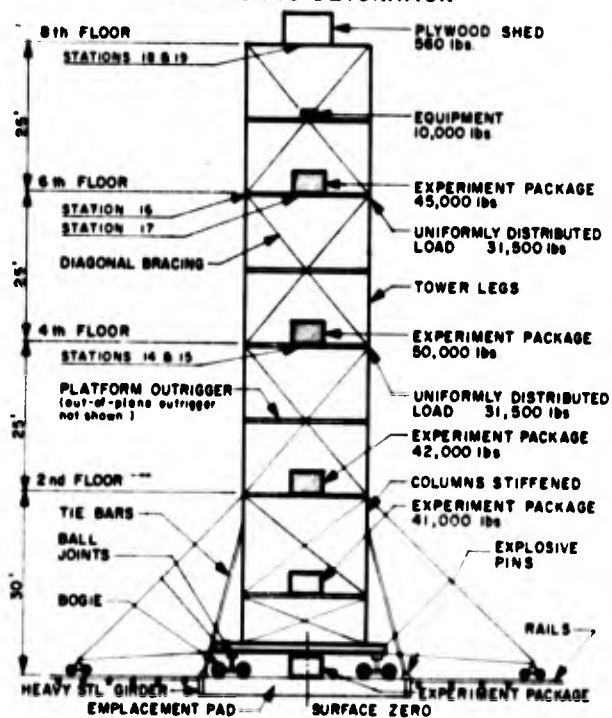


FIGURE 3
ELEVATION OF LASL MOBILE TOWER AT SURFACE ZERO

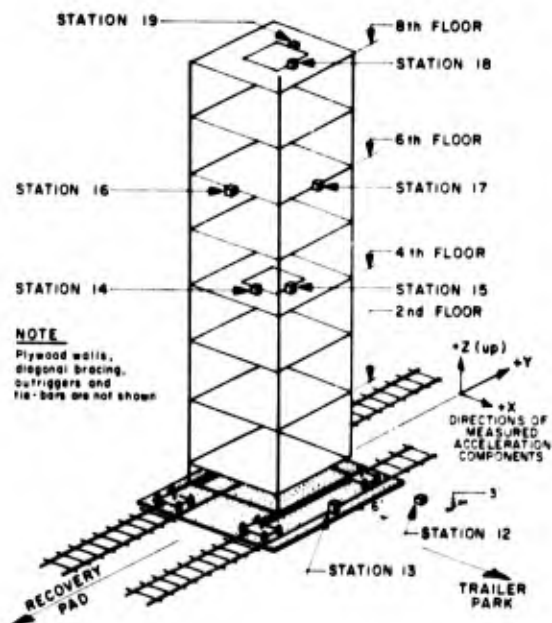


FIGURE 4
LOCATIONS OF ACCELEROMETER STATIONS
ON LASL MOBILE TOWER

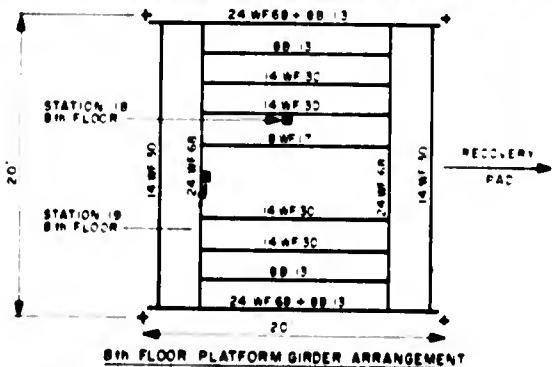
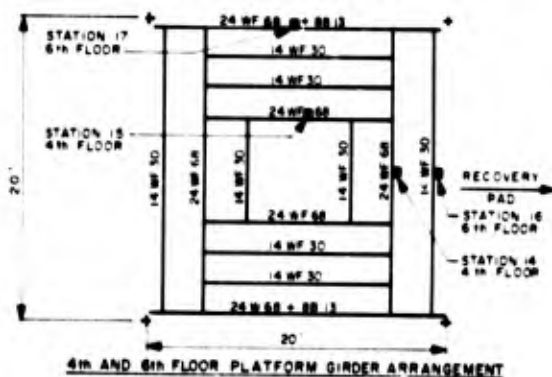


FIGURE 5 PLATFORM GIRDER SYSTEMS



Fig. 6 - LASL Mobile Tower approximately
2 minutes after detonation

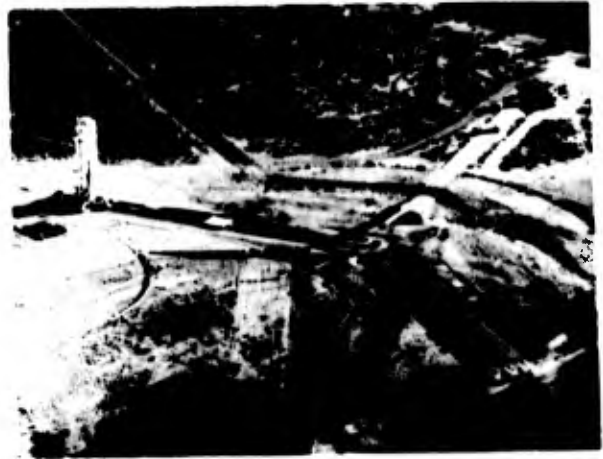


Fig. 9 - LASL Mobile Tower approximately
5 minutes after detonation



Fig. 7 - LASL Mobile Tower approximately
3 minutes after detonation



Fig. 10 - LASL Mobile Tower approximately
20 minutes after detonation



Fig. 8 - LASL Mobile Tower approximately
4 minutes after detonation



Fig. 11 - LASL Mobile Tower approximately
21 minutes after detonation



Fig. 12 - LASL Mobile Tower approximately 25 minutes after detonation

STRONG MOTION MEASUREMENTS

As a piggy-back experiment to the Pliers event, strong motion accelerometers were placed on or near the tower at eight points (stations) by LASL to measure ground motions at surface zero and the dynamic response of the tower to the expected ground shock. The locations and orientations of the accelerometer stations are shown in Figure 4. Each accelerometer measured the three orthogonal components of acceleration (two horizontal and one vertical); thus, 24 acceleration component-time histories were obtained. The acceleration-time histories were digitized at an interval of 0.000256 seconds by EG&G, Inc., Albuquerque, New Mexico. The records were not calibrated during digitization. Therefore, it was necessary for H&N to apply small base line corrections to all of the acceleration time histories.

The horizontal coupling between the tower and the emplacement pad was weak and very complex. Consequently, consideration of the horizontal mode of response was not included in the computations. This omission did not appear to adversely affect the analytical results.

The measured vertical ground motions and tower acceleration-time histories were processed and plotted by using computer program SPECANAL (Reference 3). An examination of preliminary plots of the acceleration-time records revealed that the ground at surface zero remained undisturbed until approximately

.15 sec and after detonation. It was determined that the peak tower acceleration occurred during the period of free fall between the initial and second closure pulses. It was noted that within 100 ft of the tower base, the acceleration was 100 ft/sec². Therefore, for purposes of efficiency, only .75 second of each acceleration-time history was plotted. Also were the on each plot corresponding to .15 sec and .75 sec after detonation.

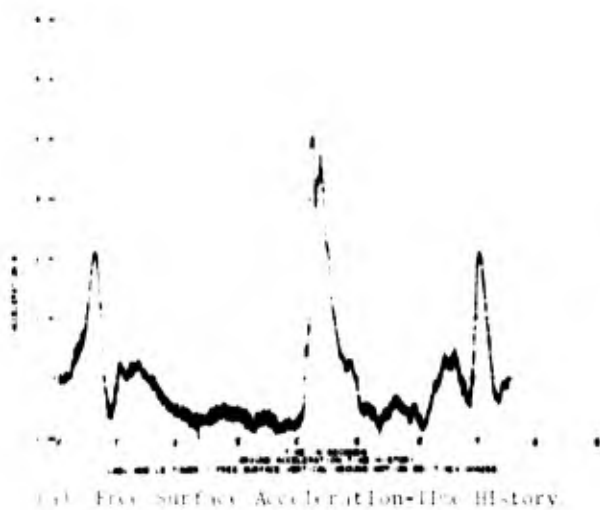
MEASURED GROUND MOTION

Accelerometers were stationed to record both the free surface (Station 12) and the emplacement pad (Station 13) ground motions. Plots of the measured vertical acceleration-time histories at Stations 12 and 13 are presented in Figures 13a and 14a, respectively. Each acceleration record was integrated and doubly integrated to obtain the velocity and displacement time histories. Plots of these time histories are presented as Figures 13b and 13c and 14b and 14c.

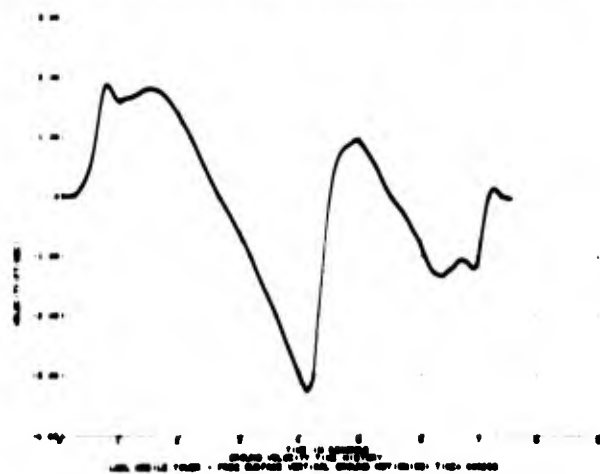
The free-surface ground motion characteristics (Figure 13) are essentially the same as those reported for many previous events (Reference 4). The initial positive acceleration pulse (2.1 g's) represents the initial compressive shock wave. This shock wave imparted a peak upward velocity of 1.9 feet per second to the ground surface. During this initial upward movement, spall separations opened in the rock between the point of detonation and the ground surface. The initial pulse was followed by a period of constant negative acceleration corresponding to a period of free fall. During this period, the positive ground displacement peaked at 3.5 inches. Upon closure of the uppermost significant spall separation, a spall closure compressive wave was transmitted to the surface. This resulted in a second positive acceleration pulse (4.1 g's) which was followed by a second period of free fall and second closure pulse together with minor oscillatory motion. The negative ground velocity peaked at -3.2 feet/second just prior to the arrival of the primary closure pulse.

The pad acceleration time history is quite different in appearance from the free surface time history in that a high frequency oscillation dominates the entire record. This oscillation is attributed primarily to ringing of the embedded casing although reflections of shock waves off the pad may also be present.

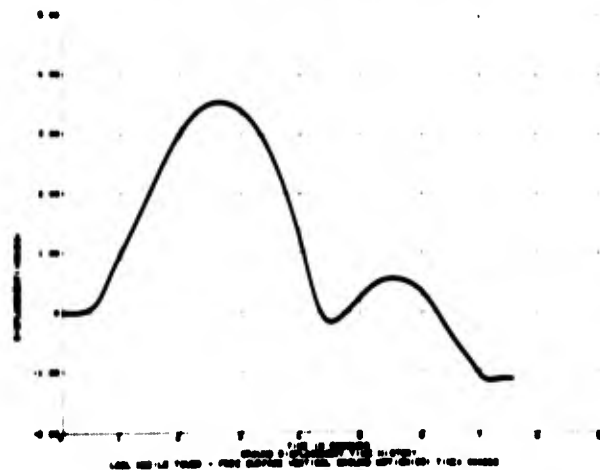
In general, the magnitudes of the velocity and displacement-time histories obtained by integrating the pad acceleration records are approximately equal to those obtained from the free surface records. This would indicate that although the pad acceleration has been disguised by the casing ringing, the amount of



(a) Free Surface Acceleration-Time History

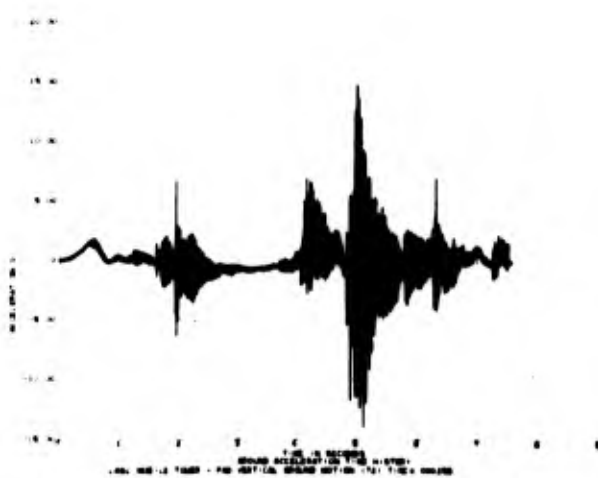


(b) Free Surface Velocity-Time History
(Obtained from Acceleration Record)

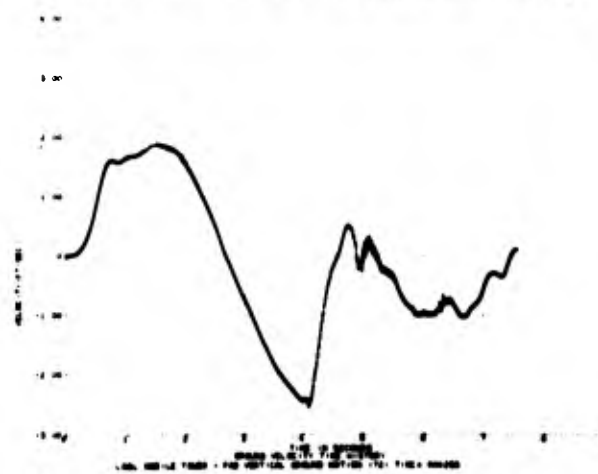


(c) Free Surface Displacement-Time History
(Obtained from the Acceleration Record)

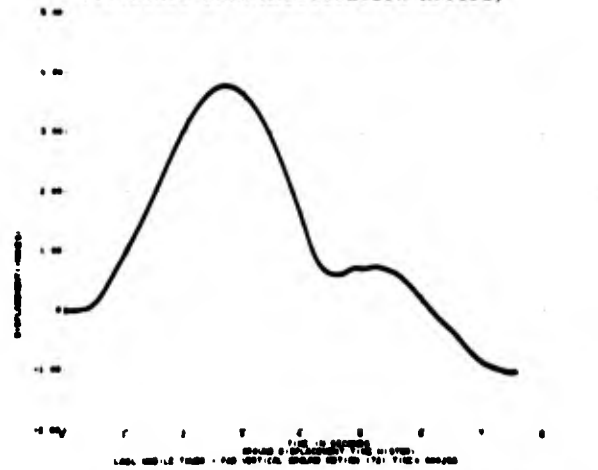
Fig. 13 - Measured Ground Motion at Station 12



(a) Emplacement Pad Acceleration-Time History



(b) Emplacement Pad Velocity-Time History
(Obtained from Acceleration Record)



(c) Emplacement Pad Displacement-Time History
(Obtained from the Acceleration Record)

Fig. 14 - Measured Ground Motion at Station 13

energy transmitted through the pad into the tower does not appear to be significantly affected by interactions between the casing, pad, and soil.

MEASURED TOWER RESPONSE

Pairs of accelerometers were mounted on the fourth, sixth, and eighth floor platforms to measure the acceleration response time histories of the tower. Typical plots of the vertical acceleration time histories measured at Stations 15, 17, and 19 are presented as Figures 15, 16, and 17. The basic characteristics of the acceleration records are, in general, similar to the characteristics of the free surface motion. However, in addition, high frequency oscillations are superimposed on the records. These oscillations are primarily attributed to ringing of the tower columns. The peak acceleration response was measured on the sixth floor (Station 16) where a spike of -12 g's was recorded. Little energy was associated with these high frequency spikes since, after the acceleration records were doubly integrated, their influence on the displacement time history was small.

ANALYTICAL TECHNIQUE

The advent of high speed digital computers has made possible the time dependent dynamic response of complex structures. In the general technique, the structure is first replaced by a lumped parameter idealization in which the actual distributed mass characteristics of the real structure are replaced by a series of masses lumped at a finite number of node points with each node having one or more degrees of freedom. The node points are then connected by a finite number of elements with each element having its own set of stiffness characteristics. The simplest element type consists of linearly elastic springs which contain only axial stiffness. This is the element type used in an in-house computer program, TDYNE, which was developed for the time dependent analysis of surface zero diagnostic towers (Reference 2).

For a distributed mass structure, partial differential equations are required to describe dynamic equilibrium. By using the lumped parameter idealization these equations are replaced by a finite number of coupled ordinary differential equations which can be most conveniently written in matrix notation. In TDYNE, coupled differential equations are solved using the mode superposition method. This method can only be applied to structures with linear stiffness properties. However, a certain amount of non-linearity, such as lumping and crushing of the base pad, can be accounted for by a continual modification of the dynamic forcing function. In this method, the analyst must first solve the characteristic value problem for the set of homogenous coupled differ-

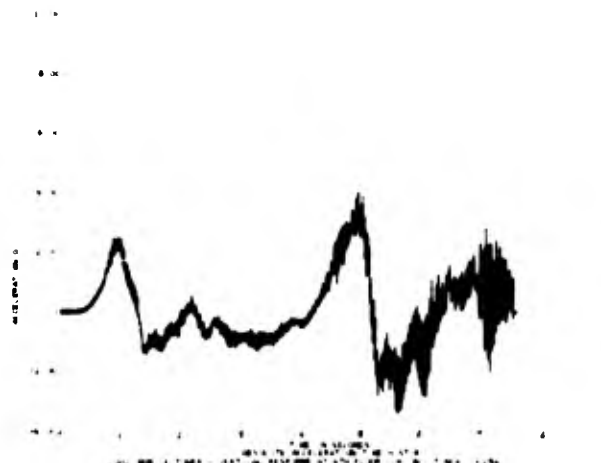


Fig. 15 - Measured acceleration record at Station 15

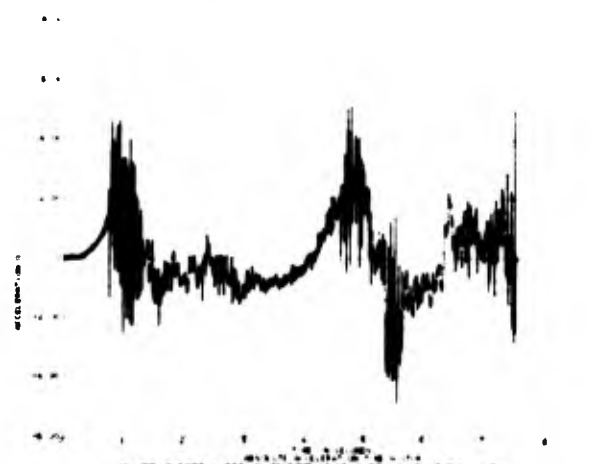


Fig. 16 - Measured acceleration record at Station 17

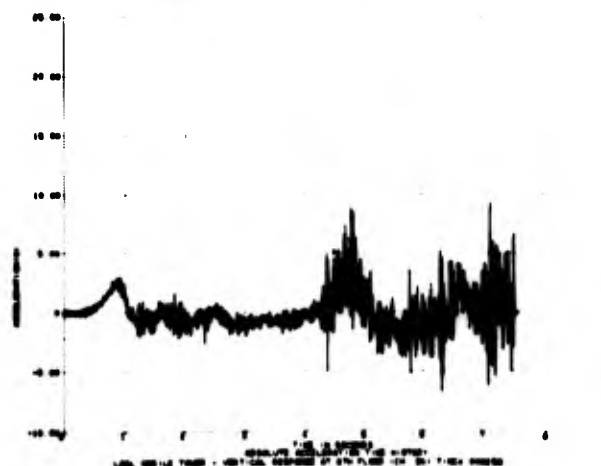


Fig. 17 - Measured acceleration record at Station 19

ential equations corresponding to free vibration of the lumped mass model. This leads to a set of eigenvectors and eigenvalues more commonly referred to as mode shape and natural frequencies of the structural system. The dynamic response of each mode is computed independently and then summed to obtain the total response of the system.

Computer program TDYNE represents a special purpose application of the general mode superposition method.

The dynamic equation of equilibrium for a lumped mass-spring system where ground motion a_t is the only applied dynamic force into the system can be easily shown to be:

$$[M]\{\ddot{X}\}_t + [C]\{\dot{X}\}_t + [K]\{X\}_t = -[M]\{1\}a_t$$

where

- $[M]$ = Diagonalized mass matrix
- $[C]$ = Viscous damping matrix
- $[K]$ = Symmetric stiffness matrix
- $\{X\}_t$ = Column vector of relative displacements with respect to the base of the structure at time t

The reader is referred to Reference 2 or any standard textbook on computerized structural dynamics for a detailed solution of this equation.

The only modification to this equation in TDYNE is to the term a_t . Where normally a_t is simply the ground motion input into the structure, in TDYNE the term can be modified if the base reaction exceeds crushing limits (i.e. yielding of columns) in the compression mode or exceeds tensile limits (i.e. dead load) in the tension mode. The derivation of the equations employed is simple but lengthy and therefore will not be given here. The equations are based on the assumption that both the base and ground accelerations vary linearly between time increments. In addition, it is consistent with this assumption that a change in state for the non-linear base only occurs at one of the incremental times, that is, that crushing and jumping both commence and end at the end of a time increment. The reader is referred to Reference 2 for the derivation of the equations.

DYNAMIC MODEL OF THE TOWER

The vertical dynamic properties of the tower were idealized using the mass-spring model presented in Figure 18. The model was tailored to match the features and capabilities of computer program TDYNE.

The dynamic model of the tower is comprised of a non-linear acting base, 17 masses,

and 20 springs. The base represents an idealization of the jumping characteristics of the tower. In general, the masses were lumped at the center and corners of each platform. Additional masses were lumped at positions corresponding to the locations of the accelerometer stations. Because of symmetry, the lumped masses of the corners of each platform, including the supporting girders and columns, were represented by only one mass per floor ($M_0 - M_6$). Also, the axial stiffnesses of the tower legs (columns) were represented by only one spring per floor ($K_1 - K_6$).

The design of the tower was such that the tower columns located between the bogies and the second floor were required to resist all lateral loads due to wind and anticipated horizontal ground motions. These columns were much larger, and therefore stiffer, than the columns located above the second floor. Thus, it was believed that lumping the masses of the corners of the first and second floor framing systems with the base mass would not significantly affect results of the computed response of the platforms where measurements were taken.

The truss outriggers were essentially self-supporting and relatively light in weight. It was assumed that they would not significantly influence the vertical response of the tower. Therefore, their effect and contribution to the tower response during the duration of the ground motion was neglected in the tower model.

The springs of the tower model were assumed to be linearly elastic. To determine the spring stiffnesses, design details of the tower were used in conjunction with an in-house standard static analysis computer code. The platforms were modeled as grids and equivalent substructure stiffness matrices were obtained through static analyses. The stiffness terms are indicated in the dynamic model (Figure 18) as springs.

The stiffness properties of the base were non-linear. The reaction-displacement properties of the base are shown in Figure 19. As long as the sum of the dead load and dynamic base reactions remained compressive and did not exceed the compressive capacity of the base columns, the tower remained coupled directly to the foundation. When the dynamic tensile reaction at the base exceeded the dead load base reaction, separation between the bogie wheels and rails occurred. This resulted in a relative tower jumping displacement, D_j , between the base of the tower and the foundation. After jumping was initiated, the tower response was resisted by a restoring force provided by the tie bar system. Figure 19 shows the calculated (tensile) spring stiffness of the tie bar system to be 3,490 kips per inch of jumping displacement. Thus, there was an increase in the tensile base reaction with

LUMPED MASSES (kips)

$W_0 = 6$	$W_9 = 5$
$W_1 = 22$	$W_{10} = 9$
$W_2 = 46$	$W_{11} = 62$
$W_3 = 25$	$W_{12} = 66$
$W_4 = 26$	$W_{13} = 16$
$W_5 = 28$	$W_{14} = 12$
$W_6 = 15$	$W_{15} = 4$
$W_7 = 45$	$W_{16} = 4$
$W_8 = 46$	$W_{17} = 4$

SPRING STIFFNESSES (kips/in)

$K_1 = 20,500$	$K_8 = 185$	$K_{15} = 375$
$K_2 = 20,500$	$K_9 = 225$	$K_{16} = 195$
$K_3 = 20,500$	$K_{10} = 225$	$K_{17} = 65$
$K_4 = 20,500$	$K_{11} = 175$	$K_{18} = 175$
$K_5 = 20,500$	$K_{12} = 160$	$K_{19} = 155$
$K_6 = 20,500$	$K_{13} = 980$	$K_{20} = 880$
$K_7 = 185$	$K_{14} = 180$	

LEGEND

- ① MASS NUMBER NODAL POINT
- I SPRING NUMBER

NOTE

Tower columns between foundation and second floor assumed very stiff

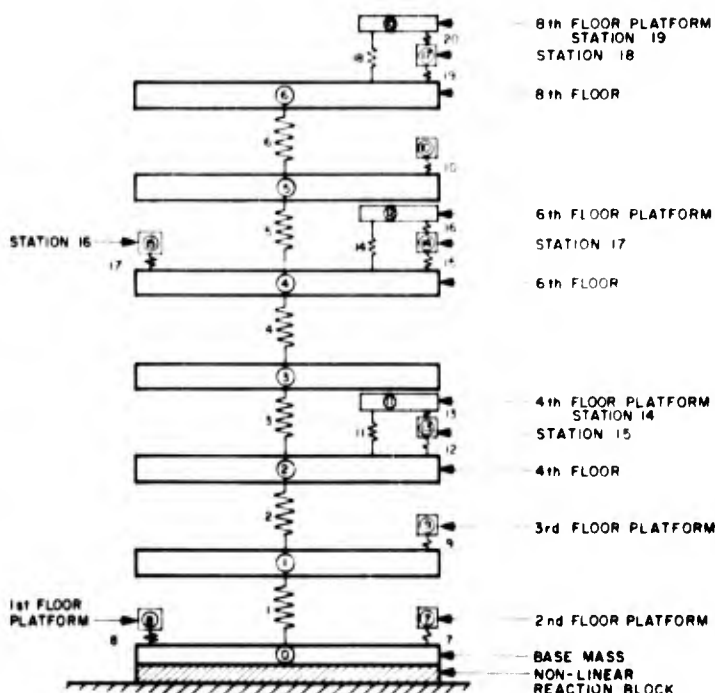


FIGURE 18
DYNAMIC MODEL OF LASL MOBILE TOWER

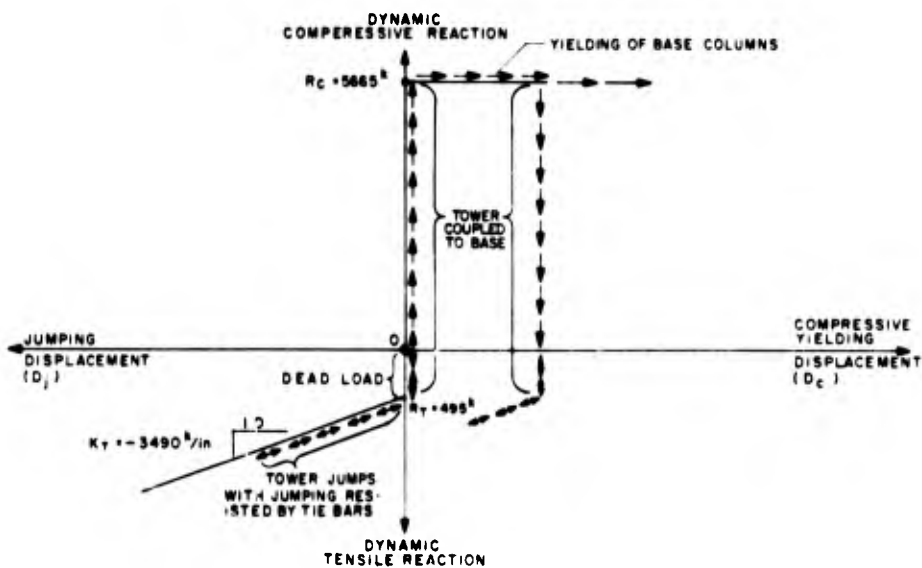


FIGURE 19
RELATIONSHIP BETWEEN DYNAMIC REACTION AND
COMPRESSIVE YIELDING AND JUMPING DISPLACEMENTS
FOR NON-LINEAR REACTION BLOCK

increasing jumping displacements.

The dead load base reaction for the tower was calculated to be 495 kips. The total compressive capacity of the base columns was set equal to the product of the yield stress and the area of the four base columns, or 6,060 kips. Because there was an initial compressive prestress in the columns due to tower dead load and payload, the dynamic compressive reaction, R_d , necessary to initiate yielding of the base columns was 5,565 kips (as shown in Figure 19). It was assumed that the yield strength of the columns did not increase if yielding was initiated and that deformations due to yielding of columns were permanent (nonrecoverable).

ANALYTICAL RESULTS

All 17 natural frequencies of the tower model were calculated and used in the integration. The natural frequencies of the tower model ranged from 6.3 to 170 cps. To obtain precision in response computations, the integration interval was set equal to the measured acceleration digitization interval (0.000256 sec.). A period of 0.25 seconds of free vibration was added to the end of each acceleration record to ensure that peak responses of the tower were obtained.

A constant viscous modal damping equal to 1/2 percent critical was assumed for all modes of the tower considered. This value was possibly too low considering the nature of the tower fabrication (bolted construction for the most part) and perhaps should have been in the range of from 1 to 2 percent critical damping. Use of the latter values may have resulted in peak responses occurring earlier in time and also may have precluded those instances where a computed peak response would occur during the free vibration era.

Four separate time-dependent modal superposition analyses were performed on the mass-spring model of the tower. The non-linear effects of jumping were not included in Analysis No. 1, and the free-surface acceleration-time history was used as the input motion. Analysis No. 2 was essentially identical to Analysis No. 1 except that the effects of jumping were included. Analyses No. 3 and 4 were identical to Analyses No. 1 and 2, respectively except that the emplacement pad acceleration-time history was used as the input motion.

At each integration interval (0.000256 sec.), the relative displacements were computed (relative to ground) at all nodal points as well as the forces in all spring elements. Since the input acceleration records were each approximately one second long, the displacements and forces were evaluated approximately 4,000 times for each analysis.

COMPARISON OF ANALYTICAL AND MEASURED RESULTS

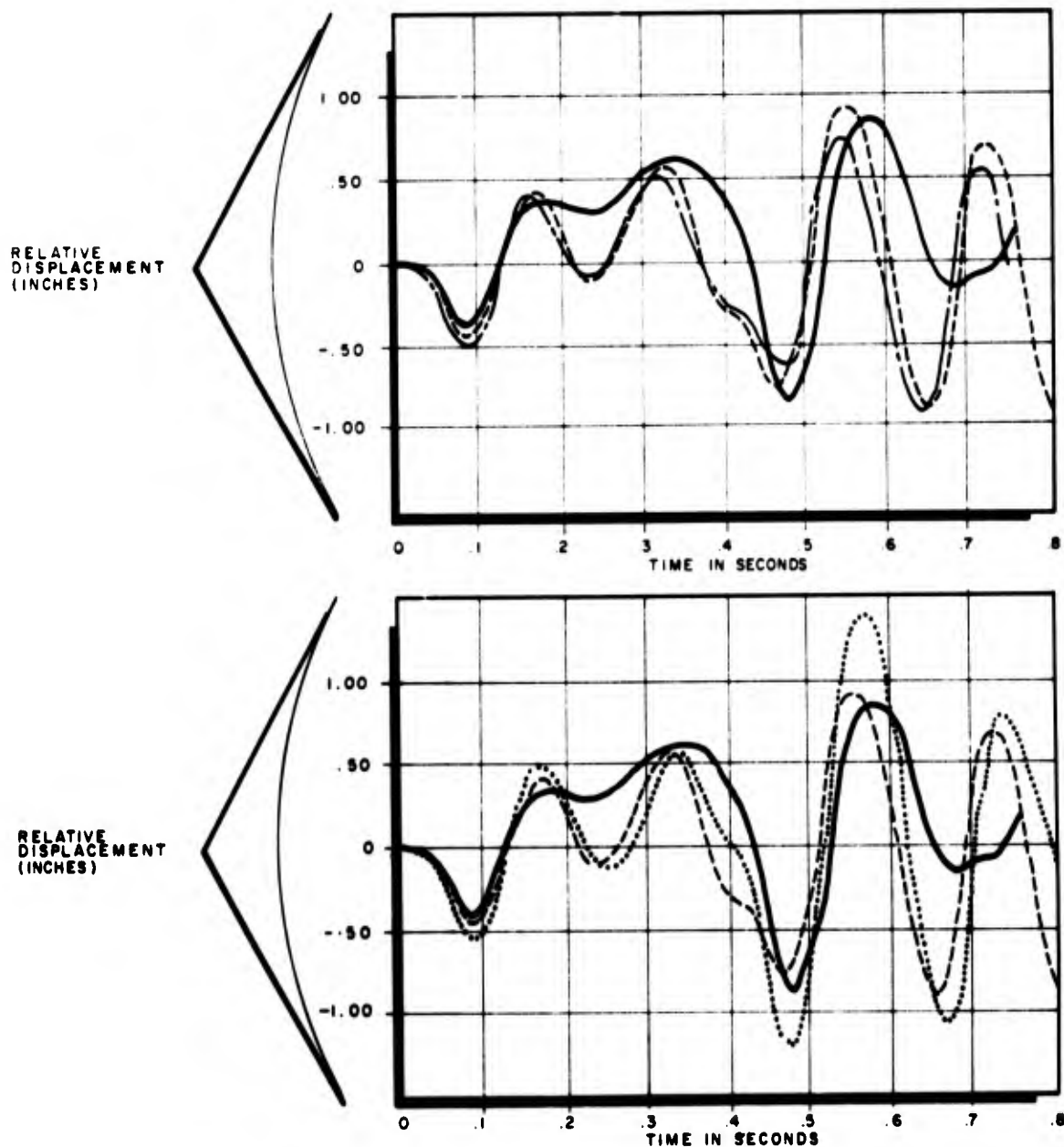
The acceleration responses recorded at each of the stations in the tower were doubly integrated to obtain the absolute displacement time histories. The pad displacement time history was then subtracted from each tower displacement record to obtain the relative displacement time history at each tower station. The relative displacement time histories at all six tower stations were all quite similar in shape and magnitude. The smallest response was at Station 16, which peaked at .85 inches, while largest response was at Station 14, which peaked at 1.15 inches.

Measured and computed relative displacement time histories for Station 15 are compared in plots presented in Figure 20. In general, the computed results agree quite closely with the measured results for the first 0.60 seconds. After 0.60 seconds the measured tower response appears to dampen much more rapidly than the computed response. It would therefore appear that perhaps the assumed value of 1/2 percent damping was rather low and a larger value of 1 to 2 percent may have been more appropriate.

In general, the analyses in which jumping was included were in closer agreement with measured results than when it was not included. Also, the analyses in which free surface motion was used as the input motion usually induced slightly larger responses as compared to responses computed using the pad motion input. Specific details with regard to comparison of analytical and measured results are provided in Reference 1. The peak base jumping displacement obtained from free surface motion analyses was 0.38 inches while the peak base jumping displacement obtained from the pad motion analyses was 0.18 inches. This suggests there may have been a small amount of damping of the input motion due to interaction between the casing, pad, and soil.

CONCLUSION

It is apparent that the time dependent response of surface zero diagnostic towers and other similar types of structures subjected to severe ground shocks can be reasonably predicted provided that reliable input ground motions are established. It is recommended that in future analyses a larger value of damping be used (≈ 2 percent) for structures of this type. Usage of free surface ground motions in lieu of pad motions appears to lead to a conservative but reasonably accurate prediction of structural response. This conclusion is significant since free surface motions can be more easily predicted than pad motions. It can also be concluded that the inclusion of the non-linear effect of tower jumping in the analysis significantly improved the correlation



- MEASURED WITH RESPECT TO THE PAD (OBTAINED FROM ACCELERATION RECORDS WITH BASE LINE CORRECTION)
- COMPUTED USING PAD MOTION INPUT - NO JUMPING
- COMPUTED USING PAD MOTION INPUT - WITH JUMPING
- COMPUTED USING FREE SURFACE MOTION - WITH JUMPING

FIGURE 20
COMPARISONS OF MEASURED AND COMPUTED
RELATIVE DISPLACEMENT - TIME HISTORIES
AT STATION 15

between measured and computed results.

ACKNOWLEDGEMENT

The writers wish to thank LASL for their cooperation in conduction of this study and for usage of the photographs presented herein.

REFERENCES

1. R. E. Bachman, "Postshot Study Dynamic Response of LASL Mobile Tower Pliers Event," HN-20-1037, April 1970.
2. R. P. Kennedy and R. Semmens, "TDYNE, A Computer Program to Perform Modal and Time Dependent Dynamic Analysis of Spring Mass Systems with Crushable and Jumping Bases Subject to Ground Motion," HN-20-1027, June 1969.
3. R. P. Kennedy and G. Tsacoyeanes, "SPECANAL, A Computer Program to Generate Response Spectra, Power Spectral Density, and Response-Time Histories for Elastic Single Degree of Freedom Oscillators with Viscous Damping Subjected to Digitized Ground Motion-Time Histories," HN-20-1030, October 1969.
4. R. P. Kennedy, "Structural Response to Close-In Vertical Ground-Motion from Underground Nuclear Tests at Pahute Mesa," HN-20-1028, July 1969.

BOUNDS FOR THE RESPONSE OF A CONSERVATIVE SYSTEM UNDER DYNAMIC LOADING

H. Brauchli
The University of Alabama in Huntsville
Huntsville, Alabama

A method based on Liapunov theory is presented to obtain bounds for the energy increase in a discrete conservative system subject to time-dependent loading. Applications to simple systems approximating a column and a circular arc are given.

INTRODUCTION

Dynamic stability, particularly snap-buckling caused by dynamic loading, is a most important problem of structural analysis.^[1] Methods to obtain static buckling loads are well developed (see e.g. [2 - 5] for buckling of shells), but little has been done about dynamic buckling analysis. Most authors limit their analysis to small deflections (i.e. linearization) or to special loading functions (δ-pulse, step load, rectangular or triangular load, or they depend on some kind of approximation [6 - 10]). The need for a more general and rigorous approach has been recognized. Martin [11 - 14] and most recently Wierzbicki [15] obtained some results on displacement bounds for elastic and inelastic structures. Yet these apply to a restricted class of loading functions only, e.g. oscillating loads are excluded.

As a first step towards a more rigorous approach, we present here a method based on Liapunov theory, applicable to nonlinear discrete conservative systems and arbitrary loading functions. We are interested in the behavior near a stable equilibrium position corresponding to a minimum of the potential. The generalized force due to the external load is supposed to be a product of a time-dependent amplitude and a function of coordinates derivable from a potential. In addition, we assume the generalized force to vanish at the equilibrium position. Consequently, the initial deflections and velocities will have a decisive influence on the behavior of the system. We prove, that the system remains stable if the load amplitude tends fast enough to a limit value smaller than the Euler load of the static problem. An inequality for the energy increase of the system is obtained, which can be used to find bounds for the load amplitude against snap-buckling. The results indicate that the special loading functions

mentioned above are not quite representative for the general response of the structure, e.g. a load amplitude oscillating around a limit value is much more dangerous than the corresponding step load. The bounds against dynamic buckling obtained by this method are rigorous but not exact: buckling under an admissible load amplitude is strictly excluded but the critical load may be higher than the one given by the bound.

DESCRIPTION OF THE SYSTEM

Let $T(x^k, \dot{x}^j)$ and $U(x^k)$ be the kinetic and potential energy function of the system, respectively. The differential equations of motion are given as the Lagrange equations

$$\frac{\partial T}{\partial \dot{x}^k} - \frac{\partial T}{\partial x^k} + \frac{\partial U}{\partial x^k} = Q_k = P(t) \frac{\partial W}{\partial x^k}, \quad (1)$$

where Q_k stands for the generalized force which, except for the time-depending amplitude, is derivable from the external potential function W . We assume in the following, that all energy functions have continuous second derivatives and that $P(t)$ is continuously differentiable.

It is well-known that the kinetic energy is a quadric form in the velocities,

$$T = \frac{1}{2} m_{ij}(x^k) \dot{x}^i \dot{x}^j \quad (2)$$

with a symmetric and positive definite matrix m_{ij} .

If we assume now that the origin of coordinates is an equilibrium position of (1), the potential may be represented--up to an additive constant--as

$$U(x^k) = \frac{1}{2} c_{ij} (x^k)^i x^j \quad (3)$$

with a symmetric matrix [16]. Furthermore, c_{ij} will be positive definite for small deflections if the origin is stable for $P(t) = 0$. Similarly,

$$\frac{\partial W}{\partial x^k} = q_{ki} (x^j)^i x^j \quad (4)$$

where q_{ki} is symmetric at the origin. Now the total energy E and its time derivative are easily expressed in matrix notation,

$$E(x^m, \dot{x}^k) = \frac{1}{2} \dot{x}^T M \dot{x} + \frac{1}{2} x^T C x, \quad (5)$$

$$E' = P(t) \dot{x}^T Q x. \quad (6)$$

In a linear system all matrices are constant and symmetric.

LIAPUNOV ANALYSIS

It is well known (Theorem of Lagrange) that a minimum of the potential of a conservative system corresponds to a stable equilibrium position. In this case the total energy (5) serves as a Liapunov function for stability; it is positive definite and its time-derivative is zero [17]. A dynamic load applied to the system changes its energy according to (6). Now a simple choice of a Liapunov function is

$$V(x, \dot{x}, t) = e^{-h(t)} E(x, \dot{x}) \quad (7)$$

Its derivative is

$$V'(x, \dot{x}, t) = -e^{-h(t)} (h' E - E') \quad (8)$$

With

$$h = \max_{t \in \mathbb{R}_+} |\dot{x}^T Q x| / E(x, \dot{x}), \quad (9)$$

$$h(t) = \int_0^t |P(t')| dt' \quad (10)$$

(8) is smaller equal zero in the domain

$$\mathcal{D} = \{x, \dot{x} \mid E(x, \dot{x}) \leq s\} \quad (11)$$

If the integral

$$A = \int_0^\infty |P(t)| dt \quad (12)$$

converges, $V(x, \dot{x}, t)$ satisfies all conditions for a Liapunov function for stability in the domain \mathcal{D} ; it is positive definite and decrescent and has a continuous negative semidefinite derivative. The convergence of (12) implies in particular that the load amplitude tends to zero as t goes to infinity. This condition can be relaxed by decomposing the load amplitude into a static and a dynamic part. Assume that the limit

$$P_s = \lim_{t \rightarrow \infty} P(t) \quad (13)$$

exists and define

$$P_d = P(t) - P_s. \quad (14)$$

The static load P_s may now be included in the energy expression. Let

$$\tilde{E}(x, \dot{x}) = E(x, \dot{x}) - P_s W(x) \quad (15)$$

and define

$$\tilde{V}(x, \dot{x}, t) = e^{-k(t)} \tilde{E}(x, \dot{x}) \quad (16)$$

with

$$\mu = \max_{t \in \mathbb{R}_+} \frac{|\dot{x}^T W x|}{\tilde{E}(x, \dot{x})}, \quad (17)$$

and

$$\tilde{A} = \lim_{t \rightarrow \infty} \int_0^t |P_d(t')| dt' \quad (19)$$

The modified energy \tilde{E} is clearly positive definite in \mathcal{D} for small values of P_s . The smallest value of the static load P_s for which \tilde{E} is not definite is called the Euler load P_E . It is the buckling load for the corresponding static problem. In view of the Theorem of Lagrange it is natural to expect the system (1) to be unstable if P_s exceeds P_E . Assume, on the other hand, that P_s is smaller than P_E . It then follows from

$$\tilde{V}(x, \dot{x}, t) \leq \tilde{E}(x, \dot{x}) \quad (20)$$

that the function \tilde{V} is decrescent. Furthermore, if the limit \tilde{A} is finite,

$$\tilde{V}(x, \dot{x}, t) \geq e^{-\tilde{A}} \tilde{E}(x, \dot{x}) \quad (21)$$

and \tilde{V} is positive definite. Finally,

$$\tilde{V}'(x, \dot{x}, t) = -e^{-k(t)} (\mu \tilde{E} - P_d(t) \dot{x}^T Q x) \quad (22)$$

is negative semidefinite in view of (17) and (18). Hence, we proved the following

Theorem: The system (1) is stable if the two conditions

$$P_s < P_l, \quad \tilde{A} < 0$$

are met.

This means that the system is stable under load amplitudes tending fast enough to a limit value smaller than the Euler load. In particular, the peak value of the load amplitude is of no influence.

We have to expect instability if the first condition is violated. If the second condition is violated, instability may or may not occur. As an example, consider linear systems with periodic load amplitudes. It is well known that in this case stability depends on the frequency and amplitude of the load function [18].

BOUNDS FOR DEFLECTIONS

Stability implies that the deflections and velocities of the mechanical system remain smaller than any preassigned bound, if only the initial deflections and velocities are small enough. With the Liapunov function (16) we obtain an inequality for the energy,

$$\tilde{E}[x(t), \dot{x}(t)] \leq e^{\tilde{A}t} \tilde{E}[x(0), \dot{x}(0)]. \quad (23)$$

This may be used to compute the admissible level of initial disturbances,

$$\dot{x}_0^T M \dot{x}_0 + x_0^T (C - P_s Q) x_0 \leq 2 U^* \exp \left(- \int_0^\infty |P_d(t)| dt \right) \quad (24)$$

for a given critical energy level U^* . For small initial disturbances, the matrices in (24) may be considered constants. In this case (24) defines an ellipsoid in phase space which is centered at the origin.

SNAP-BUCKLING

In some systems a critical energy level is naturally defined through a saddle point of the potential function $U(x)$. In this case, we speak of snap-buckling. If we understand U^* to be the value of the potential at the saddle-point, (24) gives the necessary restriction on the initial disturbances in order to avoid snap-buckling for a given load amplitude. Alternately, if the initial disturbances are prescribed, we can read it as an inequality defining admissible load amplitudes:

$$\int_0^\infty |P_d(t)| dt \leq \ln \frac{U^*}{E_0} \quad (25)$$

If the load amplitude is given except for an unknown factor,

$$P_d(t) = P r(t), \quad \int_0^\infty |r(t)| dt = 1 \quad (26)$$

a safe load

$$P_{\text{safe}} = \ln \frac{U^*}{E_0} \quad (27)$$

may be defined.

COMPARISON WITH δ - PULSE RESPONSE

As an extreme case we may consider a load amplitude of the form of a δ -function,

$$P(t) = P \delta(t) \quad (28)$$

Then the velocities undergo a jump

$$\Delta \dot{x} = M^{-1} Q x_0 P \quad (29)$$

at time zero, while the position remains unchanged. The new energy is

$$E = \frac{1}{2} (\dot{x}_0 + P M^{-1} Q x_0)^T M (\dot{x}_0 + P M^{-1} Q x_0) + U(x_0) \quad (30)$$

Comparison of (30) with (24) for a δ -pulse yields the inequality

$$E_0 e^{\lambda P} \geq E_0 + \dot{x}_0^T Q x_0 P + \frac{1}{2} x_0^T Q^T M^{-1} Q x_0 P^2 \quad (31)$$

If we restrict the discussion to small initial deflections and velocities the matrices in (30) and (31) are symmetric and constant. For this case an algebraic derivation of (31) could be given.

If a critical energy U^* is given, we obtain, instead of (24), the inequality

$$E_0 + \dot{x}_0^T Q x_0 P + \frac{1}{2} x_0^T Q^T M^{-1} Q x_0 P^2 \leq U^* \quad (32)$$

Considered as a condition on the initial deflections and velocities, (32) again defines an ellipsoid in phase space, but not centered at the origin. Clearly the condition (24) is more stringent than (32).

Alternately, (32) may be used as a quadric equation to define a safe load. This will in general be bigger than (27). Numerical results for a typical two-degree-of-freedom system (19) show that the actual critical load exceeds the safe load obtained from (32) by at least 2%.

THE INVERTED DOUBLE PENDULUM

Consider a system consisting of two bars connected and supported by hinges with torsional springs under a vertical dynamical load. If the motion is restricted to a vertical plane, there are two degrees of freedom. Let ψ and $\psi + \chi$ denote the respective angular deflection and $F(\psi)$ the potential function of the spring torque. Then

$$T = \frac{m l^2}{6} \dot{\psi}^2 + 3 \cos \chi \dot{\psi}^2 + (2 + 3 \cos \chi) \dot{\psi} \dot{\chi} + \dot{\chi}^2, \quad (33)$$

$$U = F(\psi) + F(\psi + \chi) \quad (34)$$

represent the kinetic and potential energy and

$$W = l^2 2 - \cos \psi - \cos(\psi + \chi) \quad (35)$$

the negative potential of a static unit load. With the matrices

$$M = \frac{m l^2}{6} \begin{pmatrix} 16 & 5 \\ 5 & 2 \end{pmatrix} \quad (36)$$

$$C = k \begin{pmatrix} 1 & 0 \\ 0 & 1 \end{pmatrix} \quad (37)$$

$$Q = l^2 \begin{pmatrix} 2 & 1 \\ 1 & 1 \end{pmatrix} \quad (38)$$

of the linearized system we find the Euler load

$$P_E = \frac{3\sqrt{5}}{2} \frac{k}{l} = .3820 \frac{k}{l}. \quad (39)$$

For the linearized system λ is computed as the biggest root of the determinantal equation

$$\begin{vmatrix} \lambda M & Q \\ Q & C \end{vmatrix} = 0 \quad (40)$$

i.e.,

$$\lambda = \sqrt{6mk} = 2.45 \sqrt{mk}. \quad (41)$$

THE FIVE-HINGED ARCH UNDER DYNAMIC PRESSURE

Consider a system of four bars connected by hinges and springs, and supported by

hinges without springs at two points, under a dynamic pressure load. The configuration of the system is described by four angles $\alpha_1, \alpha_2, \beta_1, \beta_2$ subject to the conditions

$$F = \sin \alpha_1 + \sin \alpha_2 - \sin \beta_1 - \sin \beta_2 = 0 \quad (42)$$

$$G = L/l - \cos \alpha_1 - \cos \alpha_2 - \cos \beta_1 - \cos \beta_2 = 0 \quad (43)$$

We are dealing with a two-degree of freedom system, but at least three parameters are needed to represent its configuration globally without singularities. The configuration space can be shown to be a regular and orientable differentiable manifold if

$$2 < L/l < 4, \quad (44)$$

or

$$0 < L/l < 2. \quad (45)$$

Its genus may be determined--using, say, Morse theory [16]--to be zero or four, respectively. Hence for (44) it is a sphere. for (45) a "sphere with four handles". The springs have the effect that we have to consider the covering space of the kinematical configuration space. For (44) this will be a sphere again, while for (45) it will no longer be a closed manifold.

A simple way to introduce coordinates can be found if we restrict the discussion to the shallow arch, i.e. to small angles, and satisfy the conditions (42) and (43) up to quadric terms only. Let

$$\begin{aligned} \sqrt{2} \alpha_1 &= \xi + \eta + \zeta, \\ \sqrt{2} \alpha_2 &= \xi - \eta - \zeta, \\ \sqrt{2} \beta_1 &= \xi + \eta - \zeta, \\ \sqrt{2} \beta_2 &= \xi - \eta + \zeta. \end{aligned} \quad (46)$$

Clearly, the configuration will be symmetric as long as $\eta=0$. With (46), (42) is satisfied up to second order terms. Instead of (43) we find

$$G = \xi^2 + \eta^2 + \zeta^2 - R^2 = 0 \quad (47)$$

The area below the arch may be written as

$$A = \sqrt{2} l^2 (2\xi + \zeta). \quad (48)$$

It is maximum for

$$\xi^2 = 2\gamma, \eta = 0, \xi = \gamma; \gamma = R/\sqrt{3} \quad (49)$$

We assume the springs to be undeflected at position (49). The potential energy then is

$$U = k[(\xi - \zeta - \gamma)^2 + 2\eta^2 + 2(\zeta - \eta)^2] \quad (50)$$

The critical points of (50) are found from the condition

$$dU = k\Lambda dG \quad (51)$$

leading to the system

$$\begin{aligned} (1-\Lambda)\xi - \zeta &= \gamma \\ (2-\Lambda)\eta &= 0 \\ -\xi + (3-\Lambda)\zeta &= \gamma \end{aligned} \quad (52)$$

The characteristic equation

$$(\Lambda-2) \wedge (\Lambda^3 - 8\Lambda^2 + 19.6\Lambda - 13.6) = 0 \quad (53)$$

has six solutions. The critical points are

	ξ/γ	η/γ	ζ/γ	$U/k\gamma^2$	type
A	2	0	1	0.	minimum
C	-2.1462	0.	-.6276	11.6414	minimum
B+	-1	2	0	14.0000	saddle
B-	-1	-2	0	14.0000	saddle
D	-1.3014	0	1.8184	18.3116	maximum
E	.4476	0	-2.1908	33.6004	maximum

Hence, there are two different minima, connected by two saddle points with the same critical energy

$$U^* = 14k\gamma^2 = 2.8 k R^2 \quad (54)$$

Asymmetric buckling gives rise to the Euler load

$$P_E = 2k\gamma \quad (55)$$

If a static load is present we obtain instead of (54)

$$U^* = 2.8(1-\gamma)^2 k R^2 \quad (56)$$

with the parameter

$$\pi = P_s / P_t \quad (57)$$

Introducing local coordinates x, y in the vicinity of the equilibrium point A,

$$\xi = \gamma(2+x), \eta = \gamma y, \zeta = \gamma(1-2x - \frac{5}{2}x^2 - \frac{1}{2}y^2) \quad (58)$$

we find for the linearized system the matrices

$$M = \frac{2mk^2\gamma^2}{3} \begin{pmatrix} 2 & \\ & 1 \end{pmatrix} \quad (59)$$

$$C = 2k\gamma^2 \begin{pmatrix} 17 & \\ & 2 \end{pmatrix} \quad (60)$$

$$W = \frac{\gamma}{\sqrt{2}} k^2 \begin{pmatrix} 5 & \\ & 1 \end{pmatrix} \quad (61)$$

Equation (40) gives in this case

$$\lambda = 22.14 \sqrt{\frac{mk}{k}} \quad (62)$$

ACKNOWLEDGEMENT

This work was supported by NASA Grant No. NGL 01-002-001 in the early stage and by the AFOSR, through contract No. F44620-69-C-0124, in the final phase. It is a pleasure for me to express my appreciation to these agencies for their support.

REFERENCES

1. H. L. Langhaar "General Theory of Buckling," Applied Mechanics Reviews, Vol. 11, pp. 585-588, 1958.
2. W. T. Koiter. "Elastic stability and post-buckling behavior," Proceedings of the Symposium on Nonlinear Problems, edited by R. E. Langer, University of Wisconsin Press, 1963.
3. W. T. Koiter, "General equations of elastic stability for thin shells," to Honor L. H. Donnell edited by D. Muster, University of Houston, 1967.
4. B. Budiansky, "Notes on non-linear shell theory," Journal of Applied Mechanics, Transactions of the American Society of Mechanical Engineers, Vol. 35, Series E, pp. 393-401, 1968.
5. D. A. Danielson, "Buckling and initial postbuckling behavior of spheroidal shells under pressure," AIAA Journal Vol. 7, No. 5, pp. 935-944.

6. W. Eckhaus, "Studies in nonlinear stability theory," Springer Verlag, 1965.
7. B. Budiansky and J. W. Hutchinson, "Dynamic buckling of imperfection sensitive structures," Proceedings of the XI International Congress on Applied Mechanics (Springer Verlag Berlin).
8. J. W. Hutchinson and B. Budiansky, "Dynamic buckling estimates," AIAA Journal 4, pp. 525-530, 1966.
9. B. Budiansky, "Dynamic buckling of elastic structures: criteria and estimates," Proceedings of the International Conference on Dynamic Stability of Structures, Pergamon Press, New York, 1967.
10. B. Budiansky and J. W. Hutchinson, "A survey of some buckling problems," AIAA Journal 4, pp. 1505-1510, 1966.
11. J. B. Martin, "Impulsive loading theorems for rigid-plastic continua," Journal of the Engineering Mechanics Division, ASCE 90, EMS, pp. 27-42, 1964.
12. J. B. Martin, "A displacement bound technique for elastic continua subjected to a certain class of dynamic loading," Journal of the Mechanics and Physics of Solids, Vol. 12, pp. 165-176, 1964.
13. J. B. Martin, "A displacement bound principle for inelastic continua, subjected to a certain class of dynamic loading," Journal of Applied Mechanics, ASME Vol. 32, pp. 1-6, 1965.
14. J. B. Martin, "Displacement bounds for dynamically loaded elastic structures," Journal of Mechanical Engineering Sciences, Vol. 10, pp. 213-218, 1968.
15. T. Wierbicki, "Bounds on large dynamic deformations of structures," Journal of the Engineering Mechanics Division, ASCE, EM3, June 1970.
16. J. Milnor, "Morse theory," Annals of Mathematics Studies, Princeton University Press, Princeton, 1963.
17. W. Hahn, "Theorie und anwendung der direkten methode von Ljapunov," Erg. d. Math. U. Grenzgeb., Springer Verlag, Berlin, 1959.
18. V. V. Bolotin, "The dynamic stability of elastic systems," Holden Day, San Francisco, 1964.
19. M. Cash, "Static and dynamic stability of a conservative two-degree-of-freedom system," Master Thesis UAH, 1970.

THREE DEGREE OF FREEDOM SPRING MASS EJECTION SYSTEM (U)

R. MUSKAT
AEROSPACE CORPORATION
SAN BERNARDINO, CALIFORNIA

The problem of dispensing three objects by spring from a tube, subject to a set of optional constraints is solved. The required initial displacements and stiffnesses of each spring in a three spring-mass system are determined such that at a given instant of time a specified velocity for each mass is obtained. Due to the unusual boundary conditions, the solution is in the form of a transcendental equation in two unknowns. Since unique boundary conditions do not exist, a family of solutions are obtained. The desired condition occurs when the force in the springs at time zero is a minimum and the initial displacements and final stroke are within the physical constraints.

NOMENCLATURE

- 1) A_{ij} = amplitude of the i^{th} mass displacement due to the j^{th} mode.
- 2) D_i = initial displacement ratio
- 3) E = vector with elements E_i .
- 4) E_i = required velocity ratio of i^{th} mass to required velocity of mass 1.
- 5) $F(t)$ = forcing function (pounds).
- 6) K = stiffness of spring 1 (pound/inch).
- 7) K_i = stiffness of i^{th} spring (pound/inch).
- 8) m = mass of each body (pounds - sec^2/inch).
- 9) S = vector defined by equation 30.
- 10) t = time (sec).
- 11) t_a = time at which all masses have the required velocity simultaneously (sec).
- 12) V = required velocity of mass 1.
- 13) V_i = required velocity of the i^{th} mass (inch/sec).
- 14) X_i = spring stiffness ratio of i^{th} spring to the stiffness of spring 1.
- 15) Y_i = displacement of i^{th} mass measured from its equilibrium position (inches).
- 16) α_j = the j^{th} mode phase angle (radians).
- 17) β_i = ratio of ω_i to $(K)^{1/2}$.
- 18) γ_{ij} = matrix relating A_{ij} to A_{1j} .
- 19) Δ = initial displacement of mass 1.
- 20) ϵ = matrix with element ϵ_{ij} .
- 21) ϵ_{ij} = value defined by equation 29B.
- 22) ζ_i = ratio of σ_i to c_3 .
- 23) η_{ij} = elements defined by equations 21A to C and 25A to C.
- 24) λ_{ij} = value defined by equation 29C.
- 25) ρ_j = vector relating A_{1j} to Δ .

- 26) σ = vector defined by equation 33.
 27) σ_i = i^{th} element of the σ vector.
 28) ϕ = value defined by equation 36.
 29) ψ_{ij} = value defined by equation 29A.
 30) ω_j = the j^{th} mode frequency (1/sec).

1. INTRODUCTION

The mathematical analysis of single degree of freedom systems and multi-degree of freedom concentrated-mass systems is well documented in the dynamics and structural dynamics literature. For the vast majority of these cases, the boundary conditions are such that a unique solution can be obtained. The boundary conditions for the system under consideration do not permit a direct solution.

Figure 1 shows a three degree of freedom system in which three masses are connected in series by means of springs. The spring connected to the first mass is attached to a fixed support. The purpose of the system is to eject the masses from a constraining tube with a required set of velocities at the instant of release. (Figure 1)

The unknowns in the problem are:

1. The initial displacements of each spring.
 - a. $Y_1(0)$; initial displacement of spring 1,
 - b. $Y_2(0) - Y_1(0)$; initial displacement of spring 2,
 - c. $Y_3(0) - Y_2(0)$; initial displacement of spring 3.
2. The stiffness of each spring.
 - a. K_1 ; stiffness of spring 1,
 - b. K_2 ; stiffness of spring 2,
 - c. K_3 ; stiffness of spring 3.
3. The time (t_a) at which all 3 masses are released with the desired velocities.

The solution of the problem for an assumed relationship between the initial displacements, is obtained by finding the roots of a transcendental equation in two unknowns, the time at release (t_a) and the stiffness of spring 1 (K). The numerical values for these two unknowns must be

determined by utilizing the constraints of the problem which are 1) t_a must be less than one-half the shortest period, 2) the force in the springs at time zero must be a minimum ($K_1 Y_1(0) = \text{minimum}$) and 3) the total length of the system when the masses reach their final velocities (the compressed length of each spring plus the stroke of each spring plus the length of each mass) must be less than the length of the constraining tube. The solution is valid only for an assumed relationship between the initial displacements. This relationship must be varied to obtain the desired solution. A computer program was written to solve the transcendental equation and evaluate the minimum non-zero solution. (Appendix a)

MATHEMATICAL ANALYSIS

Eject 3 masses out of a tube utilizing 3 springs. The three masses must have exit velocities of V_1 , V_2 and V_3 respectively.

Boundary conditions:

Static $t \leq 0^-$ $F(t) = F$
 No acceleration or velocity.
 The total force on each mass must be the same.

Dynamic $t \leq 0^+$ $F(t) = 0$

$$\dot{Y}_i(t=0) = 0 \quad i = 1, 2, 3 \quad \text{Eq 1B}$$

$$\dot{Y}_i(t=t_a) = V_i \text{ in/sec } i = 1, 2, 3 \quad 2B$$

STATIC ANALYSIS $|t \leq 0^-|$

$$\ddot{Y}_i = \ddot{Y}_1 = 0$$

From Figure 3: Equilibrium Equations

$$F(t) = F = K_3(Y_3 - Y_2) \sum F_y @ \text{mass 3} \quad \text{Eq 1}$$

$$K_3(Y_3 - Y_2) = K_2(Y_2 - Y_1) \sum F_y @ \text{mass 2} \quad 2$$

$$K_2(Y_2 - Y_1) = K_1 Y_1 \sum F_y @ \text{mass 3} \quad 3$$

From Equation 3:

$$K_2 = \left[Y_1 / (Y_2 - Y_1) \right] K_1 \quad 4$$

From Equations 4 and 2:

$$K_3 = \left[Y_1 / (Y_3 - Y_2) \right] K_1 \quad 5$$

$$\text{Let } Y_1 = D_1 \Delta \quad (\Delta < 0) \quad 6$$

$$K_1 = X_1 K \quad 7$$

$$\text{and } D_1 = X_1 = 1 \quad 8$$

Therefore, from equations 4, 6, and 7:

$$X_2 = 1 / (D_2 - 1) \quad 9$$

From equations 5,6 and 7:

$$X_3 = 1 / (D_3 - D_2) \quad \text{Eq 10}$$

$$\text{Unknowns } K, \Delta, D_2, D_3 \quad 11$$

DYNAMIC ANALYSIS $|t \geq 0^+$

From Figure 3: Equations of Motion

$$m\ddot{Y}_1 + K_1 Y_1 - K_2 (Y_2 - Y_1) = 0 \quad 12A$$

$$m\ddot{Y}_2 + K_2 (Y_2 - Y_1) - K_3 (Y_3 - Y_2) = 0 \quad 12B$$

$$m\ddot{Y}_3 + K_3 (Y_3 - Y_2) = 0 \quad 12C$$

General Solution:

$$Y_i = A_{ij} [\sin(\omega t + \alpha)]_j \quad 13A$$

$$\text{Therefore: } \dot{Y}_i = A_{ij} [\omega \cos(\omega t + \alpha)]_j \quad 13B$$

$$\ddot{Y}_i = -A_{ij} [\omega^2 \sin(\omega t + \alpha)]_j \quad 13C$$

where i is the spring number 1,2 or 3
and j is the mode number 1, 2 or 3.

The Boundary Conditions

$$\dot{Y}_i(0) = 0 \quad 14A$$

$$\dot{Y}_i(t_a) = E_i V \text{ (where } E_i \text{ \& } V \text{ are known and } t_a \text{ is unknown)} \quad 14B$$

$$Y_i(0) = D_i \Delta \quad 14C$$

EVALUATION OF ω_j 's

$$Y_i = A_i \sin(\omega t + \alpha) \quad 15A$$

$$\dot{Y}_i = A_i \omega \cos(\omega t + \alpha) \quad 15B$$

$$\ddot{Y}_i = -A_i \omega^2 \sin(\omega t + \alpha) = -\omega^2 Y_i \quad 15C$$

substituting equations 15 into 12 and simplifying:

$$(-m\omega^2 + K_1 + K_2)A_1 - K_2 A_2 + 0A_3 = 0 \quad 16A$$

$$-K_2 A_1 + (-m\omega^2 + K_2 + K_3)A_2 - K_3 A_3 = 0 \quad 16B$$

$$0A_1 - K_3 A_2 + (-m\omega^2 + K_3)A_3 = 0 \quad 16C$$

To insure non-zero displacements (i.e., $A_i \neq 0$ $i = 1, 2 \text{ \& } 3$) the determinate of the coefficients in equations 16 must be 0. Thus:

$$\begin{vmatrix} -m\omega^2 + K_1 + K_2 & -K_2 & 0 \\ -K_2 & -m\omega^2 + K_2 + K_3 & -K_3 \\ 0 & -K_3 & -m\omega^2 + K_3 \end{vmatrix} = 0 \quad 17$$

Therefore:

$$(m\omega^2)^3 - (m\omega^2)^2 [K_1 + 2K_2 + 2K_3] + (m\omega^2) [K_1 K_2 + 2K_1 K_3 + 3K_2 K_3] - K_1 K_2 K_3 = 0 \quad 18$$

with assumed values of D_2 and D_3 equation 18 can be solved for ω as a function of K

Therefore:

$$\omega_1 = \beta_1 (K)^{1/2} \quad 19A$$

$$\omega_2 = \beta_2 (K)^{1/2} \quad 19B$$

$$\omega_3 = \beta_3 (K)^{1/2} \quad 19C$$

A relationship between the A_{ij} 's can now be determined by substituting equations 19 into 16

$$A_{ij} = \gamma_{ij} A_{1j} \text{ no summation} \quad 20A$$

$$\text{and } \gamma_{1j} = 1 \text{ for all } j\text{'s} \quad 20B$$

$$\gamma_{2j} = (-m\omega_j^2 + K_1 + K_2) / K_2 \quad 20C$$

$$\text{and } \gamma_{3j} = K_3 (-m\omega_j^2 + K_1 + K_2) / [K_2 (-m\omega_j^2 + K_3)] \quad 20D$$

$$\eta_{1j} = A_{1j} \sin[\beta_j (K)^{1/2} t + \alpha_j] \text{ no summation} \quad 21A$$

$$\eta_{2j} = A_{1j} \beta_j (K)^{1/2} \cos[\beta_j (K)^{1/2} t + \alpha_j] \quad 21B$$

$$\eta_{3j} = -A_{1j} \beta_j^2 K \sin[\beta_j (K)^{1/2} t + \alpha_j] \text{ no summation} \quad 21C$$

$$Y_i = \gamma_{ij} \eta_{1j} \quad 21D$$

$$\dot{Y}_i = \gamma_{ij} \eta_{2j} \quad 21E$$

$$\ddot{Y}_i = \gamma_{ij} \eta_{3j} \quad 21F$$

From the boundary condition that $\dot{Y}_i(0) = 0$

$$\begin{Bmatrix} 0 \\ 0 \\ 0 \end{Bmatrix} = \begin{bmatrix} \gamma_{11} A_{11} \beta_1 & \gamma_{12} A_{12} \beta_2 & \gamma_{13} A_{13} \beta_3 \\ \gamma_{21} A_{11} \beta_1 & \gamma_{22} A_{12} \beta_2 & \gamma_{23} A_{13} \beta_3 \\ \gamma_{31} A_{11} \beta_1 & \gamma_{32} A_{12} \beta_2 & \gamma_{33} A_{13} \beta_3 \end{bmatrix} \begin{Bmatrix} \cos \alpha_1 \\ \cos \alpha_2 \\ \cos \alpha_3 \end{Bmatrix} \quad 22$$

The determinate of the square matrix cannot be 0

$$\text{Therefore } \cos \alpha_1 = \cos \alpha_2 = \cos \alpha_3 = 0 \quad 23$$

$$\alpha_j = \pi/2$$

Thus

$$\eta_{4j} = A_{1j} \cos \left| \beta_j(K)^{1/2} t \right| \quad \text{no summation} \quad 25A$$

$$\eta_{5j} = -A_{1j} \beta_j(K)^{1/2} \sin \left| \beta_j(K)^{1/2} t \right| \quad \text{no summation} \quad 25B$$

$$\eta_{6j} = -A_{1j} \beta_j^2 K \cos \left| \beta_j(K)^{1/2} t \right| \quad \text{no summation} \quad 25C$$

$$\dot{Y}_i = \gamma_{ij} \eta_{4j} \quad 25D$$

$$\dot{Y}_i = \gamma_{ij} \eta_{5j} \quad 25E$$

$$\ddot{Y}_i = \gamma_{ij} \eta_{6j} \quad 25F$$

From the boundary condition that $Y_i(0) = D_i \Delta$

$$\Delta \begin{Bmatrix} D_1 \\ D_2 \\ D_3 \end{Bmatrix} = \begin{Bmatrix} \gamma_{11} & \gamma_{12} & \gamma_{13} \\ \gamma_{21} & \gamma_{22} & \gamma_{23} \\ \gamma_{31} & \gamma_{32} & \gamma_{33} \end{Bmatrix} \begin{Bmatrix} A_{11} \\ A_{12} \\ A_{13} \end{Bmatrix} \quad 26$$

Therefore:

$$\begin{Bmatrix} A_{11} \\ A_{12} \\ A_{13} \end{Bmatrix} = \Delta^{-1} \begin{Bmatrix} \gamma_{11} & \gamma_{12} & \gamma_{13} \\ \gamma_{21} & \gamma_{22} & \gamma_{23} \\ \gamma_{31} & \gamma_{32} & \gamma_{33} \end{Bmatrix} \begin{Bmatrix} D_1 \\ D_2 \\ D_3 \end{Bmatrix} \quad 27$$

$$\text{or } A_{1j} = \rho_j \Delta \quad 28$$

Substituting 28 into 25

$$\psi_{ij} = \gamma_{ij} \rho_j \quad \text{no summation} \quad 29A$$

$$\epsilon_{ij} = -\gamma_{ij} \rho_j \beta_j \quad \text{no summation} \quad 29B$$

$$\lambda_{ij} = -\gamma_{ij} \rho_j (\beta_j)^2 \quad \text{no summation} \quad 29C$$

$$Y_i = \psi_{ij} \Delta \cos \left| \beta_j(K)^{1/2} t \right| \quad 29D$$

$$\dot{Y}_i = \epsilon_{ij} \Delta (K)^{1/2} \sin \left| \beta_j(K)^{1/2} t \right| \quad 29E$$

$$\ddot{Y}_i = \lambda_{ij} \Delta K \cos \left| \beta_j(K)^{1/2} t \right| \quad 29F$$

From the boundary condition that $\dot{Y}_i(t_a) = E_i V$

$$V \begin{Bmatrix} E_1 \\ E_2 \\ E_3 \end{Bmatrix} = \Delta (K)^{1/2} \begin{Bmatrix} \epsilon_{11} & \epsilon_{12} & \epsilon_{13} \\ \epsilon_{21} & \epsilon_{22} & \epsilon_{23} \\ \epsilon_{31} & \epsilon_{32} & \epsilon_{33} \end{Bmatrix} \begin{Bmatrix} \sin \beta_1(K)^{1/2} t_a \\ \sin \beta_2(K)^{1/2} t_a \\ \sin \beta_3(K)^{1/2} t_a \end{Bmatrix} \quad 30$$

Equation 30 represents 3 equations in 3 unknowns Δ , K , t_a for the assumed values of D_i 's. Therefore:

$$V \left| E \right| = \Delta (K)^{1/2} \left| \epsilon \right| \left| s \right| \quad 31$$

$$V \left| \epsilon \right|^{-1} \left| E \right| = \Delta (K)^{1/2} \left| s \right| \quad 32$$

$$V \left| s \right| = \Delta (K)^{1/2} \left| s \right| \quad 33$$

$$V \sigma_1 = \Delta (K)^{1/2} \sin \beta_1(K)^{1/2} t_a \quad 34A$$

$$V \sigma_2 = \Delta (K)^{1/2} \sin \beta_2(K)^{1/2} t_a \quad 34B$$

$$V \sigma_3 = \Delta (K)^{1/2} \sin \beta_3(K)^{1/2} t_a \quad 34C$$

$$\sigma_1 / \sigma_3 = (\sin \beta_1(K)^{1/2} t_a) / (\sin \beta_3(K)^{1/2} t_a) \quad 35A$$

$$\sigma_2 / \sigma_3 = (\sin \beta_2(K)^{1/2} t_a) / (\sin \beta_3(K)^{1/2} t_a) \quad 35B$$

$$\text{Let } \phi = (K)^{1/2} t_a \quad \zeta_1 = \sigma_1 / \sigma_3 \quad \zeta_2 = \sigma_2 / \sigma_3 \quad 36$$

$$\zeta_1 \sin \beta_3 \phi = \sin \beta_1 \phi \quad 37A$$

$$\zeta_2 \sin \beta_3 \phi = \sin \beta_2 \phi \quad 37B$$

The solution obtained from Equation 30 must be checked to verify that they satisfy the constraints:

$$\text{CONSTRAINTS: } F(t) = F \text{ minimum} \quad 38A$$

$$\text{i.e., } K \Delta \text{ minimum} \quad 38B$$

and at $t = t_a$ mass 3 must be in contact with the tube.

Assume that the compressed length of each spring is equal to its initial deflection, i.e., compressed length_i = $D_i \Delta$

Therefore: The total length of the system at $t = t_a$ is 39

$$\left| D_1 \Delta + (D_2 - D_1) \Delta + (D_3 - D_2) \Delta \right| (= \text{compressed length of springs})$$

$$+ \left| D_3 \Delta \right| \quad (\text{initial displacement of spring system})$$

$$+ Y_3(t_a) + \text{length of mass}_1 + \text{length of mass}_2 \quad 40$$

$$+ \text{length of mass}_3, \text{ that is, in contact with the tube } \leq \text{tube length}$$

$$\text{or } \left| 2D_3 \Delta \right| + Y_3(t_a) + \text{Length due to masses}$$

$$\leq l_{\text{tube}} \quad 41$$

DISCUSSION

The minimum non-zero solution to equation 37A is the relationship required between $(K)^{1/2}$ and t_a for a given set of initial displacement coefficients D_1, D_2 & D_3 . This solution also dictates the value for the product of $(K)^{1/2}$ times Δ which is directly related to the force $F(t)$ at $t \leq 0^-$.

Utilizing the relations of $t_a (K)^{1/2}$ and $\Delta (K)^{1/2}$ for the given D_i 's, with the system constraints, it is possible to determine a satisfactory solution for the problem.

EXAMPLE

In Figure 1, let:

$$l_1 = 2.7 \text{ in}$$

$$l_2 = 0.5 \text{ in}$$

$$l_3 = 2.0 \text{ in}$$

$$l_4 = 2.0 \text{ in}$$

$$l_{\text{tube}} = 7.7 \text{ in}$$

Let

$$v_1 = 60 \text{ in/sec}$$

$$v_2 = 120 \text{ in/sec}$$

$$v_3 = 180 \text{ in/sec}$$

The minimum values for $\Delta (K)^{1/2}$ for a prescribed D_2 (see Equation 6, $Y_2 = D_2 \Delta$) are given in Table 1. Also shown in Table 1 are the values for D_3 and $t_a (K)^{1/2}$ which yield these minimums. The results are depicted graphically in Figures 4 and 5.

An iterative procedure must now be employed to obtain numerical values for each parameter. For an initial trial, assume that the compressed length and the length beyond the equilibrium position of each spring at time t_a is equal to the initial displacement of each spring. Thus, the total length of the system at time t_a is $3D_3\Delta + \text{length of the masses or total length} = 3D_3\Delta + l_2 + l_3 + l_4 = 3D_3\Delta + 4.5$. This must be less than the length of the constraining tube or $3D_3\Delta + 4.5 \leq 7.7$.

$$\text{Therefore: } \Delta \leq 1.067/D_3$$

The lower bound on Δ is determined by the force constraint. That is, $\Delta K \leq 200 \text{ lbs.}$ (Given value)

$$\text{Therefore: } \left[\Delta (K)^{1/2} \right]^2 / \Delta \leq 200 \text{ lbs.}$$

$$\text{or } \Delta \geq \left[\Delta (K)^{1/2} \right]^2 / 200$$

The numerical values for these limits are given in Table 2.

The largest value of Δ for the lowest value of $\Delta (K)^{1/2}$ possible is taken as the first trial solution. Thus, the numerical solution for $(K)^{1/2}$ and t_a can be determined using this Δ and the values of $\Delta (K)^{1/2}$ and $t_a (K)^{1/2}$.

Now, knowing the value of K , the periods of each spring can be evaluated and checked to determine if t_a is sufficiently small so that no mass had a negative velocity at any previous time. Also, the initial assumption for the total length of the system at time t_a can be checked. If a discrepancy is uncovered, then the upper limit on Δ can be reevaluated and the procedure repeated.

Thus, to continue the example, the first trial for Δ is = 0.118. (The largest valid Δ for the smallest $\left[\Delta (K)^{1/2} \right]$). Therefore:

$$D_2 = 7.5$$

$$D_3 = 9.0$$

$$-\Delta (K)^{1/2} = 4.85$$

$$t_a (K)^{1/2} = 0.534$$

Thus:

$$(K)^{1/2} = 41.1$$

$$K = 1689.3 \text{ lbs/in}$$

$$t_a = 0.013 \text{ seconds}$$

Now, to check that t_a is sufficiently small so as to insure that no mass will at any time have a negative velocity, the minimum value of $(K)^{1/2}$ such that $\dot{Y}_i = 0$ is 1.973.

$$\text{Therefore: } t (\dot{Y}_i = 0) = 0.048$$

Thus, t_a is less than $t (t_a < 0.048)$. \therefore O.K.

Check the initial displacement assumption.

$$Y_3(t = t_a) = (K)^{1/2} = t_a (K)^{1/2} = 0.534 = 0.525$$

$$Y_3(t = 0) = D_3 \Delta = 0.0 - (-0.118) = 1.062$$

$$Y_2(t = 0) = D_2 \Delta = 7.5 - (-0.118) = -0.885$$

$$Y_1(t = 0) = D_1 \Delta = -0.118$$

Assumed initial compressed length

$$\begin{aligned} K_1 \Delta + \ell_{\text{mass 1}} &= (K_2 - K_1) \Delta + \ell_{\text{mass 2}} \\ &+ (K_3 - K_2) \Delta + \ell_{\text{mass 3}} = K_3 \Delta + \ell_{\text{mass 1}} \\ &+ \ell_{\text{mass 2}} + \ell_{\text{mass 3}} = 1.062 + 2 + 2 + 0.5 = \\ &5.562 \text{ in.} \end{aligned}$$

Initial displacement

$$= Y_3(t = 0) = 1.062 \text{ in.}$$

Displacement at $t = t_a$

$$= Y_3(t = t_a) = 0.525$$

Therefore: total required length = 7.149

< 7.7 Therefore: O.K.

All the boundary conditions are satisfied and therefore no iteration is necessary.

Thus, this example problem is solved utilizing a three spring system with the following properties.

$$K_1 = 1689 \text{ lbs/in}$$

$$K_2 = 260 \text{ lbs/in}$$

$$K_3 = 1126 \text{ lbs/in}$$

$$\Delta_1 = (\text{initial displacement of mass 1}) \\ = -0.118 \text{ inches.}$$

$$\Delta_2 = (\text{initial displacement of mass 2}) \\ = -0.885 \text{ inches.}$$

$$\Delta_3 = (\text{initial displacement of mass 3}) \\ = -1.062$$

CONCLUSION AND SUMMARY

A system consisting of three springs and three masses joined in series can be employed to dispense objects from a tube with a set of required initial velocities.

The mathematical solution to the problem of determining the spring characteristics and initial displacements within the constraints is an optimization problem. The criterion is either minimization of the allowable

static force required to confine the masses in the tube or a minimization of the total displacement at time of release.

The release of the masses must be performed by means of limiting the stretched lengths of the springs. Each spring can be tied such that it will become disjoint from the adjacent masses at the correct time.

TABLE 1

D_2	D_3	$-\Delta(K)^{1/2}$	$t_a(K)^{1/2}$
2.5	3.5	8.22	0.723
3.0	4.0	7.23	0.675
3.5	5.0	6.42	0.691
4.0	5.5	5.93	0.660
4.5	6.0	5.64	0.630
5.0	6.5	5.27	0.628
5.5	7.0	5.20	0.597
6.0	7.5	5.16	0.569
6.5	8.0	4.97	0.565
7.0	8.5	5.00	0.538
7.5	9.0	4.85	0.534
8.0	9.5	4.89	0.511
8.5	10.0	4.82	0.503
9.0	10.5	4.68	0.503
9.5	11.0	4.78	0.477
10.0	11.5	4.71	0.471

TABLE 2

D_2	D_3	$\left[\Delta(K)^{1/2}\right]^2 / 200$	$1.067/D_3$
2.5	3.5	0.338	0.305
3.0	4.0	0.261	0.267
3.5	5.0	0.206	0.213
4.0	5.5	0.175	0.194
4.5	6.0	0.159	0.178
5.0	6.5	0.139	0.164
5.5	7.0	0.135	0.152
6.0	7.5	0.133	0.142
6.5	8.0	0.124	0.133
7.0	8.5	0.125	0.126
7.5	9.0	0.118	0.119
8.0	9.5	0.119	0.112
8.5	10.0	0.116	0.107
9.0	10.5	0.110	0.102
9.5	11.0	0.114	0.097
10.0	11.5	0.111	0.093

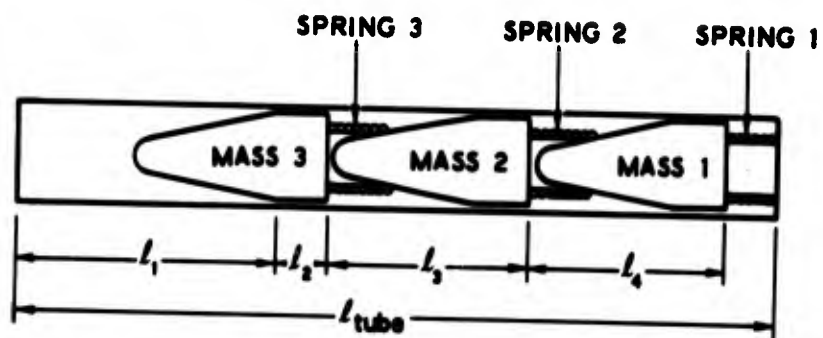


FIGURE 1

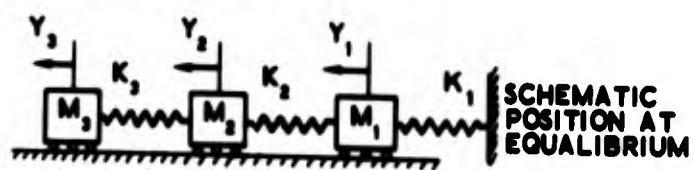


FIGURE 2

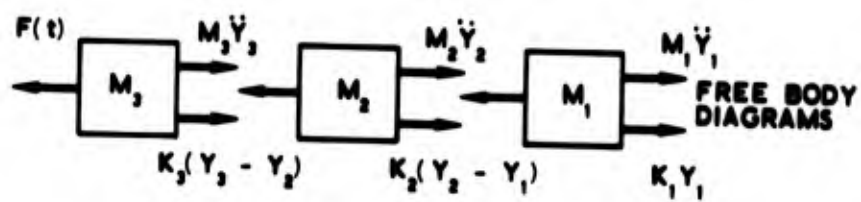


FIGURE 3

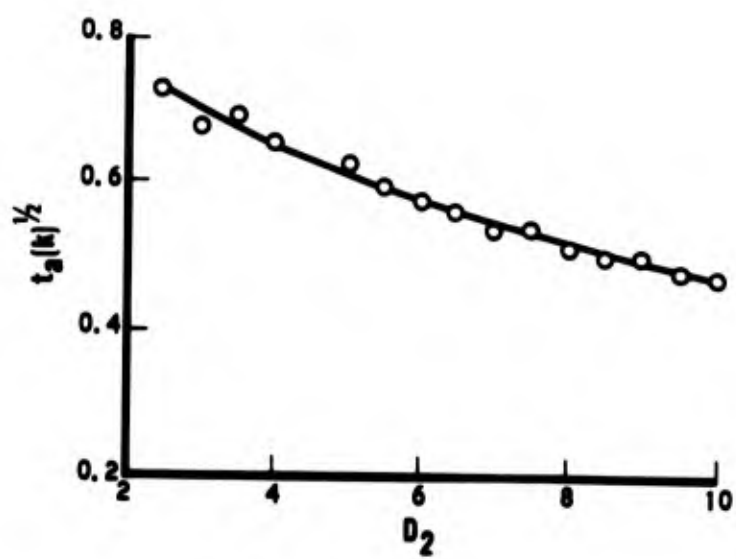


FIGURE 4

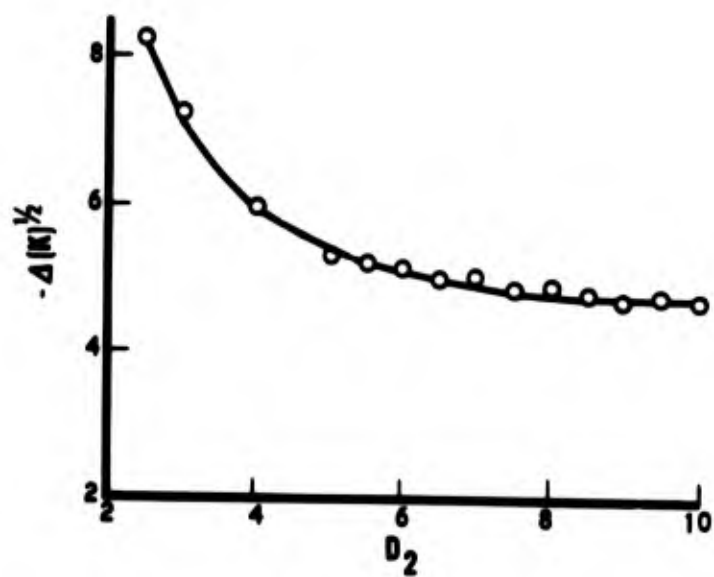


FIGURE 5

BLANK PAGE

STRUCTURAL DYNAMICS OF A PARABOLOIDAL ANTENNA

Myron L. Gossard and William B. Halle, Jr.
Lockheed Missiles & Space Company
Sunnyvale, California

The antenna consists of a number of flexible, parabolically curved ribs which project radially from a central hub and which are interconnected by a lightweight, reflecting mesh. To study the dynamic behavior of such a structure, finite element methods are used to generate inertia and stiffness coefficients that form the basis of an eigenproblem for the natural frequencies and modes of the antenna, which are the objects of the analysis herein. A preliminary Fourier decomposition of the problem is made in the antenna's circumferential direction. Thereby, two kinds of computational difficulty are avoided: (1) the large and unwieldy original problem is separated into a number of relatively small and independent problems, and (2) the need is removed to cope with an R -fold redundant repetition of frequencies and modes that would ordinarily occur for the R -ribbed axisymmetric structure.

INTRODUCTION

The antenna under specific consideration is designed for deployment and use in space after being carried there in a compactly stowed condition. The structure consists typically of a circular paraboloidal reflector fabricated of hub, ribs, and mesh. The ribs and mesh are wrapped around the hub in stowage, and the strain energy thus accumulated powers the deployment operation.

This paper describes an analytical procedure for a digital computation program to obtain the natural modes and frequencies of vibration of the antenna when deployed and free in space. Numerical results for a representative structure are given in computer-drawn graphical displays.

Antennas of the flex-rib design are becoming increasingly popular [1-3]. However, no dynamic analysis has been found which treats the structure in a complete manner.

GENERAL CONSIDERATIONS

The arrangement of the actual reflector is sketched in Fig. 1. The analytical model, shown in Figs. 2 and 3, idealizes the structure into finite beam and string elements. Geometric axes consist of an $X Y Z$ inertial reference frame, and local $x y z$ axes at analytical points on the ribs as shown. The small displacements $\xi, \eta, \zeta, \phi, \theta, \psi$ in and about the local $x y z$ directions and relative to the inertial frame, in natural vibration, are the objects of the analysis.

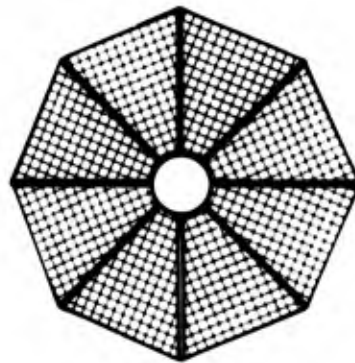


Fig. 1 - Deployed antenna

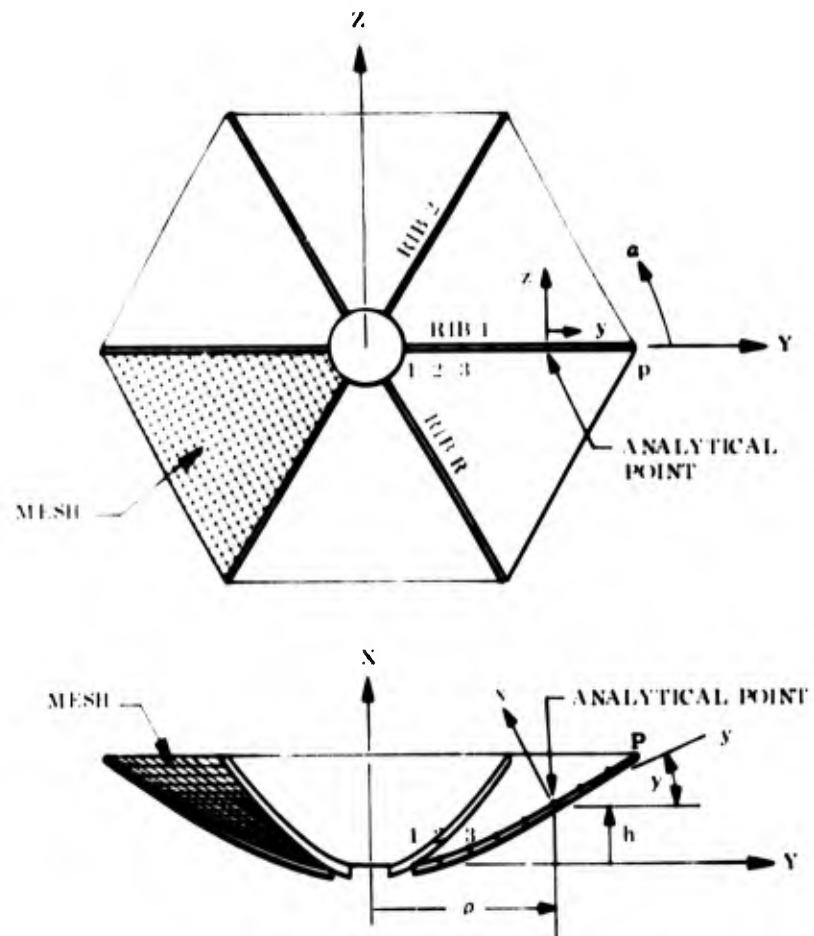


Fig. 2 - Reflector detail and coordinates

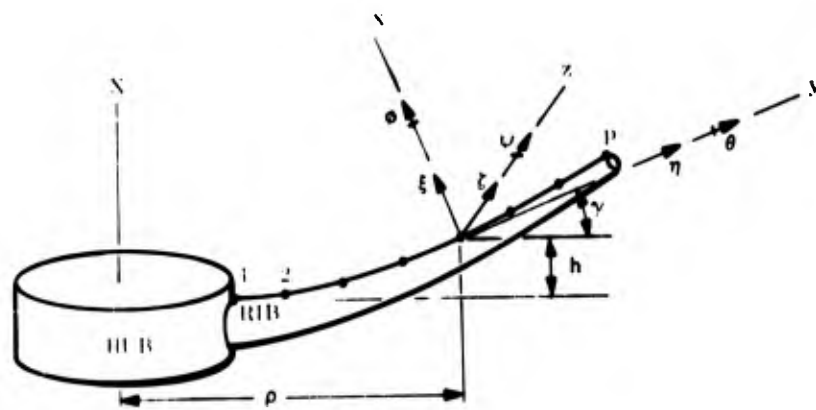


Fig. 3 - Degrees of freedom of typical rib

In order that the mesh remain taut under general deformation, the system is put under a state of self-equilibrating initial stress, such that membrane type stress deviations during vibration are an order of magnitude smaller than initial values. Stiffness properties are linearized about the initial state. Consistent results under the linearization can be obtained only when the geometric stiffening (a brief but somewhat ambiguous term for the stiffening effect of pre-stress) is accounted for throughout the structure - in hub, ribs, and mesh. Thus, the buckling tendencies of hub and ribs, which might otherwise be ignorable, must be incorporated when the counter-activity of mesh is present and vital, as is likely in very large and flexible structures.

The difficulties of dealing with geometric stiffness is offset, however, by the axisymmetry of the configuration and the attendant ability to classify the natural vibrations according to circumferential wave numbers. Indeed, such classification is mandatory for avoiding two kinds of computational difficulty. First, and most obvious, is the size of the problem in terms of degrees of freedom. When the ribs are divided into $P-1$ finite elements using P analytical points on each rib, and each point is allowed 6 degrees of freedom, then each rib will have $6P \times 6P$ mass and stiffness coefficients. The reflector with R ribs then constitutes a problem of size $6PR \times 6PR$ which can be very large. Secondly, unless special precautions are taken in advance, the computer would seek solutions having an R -fold repetition of frequencies and modes. Even if the computer could deal with such a situation, which it cannot, the information thus produced would be mostly redundant. This multiplicity of eigensolutions and the excessive size of problem are both avoided by prior separation of the overall motion into Fourier components in the circumferential direction. The natural motions associated with each component (or wave number) are uncoupled with other components, and thus a series of relatively small and well behaved problems replaces the large original problem.

THEORETICAL DEVELOPMENT

We now put the foregoing ideas into computer-oriented quantitative form by surveying briefly the following aspects of the problem: (1) primitive dynamic properties, (2) Fourier decomposition in the circumferential direction, (3) modal properties in each Fourier wave, and (4) generation of primitive mass and stiffness coefficients from basic finite element data.

Primitive Dynamic Properties

The matrix equation of natural vibration, in the Cartesian coordinates shown in Figs. 2 and 3 may be written as

$$[m] \ddot{\delta} + [k] \delta = \{0\}.$$

For brevity, damping is omitted. Here, δ is the displacement column vector covering all degrees of freedom at all analytical points on the antenna. The subvectors δ each pertain to a particular rib. Thus, in row vector form to conserve space,

$$\{\delta\} = \{\delta\}^1, \{\delta\}^2, \dots, \{\delta\}^R$$

where, for example in the case of rib 1,

$$\{\delta\}^1 = \{\xi, \eta, r, \phi, \theta, \psi\}^1, \{\xi, \eta, r, \phi, \theta, \psi\}^2, \dots, \{\xi, \eta, r, \phi, \theta, \psi\}^P.$$

Here, each δ is of size $6P \times 1$, with elements arranged first by point and then by degree of freedom. The mass and stiffness matrices $[m]$ and $[k]$ are subdivided and arranged to be compatible with δ , and are for present purposes assumed to be known, either from measurements or from computation similar to that described in the final section. Their form is typified by the stiffness matrix, which is

$$[k] = \begin{bmatrix} [k]_1^1, [k]_1^2 & & [k]_1^R \\ [k]_2^1, [k]_2^2, [k]_2^3 & & \\ & [k]_3^2, [k]_3^3, [k]_3^4 & \\ & & \ddots & \\ & & & [k]_{R-1}^{R-2}, [k]_{R-1}^{R-1}, [k]_{R-1}^R \\ [k]_R^1 & & & [k]_R^{R-1}, [k]_R^R \end{bmatrix}$$

Each submatrix $[k]$ is of size $6P \times 6P$. The stiffness matrix is symmetric (by Maxwell's reciprocity conditions) and singular (in that its product with each of six rigid-body displacement vectors is zero). Moreover, because of axisymmetry of the antenna,

$$\begin{aligned} [k]_1^1 &= [k]_2^2 = [k]_3^3 = \dots = [k]_R^R \\ [k]_R^1 &= [k]_1^2 = [k]_2^3 = \dots = [k]_{R-1}^R \\ [k]_1^R &= [k]_2^1 = [k]_3^2 = \dots = [k]_R^{R-1} \end{aligned}$$

and similarly for the mass matrix, which is also symmetric.

Fourier Decomposition

Next, the antenna displacements are expressed as a finite Fourier series (finite because the number of ribs R is finite) having coefficients that are displacement vectors to be determined by the dynamical conditions of the problem. This expansion is

$$\delta = [T] \bar{\delta}$$

where the Fourier trigonometric matrix $[T]$ is

with N and M given by

wherein

for $i = 0, M$

for $i = 1, 2, 3, \dots, N$

and similarly for the mass matrix $|\bar{m}|$. Hence, the natural vibrations are to be obtained by solving the independent sets

$$= \begin{vmatrix} 0 \\ 0 \end{vmatrix}, \quad i = 1, 2, 3, \dots, N.$$

It is now evident that the Fourier decomposition has supplanted the original problem of size $6PR \times$

106

GPR with $(R-2)/2$ or $(R-1)/2$ (as R is even or odd) problems of size $12P \times 12P$, except for wave numbers 0 and M which are of size $6P \times 6P$. In practice, only the first several wave numbers are ordinarily of interest. It is observed that the six rigid-body modes of the antenna will be found among the modes for wave numbers 0 and 1: two modes in wave 0, corresponding to rigid-body displacements in and about the X direction; four modes in wave 1, corresponding to rigid-body displacements in and about the Y and Z directions.

Modal Properties in Each Fourier Wave

The final step requires solution of the eigenproblems that belong to the various circumferential waves. These eigenproblems are

$$-\omega_{Ci}^2 [\bar{m}]_{Ci}^T \hat{\delta}_{Ci} - [\bar{k}]_{Ci}^T \hat{\delta}_{Ci} = 0, \quad i = 0, M$$

$$-\omega_{Csi}^2 \begin{bmatrix} [\bar{m}]_{Ci}^T, [\bar{m}]_{Si}^T \\ [\bar{m}]_{Ci}^T, [\bar{m}]_{Si}^T \end{bmatrix} \begin{bmatrix} \hat{\delta}_{Ci} \\ \hat{\delta}_{Si} \end{bmatrix} = 0, \quad i = 1, 2, 3, \dots, N.$$

Their solutions may be expressed as

$$\begin{bmatrix} \hat{\delta}_{Ci} \end{bmatrix} = \text{modal matrix,}$$

$$[\omega]_{Ci} = \text{frequency matrix, for } i = 0, M$$

$$\begin{bmatrix} \begin{bmatrix} \hat{\delta}_{Ci} \\ \hat{\delta}_{Si} \end{bmatrix} \end{bmatrix} = \text{modal matrix,}$$

$$[\omega]_{Csi} = \text{frequency matrix,}$$

$$\text{for } i = 1, 2, 3, \dots, N.$$

These results may be used in a final transformation of coordinates that yields a completely independent equation of natural vibration for each of the antenna modes in each wave class. Thus, if we put

$$|\hat{\delta}|_{Ci} = \begin{bmatrix} \hat{\delta}_{Ci} \end{bmatrix} |q|_{Ci}, \quad i = 0, M$$

$$\begin{bmatrix} |\hat{\delta}|_{Ci} \\ |\hat{\delta}|_{Si} \end{bmatrix} = \begin{bmatrix} \begin{bmatrix} \hat{\delta}_{Ci} \end{bmatrix} \\ \begin{bmatrix} \hat{\delta}_{Si} \end{bmatrix} \end{bmatrix} |q|_{Csi}, \quad i = 1, 2, 3, \dots, N$$

where the $|q|$ are generalized displacement coordinates, then in consequence of the familiar orthogonality properties of the eigensolutions, the equations in the various wave classes transform to

$$[M]_{Ci}^T \ddot{q}_{Ci} + [K]_{Ci}^T q_{Ci} = 0, \quad i = 0, M$$

$$[M]_{Csi}^T \ddot{q}_{Csi} + [K]_{Csi}^T q_{Csi} = 0, \quad i = 1, 2, 3, \dots, N.$$

The $[M]$ and $[K]$ are diagonal generalized mass and stiffness matrices related to the $[\bar{m}]$ and $[\bar{k}]$ by

$$[M]_{Ci}^T = \begin{bmatrix} \begin{bmatrix} \hat{\delta}_{Ci} \end{bmatrix} \end{bmatrix}^T [\bar{m}]_{Ci}^T \begin{bmatrix} \begin{bmatrix} \hat{\delta}_{Ci} \end{bmatrix} \end{bmatrix}_{Ci}$$

$$[K]_{Ci}^T = \begin{bmatrix} \begin{bmatrix} \hat{\delta}_{Ci} \end{bmatrix} \end{bmatrix}^T [\bar{k}]_{Ci}^T \begin{bmatrix} \begin{bmatrix} \hat{\delta}_{Ci} \end{bmatrix} \end{bmatrix}_{Ci}$$

$$[M]_{Csi}^T = \begin{bmatrix} \begin{bmatrix} \hat{\delta}_{Ci} \\ \hat{\delta}_{Si} \end{bmatrix} \end{bmatrix}^T \begin{bmatrix} [\bar{m}]_{Ci}^T, [\bar{m}]_{Si}^T \\ [\bar{m}]_{Ci}^T, [\bar{m}]_{Si}^T \end{bmatrix} \begin{bmatrix} \begin{bmatrix} \hat{\delta}_{Ci} \\ \hat{\delta}_{Si} \end{bmatrix} \end{bmatrix}_{Csi}$$

$$[K]_{Csi}^T = \begin{bmatrix} \begin{bmatrix} \hat{\delta}_{Ci} \\ \hat{\delta}_{Si} \end{bmatrix} \end{bmatrix}^T \begin{bmatrix} [\bar{k}]_{Ci}^T, [\bar{k}]_{Si}^T \\ [\bar{k}]_{Ci}^T, [\bar{k}]_{Si}^T \end{bmatrix} \begin{bmatrix} \begin{bmatrix} \hat{\delta}_{Ci} \\ \hat{\delta}_{Si} \end{bmatrix} \end{bmatrix}_{Csi}$$

$$i = 1, 2, 3, \dots, N.$$

Of ultimate interest in this paper are the antenna frequencies, and the corresponding modes of natural vibration in terms of displacements $\xi, \eta, \zeta, \phi, \theta, \psi$ in the local $x y z$ directions at each of the analytical points $1, 2, 3, \dots, P$ on all of the ribs. The natural frequencies, as noted previously, come from the eigensolutions as

$$\begin{aligned}
 & \begin{bmatrix} C_1 \\ C_2 \\ \vdots \\ C_M \end{bmatrix} = \begin{bmatrix} C_1 \\ C_2 \\ \vdots \\ C_M \end{bmatrix} \begin{bmatrix} 1 & 0 & \dots & 0 \\ 0 & 1 & \dots & 0 \\ \vdots & \vdots & \ddots & \vdots \\ 0 & 0 & \dots & 1 \end{bmatrix} \begin{bmatrix} 1 \\ 0 \\ \vdots \\ 0 \end{bmatrix} \\
 & \begin{bmatrix} C_{Si} \\ C_{Si} \\ \vdots \\ C_{Si} \end{bmatrix} = \begin{bmatrix} C_{Si} \\ C_{Si} \\ \vdots \\ C_{Si} \end{bmatrix} \begin{bmatrix} 1 & 0 & \dots & 0 \\ 0 & 1 & \dots & 0 \\ \vdots & \vdots & \ddots & \vdots \\ 0 & 0 & \dots & 1 \end{bmatrix} \begin{bmatrix} 1 \\ 0 \\ \vdots \\ 0 \end{bmatrix}, \quad i = 1, 2, 3, \dots, N.
 \end{aligned}$$

The full antenna modes are obtained by applying the trigonometric transformation, namely,

$$\begin{aligned}
 & \begin{bmatrix} \hat{\delta} \end{bmatrix}_{C_1} = \begin{bmatrix} T \end{bmatrix} \begin{bmatrix} \hat{\delta} \end{bmatrix}_{C_1}, \quad i = 0, M \\
 & \begin{bmatrix} \hat{\delta} \end{bmatrix}_{C_{Si}} = \begin{bmatrix} T \end{bmatrix} \begin{bmatrix} \begin{bmatrix} \hat{\delta} \end{bmatrix}_{C_1} \\ \begin{bmatrix} \hat{\delta} \end{bmatrix}_{Si} \end{bmatrix}, \quad i = 1, 2, 3, \dots, N
 \end{aligned}$$

or, in somewhat expanded form,

$$\begin{aligned}
 & \begin{bmatrix} \begin{bmatrix} \hat{\delta} \end{bmatrix}_1^1 & \begin{bmatrix} \hat{\delta} \end{bmatrix}_1^2 & \begin{bmatrix} \hat{\delta} \end{bmatrix}_1^3 & \dots \\ \begin{bmatrix} \hat{\delta} \end{bmatrix}_2^1 & \begin{bmatrix} \hat{\delta} \end{bmatrix}_2^2 & \begin{bmatrix} \hat{\delta} \end{bmatrix}_2^3 & \vdots \\ \vdots & \vdots & \vdots & \vdots \\ \begin{bmatrix} \hat{\delta} \end{bmatrix}_R^1 & \begin{bmatrix} \hat{\delta} \end{bmatrix}_R^2 & \begin{bmatrix} \hat{\delta} \end{bmatrix}_R^3 & \vdots \end{bmatrix} \\
 & \begin{bmatrix} 1 \\ 1 \\ \vdots \\ 1 \end{bmatrix} \begin{bmatrix} \cos i\alpha_1 \\ \cos i\alpha_2 \\ \vdots \\ \cos i\alpha_R \end{bmatrix} \begin{bmatrix} \begin{bmatrix} \hat{\delta} \end{bmatrix}_1^1 & \begin{bmatrix} \hat{\delta} \end{bmatrix}_1^2 & \begin{bmatrix} \hat{\delta} \end{bmatrix}_1^3 & \dots \\ \begin{bmatrix} \hat{\delta} \end{bmatrix}_2^1 & \begin{bmatrix} \hat{\delta} \end{bmatrix}_2^2 & \begin{bmatrix} \hat{\delta} \end{bmatrix}_2^3 & \vdots \\ \vdots & \vdots & \vdots & \vdots \\ \begin{bmatrix} \hat{\delta} \end{bmatrix}_R^1 & \begin{bmatrix} \hat{\delta} \end{bmatrix}_R^2 & \begin{bmatrix} \hat{\delta} \end{bmatrix}_R^3 & \vdots \end{bmatrix}_{C_1}, \quad i = 0, M
 \end{aligned}$$

$$\begin{bmatrix} \begin{bmatrix} \hat{\delta} \end{bmatrix}_1^1 & \begin{bmatrix} \hat{\delta} \end{bmatrix}_1^2 & \begin{bmatrix} \hat{\delta} \end{bmatrix}_1^3 & \dots \\ \begin{bmatrix} \hat{\delta} \end{bmatrix}_2^1 & \begin{bmatrix} \hat{\delta} \end{bmatrix}_2^2 & \begin{bmatrix} \hat{\delta} \end{bmatrix}_2^3 & \vdots \\ \vdots & \vdots & \vdots & \vdots \\ \begin{bmatrix} \hat{\delta} \end{bmatrix}_R^1 & \begin{bmatrix} \hat{\delta} \end{bmatrix}_R^2 & \begin{bmatrix} \hat{\delta} \end{bmatrix}_R^3 & \vdots \end{bmatrix}_{C_{Si}}$$

$$\begin{aligned}
 & \begin{bmatrix} 1 \\ 1 \\ \vdots \\ 1 \end{bmatrix} \begin{bmatrix} \cos i\alpha_1 \\ \cos i\alpha_2 \\ \vdots \\ \cos i\alpha_R \end{bmatrix} \begin{bmatrix} 1 \\ 1 \\ \vdots \\ 1 \end{bmatrix} \\
 & \begin{bmatrix} \begin{bmatrix} \hat{\delta} \end{bmatrix}_1^1 & \begin{bmatrix} \hat{\delta} \end{bmatrix}_1^2 & \begin{bmatrix} \hat{\delta} \end{bmatrix}_1^3 & \dots \\ \begin{bmatrix} \hat{\delta} \end{bmatrix}_2^1 & \begin{bmatrix} \hat{\delta} \end{bmatrix}_2^2 & \begin{bmatrix} \hat{\delta} \end{bmatrix}_2^3 & \vdots \\ \vdots & \vdots & \vdots & \vdots \\ \begin{bmatrix} \hat{\delta} \end{bmatrix}_R^1 & \begin{bmatrix} \hat{\delta} \end{bmatrix}_R^2 & \begin{bmatrix} \hat{\delta} \end{bmatrix}_R^3 & \vdots \end{bmatrix}_{C_1} \\
 & \begin{bmatrix} \begin{bmatrix} \hat{\delta} \end{bmatrix}_1^1 & \begin{bmatrix} \hat{\delta} \end{bmatrix}_1^2 & \begin{bmatrix} \hat{\delta} \end{bmatrix}_1^3 & \dots \\ \begin{bmatrix} \hat{\delta} \end{bmatrix}_2^1 & \begin{bmatrix} \hat{\delta} \end{bmatrix}_2^2 & \begin{bmatrix} \hat{\delta} \end{bmatrix}_2^3 & \vdots \\ \vdots & \vdots & \vdots & \vdots \\ \begin{bmatrix} \hat{\delta} \end{bmatrix}_R^1 & \begin{bmatrix} \hat{\delta} \end{bmatrix}_R^2 & \begin{bmatrix} \hat{\delta} \end{bmatrix}_R^3 & \vdots \end{bmatrix}_{Si}, \quad i = 1, 2, 3, \dots, N.
 \end{aligned}$$

Generation of Primitive Properties

As essential part of the dynamics is the accurate description of primitive mass and stiffness properties. This task is especially demanding when, as in the present case, the number of freedoms must be held to a minimum because of computer limitations. Details of the procedure will be omitted here in favor of brief remarks concerning the view taken in assembling the parts of the problem.

The antenna structure is considered to be composed of finite beam and panel elements whose boundaries and junctions are defined by the analytical points on the ribs. The analytical points may be variably spaced on a rib but are identically spaced on all ribs. The beam elements, covering ribs and hub, are prismatic with geometries, rigidities, and mass intensities that are averages of the actual values between analytical points. Elastic stiffness relations are derived in six degrees of freedom at each end, including effects of stretching, torsion, shearing, and bending for cross sections of arbitrary shape. Deflection shapes between analytical points that are associated with the elastic stiffness are used in an energy formulation to account approximately for the geometric stiffnesses arising from the pre-stress system; in this way buckling loads may be known and buckling tendencies represented. The elastic deflection shapes are also used in an energy method to obtain equivalent concentrated masses at the beam element ends, including rotatory inertia contributions.

For the mesh, consider a typical panel, say panel $i, j, 1, 2$, where i, j are two consecutive ribs and $1, 2$ are analytical points on the ribs. Stress in the mesh is assumed to be confined to tension in the i, j direction, and the mesh is therefore treated as being made of a group of parallel, closely packed strings running in the i, j direction. The strings remain straight, while displacements of their ends are identical with the rib-segment displacements. By use of the elastic deflection shapes in the energy method, sets of equivalent stiffness and masses in six degrees of freedom at each of the four corners of the mesh panel are derived, the stiffnesses being of both the elastic and geometric varieties.

The stiffness and mass coefficients just described are defined with respect to local axis systems at the analytical points that are aligned with the principal directions of the individual straight rib and hub segments. A final step resolves all displacements and forces into directions that are normal and tangential at the analytical points to the parabolically curved ribs and their planes.

The results of these numerous manipulations are the primitive stiffness and mass properties. The relations are of the forms

$$|F|_j = \begin{bmatrix} [k]_j^i & [k]_j^j & [k]_j^k \end{bmatrix} \begin{bmatrix} \delta|_i \\ \delta|_j \\ \delta|_k \end{bmatrix}, \text{ for stiffness}$$

$$|F|_j = \begin{bmatrix} [m]_j^i & [m]_j^j & [m]_j^k \end{bmatrix} \begin{bmatrix} \ddot{\delta}|_i \\ \ddot{\delta}|_j \\ \ddot{\delta}|_k \end{bmatrix}, \text{ for inertia}$$

where $|F|_j$ are the load components on the analytical points of mid-rib j that must accompany displacement or acceleration components $|\delta|$ or $|\ddot{\delta}|$ of analytical points on the three consecutive ribs i, j, k . By virtue of the axisymmetry, these relations described completely the stiffness and mass properties of the entire antenna. Submatrices $[k]_j$, $[m]_j$, etc. each have the common form

$$\begin{bmatrix} [B]_1^1, [B]_1^2 \\ [B]_2^1, [B]_2^2, [B]_2^3 \\ [B]_3^2, [B]_3^3, [B]_3^4 \\ \vdots \\ [B]_{p-1}^{p-2}, [B]_{p-1}^{p-1}, [B]_{p-1}^p \\ [B]_p^{p-1}, [B]_p^p \end{bmatrix}$$

where indices $1, 2, 3, \dots, p$ refer to the analytical points. Matrices $[k]_j$ and $[m]_j$ are symmetric, whereas $[k]_j^k = [k]_j^i$ and $[m]_j^k = [m]_j^i$ are not symmetric. Submatrices $[B]$ are size 6×6 , and are constants that depend on the geometry, the elasticities and densities of material, and the state of pre-stress.

NUMERICAL RESULTS

The following five figures, nos. 4, 5, 6, 7, and 8 are computer drawn displays of mode shapes for a

24-rib antenna. Necessary calculations were done by computer for the analysis described herein, beginning with raw data in the form of rib, mesh, and hub elasticities, densities, and geometry. Though a total of 25 modes were found for the example antenna, only five are shown here as being representative. They are modes 1, 2, and 3 for wave number 0 and the first mode for wave numbers 2 and 3. In all cases, the antenna was free in space so that six rigid body modes were included in the set. Notice that in Figs. 5 and 6 rather complex rib motion is taking place because each rib is of open section with offset shear center and with the mesh connected along the concave edge of the rib.

REFERENCES

1. "Space Erectable Large Aperture Reflectors," LMSC-A946613, 26 Mar. 1969, Lockheed Missiles & Space Company, Sunnyvale, Calif.
2. "Proposal for ATS F and G Parabolic Reflector Subsystem," LMSC-A955288, 30 Jul. 1969, Lockheed Missiles & Space Company, Sunnyvale, Calif.
3. F. A. Florio and A. T. Josloff, "Thermo/Structural Analysis of a Large Flexible Paraboloid Antenna," AIAA/ASME 9th Structures, Structural Dynamics and Materials Conference, 1-3 Apr. 1968, AIAA Paper No. 68-333

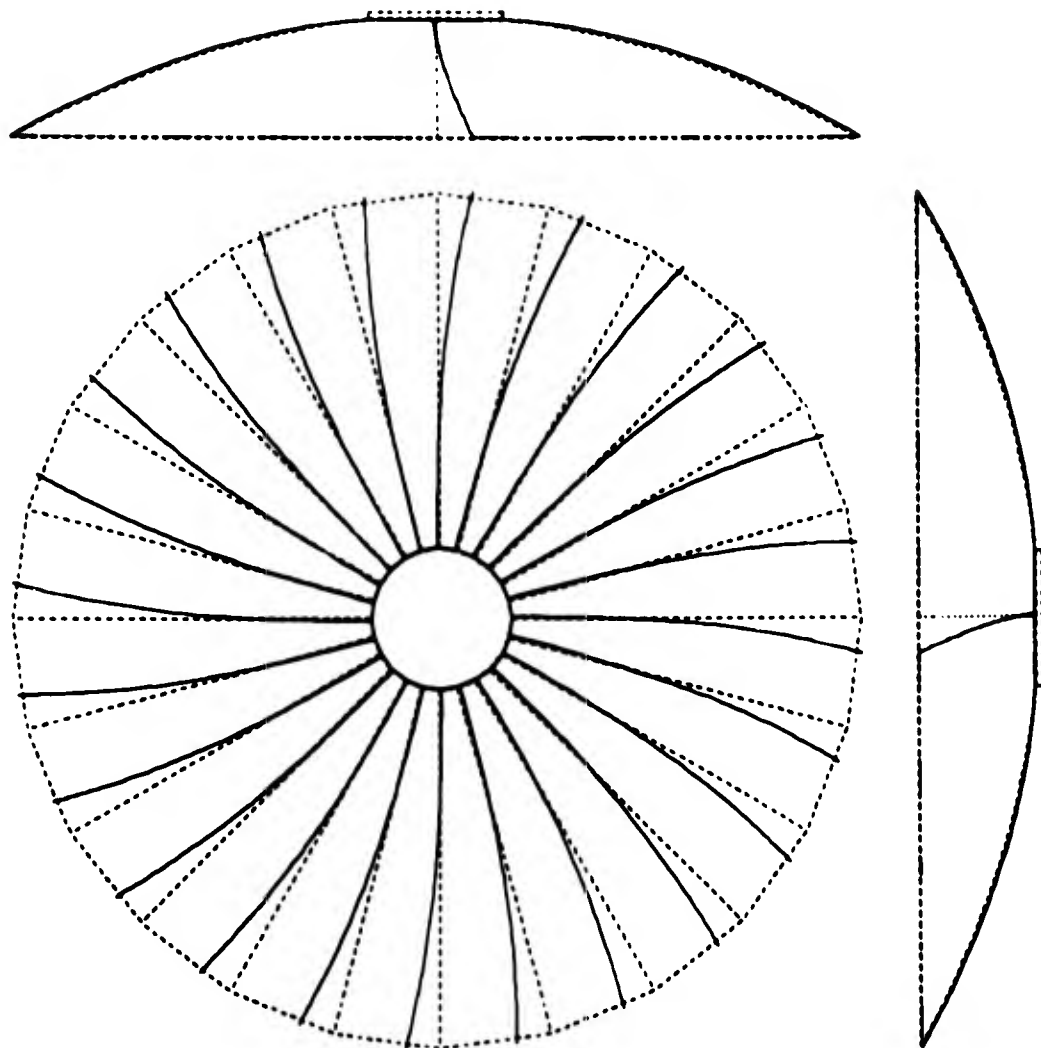


Fig. 4 - Antenna mode shape
 $\omega_1 = 1.40 \text{ CPS}$

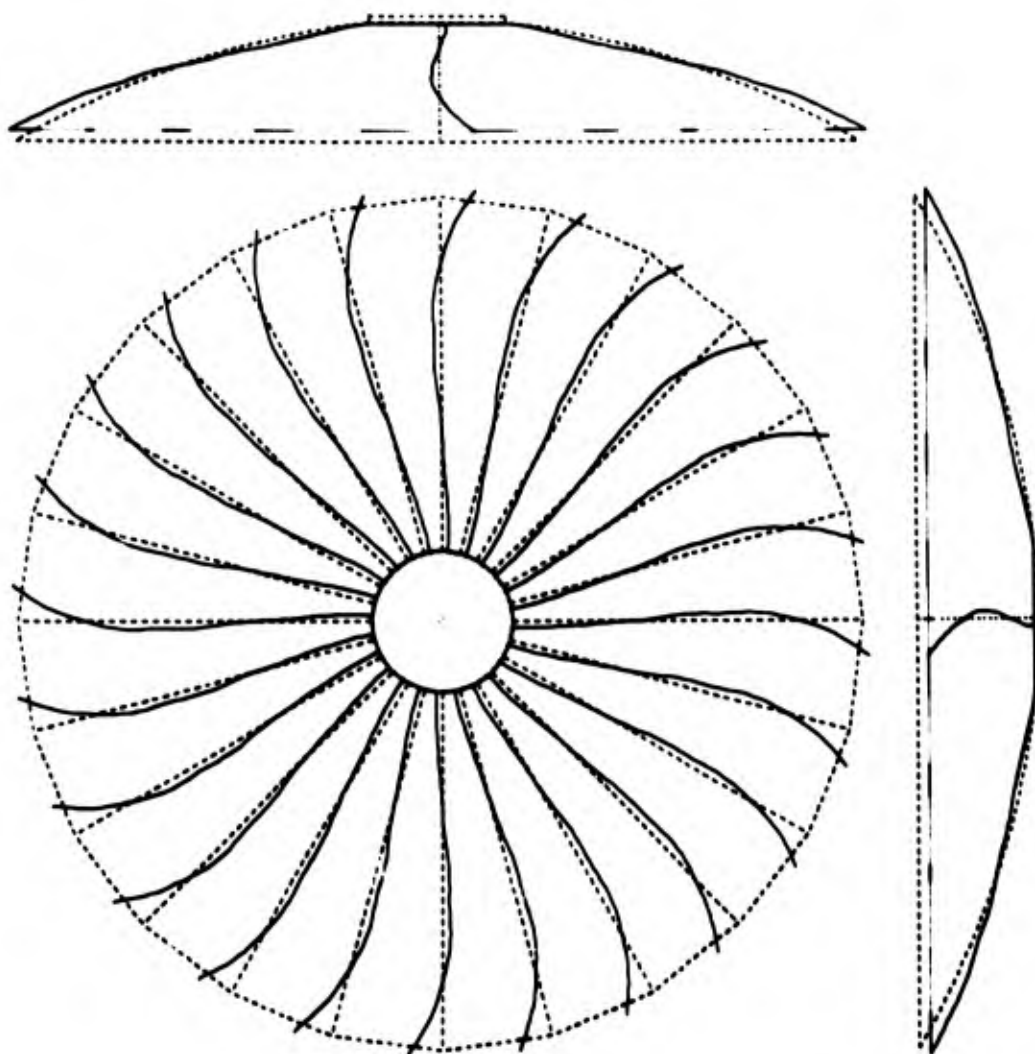


Fig. 5 - Antenna mode shape
 $\omega_2 = 9.26 \text{ CPS}$

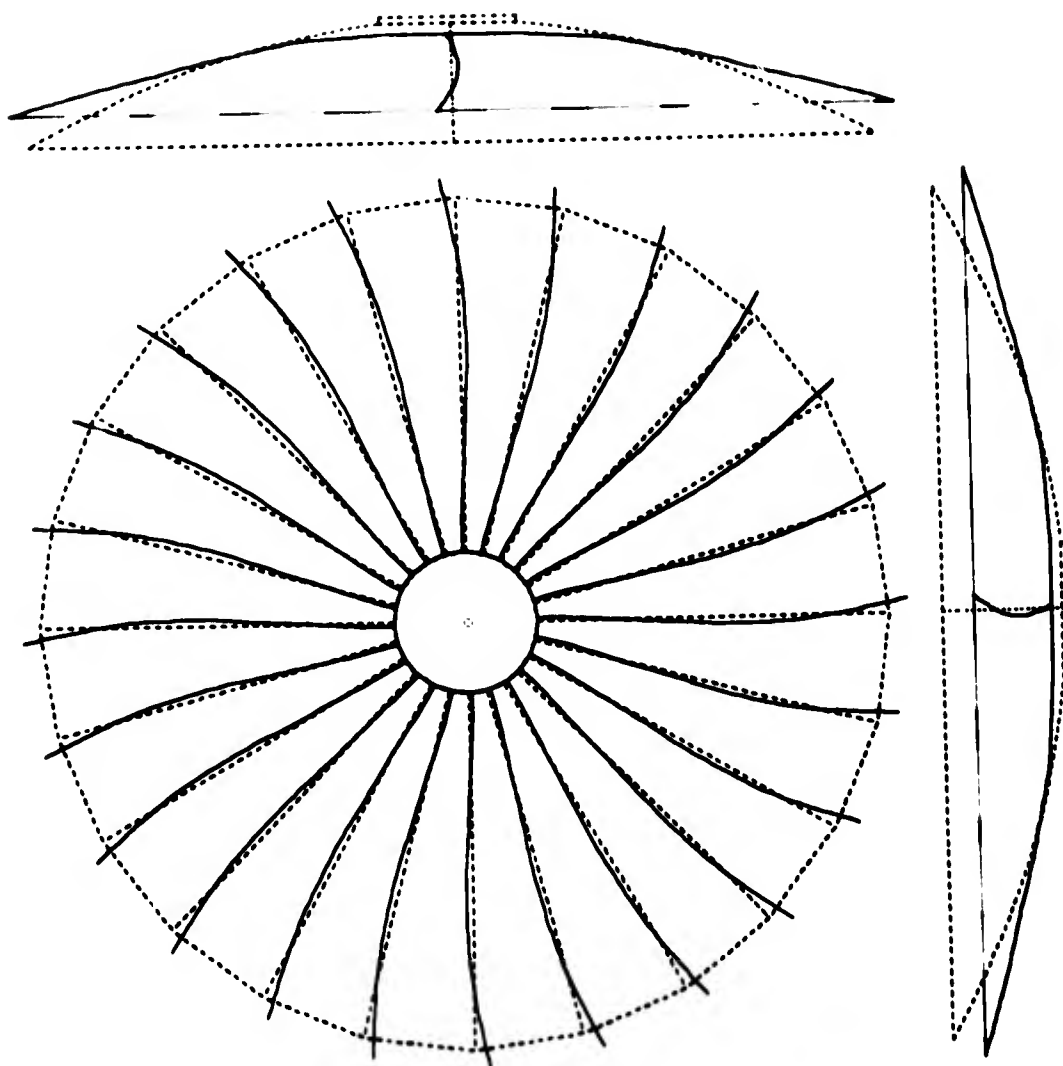


Fig. 6 - Antenna mode shape
 $\omega_3 = 15.21$ CPS

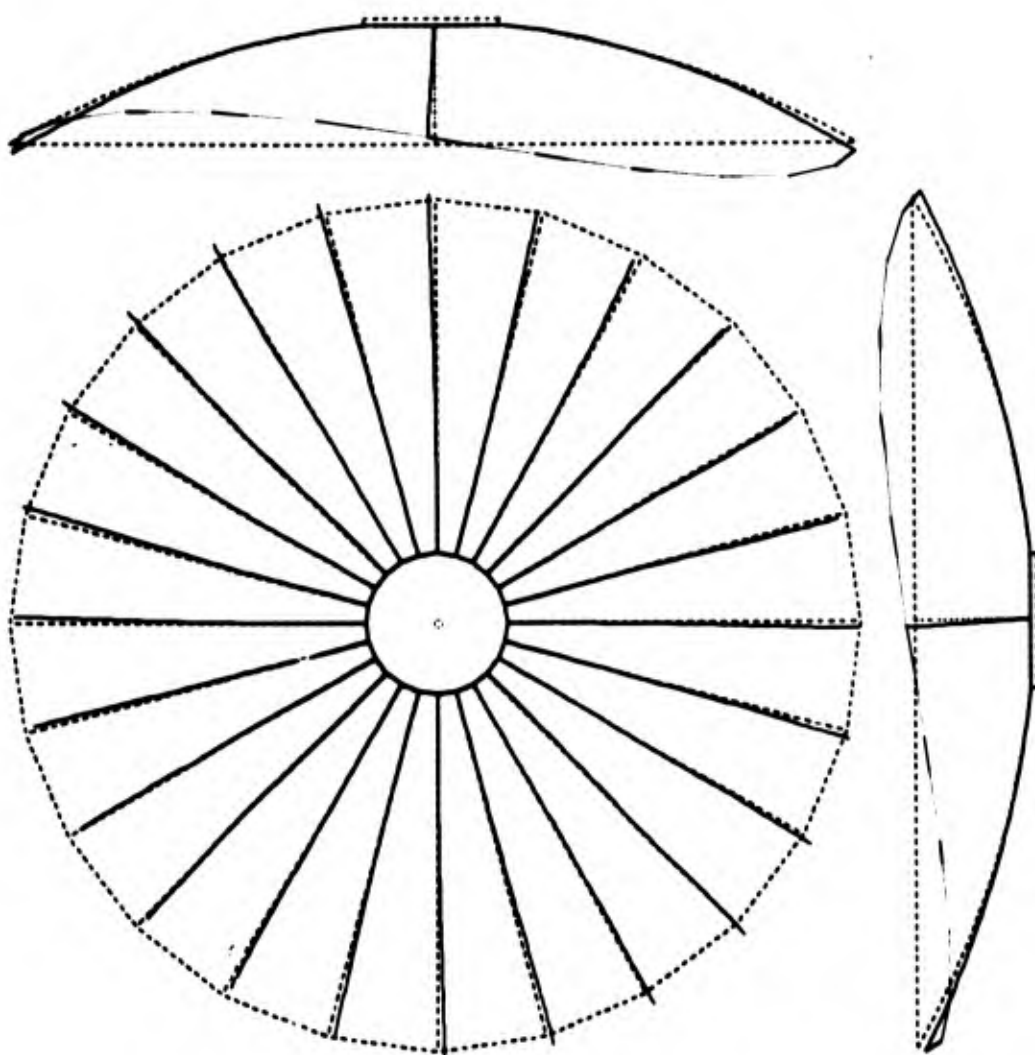


Fig. 7 - Antenna mode shape
 $\omega_1 = 8.04$ CPS

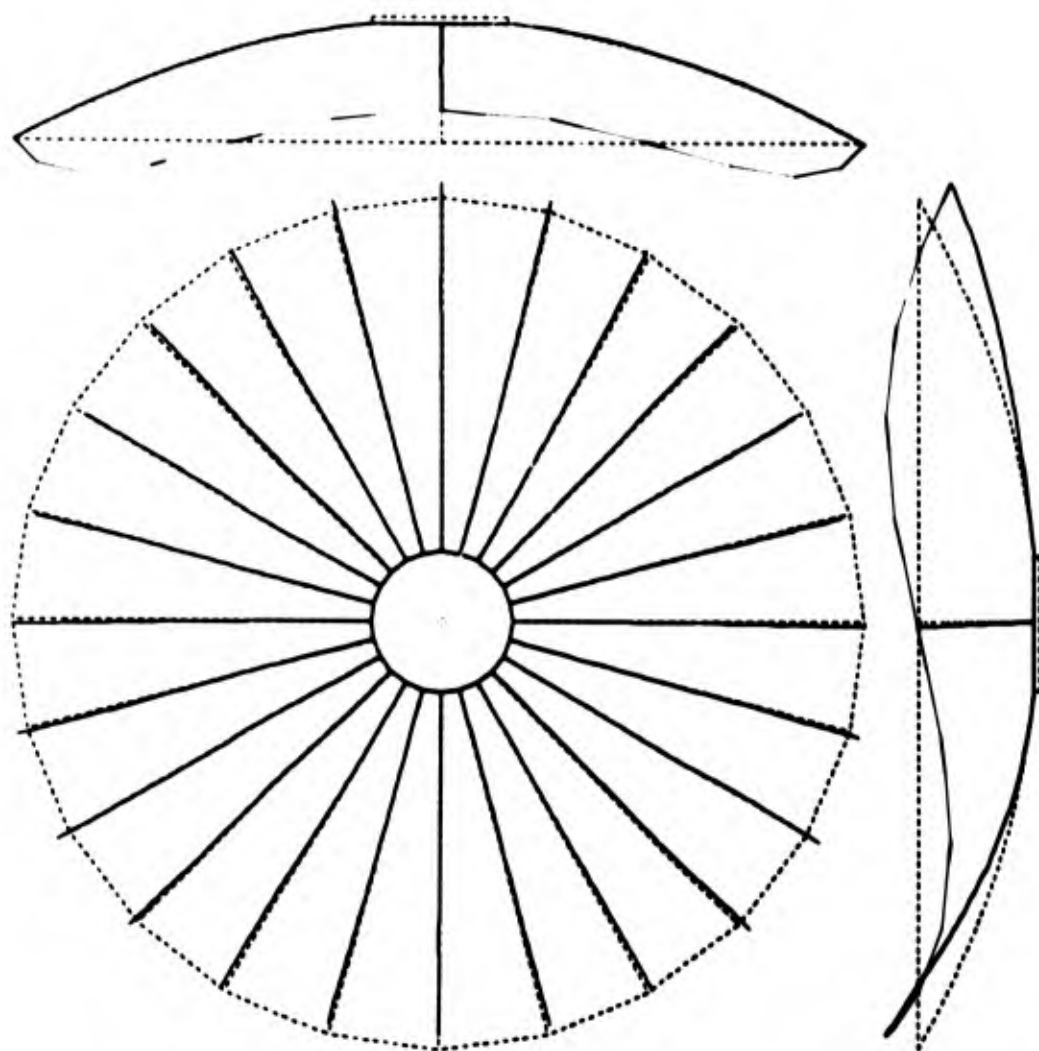


Fig. 8 - Antenna mode shape
 $\omega_1 = 8.25 \text{ CPS}$

AN APPLICATION OF COMPONENT MODE SYNTHESIS TO ROCKET MOTOR VIBRATION ANALYSIS

by

F. R. Jensen
Hercules Incorporated

and

Dr. H. N. Christiansen
Brigham Young University

Acoustic oscillations in a solid rocket combustion cavity produce accelerations on motor structure and attached components. The transmission of these loads to motor components was studied by a structural dynamics analysis of the aft dome for the Minuteman II Stage III motor. Finite element models were constructed of the aft dome structure, the nozzle, and the nozzle control unit (NCU) and solutions were obtained using the SAMIS, Structural Analysis and Matrix Interpretative System, finite element computer program. Because of SAMIS computer program limitations and model complexity, it was decided to use a component mode synthesis technique to obtain solutions for the complete aft dome structure.

Vibration tests gave natural frequencies of the NCU for the first lateral mode (23 Hz) and the first longitudinal mode (66 Hz) in reasonable agreement with calculated results, 30 and 71 Hz, respectively. The calculated frequency of the first lateral mode for the NCU was very sensitive to the fixity condition assumed. It was concluded that the observed pressure oscillations could be expected to excite major structural resonances.

INTRODUCTION

Oscillatory burning has been recognized as a problem associated with both solid and liquid propellant rocket motors for many years. In a recent investigation of causes and effects of oscillatory burning in a solid propellant motor, questions arose concerning the nature of the interaction between the exciting forces and the motor structure. The pressure oscillations and motor vibrations were observed to occur at frequencies of 500 ± 100 Hz. It was therefore natural to question whether the pressure oscillations might be exciting chamber structural resonances and, if so, the modes in which the chamber responded.

The frequency selected for the analysis was limited to the motor driving frequency. The analysis was limited to the motor aft dome and associated hardware since the motor response was greatest for this area. The mathematical model used in the analysis consists of the aft dome portion of the chamber structure (from the aft tangent lines rearward), the four nozzles, and the nozzle control equipment. A finite element stiffness-lumped mass model was used

to represent the aft dome system. The "Structural Analysis and Matrix Interpretive System (1)," (SAMIS) computer program was used to obtain solutions from the mathematical model. The SAMIS program has the capability to form mass, load, and stiffness matrices for structures modeled with a combination of line (beam) and facet (triangular-shaped plate) finite elements. Due to the complexity of the model and limitations on the problem size that could be economically handled by the SAMIS program, it was decided to employ a component mode synthesis technique. This technique combines complex structures using the modes of the structure segments.

Several different approaches to the modal synthesis analysis are reported in the literature. (2,3) The approach used here follows quite closely the detailed technical report on the subject by Hurty. (4)

The math model is discussed in the next section followed by an outline of the modal synthesis method and details of application based on use of the SAMIS computer program.

Mode shapes and natural frequencies obtained for the individual components and for the aft dome system are given in the "Results" section.

MATH MODEL

A sketch of the aft dome showing the four nozzles and the nozzle control unit (NCU) is presented in Figure 1. Since the dome has two planes of geometric symmetry, it was necessary to model only one-quarter of the total structure. Complete solutions could then be obtained by solving the one-quarter model for the natural frequencies and mode shapes corresponding to four different sets of boundary conditions. The aft dome system model was therefore made up of one-fourth of the dome structure, one-fourth of the NCU structure, and one complete nozzle. However, a nozzle by itself has a single plane of geometric symmetry and only one-half of a nozzle was modeled to obtain the component mode shapes that are used in the component mode synthesis solution.

In the finite-element models of the dome and nozzle, two to three layers of facet (plate) elements were used to represent the different materials present. One hundred and eighty-one elements were used in the nozzle model and two hundred and fifty-six elements were used in the dome model. The dome and nozzle models had approximately one hundred and thirty-one and one hundred and sixteen degrees of freedom, respectively. Even though it was possible to obtain all of the nozzle solutions by analyzing only one-half of the nozzle, it was later necessary to construct normal modes, constraint modes, and rigid body modes for a complete nozzle for use in the modal synthesis solution. The 36-element NCU model had approximately 85 degrees of freedom (the exact number of degrees of freedom varies slightly for different boundary conditions).

When a geometrically symmetrical structure is analyzed by modeling only one-half of the structure, it is necessary to obtain two solutions for the model: (1) One solution is obtained with boundary conditions applied at the plane of symmetry which allows only symmetrical motion, and (2) a second solution is obtained by applying boundary conditions at the plane of symmetry which allows only asymmetric motion. Thus, all possible modes of vibration of the total structure may be determined by analyzing twice a model of one-half of the structure.

For the dome and the NCU models, it was necessary to apply four sets of boundary conditions to obtain a complete set of mode shapes. The two planes of symmetry for the aft dome structure are the $X = 0$ plane and the $Y = 0$ plane (See Figure 1). The applicable four sets of boundary conditions are thus: (1) Symmetry about the $X = 0$ plane, symmetry about the $Y = 0$ plane; (2) asymmetry about the $X = 0$ plane, symmetry about the $Y = 0$ plane; (3) symmetry

about the $X = 0$ plane, asymmetry about the $Y = 0$ plane, and (4) asymmetry about the $X = 0$ plane, asymmetry about the $Y = 0$ plane. The preceding boundary conditions are abbreviated respectively as follows:

- (1) X-S, Y-S, (2) X-A, Y-S, (3) X-S, Y-A, and (4) X-A, Y-A.

In addition to the boundary conditions applied for symmetry considerations, boundary conditions were applied to the aft dome structure approximately at the aft tangent line (the point where the dome surface becomes tangent to the cylindrical surface) to represent the connection of the aft dome to the remainder of the motor. The remainder of the motor was assumed to be infinitely stiff, and the dome was fixed in such a manner that no translation or rotation occurs at the aft tangent line. However, this assumption is not absolutely correct and should result in natural frequencies that are slightly high.

The loading function of interest is the geometrically symmetrical internal pressure in the aft dome. Since a symmetrical load distribution tends to excite symmetrical modes of vibration, the X-S, Y-S boundary condition is of prime interest. The X-A, Y-S boundary condition which results in the lowest natural frequency for the NCU and provides results for comparison with available test results is also of interest. Thus, the major emphasis in the analysis was on the models with boundary conditions X-S, Y-S, and X-A, Y-S.

COMPONENT MODE SYNTHESIS THEORY

The matrix algebra of the component mode synthesis method is outlined briefly (See Reference 4 for additional detail).

The equations of motion for each of the three components are:

$$\begin{aligned} [m_1]\{\ddot{u}_1\} + [k_1]\{u_1\} &= \{F_1(t)\} \\ [m_2]\{\ddot{u}_2\} + [k_2]\{u_2\} &= \{F_2(t)\} \\ [m_3]\{\ddot{u}_3\} + [k_3]\{u_3\} &= \{F_3(t)\} \end{aligned} \quad (1)$$

where:

$[m_i]$ = diagonal mass matrix for the i^{th} component,

$[k_i]$ = stiffness matrix for the i^{th} component,

$\{F_i(t)\}$ = vector of loads applied to the i^{th} component,

$\{\ddot{u}_i\}, \{u_i\}$ = acceleration and displacement vectors, respectively, for the i^{th} component

Subscripts = 1- NCU, 2- Nozzle, 3-Dome

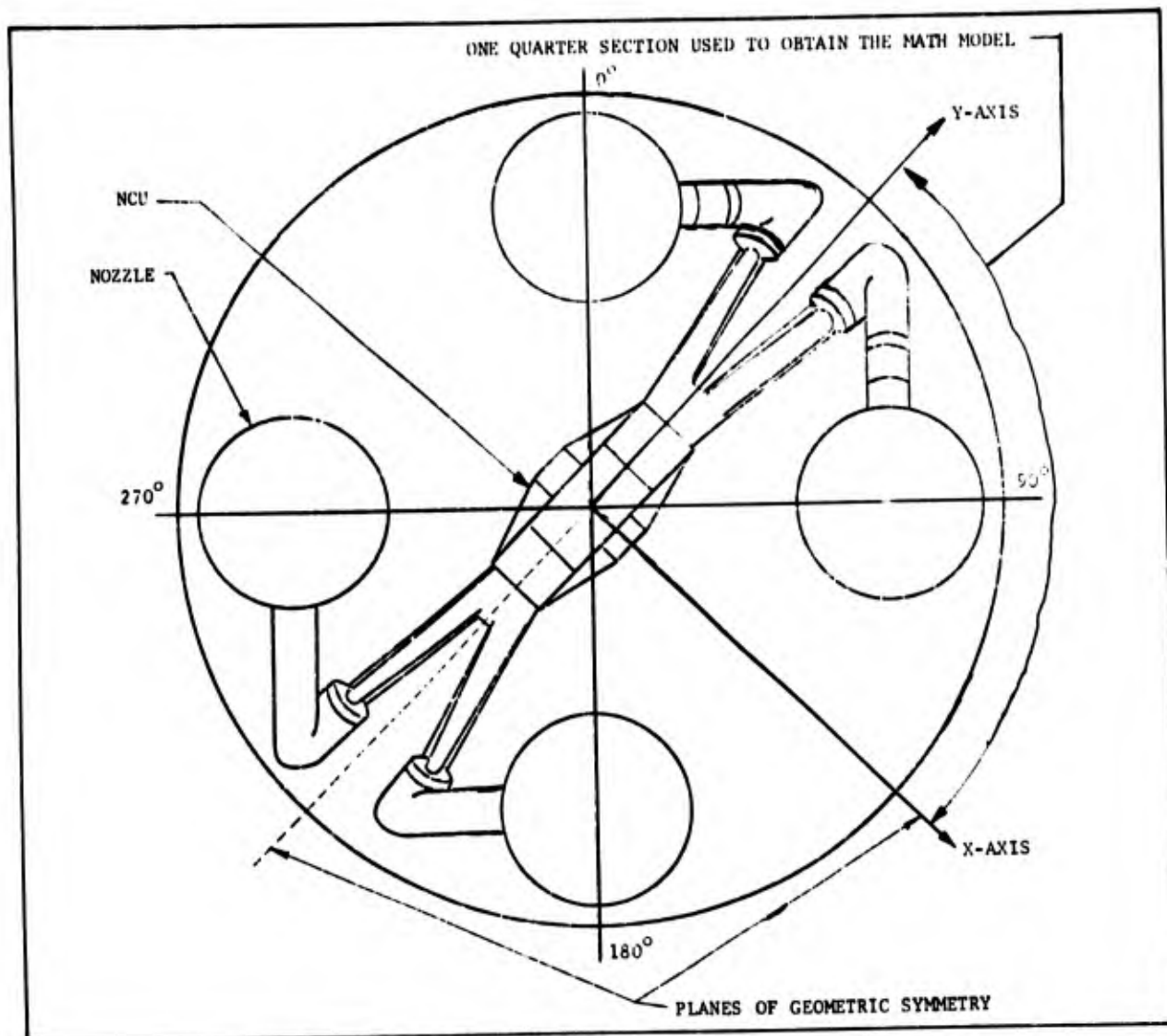


Figure 1. Stage III Minuteman Motor Aft Dome Geometry Showing Portion Used in Mathematical Model

The advantage of using component mode synthesis is to reduce the number of simultaneous equations subject to standard matrix operations. To accomplish this, the equations of motion for the individual components are expressed in terms of modal coordinates (component generalized coordinates), $\{p_i\}$. If the independent modes for the i th component are represented by the columns of matrix $[\phi_i]$, the required coordinate transformation is:

$$\{u_i\} = [\phi_i] \{p_i\} \quad (2)$$

The component modal matrix $[\phi_i]$ may be made up of three different types of modes: (1) Rigid body modes, (2) constraint modes, and (3) fixed constraint normal modes. The reduction in degrees of freedom is brought about by ignoring

the contributions of the higher-frequency normal modes to the deflected configuration.

Introducing the displacement transformation defined by Equation (2) and premultiplying by the transpose of $[\phi_i]$ produces the equations of motion for the system expressed in terms of component generalized coordinates:

$$[m] \{\ddot{p}\} + [k] \{p\} = \{P(t)\} \quad (3)$$

where

$$[m] = \begin{bmatrix} [\bar{m}_1] & & \\ & [\bar{m}_2] & \\ & & [\bar{m}_3] \end{bmatrix}; \quad \{p\} = \begin{bmatrix} p_1 \\ p_2 \\ p_3 \end{bmatrix}$$

$$[k] = \begin{bmatrix} [k_1] & & \\ & [k_2] & \\ & & [k_3] \end{bmatrix}; \quad \{P(t)\} = \begin{Bmatrix} P_1(t) \\ P_2(t) \\ P_3(t) \end{Bmatrix}$$

$[\bar{m}_i] = [\phi_i]^T [m_i] [\phi_i]$, the component generalized mass matrix

$[\bar{k}_i] = [\phi_i]^T [k_i] [\phi_i]$, the component generalized stiffness matrix

$\{P_i(t)\} = [\phi_i]^T \{F_i(t)\}$, the component generalized forces

Equation (3) is then not ready for solution because all equations in the expression are not independent. A coordinate transformation of the form $\{p\} = [\beta] \{q\}$, where $\{q\}$ is the vector of independent coordinates, is introduced to account for the fact that certain components share common nodes. The transformation matrix, $[\beta]$, is developed for a three component system by writing the equations of constraint in the form:

$$\{\bar{u}_{12}\} = [S_{12}] \{\bar{u}_{21}\}$$

$$\{\bar{u}_{13}\} = [S_{13}] \{\bar{u}_{31}\}$$

$$\{\bar{u}_{23}\} = [S_{23}] \{\bar{u}_{32}\}$$

where:

$\{\bar{u}_{ij}\}$ = the set of nodal displacement coordinates of component i which are on the common boundary with component j .

$[S_{ij}]$ = the direction cosine matrix that relates the coordinate system of component i with the coordinate system of component j .

The components $\{\bar{u}_{ij}\}$ may then be extracted from the total set of nodal displacement coordinates by the transformation:

$$\{\bar{u}_{ij}\} = [L_{ij}] \{u_i\}$$

where:

$[L_{ij}]$ = a transformation matrix that contains zeros and ones as appropriate.

Then, since

$$\{u_i\} = [\phi_i] \{p_i\},$$

$$\{\bar{u}_{ij}\} = [L_{ij}] [\phi_i] \{p_i\}$$

and:

$$[L_{12}][\phi_1]\{p_1\} = [S_{12}][L_{21}][\phi_2]\{p_2\}$$

$$[L_{13}][\phi_1]\{p_1\} = [S_{13}][L_{31}][\phi_3]\{p_3\}$$

$$[L_{23}][\phi_2]\{p_2\} = [S_{23}][L_{32}][\phi_3]\{p_3\}$$

or:

$$\begin{bmatrix} L_{12}\phi_1 & -S_{12}L_{21}\phi_2 & \\ L_{13}\phi_1 & 0 & -S_{13}L_{31}\phi_3 \\ 0 & L_{23}\phi_2 & -S_{23}L_{32}\phi_3 \end{bmatrix} \begin{Bmatrix} p_1 \\ p_2 \\ p_3 \end{Bmatrix} = \begin{Bmatrix} 0 \\ 0 \\ 0 \end{Bmatrix}$$

The above equation is in the form,

$$[A]\{p\} = \{0\},$$

which may be partitioned as follows:

$$\begin{bmatrix} A_D & A_I \end{bmatrix} \begin{Bmatrix} p_D \\ p_I \end{Bmatrix} = \begin{Bmatrix} 0 \\ 0 \end{Bmatrix}, \quad (4)$$

where $\{p_D\}$ is an arbitrary set of dependant modal coordinates and $\{q\}$ is the corresponding set of independent modal coordinates. Equation (4) may be rearranged to give:

$$\{p_D\} = -[A_D]^{-1} [A_I] \{q\}.$$

or

$$\{p\} = \begin{Bmatrix} \{p_D\} \\ \{q\} \end{Bmatrix} = \begin{bmatrix} -[A_D]^{-1} [A_I] \\ [I] \end{bmatrix} \{q\}$$

from which we recognize the coefficient matrix to be $[\beta]$. The only restrictions on the way in which the $[A]$ matrix is partitioned are that $[A_D]$ must have an inverse. When the $[A]$ matrix was written out, it was seen that by selecting the proper columns, $[A_D]$ could be selected to be a unit diagonal matrix. Thus, with proper selection of $[A_D]$,

$$[\beta] = \begin{bmatrix} -[A_I] \\ [I] \end{bmatrix}$$

With the use of the $[\beta]$ transformation matrix, the system equations of motion, (3), may be expressed in system generalized coordinates, $\{q\}$:

$$[\beta]^T \ddot{\{q\}} + [\beta]^T [k] [\beta] \{q\} = [\beta]^T \{P(t)\}$$

or

$$[M] \ddot{\{q\}} + [K] \{q\} = \{Q(t)\} \quad (5)$$

The generalized forces, $\{Q(t)\}$, will consist only of excitation from external sources.

APPLICATION OF MODAL SYNTHESIS

Details of the application of the modal synthesis technique based on use of the SAMIS computer program are discussed below. The steps used to obtain system natural frequencies and mode shapes are listed as:

1. Input Data Generator Program

Data describing each finite element model were input to an Input Data Generator program to convert the data to SAMIS format. Output from this program was a SAMIS element data deck for each component and a set of rigid body modes, $\{\phi_i^R\}$.

2. SAMIS Program - I

SAMIS was programmed to create the component mass and stiffness matrices, $[m_i]$ and $[k_i]$, from the element data deck. Constraints were applied to $[m_i]$ and $[k_i]$ and the homogeneous component equations of motion were solved to obtain the component fixed constraint natural frequencies and mode shapes, $\{\phi_i^N\}$. The fixed constraints include the points that are common between components.

The usual SAMIS normal mode solution provides only translation components of the displacement at each node. To obtain the corresponding rotation components of the normal modes, the force-deflection relationship for a component is written as

$$\{F_i\} = [k_i]\{u_i\} \quad (6)$$

or

$$\begin{Bmatrix} \{F\} \\ \{M\} \end{Bmatrix} = \begin{bmatrix} [k_{11}] & [k_{12}] \\ [k_{21}] & [k_{22}] \end{bmatrix} \begin{Bmatrix} \{u\} \\ \{\theta\} \end{Bmatrix}$$

where

$\{M\}$ = the applied moment vector, and

$\{\theta\}$ = the vector of angular displacements.

Since the applied moments are zero and since $\{u\}$ represents the calculated translation components of the normal modes, the corresponding rotation components are:

$$\{\theta\} = -[k_{22}]^{-1} [k_{21}]\{u\}$$

The constraint modes, $\{\phi_i\}$, for each component are obtained by a similar matrix partitioning. (A single constraint mode is the displacement vector which results when a single constraint coordinate is given a unit displacement and all other constraints are fixed.) Equation (6) may be partitioned as follows:

$$\begin{bmatrix} [k_{11}] & [k_{12}] \\ [k_{21}] & [k_{22}] \end{bmatrix} \begin{Bmatrix} \{u\} \\ \{u^c\} \end{Bmatrix} = \begin{Bmatrix} \{F\} \\ \{R^c\} \end{Bmatrix}$$

where:

$\{u^c\}$ = the displacement vector for all constrained coordinates

$\{R^c\}$ = the vector of forces applied at the constraints to maintain either zero or unit displacement.

Since the applied forces, $\{F\}$, are zero, the partitioned equations may be solved for $\{u\}$:

$$\{u\} = -[k_{11}]^{-1} [k_{12}]\{u^c\}$$

A complete constraint mode is obtained by considering the total displacement vector $\{u\}$ and $\{u^c\}$.

3. SAMIS Program - II

The SAMIS program is used to perform the matrix manipulations necessary to obtain the system generalized mass and stiffness matrices. The system dynamic matrix is then formed and the usual SAMIS eigenvalue routine is used to obtain system natural frequencies and mode shapes.

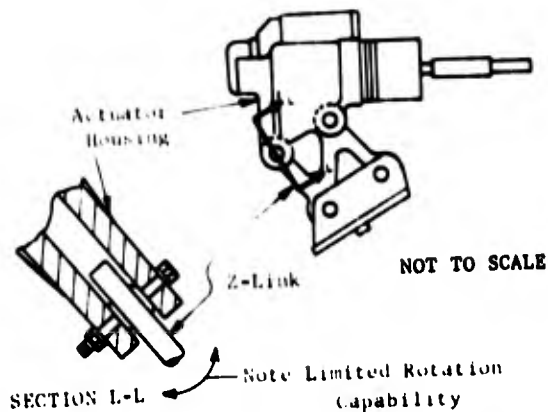
RESULTS

The fixed constraint normal modes, $\{\phi_i^N\}$, were calculated for each component for use in forming the modal matrix, $\{\phi_i\}$. Since a knowledge of the component mode shapes and corresponding natural frequencies is useful in visualizing the system normal mode results, individual component natural frequencies and mode shapes are discussed below:

1. NCU Component Results

As indicated in Figure 1, the NCU consists of an equipment housing mounted to nozzle actuators which are in turn attached through a Z-link connection to the nozzle stack. The actuator push rod is connected to the nozzle. Thus, the NCU model is constrained at two points where the Z-link attaches to the nozzle stack and at one point where the actuator push rod attaches to the nozzle. The bolted connections of the Z-link contain bearings as shown in the sketch at the top of the next page.

It was determined that the lowest natural mode of the NCU occurred when X-A, Y-S boundary conditions were used. To study the effect of the Z-link fixity condition on the natural frequency, solutions were obtained with ball joints modeled at each bolted connection on the Z-link, (4 ball joints), and with only ball joints modeled at the point of attachment to the nozzle stack (2 ball joints). The two



ball joint model had a low natural frequency of 30 Hz compared with 4.9 Hz for the four-ball joint model. Thus, the low natural frequency is apparently very sensitive to the Z-link fixity conditions. Vibration test results indicate a low natural frequency of 23 Hz for the NCU. Therefore, the two-ball joint model was used to represent the NCU.

The four lowest natural frequencies of the NCU when X-S, Y-S boundary conditions are used were 71, 378, 386, and 937 Hz. The lowest natural frequency of 71 Hz compares favorably with test results which indicate a low natural frequency of 66 Hz for corresponding boundary conditions.

2. Dome Component Results

The fixed constraint normal modes and corresponding natural frequencies for the dome were determined for use in the modal synthesis solution. In addition, a solution for the dome was obtained with the internal (component interface) constraints free. If the effects of the NCU and the nozzle are small, the free constraint solution for the dome should approximate the aft dome system solution. The first five natural frequencies for the dome model with fixed and, with free constraints, are shown in Table I.

Propellant is bonded to the aft dome between the nozzle ports and the aft closure. The propellant has the effect of increasing the mass and stiffness of the dome structure. To approximate the effect of the propellant on the dome model, the mass values of appropriate elements were increased to reflect the mass of a six-inch thickness of propellant. As shown in Table I, the added mass was responsible for a reduction in the first natural frequency from 627 to 436 Hz.

3. Nozzle Component Results

The five lowest natural frequencies for the nozzle for both sets of boundary conditions are presented in Table II.

TABLE I
NATURAL FREQUENCIES FOR THE DOME MODEL
WITH X-S, Y-S BOUNDARY CONDITIONS

Mode Number	Natural Frequencies (Hz)		
	Without Propellant		With Propellant
	Fixed Constraints	Free Constraints	Fixed Constraints
1	627	524	436
2	952	888	452
3	1106	983	507
4	1595	1206	867
5	1803	1221	1003

TABLE II
NOZZLE NATURAL FREQUENCIES

Mode Number	Natural Frequency (Hz) Boundary Condition	
	Symmetric Modes	Asymmetric Modes
1	241	314
2	455	497
3	660	559
4	1210	932
5	1670	1207

4. Aft Dome System - Modal Synthesis Results

The system model was found to have 18 natural frequencies below 1000 Hz. As expected, some of the system natural modes were found to correspond quite closely with component natural frequencies. For example, the system first natural frequency of 69 Hz was found to consist almost entirely of NCU motion (corresponds to 71 Hz component natural frequency).

The system natural mode which corresponds with the dome first natural mode occurred at 420 Hz (compares with 436 Hz component natural frequency). The second dome mode occurred at 438 Hz and the third at 501 Hz (corresponding component frequencies 452 Hz and 507 Hz, respectively).

CONCLUSIONS

It was concluded that the component mode synthesis technique, when used in conjunction with a finite element and matrix interpretive computer program such as SAMIS, provides a

powerful tool for dynamics analysis of structural models with large numbers of degrees of freedom.

Based on results from the structural dynamic analysis, it was concluded that the 500 ± 100 Hz pressure oscillation forcing function could excite several major aft dome structural resonances. The dome could be expected to respond in any of the first four basic dome modes. In addition, the hardware (nozzles, actuators, and NCU) respond in several different modes in the frequency range of interest. It would be necessary to calculate the system response to an internal oscillating pressure to determine the extent of participation of a particular component in a particular mode.

REFERENCES

1. Melosh, R. J., "Structural Analysis and Matrix Interpretive System, (SAMIS)," Program Report, T. M. No. 33-307, Revision 1 JPL, California Institute of Technology, Pasadena, California, 15 December 1966.
2. Hou, S., "Review of Modal Synthesis Techniques and a New Approach," Shock and Vibration Bulletin, No. 40, Naval Research Laboratory, Washington, D. C., December 1969.
3. Benfield, W. A., and Hruda, R. F., "Vibration Analysis of Structures by Component Mode Substitution," Papers of AIAA/ASME 11th Structures, Structural Dynamics and Materials Conference, Denver, Colorado, April 1970.
4. Hurty, W. C., "Dynamic Analysis of Structural Systems by Component Mode Synthesis," Report T. R. No. 32-530, JPL, California Institute of Technology, Pasadena, California, January 1964.

BLANK PAGE

COMPARISON OF CONSISTENT AND LUMPED MASS MATRIX
SOLUTIONS WITH THE EXACT SOLUTION FOR A
SIMPLY-SUPPORTED TIMOSHENKO BEAM

C. Baum, J. T. Higney
Gibbs & Cox, Inc.
New York, New York

and

* A. Jenks
Esso International Inc.
New York, New York

A wide variety of consistent mass matrix schemes have been developed for use in finite element analysis. The methods have been proposed in order to increase the accuracy of solutions without increasing the number of mass points. However, in dynamic analysis the fundamental criterion for model complexity is the number of degrees of freedom of the model and not the number of mass points. In order to determine the comparative accuracy of lumped mass and consistent mass (using McCalley's formulation) matrices, a series of test problems were solved and the solutions compared with the exact solutions for Timoshenko beams. The solutions were obtained for simply-supported beams of various L/D ratios and various levels of model complexity. The comparison was carried out for three criteria: frequency, midspan bending moment due to a velocity-shock and modal mass. The study indicated that a lumped mass matrix is a better mathematical model of a simply-supported beam than a consistent mass matrix of the same number of degrees of freedom when frequency is the primary criterion. The lumped mass matrix is less distinguishably better when comparing midspan bending moments. For the modal mass criterion the consistent mass matrix has higher accuracy. The implications of this study for DDAM are also discussed.

INTRODUCTION

The extensive use of the finite-element method, especially in dynamic analysis, has generated considerable interest in the accurate representation of both the stiffness and the mass of various structural elements. Beams, in particular, have been examined with the intent of providing a matrix formulation which best represents the distributed character of the mass in a beam. Formulations which have off-diagonal terms are called consistent mass matrices, as opposed to lumped mass matrices which have only diagonal terms. Further, consistent mass matrices generally assign both translational and rotational degrees of freedom to each end of a beam segment, while the usual practice with lumped mass matrices is to account for only

translational degrees of freedom. It is generally recognized that the accuracy of the results of a finite-element analysis is directly related to the level of complexity of the mathematical model, but model complexity carries a concomitant increase in cost. Consistent mass matrices have therefore been proposed in order to increase the accuracy of solutions without increasing the number of mass points in the model of a beam. However, in dynamic analysis the fundamental criterion for model complexity is the number of degrees of freedom (dof) of the model and not the number of mass points.

Simply-supported beam models are shown in Figure 1 with six degrees of freedom each for both the consistent and lumped mass matrices. The consistent mass model has

* Mr. Jenks was with Gibbs & Cox, Inc. at the time this work was done.

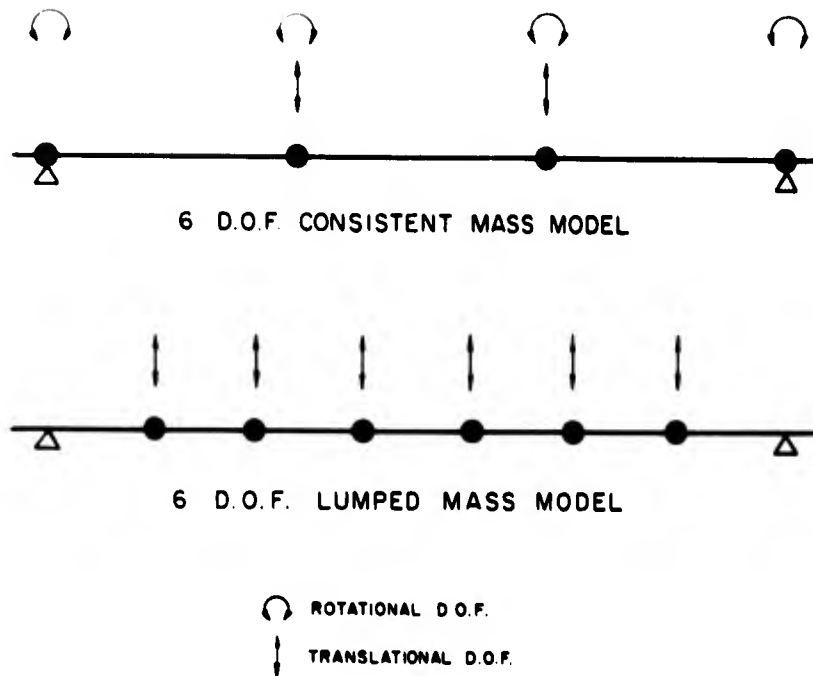


Fig. 1 - Typical mass matrix models

two midspan mass points, each of which has a translational and a rotational degree of freedom. In addition, the end points each have a rotational degree of freedom since a simply-supported beam has rotational freedom, but not translational freedom, at the ends. It should be noted in passing that the dof of a consistent mass model is influenced by the end conditions of the beam being modelled, e. g., a two mass point consistent mass model of a fixed-fixed beam would have only four dof. The lumped mass model has six mass points, each of which has a translational dof. The number of dof used in a lumped mass model is therefore independent of the end conditions of the beam being modelled.

Degrees of freedom may be thought of as the analyst's coin of the realm in that they govern the computational size of a problem. With this in mind, the accuracy of a consistent mass matrix which requires six dof (two translational and four rotational) to provide a two mass point representation of a simply-supported beam should properly be compared with that of a six mass point lumped mass model which contains translational dof only. Such a comparison, at various levels of model complexity, is carried out in this paper.

PROBLEM

In order to determine the comparative accuracy of lumped mass and consistent mass models with equal numbers of dof, a series of test problems was set up. Exact solutions for

Timoshenko beams were also obtained to use as standards for calculating the errors in the lumped mass and consistent mass solutions. The specific problem chosen for investigation was that of a simply-supported beam of circular cross-section with a diameter of one foot. This beam was then analyzed with lengths of 3, 8 and 20 feet, providing length to diameter (L/D) ratios of 3, 8 and 20, respectively. The beam was assumed to be subject to an idealized base motion input and the resultant inertia forces and stresses were calculated in accord with the Navy's Dynamic Design Analysis Method (DDAM), as outlined in Reference (1).

The choice of simply-supported beams was based on making the problem both tractable and relevant. Since the solution for the frequencies of a simply-supported Timoshenko beam as contained in Flugge, Reference (2), is a more convenient transcendental equation than any other type of support, the accuracy of the solution for any number of modes is more easily maintained. Further, the simply-supported beam is a frequently occurring primary element in the dynamic shock analyses with which the authors have been involved, e. g., turbine shafts. Similarly, the range of L/D ratios chosen for the analysis is predicated on ratios considered typical of shipboard equipment.

The material contained in Flugge was extended to allow calculation of the modal mass, which is defined in Reference (1) as a measure

of the reaction force exerted on the input base, and the midspan bending stress.

The particular consistent mass matrix formulation used for this study is the one developed by McCalley, Reference (3). This formulation is more general than the well-known Archer formulation, Reference (4), in that it includes the effects of shear deformation and rotary inertia. It is considered in the two papers by Mains, References (5) and (6), to be the most accurate consistent mass formulation and was also used as a standard of comparison in the paper by Kapur, Reference (7). A consistent mass matrix with four translational dof at four mass points, derived by eliminating rotational dof from the McCalley formulation, was also included with the desire to test the accuracy of a matrix having only translational dof, but still retaining off-diagonal terms. The present study compares the lumped and consistent mass matrix solutions at various levels of complexity, i. e., varying numbers of degrees of freedom from 3 to 8, with the solutions for Timoshenko beams. Comparison is also made to the three degrees of freedom, lumped mass, solution by Harrington and Vorus, Reference (8).

The solutions in this study involve far fewer dof than those of Mains and are thus thought to be more representative of the complexity level generally used for dynamic shock analyses of shipboard equipment. It is to be noted that in both the lumped and consistent mass solutions, as well as the Harrington and Vorus solutions, flexibility matrices which included the effect of shear deflection were used.

The lumped mass matrices used in this study were set up by spacing the mass points equally along the beam. The weight at each mass point was equal to:

$$w = \frac{W}{n+1}$$

where w = weight at each point, lbs.
 W = weight of the entire beam, lbs.
 n = number of mass points, i. e., number of degrees of freedom

Then the weight fraction of the entire beam represented in the "n" dof model is:

$$F = \frac{n}{n+1}$$

where F = weight fraction

In the tests of the Harrington and Vorus formulation the spacing was one mass point at .173 of the beam length from each end with one mass point at the center. The weight fractions were .265 W for the side points and

.363 W for the center point. These are the length fractions and weight fractions recommended in the paper by Harrington and Vorus as the optima for a simply-supported beam represented by three lumped masses. Thus the Harrington and Vorus model has 89 per cent of the beam weight represented, whereas a three degree of freedom lumped mass model would contain only 75 per cent of the beam weight. The consistent mass matrices cannot be discussed on the same basis because of the off-diagonal terms.

The many criteria by which the accuracy of solution to a problem can be compared were reduced to three; namely, frequency, modal mass and midspan bending stresses due to a velocity-shock base motion. The criterion of frequency is considered of primary importance because of the necessity of accurately calculating the effects of resonances with other components in a complex equipment model. The authors have experienced instances of very high "g" loads where a single element in a model is in resonance with all or several of the other elements in the model in one particular mode as though the model were acting as a 2 mass system. If the single element is a bending element then the accuracy of frequency calculation may be the most critical aspect of the bending element model. The subject of resonances in DDAM is well discussed in References (9) and (10). The importance of frequency must also be considered because of dependence of accelerations on frequency for a velocity-shock input. The modal mass is used to determine foundation forces and is therefore of importance where the beam element is mounted within an equipment or on a foundation which is itself being stress analyzed. Since dynamic shock analyses for naval equipment are used primarily to determine the stresses induced by the shock, the accuracy of midspan bending stress values is also examined. For this study a velocity-shock input of 1 inch per second without modal weight dependence was used because it was felt that modal weight dependence of the input as described in Reference (1) might cloud the issue.

For purposes of clarity it should be noted that for a simply-supported beam only the odd numbered modes provide a non-zero response, e. g., a four dof model will provide non-zero midspan bending stresses only for the first and third modes. In this comparison no attempt is made to comment on the merit of answers in terms of conservative or nonconservative results, i. e., higher than correct or lower than correct stresses, only on the accuracy of a solution when compared to the Timoshenko beam solution.

RESULTS

A plot of the per cent error in frequency as a function of mode number for an L/D of 20

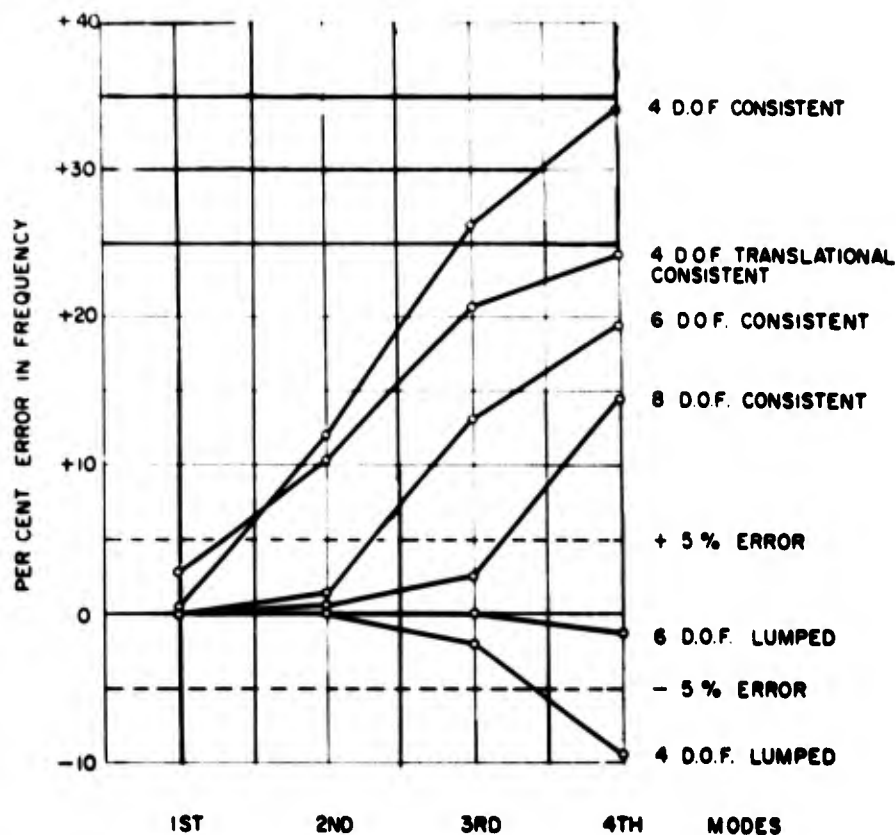


Fig. 2 - Frequency error versus mode number

is shown in Figure 2. Six different curves are plotted, one each for three consistent mass matrix solutions according to McCalley, one for a translational consistent mass matrix solution and two for lumped mass matrix solutions. The most obvious result to be gleaned from this plot is the greater accuracy of the lumped mass solutions for an equal number of dof. For example, the frequency error for the third mode (in a 6 dof solution) is 13 per cent for a consistent mass solution, while it is less than 1 per cent for a lumped mass solution.

The grouping of the solutions, in Figure 2, by error direction also merits consideration. The consistent mass matrices deviate on the side of positive errors. This would appear to be a characteristic of consistent mass matrices. The lumped mass matrices characteristically deviate to lower frequency values.

A more detailed examination of the curves shows a useful "rule of thumb" is that the number of accurate modal frequencies in consistent mass matrix solutions is equal to the number of translational dof in the matrix,

i. e., the six dof consistent mass matrix has two translational dof and exhibits two accurate frequencies. In this context, any frequency with an error of less than 5 per cent is considered to be of acceptable accuracy. The consistent mass matrix was derived by McCalley on the basis of energy in the deflected beam. It must therefore be concluded that there is little correlation between the accurate representation of energy in a mass matrix and the accuracy of the frequencies which that matrix generates.

The work of Harrington and Vorus which optimizes a three degree of freedom lumped mass matrix by varying the mass quantities and locations was also examined. The Harrington and Vorus formulation leads to large errors in third-mode frequency values and thus does not provide improvement equal to one dof, i. e., is not as good as a four degree of freedom lumped mass solution. The results for this formulation are not a smooth function of the mode number and are not shown on Figure 2.

Since the initial results of this study indicated a correlation between the number of

translational dof and the number of accurate frequencies, a pure translational consistent mass matrix was generated for the case of four dof with an L/D ratio of 20. The results for this case are plotted on Figure 2 and it can be seen that there is improvement over the four dof consistent mass matrix of McCalley but that the results are still not as good as the four dof lumped mass matrix. This is especially interesting because both the four dof lumped and the four dof translational consistent mass matrices have the same number of mass points and are therefore used with the same flexibility matrix. This may be taken as further indication of the lack of correlation between energy and frequency. The lumped mass matrices exhibited very good frequency accuracy for at least one half the number of dof. However, the translational consistent mass matrix did not adhere to the accuracy criteria of either the consistent mass matrices or the lumped mass matrices.

A complete tabulation of frequencies, for all values of L/D, is contained in Table 1. An examination of Table 1 will show that the trends illustrated in Figure 2 are substantially unchanged at the L/D values of 3 and 8.

Less pattern emerges when the midspan bending stress is considered, even if consideration is limited to an L/D ratio of 20. An important limitation must be observed in that large frequency errors will cause midspan bending stress errors due the dependence of the input acceleration on frequency. These frequency induced errors in the midspan bending stress may be of a compensating nature, e. g., the third mode frequency error for a four dof consistent mass is +26.3 per cent with a midspan bending moment error of -7.8 per cent. Without the frequency error the

midspan bending stress error would have been -34.1 per cent. These compensating errors may not be undesirable but should be used with some trepidation since they would not always occur with an input motion more complex than the simple velocity-shock used in this study. Table 2 shows the per cent errors in midspan bending stress values for an L/D of 20. Table 2 contains only those values of midspan bending stress for which the frequency errors were minimal, i. e., no bending stress data with compensating errors are included. The advantage of the lumped versus the consistent mass matrix is again evident but not as strongly. Further, as seen in Table 2, the accuracy of the stresses is very much less than that of the frequencies. A complete tabulation of midspan bending stresses for all values of L/D is contained in Table 3.

It is in the calculation of modal mass that the consistent mass matrices prove more accurate than the lumped mass matrices. Recall that the modal mass for any one mode of a multiple mass system can be thought of as the mass in a single degree of freedom system which has the same frequency as the one mode and produces the same base force for the same input. In calculating modal mass the authors found that the proper manner of dealing with the consistent mass matrix was not covered in Reference (3) but rather that McCalley's class notes, Reference (11), were found necessary. The modal mass correlation is therefore of special importance where the bending member is part of a larger system and stresses in supporting members are to be calculated. The modal mass comparison is presented in Table 4 in which the greater accuracy of the consistent mass matrices particularly for an L/D ratio of 20 can be seen. This superiority is most evident when one compares values for

TABLE 1
Frequencies in Radians per Second

L/D =		3				8				20			
Mode No. =		1	2	3	4	1	2	3	4	1	2	3	4
Matrix Type	dof												
Exact	-	4055	12998	23466	34300	627.4	2387	5004	8197	101.9	404.1	896.5	1564
Harrington & Vorus	3	4090	13440	17170	-	625.6	2537	3772	-	101.4	430.5	673.9	-
Consistent	4	4125	17850	36320	65930	631.3	2783	6823	13590	102.4	452.5	1132	2098
Translational Consistent	4	-	-	-	-	-	-	-	-	104.6	445.9	1084	1944
Lumped	4	4139	13150	22000	28000	629.9	2402	4901	7247	102.0	403.9	880.8	1415
Consistent	6	4120	14170	35600	47100	625.0	2435	6120	10760	102.0	410.0	1014	1867
Lumped	6	4145	13370	23280	31870	630.1	2415	5044	8039	102.0	404.9	896.1	1543
Consistent	8	-	-	-	-	-	-	-	-	102.0	406.4	919.0	1793

only those modes which have acceptable frequency accuracy (less than 5 per cent error). For example, the modal mass for mode 1 is 16.064 for a 4 dof consistent mass solution,

while it is 15.078 for a comparable lumped mass solution. The value of 16.064 is quite close to the exact value of 16.103.

TABLE 2
Per Cent Errors in Bending Stress Values
(L/D = 20)

Matrix Type	dof	Mode No.	
		1	3
Harrington & Vorus	3	+11.6	*
Consistent	4	+16.5	*
Translational Consistent	4	- 2.2	*
Lumped	4	- 4.6	-45.2
Consistent	6	- 4.2	*
Lumped	6	- 2.2	-21.4
Consistent	8	+ 5.1	+28.2

* Not tabulated because of large frequency error in this mode.

TABLE 3
Bending Stress Values in Pounds Per Square Inch

L/D =		3		8		20	
Mode No. =		1	3	1	3	1	3
Matrix Type	dof						
Exact	-	303.2	52.8	359.0	96.9	369.2	118.0
Harrington & Vorus	3	373.8	83.2	406.8	132.0	412.1	147.7
Consistent	4	383.6	22.7	423.3	93.3	430.2	108.7
Translational Consistent	4	-	-	-	-	361.1	79.7
Lumped	4	321.5	36.4	347.9	57.7	352.1	64.7
Consistent	6	323.3	70.9	350.5	85.1	353.8	88.1
Lumped	6	330.2	54.2	356.9	83.6	361.1	92.7
Consistent	8	-	-	-	-	388.2	151.2

TABLE 4
Modal Mass Comparison

L/D =		3		8		20	
Mode No. =		1	3	1	3	1	3
Matrix Type	dof						
Exact	-	2.307	.243	6.392	.678	16.103	1.769
Harrington & Vorus	3	2.387	.279	6.384	.725	15.969	1.806
Consistent	4	2.280	.071	6.371	.811	16.064	2.238
Translational Consistent	4	-	-	-	-	15.864	1.275
Lumped	4	2.262	.126	6.032	.336	15.078	.840
Consistent	6	2.341	.171	6.452	.677	16.104	1.817
Lumped	6	2.338	.192	6.235	.511	15.595	1.277
Consistent	8	-	-	-	-	16.104	1.695

Possible future extensions of this investigation should be mentioned. The accuracy of modal mass representation by the consistent mass matrices leads to an interest in the investigation of beams flexibly supported at the ends, rather than rigidly supported. Further, it would also be of interest to extend the investigation of beams with a small L/D ratio to higher numbers of degrees of freedom so as to examine convergence of the solutions obtained with different types of matrices.

The study of fixed-fixed beams would also be of interest both by itself and as a mode shape of a multi-span beam. Since, for a uniform equally-spaced multi-span beam the modes excited by a velocity-shock input are those in which the separate spans are closely approximated by a fixed-fixed beam. Further, a consistent mass matrix model requires no dof at the end points of a fixed-fixed beam, i. e., a 6 dof fixed-fixed beam has 3 mass points compared with only 2 mass points on a 6 dof simply-supported beam, and may therefore evidence important differences when compared with a lumped mass model.

CONCLUSIONS

The single most important conclusion of the present study is the greater accuracy of frequencies determined by a lumped mass matrix when compared with a consistent mass matrix. The study is, of course, based on a simply-supported beam represented by a limited number of dof. The conclusion that lumped mass matrices are superior must be tempered by the less conclusive results for midspan bending moment and the opposite conclusion reached in examining modal mass. Each analyst should consider the relative importance of the various parameters for a

particular case before deciding on a particular type of matrix formulation.

Several recently developed computer programs have used various consistent mass matrix schemes to represent bending elements. The present study brings the purposefulness of the added complexity of such computer programs very much into question for at least simply-supported beams. The entire dynamic analysis community must now evaluate each individual instance of the use of consistent mass matrices to insure the necessity for and appropriateness of the added complexity.

ACKNOWLEDGMENT

Thanks are due to Mr. J. D. Richardson for supervision and encouragement of this paper and to Gibbs & Cox, Inc. for sponsoring this study.

REFERENCES

- (1) R. O. Belsham and G. J. O'Hara, "Shock Design of Shipboard Equipment - Part I: Dynamic Design Analysis Method", Bureau of Ships, Navy Department, NAVSHIPS 250-423-30, May 1961
- (2) W. Flugge, editor, Handbook of Engineering Mechanics, p. 61-16, McGraw Hill Book Co., Inc., New York, N. Y., 1962
- (3) R. B. McCalley, Jr., "Mass Matrix for a Prismatic Beam Segment", Rept. No. KAPL-M-6913, Knolls Atomic Power Lab., General Electric, Schenectady, N. Y., March 1968

- (4) J. S. Archer, "Consistent Mass Matrix for Distributed Mass Systems", ASCE Journal of the Structural Division, Vol. 89 No. ST4 August 1963
- (5) R. M. Mains, "Comparisons of Consistent Mass Matrix Schemes", The Shock and Vibration Bulletin No. 39, Part 3, January 1969
- (6) R. M. Mains, "Further Comparisons of Consistent Mass Matrix Schemes", The Shock and Vibration Bulletin No. 40, Part 4, December 1969
- (7) K. K. Kapur, "Vibrations of a Timoshenko Beam, Using Finite Element Approach", The Journal of the Acoustical Society of America, Vol. 40, No. 5, 1966
- (8) R. L. Harrington and W. S. Vorus, "Dynamic Shock Analysis of Shipboard Equipment", Marine Technology, Vol. 4, No. 4, October 1967
- (9) R. B. McCalley, Jr., "Velocity Shock Transmission in Two Degree Series Mechanical Systems", The Shock and Vibration Bulletin No. 23S, June 1956
- (10) J. T. Hagney, "Application of Perturbation Techniques to the Navy's Dynamic Design Analysis Method", The Shock and Vibration Bulletin No. 40, Part 7, December 1969
- (11) R. B. McCalley, Jr., Notes for Short Course on Normal Modes, Shock and Vibration, The Pennsylvania State University, 1968

DISCUSSION

Mr. Werner (Agbabian Jacobsen Associates): I am troubled by something I saw in your first slide and that is in your lumped mass method, why did you not also look at both translational and rotational degrees of freedom?

Mr. Baum: We could have done that as well. We had a limited amount of time, and we limited ourselves to these models. The lumped translational-only arrangement provides the largest number of mass points for a given number of degrees of freedom. Since this appeared to be working so well, and since we had limited amounts of time, we spent a little more time on the consistent mass matrix solutions in the hope of getting more accuracy if we played with various forms.

Mr. Werner: I would think that in checking the two methods this would be a more reasonable way to do it if you are looking at the same model in both cases. I do not think you were looking at the same model for both cases.

Mr. Baum: We were looking at the same model in the case of the translational consistent mass matrix. In that sense we were, and I also think that the essential thing was that we had an absolute standard with which to compare it and we found that this rather naive lumped mass matrix form compared extraordinarily well. We went on to improve on that. Also, I think that for the L/D ratio of 20 there probably would not be much difference. For the shorter L/D ratios there might have been a considerable difference and in that case, as you will be able to see in the paper, some of the data are not quite as conclusive for an L/D ratio of 3. In that case I think the inclusion of the rotational inertias might have been quite appropriate.

Mr. Bort (Naval Research Laboratory): One of the things about McCalley's mass matrix is that he assumes that he has a Timoshenko beam between each pair of mass points. It would seem to me that you should get the exact answer if you were using it to calculate the response of a Timoshenko beam.

Mr. Baum: I think you would get the exact answer if you were using an infinite number of degrees of freedom, which in essence is what you are dealing with in the exact answer, is it not? That occupies a lot of space in the computer.

Mr. Naylor (Canada): What was your standard for comparison of errors?

Mr. Baum: The standard for comparison of errors was the exact solution for a Timoshenko beam. Specifically we took the work that is contained in Flugge's Handbook of Engineering Mechanics, with which you may be familiar, and we extended that to get the stresses and modal mass.

Mr. Naylor: How well does that compare with actual life? If you had a natural physical specimen how do these various comparisons compare with the actual measured frequencies?

Mr. Baum: We did not do any actual test work. However, I think that that form of the solution is often considered to be a good standard short of some very complex forms. We do not have any experimental facilities and we had no way of getting experimental data.

Mr. Leibowitz (Naval Ship Research and Development Center): On a graph you presented percentage error; what was your standard or criterion? What was your true value? You included in your analysis bending and shearing flexibility. What did you measure your finite element result against?

Mr. Baum: Against the solution for a Timoshenko beam.

Mr. Leibowitz: How was it obtained?

Mr. Baum: It was obtained by the method contained in Flugge which provides a very simple form of a transcendental equation for the case of a simply supported beam. For other types of support the transcendental equation becomes considerably

stickier. I do not remember the exact form but I think it is just the sine form. This proved to be quite a workable form of the equation and was one of the things that influenced us to consider a simply supported beam. The transcendental equation takes messier forms for other types of end conditions.

Mr. Leibowitz: At the Naval Ship Research and Development Center some 15 years ago we tackled this problem and we got an exact solution to the Timoshenko equation including shear and bending flexibility. It was of a transcendental form. We found it took at least 20 modes, 20 degrees of freedom, to get within 1 percent of error for about 6 modes of vibration. We tried 10, 20, 40 and 80 degrees of freedom. We went down to 10 modes, and the results were not very good. I am rather surprised that you got such excellent results at 6 modes, 6 degrees of freedom.

Mr. Baum: It may be that the L/D ratio of the beam had an influence on that. The exact accuracies were 2 percent or less. This is only for the first mode.

Mr. Leibowitz: You can ignore the shear for the first mode but you cannot do it in your higher modes. We tried staggering the various properties of the beam.

Mr. Baum: It is possible that the form that we used was slightly different. I will continue this discussion later if I may. Maybe you can reference* the work that you were discussing.

*Editors note. R. C. Leibowitz and E. H. Kennard, Theory of Freely Vibrating Nonuniform Beams Including Methods of Solution and Applications to Ships. TMB Report 1317, May 1961.

BLANK PAGE

APPLICATION OF APPROXIMATE TRANSMISSION MATRICES
TO DESCRIBE TRANSVERSE BEAM VIBRATIONS

R. D. Roake
Ranjit Roy

University of Missouri-Rolla
Rolla, Missouri

A study is made of the application and accuracy of using approximate transmission matrices to determine principal modes of uniform and nonuniform continuous Bernoulli-Euler beam elements. The work emphasizes three aspects of the approximate transmission matrices: obtaining the matrices to different levels of accuracy, evaluation of resulting error levels in principal mode frequency roots obtained via these matrices, and the application to determining the frequency roots for several cases of nonuniform beams.

The approximate transmission matrix is obtained by expanding the differential equation which defines the transmission matrix in a Maclaurin series about the origin of a beam segment. This method as a model to the continuum, has been compared to commonly used lumped parameter models. These comparisons are based upon the principal mode frequency root errors and indicate the affect of the series truncation on the convergence of the frequency roots.

INTRODUCTION

A transmission matrix describes the manner in which sinusoidal forces and motions are transmitted through a linear elastic element during steady state conditions. The use of transmission matrices in describing mechanical vibration problems in lumped parameter or continuous form has been relatively recent. The earliest application of this method was the steady state description of four terminal electrical networks in which case the method is commonly designated "four pole parameters". Molloy [1] was one of the first to systematically apply four pole parameters to acoustical, mechanical, and electromechanical vibration problems. Pestel and Leckie [2] have catalogued transmission matrices, which they term transfer matrices, for uniform elastomechanical elements up to twelfth order. Rubin [3] has extended the application of transmission matrices through a completely general treatment. The objective herein is to present a means of obtaining an approximate transmission matrix for non-uniform continuous systems where closed form solutions are not attainable. The method is applied to the particular case of transverse vibrations of Bernoulli-Euler beams.

REVIEW OF TRANSMISSION MATRICES

A general transmission element is shown in Fig. (1). The state vector, $\{\Psi\}$, is a

column vector consisting of elements which describe the forces (and/or moments) and displacements (translational or angular) at the point of interest.

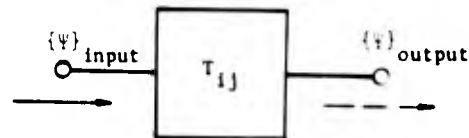


Fig. 1 General Transmission Element

A common form of the transmission matrix is given by:

$$\{\Psi\}_{\text{input}} = [T] \{\Psi\}_{\text{output}} \quad (1)$$

where $[T]$ is designated the "Forward Transmission Matrix". The arrows in Fig. (1) indicate the direction of positive forces and displacements. The forces in the respective state vectors are those applied to the input and those applied by the output ends.

The transmission matrix approach is best suited for elements in an end-to-end arrangement, e.g., several elements interconnected or

a single element subdivided into $N-1$ segments as shown in Fig. (2).

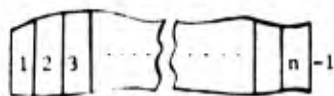


Fig. 2

Employing the definition from eq. (1):

$$\{\psi_1\} = [T_1] \{\psi_2\}$$

as $\{\psi_1\}_{\text{output}} = \{\psi_2\}_{\text{input}}$.

Likewise, one can write

$$\{\psi_2\} = [T_2] \{\psi_3\}$$

$$\{\psi_3\} = [T_3] \{\psi_4\}$$

$$\{\psi_{N-1}\} = [T_{N-1}] \{\psi_N\}$$

where the state vector at any point is designated as:

$$\{\psi_i\}; i = 1, 2, 3, \dots, n$$

representing the state vector of the i^{th} segment at the input end. Thus, for the total system:

$$\{\psi_1\} = [T_1] [T_2] [T_3] \dots [T_{N-1}] \{\psi_N\} \quad (2)$$

which is obtained by successive substitution of state vectors.

For a transverse Bernoulli-Euler beam element the state vector at point i is:

$$\{\psi_i\} = \begin{Bmatrix} V_i \\ M_i \\ w_i \\ \dot{w}_i \end{Bmatrix}$$

where: V_i = transverse shearing force at point i

M_i = bending moment at point i

w_i = transverse displacement at point i

\dot{w}_i = slope at point i

For continuous systems one can also form a differential equation which defines the state vector for a given type of element. This is

illustrated by considering a dx segment of a Bernoulli-Euler beam element as shown in Fig.(3).

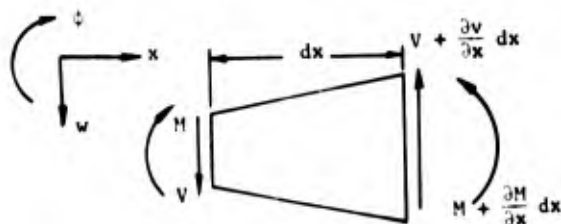


Fig. 3 Elastic Beam Increment

For a negative displacement at end B of the element the forces and moments acting on the element are as shown in Fig. (3). Taking sinusoidal displacements:

$$w = w_0 \sin \omega t$$

$$\frac{d^2 w}{dt^2} = -\omega^2 w$$

Summing forces on the dx element for dynamic equilibrium gives:

$$\frac{dV}{dx} = \rho A(x) \omega^2 w. \quad (3)$$

Summing moments about point A and neglecting terms of order $(dx)^2$ gives:

$$\frac{dM}{dx} = -V \quad (4)$$

From basic mechanics of materials:

$$EI(x) \frac{d^2 w}{dx^2} = -M$$

$$\text{or} \quad \frac{d\phi}{dx} = -\frac{M}{EI(x)} \quad (5)$$

$$\text{as} \quad \frac{dw}{dx} = \phi. \quad (6)$$

Collecting eqs. (3) - (6) in matrix form gives:

$$\frac{d}{dx} \begin{Bmatrix} V \\ M \\ w \\ \phi \end{Bmatrix} = \begin{bmatrix} 0 & 0 & \rho A(x) \omega^2 & 0 \\ -1 & 0 & 0 & 0 \\ 0 & 0 & 0 & 1 \\ 0 & -1/EI(x) & 0 & 0 \end{bmatrix} \begin{Bmatrix} V \\ M \\ w \\ \phi \end{Bmatrix} \quad (7)$$

which is the differential equation defining the state vector consistent with Bernoulli-Euler beam theory and of the form:

$$\frac{d\{\psi(x)\}}{dx} = [A(x)] \{\psi(x)\} \quad (8)$$

where:

$$[A(x)] = \begin{bmatrix} 0 & 0 & Z(x) & 0 \\ -1 & 0 & 0 & 0 \\ 0 & 0 & 0 & 1 \\ 0 & -Y(x) & 0 & 0 \end{bmatrix} \quad (9)$$

$$\left. \begin{aligned} Z(x) &= \rho A(x) \omega^2 \\ Y(x) &= 1/EI(x). \end{aligned} \right\} \quad (10)$$

GOVERNING DIFFERENTIAL EQUATION

The technique used herein to obtain the transmission matrix is relatively recent, used by Pipes [4], and is pertinent to the expansion methods to be employed to obtain approximate forms. The forward transmission matrix, as it relates the input state vector of a continuous element to the state vector at any particular point x along the element, is given by:

$$\{\Psi(0)\} = [T(x)] \{\Psi(x)\} \quad (11)$$

where $\{\Psi(0)\}$ represents the state vector at the input end, i.e., where $x = 0$.

Differentiating eq. (11) and eliminating $\{\Psi(x)\}$ which cannot be a null vector for a non-trivial solution gives:

$$\frac{d}{dx} [T(x)] = - [T(x)] [A(x)] \quad (12)$$

which is a first order matrix differential equation defining the transmission matrix for the continuous system of interest.

One can obtain as many initial conditions as required to solve eq. (12) by shrinking $\Delta x \rightarrow 0$ in eq. (11) which gives:

$$\begin{aligned} \{\Psi(0)\} &= [T(0)] \{\Psi(0)\} \\ \therefore [T(0)] &= [I] \end{aligned} \quad (13)$$

Substituting this result into eq. (12) gives

$$[T(0)]' = -[T(0)][A(0)] = -[A(0)]. \quad (14)$$

Further differentiation of eq. (12) and substitutions from eqs. (13) and (14) gives:

$$[T(0)]'' = +[A(0)]^2 - [A(0)]' \quad (15)$$

$$\begin{aligned} [T(0)]''' &= -[A(0)]^3 + [A(0)]' [A(0)] + \\ & 2 [A(0)][A(0)]' - [A(0)]'' \end{aligned} \quad (16)$$

This process can be continued to obtain as many initial conditions as required to evaluate the constants which arise in solving eq. (12).

APPROXIMATE TRANSMISSION MATRICES BY POWER SERIES EXPANSION

For non-uniform systems where a closed form solution cannot be found for eq. (12) an approximate method would be applicable. Pestel and Leckie [2] have briefly described how the Runge-Kutta and Picard iteration methods can be employed to numerically integrate the state vector equation, eq. (8), resulting in a transmission matrix. A more direct method is to expand the differential equation defining the transmission matrix in a Maclaurin series and retain as many terms as necessary to provide the accuracy desired.

Consider a single transmission segment and expand $[T(x)]$ in a Maclaurin series about the origin of this continuous segment giving:

$$\begin{aligned} [T(x)] &= [T(0)] + x[T(0)]' + \frac{x^2}{2!} [T(0)]'' \\ &+ \frac{x^3}{3!} [T(0)]''' + \dots \text{higher order terms} \end{aligned} \quad (17)$$

The condition for the Maclaurin series that the function be piecewise analytic in this case requires through eq. (12) that the variables in $[A(x)]$ be piecewise analytic. In particular these functions must be analytic in the region between the points i and $i+1$ of the continuum for which the transmission matrix is being approximated.

If one uses the initial conditions from eqs. (13) through (16) and substitutes them into eq. (17) we obtain the approximate transmission matrix in terms of the system parameters:

$$\begin{aligned} [T(x)] &= [I] - x[A(0)] + \frac{x^2}{2!} \{ [A(0)]^2 \\ &+ [A(0)]' \} + \frac{x^3}{3!} \{ -[A(0)]^3 + \\ &+ [A(0)]' [A(0)] + 2[A(0)][A(0)]' - [A(0)]'' \} \\ &+ \dots - O(x)^4 + \dots \end{aligned} \quad (18)$$

This expression is valid for any system once the governing $[A]$ matrix has been determined. The above series form of the transmission matrix has an infinite number of terms. The objective herein has been to assess the accuracy of the series when applied to a Bernoulli-Euler beam element and truncated after the second, third, and fourth terms.

EVALUATION OF THE APPROXIMATE TRANSMISSION MATRIX

To evaluate the accuracy of describing principal modes via the approximate transmission matrix, several classes of uniform and non-uniform beams were treated. One-dimensional

systems, i.e., vibration systems governed by the one-dimensional wave equation, have been previously examined [5]. For the one-dimensional system the matrix is of second order and it has been found that a matrix including the first four terms describes principal modes to a level of accuracy equal to or better than the best lumped parameter models.

Error criteria chosen for the accuracy comparison was that of the principal mode frequency root error. This parallels comparisons made by other authors [6], [7], [8], [9] for several types of lumped parameter models and the approach termed the consistent mass matrix. Frequency root errors were assessed when the approximate transmission matrix was applied to the uniform beam with fixed-fixed and fixed-free boundary conditions. Also, several cases of non-uniform beams were treated with fixed-pinned and fixed-free ends.

The boundary conditions chosen with the uniform beam were selected such that a comparison could be made with commonly used lumped parameter models which display the following characteristics:

- (1) If neither end is free the errors are proportional to $1/N^4$ for large N .
- (2) In cases where one or both ends are free the errors are proportional to $1/N^2$ for large N .

Hence, an evaluation with the chosen boundary conditions should provide a basis of comparison between the lumped parameter models and the present approach.

For the uniform beam the two functions occurring in $[A(x)]$ are constants; hence, eq. (18) reduces to:

$$[T(x)] = [I] - x[A(0)] + \frac{x^2}{2} [A(0)]^2 - \frac{x^3}{3!} [A(0)]^3 + \dots \quad (19)$$

In appendix A the matrix $[T(x)]$ is expanded including the first four terms as shown above. The matrix describes one segment of a beam. For a beam of length L divided into N segments, $x = L/N$. Applying eq. (2) one can write:

$$\{\psi\}_{\text{input}} = [T]\{\psi\}_{\text{output}}$$

where $[T]$ is the product of N matrices, which in this case are equal, all of the form of eq. (19). To find the frequency roots a 2×2 frequency determinant, selected from the total transmission matrix according to the boundary conditions chosen, is iteratively solved.

This procedure was completed for the two boundary conditions chosen and the errors in

the first three principal mode frequency roots were examined as a function of N . Figures 4 and 5 give typical results. It was found that these errors behave approximately proportional to $1/N^2$ when the first two or three terms in the series are used and as $1/N^3$ when the first four terms are retained in each matrix.

An evaluation of the frequency root errors was also made for several non-uniform beams. First, a linearly tapered rectangular section with boundary conditions of fixed-pinned ends was chosen. Mabie [10] has treated this problem and a closed form solution is available to establish frequency root errors. The transmission matrix was established for a general segment as shown in Fig. (6).

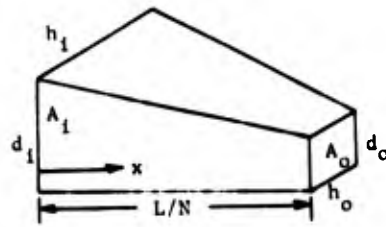


Fig. 6 Non-Uniform Element

For a beam element as shown in Fig. 6 where the depth and/or height vary linearly, the area and moment of inertia are polynomials of the form:

$$\left. \begin{aligned} A(x) &= A_1(1+c_1x+c_2x^2) \\ I(x) &= I_1(1+B_1x+B_2x^3+B_3x^3+B_4x^4) \end{aligned} \right\} \quad (20)$$

where subscript i refers to the input face and ρ and E have been assumed to be constant. The approximate transmission matrix including four terms in the series is presented for a segment of the linearly tapered beam in appendix B.

A second non-uniform system used was a linearly tapered circular cross section beam. In this beam the diameter varies linearly. It can be shown that the cross sectional area and inertia of a typical segment for this beam satisfies the same order polynomial as those for the beam in Fig. 6, see eq. (20). The C_1 and B_1 constants for this case are also given in appendix C. Boundary conditions chosen for the circular beam were fixed-free ends. This corresponds to a case treated by G. W. Housner [11] where the exact frequency roots are given.

Two typical sets of curves are presented here to describe the error comparisons for the non-uniform systems. Figure 7 shows the error level in the first principal mode when N equal

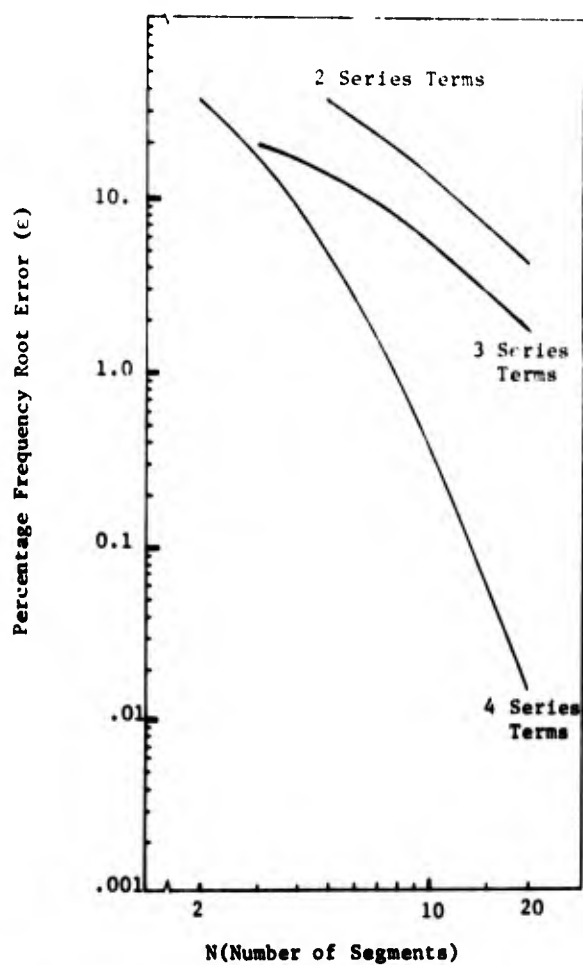


Fig. 4 First Mode Frequency Root Errors For Uniform Beams with Fixed-Fixed Ends

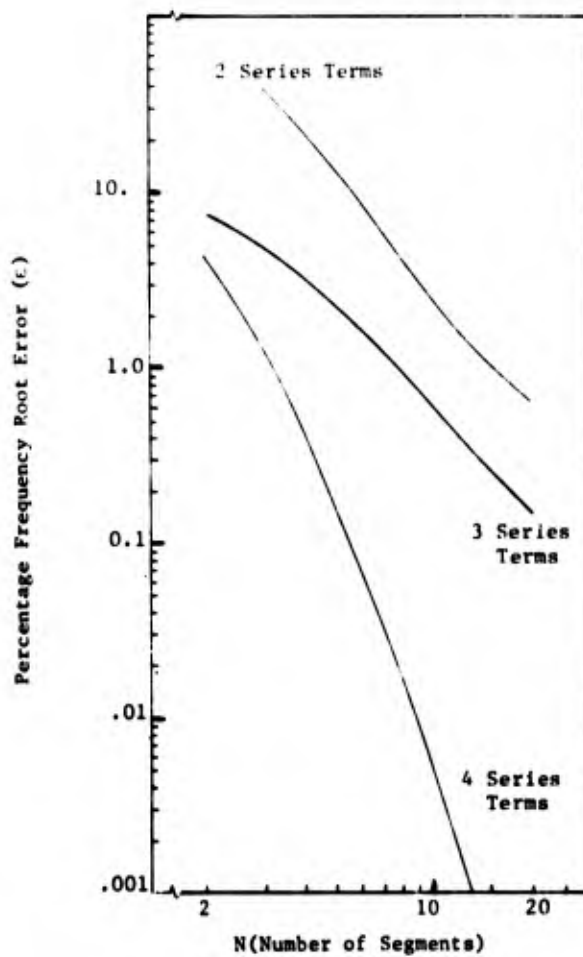


Fig. 5 First Mode Frequency Root Errors For Uniform Beams With Fixed-Free Ends



Fig. 7 First Mode Frequency Root Errors for Rectangular Section Beams With Fixed-Pinned Ends ($H=1.0$ and $D=0.5$)

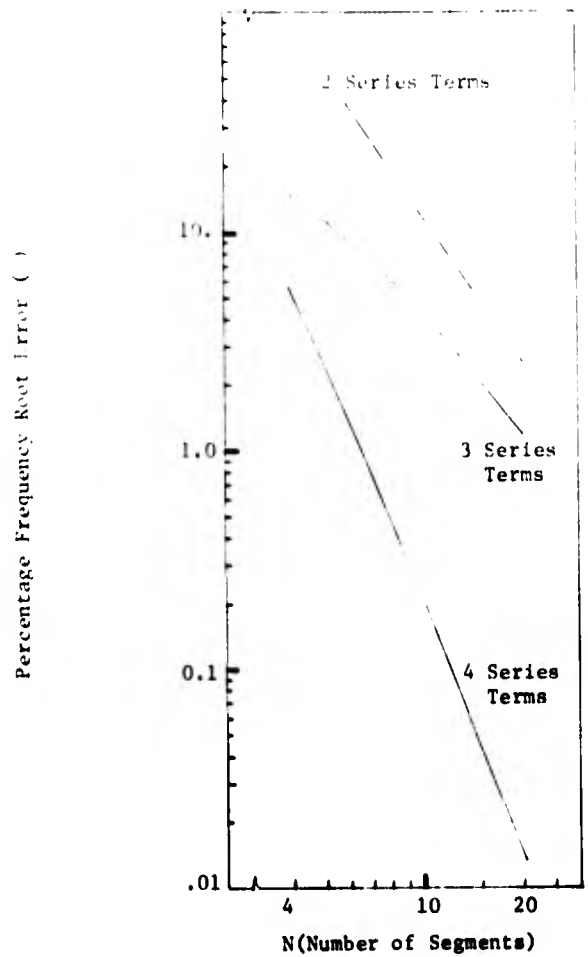


Fig. 8 First Mode Frequency Root Errors for Rectangular Section Beams With Fixed-Pinned Ends ($H=0.5$ and $D=1.0$)

length segments are used to describe a fixed-pinned beam which has constant width and a variable depth with the depth ratio (D) equal to 0.5. Figure 8 represents the same type of comparison for a constant depth, variable width beam whose width ratio (H) was chosen to be 0.5. Note both sets of curves describe the error behavior for approximate transmission matrices which retain two, three, or four terms in the series. Results for the second and third mode frequency roots were similar to those shown for the first mode.

With four terms in the series for the non-uniform beam the frequency root errors are proportional to $1/N^3$ and when two or three terms are retained errors are proportional to $1/N^2$. This behavior was also found typical for the circular non-uniform cross section beam and the uniform beams.

DIMENSIONLESS FREQUENCY ROOTS FOR NON-UNIFORM BEAMS OF RECTANGULAR SECTION

Non-dimensional frequency roots have been calculated for wedge shaped beams as shown in Fig. 6 using the approximate method described herein. Boundary conditions of fixed-fixed and pinned-pinned ends were selected as data for these types of beams has not been found in the literature.

The dimensionless parameter β ,

$$\beta = \frac{1}{10} \left[\frac{\omega^2 A_c L^4}{EI_0} \right] \quad (19)$$

has been calculated for these beams and is presented in table form in Appendix D. These calculations were completed using the four term matrix and 20 segments per beam which should constitute no more than 1% error in the highest mode (third mode) calculated. Typical constants were chosen in order to complete the calculations and the results were put into the dimensionless form. The β parameter is given for different depth (D) and width (H) ratios where D and H are defined by:

D = ratio of depth at small end to depth at large end

H = ratio of width at small end to width at large end

Note these results apply only to the linearly tapered rectangular beams.

CONCLUSIONS

On the basis of the operations performed and results obtained, the following conclusions are given:

1. The approximate transmission matrix gives consistent principal mode frequency root errors when applied to uniform and non-uniform beam elements.

2. Commonly used lumped parameter models have principal mode frequency root errors which are proportional to $1/N^2$ or $1/N^4$, depending upon end conditions. In comparison, the four term approximate transmission matrix produces errors proportional to $1/N^3$.
3. The approximate transmission matrix can be applied to single, non-uniform beam elements more directly than lumped parameter models as this approach uses directly the variable mass and bending rigidity functions, and their derivatives, rather than equivalent cross sectional properties.
4. The approximate transmission matrix approach can be used with higher order beam theories if the governing [A] matrix is extended to include the elastic or dynamic affects appropriate to such theories.
5. The application of the approximate matrix follows that of the general transmission matrix theory. Hence, it is ideally suited for any system of elements in an end-to-end arrangement, but is not as easily applied to systems with a large number of branched elements.

NOMENCLATURE

A	= Cross sectional area
[A]	= Matrix which characterizes the system
E	= Young's Modulus of Elasticity
I	= Area moment of inertia
[I]	= Identity matrix
M	= Bending moment
N	= Number of segments
[T]	= Transmission matrix
V	= Transverse shear force
w	= Transverse beam deflection
ϕ	= Slope of the beam
{ ψ }	= State vector (column matrix)
ρ	= Mass density per unit volume
ω	= Circular frequency
ω_e	= Exact frequency root
ω_A	= Approximate frequency root
ϵ	= $ (\omega_e - \omega_A)/\omega_e \times 100$

APPENDIX A

MATRIX FORMS FOR THE UNIFORM SYSTEM

$$[A(0)] = \begin{bmatrix} 0 & 0 & a & 0 \\ -1 & 0 & 0 & 0 \\ 0 & 0 & 0 & 1 \\ 0 & -b & 0 & 0 \end{bmatrix} \quad \text{Where} \quad \begin{aligned} a &= \rho A(0)\omega^2 \\ b &= 1/EI(0) \end{aligned}$$

$$[A(0)]^2 = [A(0)][A(0)] = \begin{bmatrix} 0 & 0 & 0 & a \\ 0 & 0 & -a & 0 \\ 0 & -b & 0 & 0 \\ b & 0 & 0 & 0 \end{bmatrix}$$

$$[A(0)]^3 = [A(0)]^2[A(0)] = \begin{bmatrix} 0 & -ab & 0 & 0 \\ 0 & 0 & 0 & -a \\ b & 0 & 0 & 0 \\ 0 & 0 & ab & 0 \end{bmatrix}$$

$$[T(x)] = \begin{bmatrix} 1 & \frac{x^3 ab}{6} & -xa & \frac{x^2 a}{2} \\ x & 1 & \frac{x^2 a}{2} & \frac{x^3 a}{6} \\ \frac{x^3 b}{6} & \frac{x^2 b}{2} & 1 & -x \\ \frac{x^2 b}{2} & xb & \frac{-x^2 ab}{6} & 1 \end{bmatrix}$$

APPENDIX B

MATRIX FORMS FOR NON-UNIFORM SYSTEMS

$$[A(0)] = \begin{bmatrix} 0 & 0 & Z & 0 \\ -1 & 0 & 0 & 0 \\ 0 & 0 & 0 & 1 \\ 0 & -Y & 0 & 0 \end{bmatrix} \quad \begin{aligned} Z &= \rho A_1 \omega^2 \\ Y &= 1/EI_1 \end{aligned}$$

$$[A(0)]' = \begin{bmatrix} 0 & C_1 Z & 0 & 0 \\ 0 & 0 & 0 & 0 \\ 0 & 0 & 0 & 0 \\ 0 & B_1 Y & 0 & 0 \end{bmatrix} \quad [A(0)]'' = \begin{bmatrix} 0 & 0 & 2C_2 Z & 0 \\ 0 & 0 & 0 & 0 \\ 0 & 0 & 0 & 0 \\ 0 & (-2B_1 Y + 2B_2 Y) & 0 & 0 \end{bmatrix}$$

$$[A(0)]^2 = \begin{bmatrix} 0 & 0 & 0 & Z \\ 0 & 0 & -Z & 0 \\ 0 & -Y & 0 & 0 \\ Y & 0 & 0 & 0 \end{bmatrix} \quad [A(0)]' [A(0)] = \begin{bmatrix} 0 & 0 & 0 & C_1 Z \\ 0 & 0 & 0 & 0 \\ 0 & 0 & 0 & 0 \\ -YB_1 & 0 & 0 & 0 \end{bmatrix}$$

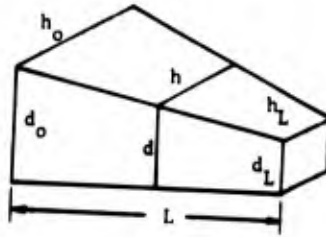
$$[A(0)][A(0)]' = \begin{bmatrix} 0 & 0 & 0 & 0 \\ 0 & 0 & -C_1 Z & 0 \\ 0 & YB_1 & 0 & 0 \\ 0 & 0 & 0 & 0 \end{bmatrix}$$

$$[A(0)]^3 = \begin{bmatrix} 0 & -ZY & 0 & 0 \\ 0 & 0 & 0 & -Z \\ Y & 0 & 0 & 0 \\ 0 & 0 & ZY & 0 \end{bmatrix}$$

$$[T(x)] = \begin{bmatrix} 1 & \frac{1}{6} X^3 ZY & (-XZ - \frac{1}{2} X^2 C_1 Z - \frac{1}{3} X^3 C_2 Z) & (\frac{1}{2} X^2 Z + \frac{1}{6} X^3 C_1 Z) \\ X & 1 & (-\frac{X^2}{2} Z - \frac{1}{3} X^3 C_1 Z) & (\frac{1}{6} X^3 Z) \\ -\frac{1}{6} X^3 Y & (-\frac{1}{2} X^2 Y + \frac{1}{3} X^3 YB_1) & 1 & -X \\ (\frac{1}{2} X^2 Y - \frac{1}{6} X^3 YB_1) & XY - \frac{1}{2} X^2 YB_1 + \frac{1}{6} X^3 Y(2B_1^2 - 2B_2) & (-\frac{1}{6} X^3 ZY) & 1 \end{bmatrix}$$

APPENDIX C

RECTANGULAR CROSS SECTION SEGMENT



- h_0 = Width at large end, $x = 0$
- d_0 = Depth at large end, $x = 0$
- h_L = Width at small end, $x = L$
- d_L = Depth at small end, $x = L$

- L = Length of the beam segment
- H = h_L/h_0 , Width ratio
- D = d_L/d_0 , Depth ratio

With the above definition the constants in the matrix (and expression 20) become:

$$\begin{aligned} C_1 &= -(2 - 2H)/L \\ C_2 &= (1 - H)(1 - D)/L^2 \\ B_1 &= -\{3(1 - D) + (1 - H)\}/L \\ B_2 &= 3\{(1 - D)^2 + (1 - H)(1 - D)\}/L^2 \\ B_3 &= -\{(1 - D)^3 + 3(1 - H)(1 - D)^2\}/L^3 \\ B_4 &= \{(1 - H)(1 - D)^3\}/L^4 \end{aligned}$$

CIRCULAR CROSS SECTION SEGMENT

- d_0 = diameter at large end, $x = 0$
- d_L = diameter at small end, $x = L$
- D = d_L/d_0 = diameter ratio

For the circular cross section case the C_i and B_i constants have the value:

$$\begin{aligned} C_1 &= -2(1 - D)/L \\ C_2 &= (1 - D)^2/L^2 \\ B_1 &= -4(1 - D)/L \\ B_2 &= 6(1 - D)^2/L^2 \\ B_3 &= -4(1 - D)^3/L^3 \\ B_4 &= (1 - D)^4/L^4 \end{aligned}$$

APPENDIX D

TABLE I First mode dimensionless frequency parameter - Fixed-Fixed ends

D	H=0.0	H=0.2	H=0.4	H=0.6	H=0.8	H=1.0
0.0	8.9740	7.7676	6.9748	6.4256	6.0181	5.7013
0.1	11.6416	11.6292	11.1152	10.6423	10.2432	9.9084
0.2	14.3586	15.3701	15.1065	14.7360	14.3670	14.0294
0.3	17.0394	19.0380	19.0802	18.8031	18.4699	18.1543
0.4	19.7089	22.7287	23.0425	22.9014	22.6418	22.3488
0.5	22.3913	26.4476	27.0684	27.0815	26.8979	26.6564
0.6	25.1058	30.2224	31.1872	31.3598	31.2640	31.0618
0.7	27.8448	34.0741	35.3815	35.7382	35.7382	35.6140
0.8	30.6401	38.0227	39.6822	40.2432	40.3903	40.2677
0.9	33.4798	42.0000	44.0628	44.8475	45.0933	45.0933
1.0	36.3405	46.0703	48.5921	49.5652	49.9735	40.0554

TABLE II Second mode dimensionless frequency parameter - Fixed-Fixed ends

D	H=0.0	H=0.2	H=0.4	H=0.6	H=0.8	H=1.0
0.0	55.9354	49.3481	46.3026	44.3965	43.0316	41.9469
0.1	80.9533	79.8806	77.6961	75.9671	74.5411	73.3301
0.2	105.7369	109.8734	108.2370	107.2971	105.9666	104.7430
0.3	130.3917	139.6342	139.6414	138.6374	137.4202	136.2691
0.4	155.0867	169.7250	170.9336	170.3791	169.4234	168.2303
0.5	180.1869	200.0252	202.7633	202.7633	202.0222	201.1182
0.6	205.6858	231.1670	235.1737	235.8845	235.5290	234.8189
0.7	231.9892	262.8064	268.5930	270.1128	270.1128	269.3523
0.8	258.4458	295.2795	303.0215	305.7144	305.7144	305.7144
0.9	285.5476	328.8042	337.2539	340.0947	341.5193	341.5193
1.0	312.7712	362.6592	372.7219	378.7056	378.7056	379.3064

TABLE III Third mode dimensionless frequency parameter - Fixed-Fixed ends

D	H=0.0	H=0.2	H=0.4	H=0.6	H=0.8	H=1.0
0.0	193.4012	171.7901	166.8218	160.5034	158.6267	155.9168
0.1	296.5142	265.9878	284.3491	280.2000	275.8250	273.7781
0.2	400.8418	406.1902	402.8970	398.9126	395.8359	393.6892
0.3	504.3540	521.8347	521.8347	520.4253	516.2085	515.4197
0.4	609.8870	640.8113	645.4597	640.7625	638.7910	638.9568
0.5	709.7261	755.0422	766.6921	769.1563	765.0422	763.1223
0.6	821.5481	885.5708	894.7815	896.6289	892.9335	893.9731
0.7	932.0984	1013.4370	1023.2890	1026.7480	1026.7480	1026.7480
0.8	1046.6260	1141.3030	1161.4680	1161.4680	1161.4680	1165.6780
0.9	1162.2570	1271.2560	1291.1450	1298.9220	1298.9910	1297.8100
1.0	1279.5230	1406.7660	1432.3530	1446.4060	1442.8860	1446.4060

TABLE IV First mode dimensionless frequency parameter - Pinned-Pinned ends

D	H=0.0	H=0.2	H=0.4	H=0.6	H=0.8	H=1.0
0.0	0.0859	0.2371	0.3152	0.3661	0.4024	0.4200
0.1	0.6608	1.0760	1.2583	1.3716	1.4501	1.5080
0.2	1.3595	1.8899	2.1163	2.2541	2.3479	2.4160
0.3	2.1190	2.7229	2.9753	3.1255	3.2258	3.2973
0.4	2.9276	3.5836	3.8515	4.0069	4.1081	4.1785
0.5	3.7823	4.4738	4.7494	4.9046	5.0028	5.0689
0.6	4.6713	5.3935	5.6708	5.8241	5.9130	5.9721
0.7	5.6003	6.3420	6.6159	6.7583	6.8404	6.8901
0.8	6.5645	7.3187	7.5848	7.7189	7.7856	7.8238
0.9	7.5622	8.3229	8.5777	8.6933	8.7538	8.7824
1.0	8.5947	9.3538	9.5925	9.6914	9.7305	9.7401

TABLE V Second mode dimensionless frequency parameter - Pinned-Pinned ends

D	H=0.0	H=0.2	H=0.4	H=0.6	H=0.8	H=1.0
0.0	26.3564	21.5881	19.8416	18.9422	18.3945	18.0237
0.1	37.0041	35.3907	34.1425	33.4032	32.9328	32.5920
0.2	48.4684	47.8833	46.7755	46.0677	45.6109	45.2983
0.3	60.1833	60.2408	59.2292	58.5481	58.0996	57.7682
0.4	72.2437	72.8051	71.8670	71.1980	70.8078	70.4996
0.5	84.6753	85.6724	84.8529	84.2497	83.8429	83.5781
0.6	97.5209	99.0511	98.2846	97.6734	97.2924	97.0262
0.7	110.8260	112.7025	112.0072	111.5584	111.1512	111.0699
0.8	124.5076	126.8000	126.2791	125.7594	125.5430	125.3702
0.9	138.8032	141.3608	140.9024	140.6277	140.4448	140.4448
1.0	153.3497	156.6163	156.0373	155.8446	155.8446	155.8446

TABLE VI Third mode dimensionless frequency parameter - Pinned-Pinned ends

D	H=0.0	H=0.2	H=0.4	H=0.6	H=0.8	H=1.0
0.0	116.3144	95.3875	90.7677	88.2125	86.6850	85.6462
0.1	176.2207	165.9484	161.5316	159.2456	157.6051	155.2500
0.2	237.5765	230.6881	226.4393	224.1876	222.5943	221.4731
0.3	299.2776	294.7495	290.7991	288.5549	286.7881	285.8411
0.4	362.3066	359.7258	355.6392	353.3142	352.2271	351.2139
0.5	426.9329	426.3750	422.5586	420.3804	419.1157	418.1287
0.6	493.9570	494.7290	491.3020	489.4221	487.9719	487.4604
0.7	562.9319	565.0398	562.1084	559.9150	558.8198	557.5435
0.8	633.6907	637.8745	635.1487	632.3315	631.2649	630.8770
0.9	707.0974	712.0308	709.1506	707.3025	707.0974	706.4819
1.0	781.6096	783.9626	786.3640	784.6338	784.2014	784.2014

REFERENCES

1. C. T. Molloy, "Four Pole Parameters in Vibration Analysis", Colloquium on Mechanical Impedance Methods for Mechanical Vibrations, Applied Mechanics Division ASME, pp. 43-68, 1958.
2. E. C. Pestel and F. A. Leckie, "Matrix Methods in Elastomechanics", pp. 51-152, McGraw-Hill, New York, 1963.
3. S. Rubin, "Transmission Matrices for Vibration and Their Relation to Admittance and Impedance", J. of Engineering for Industry, Trans. ASME, Vol. 86, pp. 6-21, Series B, No. 1, 1964.
4. L. A. Pipes, "Direct Computation of Transmission Matrices of Electrical Transmission Lines", Unpublished notes at Aerospace Corp., El Segundo, Calif., 1965.
5. R. D. Rocke, "Transmission Matrices and Lumped Parameter Models for Continuous Systems", Dynamics Laboratory Report, Calif. Institute of Technology, pp. 102-107, 1966.
6. R. K. Livesley, "The Equivalence of Continuous and Discrete Distributions in Certain Vibration Problems", Quarterly Journal of Mechanics and Mathematics, Vol. 8, pp. 353-360, 1955.
7. G. M. L. Gladwell, "The Approximation of Uniform Beams in Transverse Vibration by Sets of Masses Elastically Connected", Proc. 4th U.S. Nat'l. Congress of Applied Mechanics, pp. 169-176, 1962.
8. F. A. Leckie and G. M. Lindberg, "The Effect of Lumped Parameters on Beam Frequencies", Aeronautical Quarterly, Vol. 14, pp. 224-240, 1963.
9. J. S. Archer, "Consistent Mass Matrix for Distributed Mass Systems", J. of The Structural Division, A.S.C.E., Vol. 89, No. ST4, pp. 161-178, Aug. 1963.
10. H. H. Mable, "Transverse Vibrations of Tapered Cantilever Beams with End Support", J. of The Acoustical Society of America, Vol. 44, No. 6, pp. 1739-1741, 1968.
11. G. W. Housner and W. D. Keightley, "Vibration of Linearly Tapered Cantilever Beams", J. of The Engineering Mechanics Division, A.S.C.E., Vol. 88, No. EM2, pp. 95-126, April 1962.

BLANK PAGE

MEASUREMENT OF MOMENT-CURVATURE RELATIONSHIP FOR STEEL BEAMS

V. H. Neubert and W. Vogel
The Pennsylvania State University
University Park, Pa.

The paper presents some of the results of an experimental determination of the moment-curvature relationship for steel beams one inch wide and one-eighth inch thick. Data for a fully annealed steel and a tempered ground tool steel are reported. Specimens consisted of three parallel cantilever beams carrying a common tip mass. Tests were performed on a drop table shock machine at the Naval Research Laboratory. Accelerations of the tip mass were used to compute inertia forces and the resulting beam moments. Curvature was obtained by measuring strain at various stations on the beam.

Typical accelerometer and strain records versus time are presented. Dynamic moment-curvature plots are compared with static curves. The results with respect to increased yield and time delay in initiation of unloading are discussed. Advantages and disadvantages of this type of test are considered.

INTRODUCTION

It is presently difficult in design analysis of complex steel structures to predict the dynamic response after yielding occurs. This is partly due to the fact that accounting for dynamic effects in constitutive relationships is not completely understood. Also, much emphasis has been placed on dynamic tension or compression testing, but comparatively little data is available for elastic-plastic bending behavior where the material is deformed only slightly into the plastic range. The theoretical development of constitutive relationships in terms of moment, curvature and time based on tensile data is complicated by the fact that, during bending, strain rates vary over the beam cross-section. It was therefore felt advisable to conduct dynamic bending tests in which sufficient instrumentation was used so that the applied moment and the associated curvature could be directly measured as a function of time. The purpose of the present report is to record test procedure and present some preliminary results of bending tests of combinations of steel beams.

BACKGROUND

No attempt will be made here to review the literature dealing with elastic-plastic response of material. In references [1], [2]

and [3], literature surveys are given. Constitutive relationships for dynamic behavior have been proposed by Malvern[4] and others. In the present series of tests, Stanovsky[1] used a bilinear moment-curvature relationship with increased yield, but without rate effects. He tested two steels, a high strength steel and a mild steel. Agreement was good for curvature-time predictions, for the high strength steel. However, the mild steel was relatively sluggish in behavior, so experimental timewise curvature tended to lag behind predicted curvature. Maximum moment and maximum curvature did not happen at the same time. This led to interest in the following equation which has been considered by Plass[5]:

$$\dot{k} = \frac{\dot{M}}{EI} + R \left[\frac{M - M_{st}}{M_{st}} \right] N$$

where

k = curvature
 M = dynamic bending moment
 M_{st} = static bending moment for same curvature
 EI = elastic bending stiffness
 R and N = material constants

The equation applies in the elastic and plastic ranges during loading. In the elastic range M is practically equal to M_{st} so the term $(M - M_{st})$ is small and the usual moment-curvature relationship remains, with EI the bending stiffness. In the plastic range $\dot{M} = \frac{dM}{dt}$ may be small compared to the other term. In theoretical studies it has usually been assumed that $(M - M_{st})$ is greater than or equal to zero. Brown [6,3] conducted tests where he measured the moment-curvature relationship by a method similar to that used in the present tests, but using only one cantilever beam. He suggested some values for R with $N=1$.

APPARATUS

The tests reported here were conducted on the drop table shock machine at the Naval Research Laboratory. Each test run was given an associated drop number. The tests performed are outlined in references [7] and [8]. Some typical results are presented here.

The apparatus is shown in elevation view in Fig. 1 and in plan view in Fig. 2. Three beam specimens were used simultaneously as shown in Fig. 2. They were clamped at the base between the upper and lower clamping blocks, which were both $1\frac{1}{2}'' \times 6'' \times 8''$ and were made of mild steel. Two hardened steel bearing plates $\frac{1}{4}'' \times 6'' \times 8''$ were used to line the jaws of the clamp. In addition, six hardened fillers were located between the bearing plates and the beam specimens. These were $\frac{3}{16}'' \times 1\frac{1}{4}'' \times 6''$ when the $\frac{1}{8}''$ thick specimens were tested. The clamping blocks were bolted to a mild steel anvil block $3\frac{3}{4}'' \times 8'' \times 8''$ which was in turn bolted to the drop table of the shock machine. The arrangement was symmetrical with respect to the center line so that 6" of the specimen length was in the clamp, with $5\frac{3}{4}''$ protruding from each side. The beams carried a common tip mass, composed primarily of two steel bars $1\frac{1}{2}'' \times 1\frac{1}{2}'' \times 8''$. In order to keep the rotary inertia fairly constant for different thickness specimens, the vertical distance between the faces of the two bars was kept at $\frac{1}{2}''$ by using hardened fillers which were $\frac{3}{16}'' \times 1\frac{1}{4}'' \times 1\frac{1}{2}''$ for the $\frac{1}{8}''$ specimens.

Accelerometers were bolted to $1'' \times 1'' \times 1''$ aluminum mounting blocks on the tip mass and to the upper clamping block. To keep the apparatus completely symmetrical, accelerometers were placed on both tip masses [Fig. 3a]. Signals were recorded only from accelerometers A1 thru A8. Strain gauges were located only on the South side of the clamping blocks and were designated S1 thru S9.

INSTRUMENTATION

Some of the initial goals in taking the

measurements were (1) to determine whether the structural symmetry would carry through to acceleration and strain response, (2) to measure base motion in terms of vertical translation and rotation about the two horizontal axes, (3) to measure strain in the three beams near the base, and (4) to try to deduce the shear force in the beam from strain measurements. For number (4) two strain gauges were located $\frac{1}{4}''$ and $\frac{5}{8}''$ respectively from the tip mass on each specimen. Knowing measured strain and the constitutive relationship for the material, moment could theoretically be deduced. By equilibrium of the segment between gauges, the shear force would be equal to the difference in moment divided by the gauge spacing, provided inertia forces of the beam segments could be neglected. The pair of gauges was located near the tip mass because this was the region of the beam most likely to remain elastic and the elastic constitutive relationship should be well understood.

The accelerometers were CEC of 250 g capacity. Each weighed 0.23#.

The strain gauges were Budd Metalfilm Strain Gages, $\frac{1}{8}''$ long, C6-121-A, with Gauge Factor = $2.06 \pm 0.5\%$ and resistance = 120 Ω .

Signals from the nine strain gauges were recorded using one fourteen channel FM magnetic tape recorder, and the eight accelerometer signals were recorded on a similar recorder. One channel of each was used for a 1000 cycle per second timing signal. On this timing signal was superimposed a spike from a special circuit which was completed when the drop table contacted the lead cone decelerator on the base of the shock machine. The spike served to cross-relate the signals on the two tapes. Later it was thought advantageous to record fewer signals, so they could all be recorded on one tape.

MATERIALS

Three different steels were used: a cold-rolled steel as received, a fully annealed 1020 steel, and a tempered ground tool steel trade-named Warplis manufactured by Pittsburgh Tool Steel Wire Company, Monaca, Pennsylvania. The approximate analysis of Warplis is Carbon 0.90, Silicon 0.25, Manganese 1.10, Chrome 0.50, Tungsten 0.50 and Vanadium 0.15.

STATIC TESTS

Static bending tests were performed for all three materials. Where it was not certain that the bars had all come from the same material batch, the static tests were performed on the 6" section of specimen that had been clamped during the dynamic tests. The bars were clamped in a manner similar to the arrangement for the dynamic tests, except that one bar was tested at a time. The load

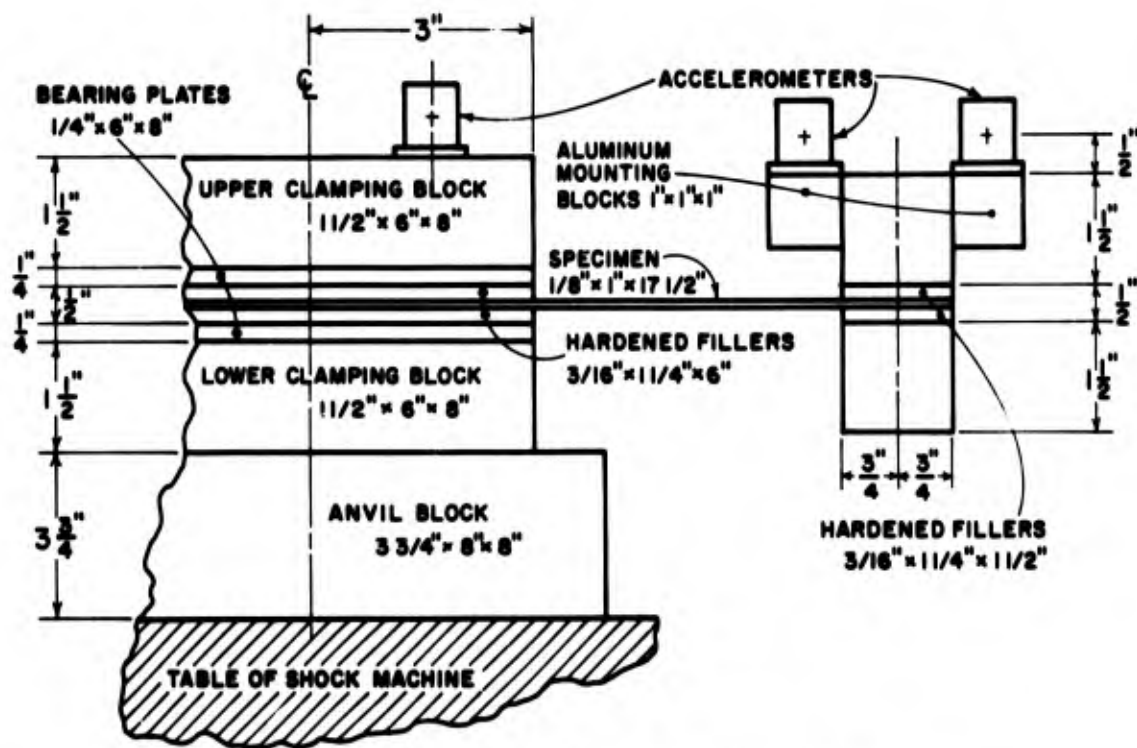


Fig. 1 Elevation View of Apparatus on Shock Machine

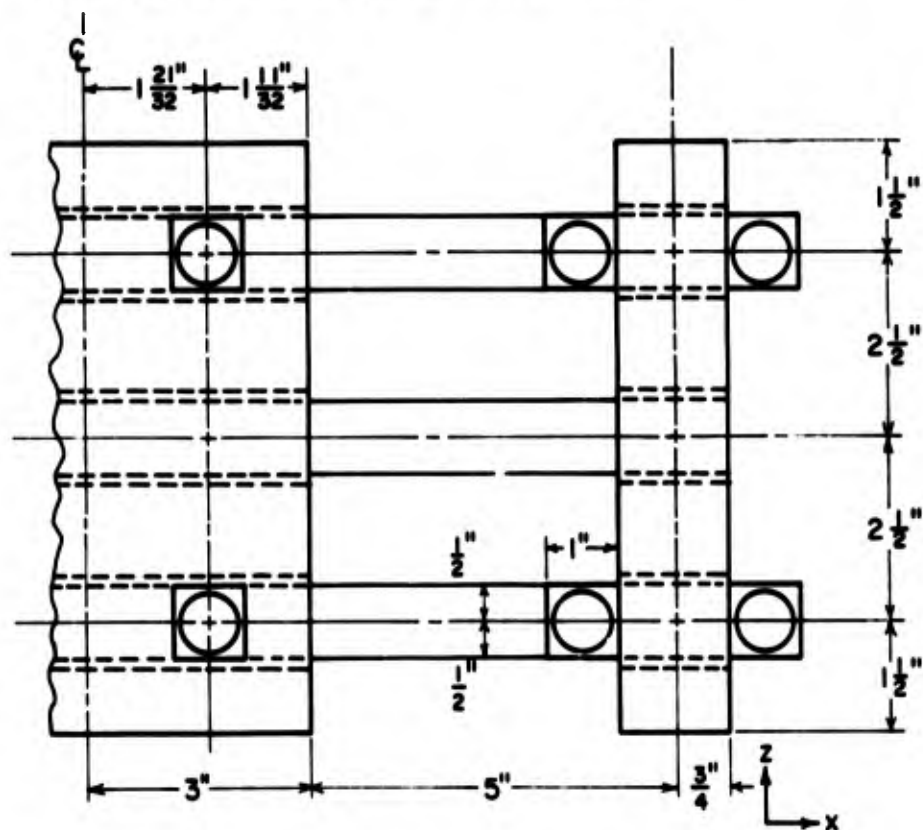


Fig. 2 Plan View of Apparatus

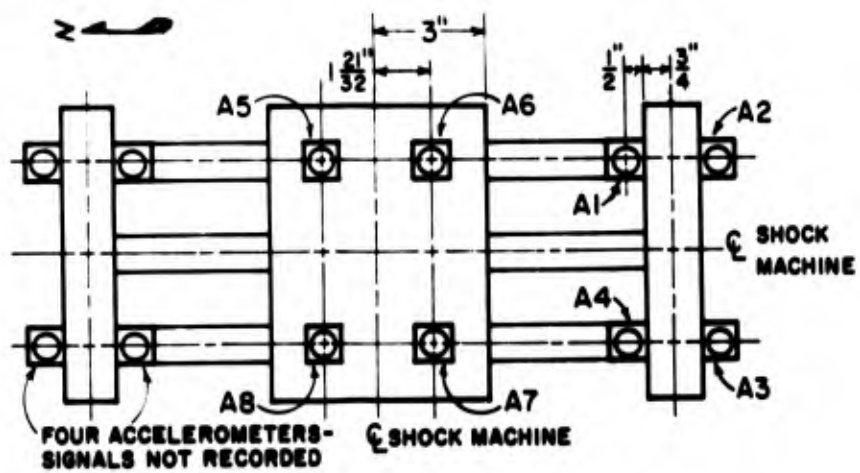


Fig. 3a Accelerometer Locations

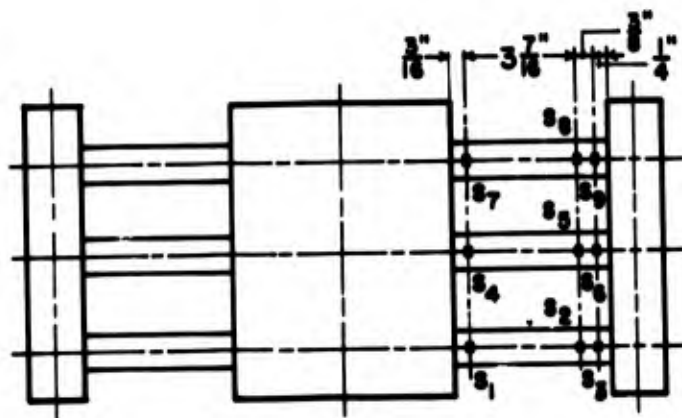


Fig. 3b Strain Gauge Locations

Fig. 3 Pick-up Locations

was applied in a controlled deformation compression tester arranged so the applied force was always vertical and passed through a point on the beam 5" from the base. The moment arm therefore decreased as the displacement of the tip became large. Force, tip displacement, moment arm and strain 3/16" from the clamp were recorded. Curvature k was obtained as the measured strain ϵ over the half depth of the beam specimen or

$$k = \frac{2\epsilon}{t}$$

DYNAMIC TEST RESULTS

The drops discussed here are listed in Table 1.

Table 1. Tests Discussed

Drop No.	Material	Beams	Drop Height	Lead Cone Weight (angle)
7	Warplis	New	15"	6 oz. (90°)
8	Warplis	Same as 7	24"	12 oz. (90°)
35	Fully Annealed	New	5-1/2"	6 oz. (120°)
37	Warplis	New	15"	6 oz. (90°)

The drop numbers are listed in the first column and the specimen material in the second column. Several drops were made with the same specimens in place. In column three "new" means this was the first drop for a set of beams. Drop 8 was a higher drop than Drop 7, but the same beams were re-loaded. The lead cone decelerators used for each drop are identified by cone weight and angle. The first pulse of the base acceleration was nearly triangular with a duration of about 0.011 seconds. In Fig. 4 the average of the four base accelerometers

$A5+A6+A7+A8$ is shown after digital filtering with a low pass filter having a cut-off of about 300 cycles per second. In Fig. 5 a typical tip mass acceleration record from accelerometer A3 is shown as plotted from digitized data. The time interval for digitizing was 0.0002 seconds and the data has not been filtered. It was judged that the ragged nature of the signal was due to noise. In Fig. 6, digitally filtered accelerations from each of the four tip mass accelerometers are plotted for Drop 37. Generally structural symmetry existed in the response except for the early time when A1 and A4 were not identical. Strain data was quite smooth without filtering, but it was filtered the same as accelerations so any time delay due to filtering would occur in all data. In Fig. 7 the base strain S4 on the center beam specimen is compared with the average $S1+S4+S7$. The difference is an indication of lack of symmetry in the deformation of the beams.

DATA EVALUATION AND RESULTS

Computations summarized here deal with simple operations to determine dynamic moment-curvature curves. Curvature was deduced by dividing the measured dynamic strain by the

half-depth of the beam. The moment was calculated according to the following equation:

$$M = m_t \ddot{y}_t h + I_t \ddot{\theta}$$

where

m_t = the tip mass, including accelerometers

\ddot{y}_t = tip acceleration

h = distance from c.g. of tip mass to strain gauge of interest

I_t = mass moment of inertia of the tip mass

$$\begin{aligned} \text{The accelerations } \ddot{y}_t &= \frac{A_1 + A_2 + A_3 + A_4}{4} \\ &= \frac{A_1 + A_2 + A_3 + A_4}{4} \\ \ddot{\theta}_t &= \frac{(A_2 - A_1) + (A_3 - A_4)}{2(2.5")} \end{aligned}$$

The tip mass was chosen to be large so the inertia force of the specimen might be neglected. In Fig. 8, the moment computed in this manner is plotted against curvature -- using unfiltered data. The crosses on the dynamic curves are spaced at 2 millisecond intervals. If one filters by eye, the initial dynamic stiffness is about the same as the static. Later the dynamic moment is higher than the static. Maximum moment and maximum curvature do not happen at the same time. Unexpectedly, the dynamic moment drops below the static moment at the onset of yielding of the outer fibers. Unloading does not occur with the same slope as elastic loading and there is a Bauschinger effect.

In Fig. 9, similar curves are shown for Drop 8, involving the same bars as in Drop 7, but from a greater drop height. There was some residual curvature after Drop 7, so the dynamic curve starts at that point. Generally the moment in the plastic region is above the static moment, and the sag occurs in the dynamic curve after initial yielding in Drop 7 does not appear in Drop 8.

In Fig. 10 static and dynamic moment-curvature plots are shown for Drop 37, which should have been identical to Drop 7. However, the maximum accelerations and curvatures were

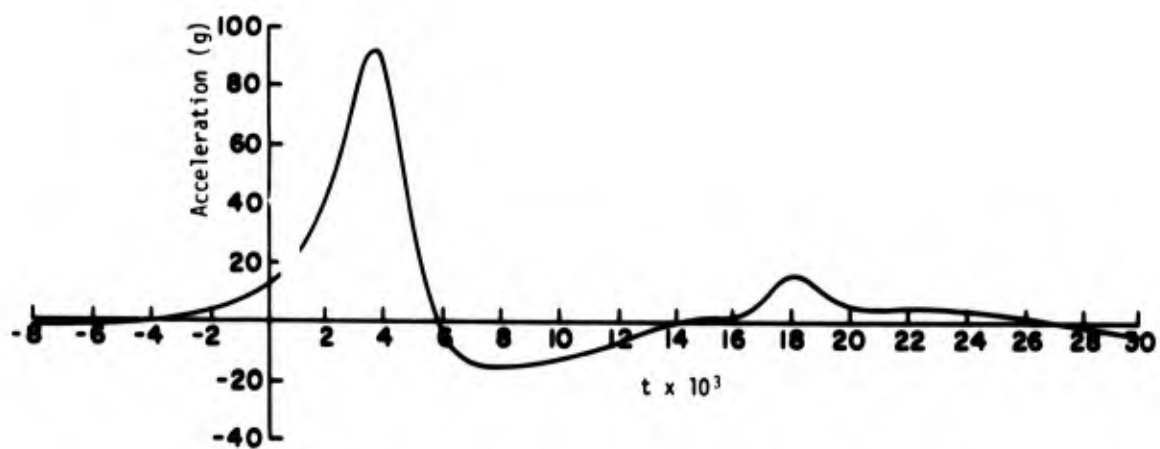


Fig. 4 Experimental Base Acceleration $\overline{A5+A6+A7+A8}$, Drop 37

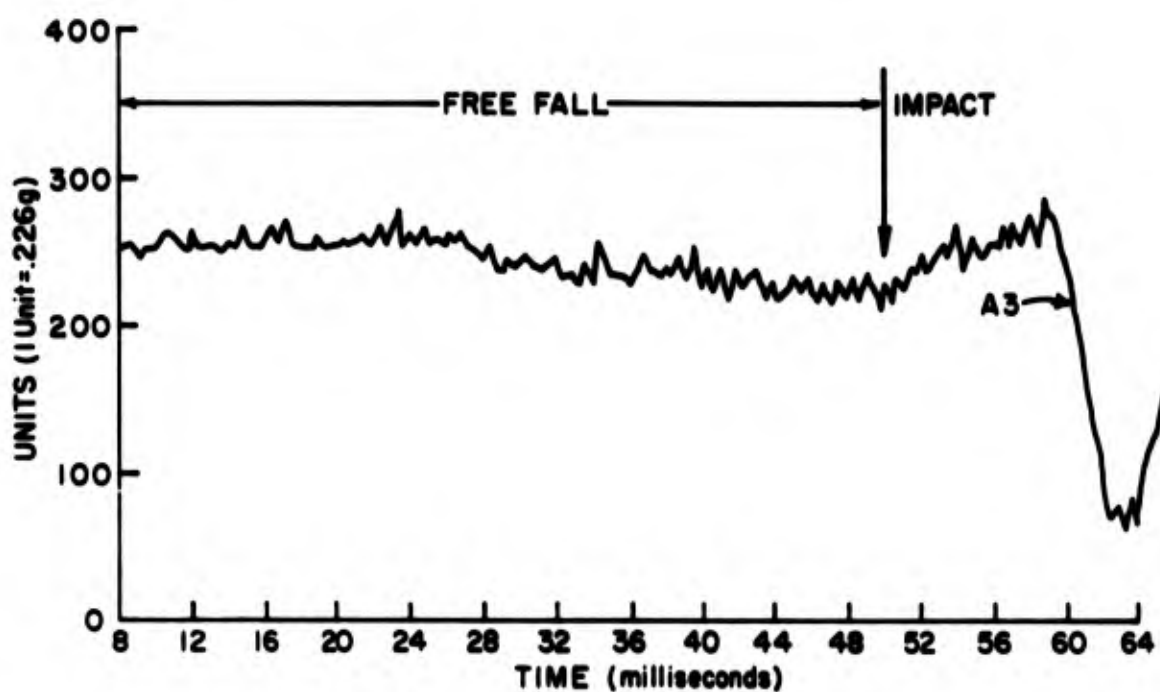


Fig. 5 Typical Tip Acceleration - Digitized

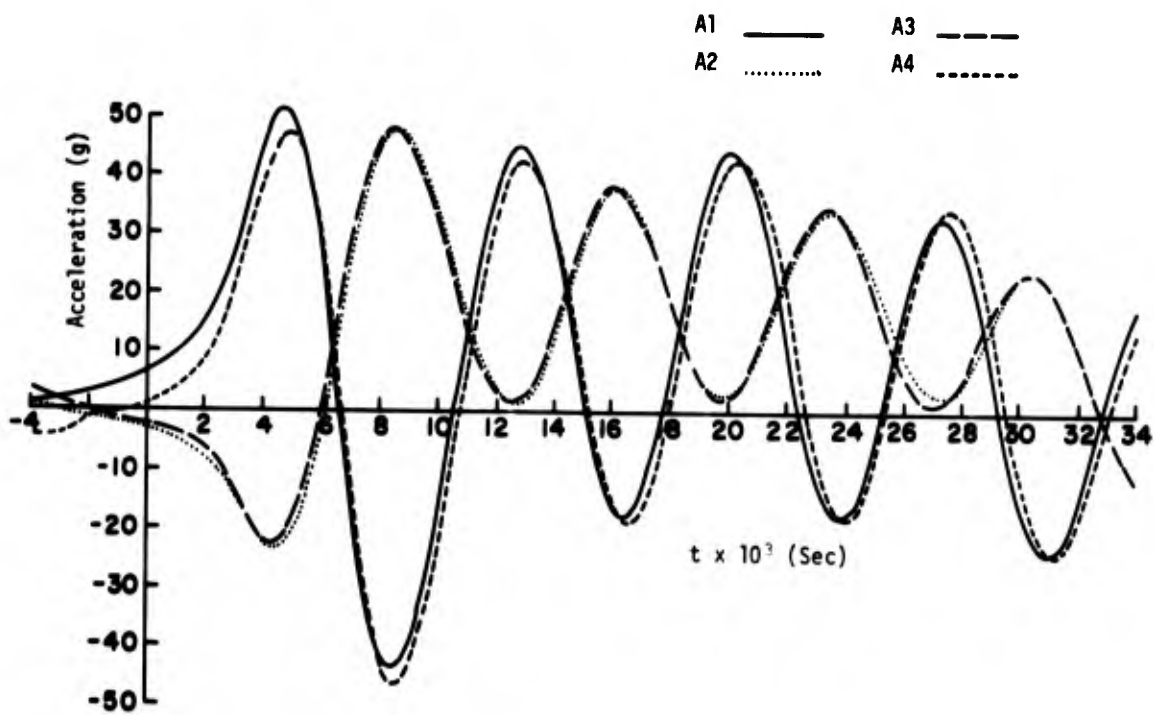


Fig. 6 Tip Mass Accelerations, A1, A2, A3 and A4, Drop 37

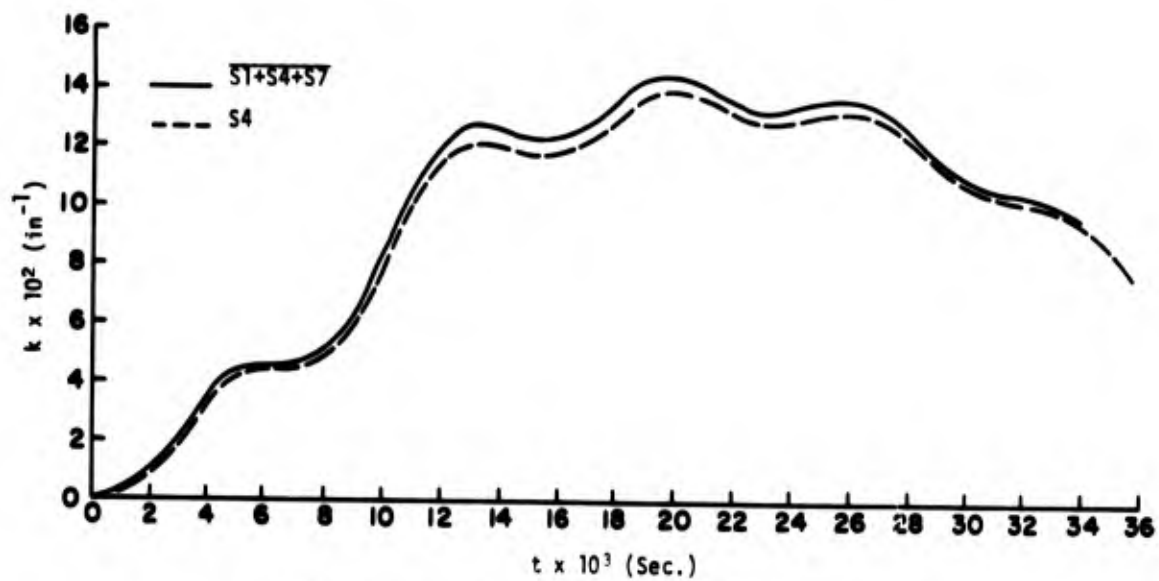


Fig. 7 Experimental Curvatures $S1+S4+S7$ and $S4$, Drop 37

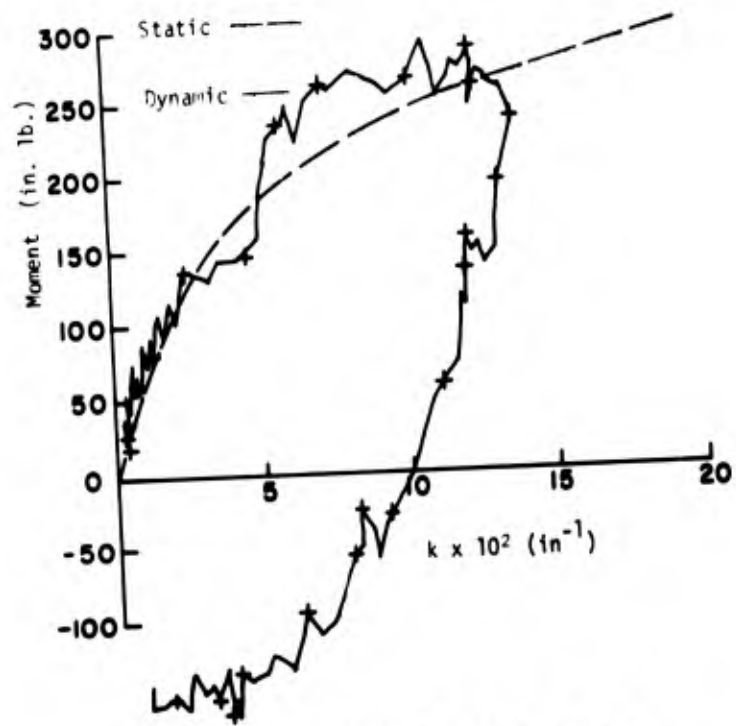


Fig. 8 Moment versus Curvature, Drop 7

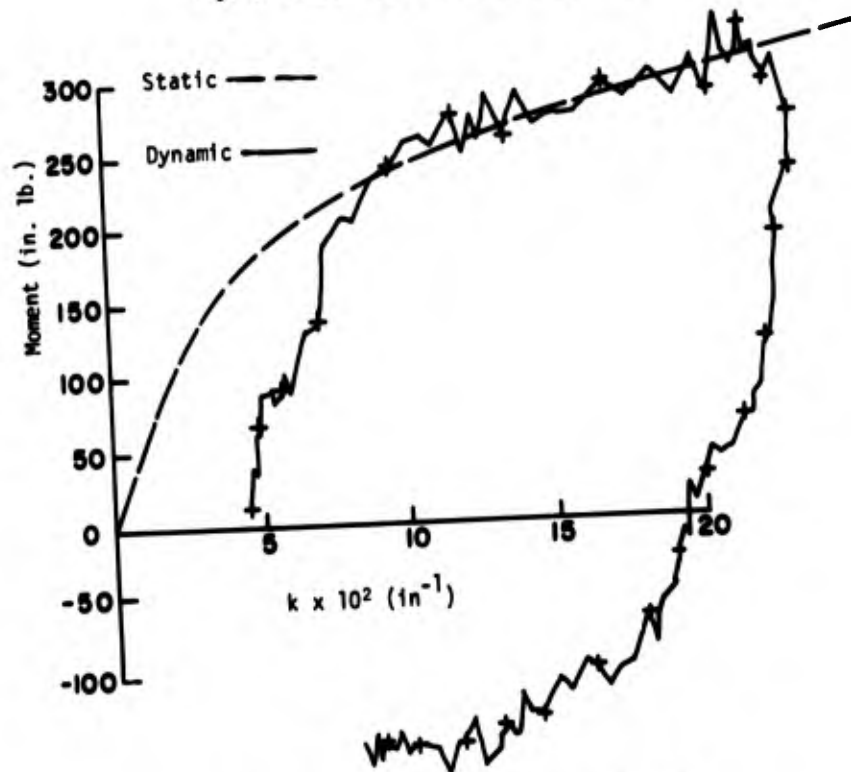


Fig. 9 Moment versus Curvature, Drop 8

somewhat higher, so the tests were not entirely repeatable. In Fig. 10 the initial dynamic stiffness is somewhat less than the static stiffness and again the dynamic moment is somewhat less than the static moment upon initiation of yielding of outer fibers. The data for Figures 10 and 11 was filtered.

In Fig. 11 the static and dynamic moment-curvatures are compared for the fully annealed steel in Drop 35. There is an increased yield and the maximum moment and maximum curvatures do not occur at the same time.

SUMMARY AND CONCLUSIONS

The data presented might be summarized briefly as follows:

- (1) The data indicates a slight rotation of the shock machine table and of the tip mass about the central specimen axis for some tests. This was assumed to have a negligible effect on the results presented here.
- (2) Results indicate there is not an instantaneous associated strain due to an applied dynamic loading. Inertia effects of the specimen could account for some delay. A more complete analysis [8] using the base acceleration as input indicates that specimen inertia does not account for all the time delay between moment and curvature.
- (3) Generally the dynamic moment is higher than the static moment except for the region just after yielding. This "sag" in the dynamic curve is not completely understood. In the data analyzed in addition to that presented here, it occurs on initial drops of the strain-hardening steels but not on re-drops of the same specimens, which implies it may be a material property. On the other hand, computation indicates that an error of 10 to 15% in the maximum translational acceleration of the tip mass would be enough to cause the sag. A study of possible errors does not indicate any one source of that magnitude. However, the sag happens about when the drop table bottoms, which is the time of peak base acceleration and large angular rotation of the tip mass. Accelerometer cross-sensitivity, cable whip, etc. might be contributing factors. Some tests have been made so that the masses do not rotate, and these may give some additional understanding.
- (4) An advantage of this test configuration is that moments and shears can be determined directly, providing the specimen mass may be neglected. A disadvantage is that both translational and rotational accelerations of the mass must be measured.

(5) Since the moment comes from eight accelerometer records and the curvature from one or more strain records, plotting of moment versus curvature requires careful synchronization in time of the various records. This was accomplished by relating visicorder traces of the data to the digitized records.

(6) The determination of shear force using the difference of the signals from two strain gauges was not successful because the specimen material did not remain elastic near the tip mass for most of the tests.

ACKNOWLEDGMENTS

The tests at the Naval Research Laboratory were coordinated by A. Dick. The assistance of J. Bachman, E. Judd, E. W. Clements and R. Kaplan in instrumenting, recording, and digitizing the data is gratefully acknowledged. The results in Figures 8 and 9 were developed and plotted from the data by Mr. C. Yang, who was at the time a graduate student at The Pennsylvania State University.

The work was supported by the Office of Naval Research under contract.

REFERENCES

1. J. J. Stanovsky, "The Shock Response of Beams with Non-Linear Material Properties", Doctoral Thesis, Department of Engineering Mechanics, The Pennsylvania State University, August, 1966.
2. J. J. Stanovsky and V. H. Neubert, "Shock Response of Beams with Non-Linear Material Properties", Office of Naval Research, Contract No. Nonr-656(28)(X), Interim Report No. 5, October, 1966.
3. V. H. Neubert and W. Brown, "Moment-Curvature-Time Relationships for Materials in Bending", Proceedings of the Army Symposium on Solid Mechanics, Army Materials and Mechanics Research Center, Watertown, Mass., 1968.
4. L. E. Malvern, "The Propagation of Longitudinal Waves of Plastic Deformation in a Bar of Material Exhibiting a Strain Rate Effect", Trans. ASME, Journal of Applied Mechanics, June 1951.
5. H. J. Plass, "Theory of Plastic Bending Waves in a Bar of Strain Rate Material", Proc. 2nd Midwest Conf. on Solid Mechanics, Purdue University, pp. 109-134, 1955.
6. W. G. Brown, "Dynamic Properties of Cold-Rolled Steel", Masters Thesis, Department of Engineering Mechanics, The Pennsylvania State University, 1966.

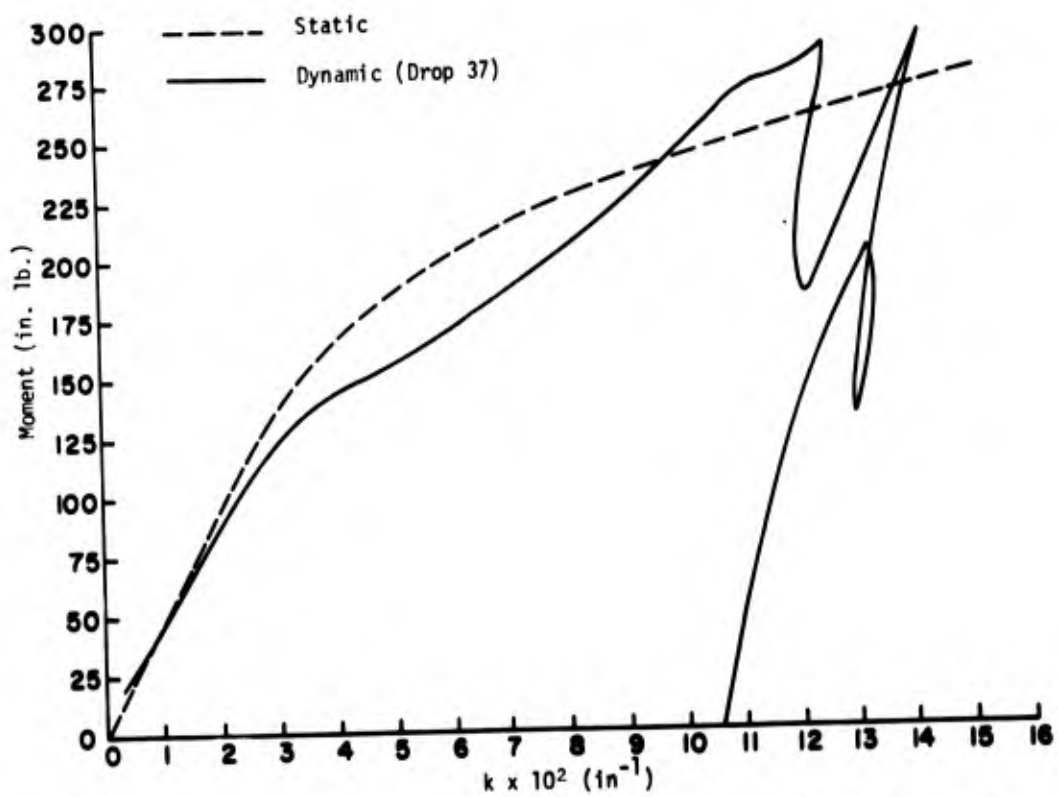


Fig. 10 Experimental Static and Dynamic Moment-Curvature at ST+S4+S7, Drop 37

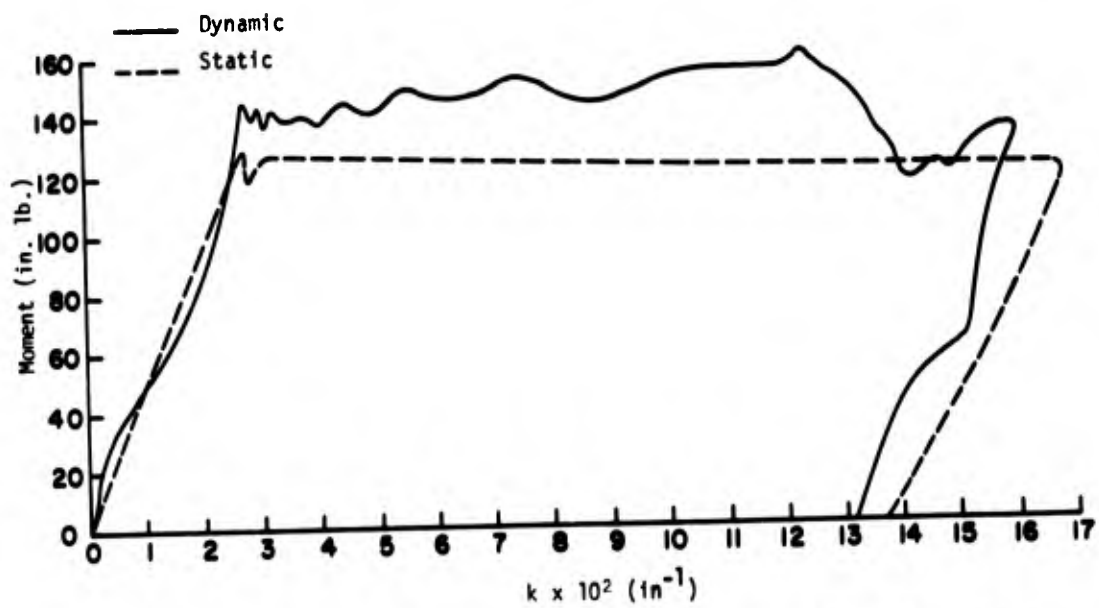


Fig. 11 Experimental Static and Dynamic Moment-Curvature, ST+S4+S7, Drop 35

State University, September, 1967.

7. V. H. Neubert, C. Yang and W. Vogel, "Dynamic Elastic-Plastic Bending Tests", in report "Shock Analysis of Structural Systems" Office of Naval Research, Contract No. Nonr-656(28)(X), Interim Report No. 8, February, 1969.
8. W. Vogel and V. H. Neubert, "The Theoretical and Experimental Dynamic Response of a Visco/plastic Beam", in report "Shock Analysis of Structural Systems" Office of Naval Research, Contract No. Nonr-656(28)(X), Interim Report No. 9, February, 1970.

CONDITION FOR SELF-SYNCHRONIZATION

The motion of mass M in Fig. 2 is described by the displacement of its mass center (x, y) and by the angular position (ϕ), the motion of the rotors is specified by the angular positions θ and θ_1 as shown in the figure. To formulate the problem in a simple form, it is assumed that when the system reaches the steady-state condition both rotors, which are driven by identical electric motors, have the same velocity, rotate in opposite directions, and maintain a constant phase angle. Therefore, the angular position is expressed as

$$\theta_1 = \omega t \quad (1)$$

$$\text{and} \quad \theta = \omega t + \sigma \quad (2)$$

where t is the time variable and σ the phase angle. The motion of the system is described by the four generalized coordinates x, y, ϕ and θ . It is assumed that the angular motion of mass M is small and may be neglected; this assumption is equivalent to considering mass M as a particle. Experimental results confirm the validity of this assumption. Consequently, the description of the system is reduced to three generalized coordinates x, y and θ . The problem is to investigate the conditions for which the rotors will maintain a constant phase angle.

The equations of Lagrange are used in developing the differential equations of motion. The kinetic energy (K.E.) and the potential energy (P.E.) of the system may be expressed as given by Eqs. (3) and (4) respectively.

$$\text{K.E.} = \frac{1}{2} M (\dot{x}^2 + \dot{y}^2) + \frac{1}{2} m [(\dot{x} - e \dot{\theta} \sin \theta)^2 + (\dot{y} - e \dot{\theta} \cos \theta)^2] + \frac{1}{2} m [(\dot{x} - e \dot{\theta}_1 \sin \theta_1)^2 + (\dot{y} + e \dot{\theta}_1 \cos \theta_1)^2] \quad (3)$$

$$\text{P.E.} = \frac{1}{2} K_x x^2 + \frac{1}{2} K_y y^2 + mg(y - e \sin \theta) + mg(y + e \sin \theta_1) \quad (4)$$

The dots over the variables indicate derivatives with respect to time.

The differential equations of motion result in the following system.

$$(M + 2m) \ddot{x} - m e \ddot{\theta} \sin \theta - m e \dot{\theta}^2 \cos \theta - m e \ddot{\theta}_1 \sin \theta_1 - m e \dot{\theta}_1^2 \cos \theta_1 + K_x x = 0 \quad (5)$$

$$(M + 2m) \ddot{y} - m e \ddot{\theta} \cos \theta + m e \dot{\theta}^2 \sin \theta + m e \ddot{\theta}_1 \cos \theta_1 - m e \dot{\theta}_1^2 \sin \theta_1 + K_y y + 2mg = 0 \quad (6)$$

$$m e^2 \ddot{\theta} - m e \ddot{x} \sin \theta - m e \ddot{y} \cos \theta - mg e \cos \theta + m e^2 \ddot{\theta}_1 - m e \ddot{x} \sin \theta_1 + m e \ddot{y} \cos \theta_1 + mg e \cos \theta_1 = T(\dot{\theta}) \quad (7)$$

where $T(\dot{\theta})$ = moment of electromagnetic forces.

The result of replacing

$$M^1 = M + 2m$$

and using

$$\theta_1 = \omega t, \quad \dot{\theta}_1 = \omega, \quad \ddot{\theta}_1 = 0$$

$$\theta = \omega t + \sigma, \quad \dot{\theta} = \omega, \quad \ddot{\theta} = 0$$

in Eqs. (5) and (6) gives the following equations.

$$\ddot{x} + \omega_x^2 x = \frac{e m \omega^2}{M^1} [\cos \omega t + \cos (\omega t + \sigma)] \quad (8)$$

$$\ddot{y} + \omega_y^2 y = \frac{e m \omega^2}{M^1} [\sin \omega t - \sin (\omega t + \sigma)] - \frac{2mg}{M^1} \quad (9)$$

$$\text{where } \omega_x^2 = \frac{K_x}{M^1} \text{ and } \omega_y^2 = \frac{K_y}{M^1}$$

The steady-state solution of Eqs. (8) and (9) is given by

$$x = \frac{e m \omega^2}{M^1 (\omega_x^2 - \omega^2)} [\cos \omega t + \cos (\omega t + \sigma)] \quad (10)$$

$$\text{and } y = \frac{e m \omega^2}{M^1 (\omega_y^2 - \omega^2)} [\sin \omega t - \sin (\omega t + \sigma)] - \frac{2mg}{M^1 \omega_y^2} \quad (11)$$

When the second derivatives of x and y are obtained by differentiating Eqs. (10) and (11) with respect to time and are replaced in Eq. (7), it results in the following equation:

$$\frac{e m \omega^4}{M^1 (\omega_x^2 - \omega^2)} [-\frac{1}{2} \sin \frac{1}{2} \omega t + \sin \sigma - \frac{1}{2} \sin \frac{1}{2} \omega t + \sin 2(\omega t + \sigma)] + \frac{e m \omega^4}{M^1 (\omega_y^2 - \omega^2)} [\frac{1}{2} \sin \omega t - \sin \sigma + \frac{1}{2} \sin (\omega t + \sigma)] + g \cos \omega t - g \cos (\omega t + \sigma) = \frac{T(\omega)}{m e} \quad (12)$$

Since the left-hand side of Eq. (12) is a function of time while the right-hand side is a constant, it is obvious that the relation is not an exact solution of Eq. (7) and is only an approximate solution which may be used to obtain an average description of the motion over the entire cycle. To this end, the unfulfilled requirement that Eq. (12) be identically satisfied is replaced by the less stringent condition that Eq. (12) be satisfied on the average.

The left-hand side of Eq. (12) is some periodic function of time with period $2\pi/\omega$. Accordingly, to find the mean value function, integration is performed over the time interval $(0, 2\pi/\omega)$ and the result divided by the period $2\pi/\omega$. The integration of Eq. (12) results in

$$\frac{e m \omega^4}{2M^1 (\omega_x^2 - \omega^2)} \int_0^{2\pi/\omega} [\sin 2\omega t + 2\sin \sigma - \sin 2(\omega t + \sigma)] dt + \frac{e m \omega^4}{2M^1 (\omega_y^2 - \omega^2)} \int_0^{2\pi/\omega} [-\sin 2\omega t - 2\sin \sigma + \sin 2(\omega t + \sigma)] dt + g \int_0^{2\pi/\omega} \cos \omega t dt - g \int_0^{2\pi/\omega} \cos (\omega t + \sigma) dt = \int_0^{2\pi/\omega} \frac{T(\omega)}{m e} dt \quad (13)$$

which is reduced to Eq. (14).

$$\sin \sigma = \frac{T_0 M^1}{m^2 e^3 \omega^4} \left[\frac{(\omega_x^2 - \omega^2)(\omega_y^2 - \omega^2)}{\omega_y^2 - \omega_x^2} \right] \quad (14)$$

$$\text{where } T_0 = \frac{\omega}{2\pi} \int_0^{2\pi/\omega} T(\omega) dt$$

Eq. (14) may be used to determine the phase angle σ , but it is important because it makes possible to formulate the condition for self-synchronization in the form $\sin \sigma < 1$

$$\text{or } \frac{T_0 M^1}{m^2 e^3 \omega^4} \left[\frac{(\omega_x^2 - \omega^2)(\omega_y^2 - \omega^2)}{\omega_y^2 - \omega_x^2} \right] < 1 \quad (15)$$

To investigate further the condition of self-synchronization as shown in relation (15), a system requiring a small torque T_0 is considered. In this case $\sin \sigma$ will be approximately equal to zero, and self-synchronization will then occur for values of $\sigma = 0^\circ$ or $\sigma = 180^\circ$. Experimental results show that when the bracket of inequality (15) is positive, the motion is stable along the x direction corresponding to a phase angle $\sigma = 0^\circ$, and when this bracket is negative, the motion occurs along the y direction which corresponds to a phase angle $\sigma = 180^\circ$.

EXPERIMENTAL INVESTIGATION OF SELF-
SYNCHRONIZATION

Experiments on self-synchronization are conducted on a system consisting of a frame supporting two electric motors with their axes horizontally aligned. The frame itself, which has a parallelepiped external shape, is mounted to a rigid foundation through airbag springs located at all four sides parallel to the axes of the two motors. Equal eccentric masses are set to the axes of the two motors which are connected electrically to run in opposite directions. The system constructed conforms to the model represented in Fig. 2, except that the two motors have their axes aligned as shown in Fig. 3. This arrangement avoids the development of a couple when the rotor phase produces a horizontal motion and also renders the system closest to the assumption of no angular motion of mass M made in the analysis.

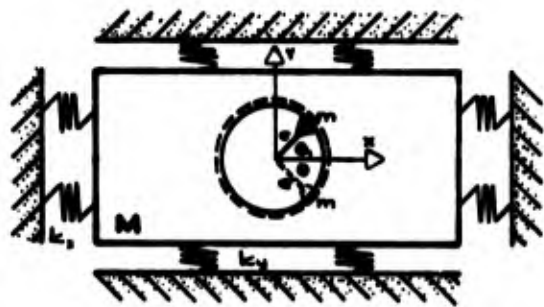


FIG. 3 SYSTEM OF TWO ALIGNED MOTORS WITH ECCENTRIC ROTORS.

By changing the air pressure of the airbag springs at the top and bottom (K_y) or of the airbag springs at the sides of the frame (K_x), it is possible to tune the system to frequencies below or above the resonant condition in either of the two directions.

The system constructed has the following characteristics:
 $Mg = 407 \#$ (weight of supporting frame and motors),
 $mge = 2.4 \#$ in (eccentricity of the rotors),
electric motors inductive type of 1 HP,
airbag springs airmount type having a total spring constant for two opposite pairs given by
 $K = 2 (100. P + 960.) \#/\text{in.}$ (16)
where P = pressure of the airbags (p.s.i.).

The natural frequency of the system in radians per second in the x or y directions is given by the following relations:

$$w_x = \sqrt{\frac{K_x}{M}} \quad \text{and} \quad w_y = \sqrt{\frac{K_y}{M}} \quad (17)$$

Setting the natural frequency equal to the nominal frequency of the motors (900 RPM) and solving Eq. (17) for the spring constant results in $k = 9300 \#/\text{in.}$ which replaced in Eq. (16) gives a value of the resonant pressure $P_r = 41.70$ psi.

A series of experiments are run at different pressures in the horizontal and vertical airbag springs, and the direction of the motion of mass M is recorded. It is observed that the rotors maintain a definite synchronization producing either a vertical or horizontal motion and that the direction depends on the relative values of the pressures P_x , P_y and the resonant pressure $P_r = 41.7$ psi. The experimental observations are summarized in Table I.

TABLE I.
OBSERVED SELF-SYNCHRONIZATION FOR SYSTEM
IN FIG. 3

Case	Relative Values for Pressures in the Airbags and Resonant Pressure	Observed Motion
1	$P_x < P_y < P_r$	Horizontal
2	$P_y < P_x < P_r$	Vertical
3	$P_y < P_r < P_x$	Horizontal
4	$P_x < P_r < P_y$	Vertical
5	$P_r < P_x < P_y$	Horizontal
6	$P_r < P_y < P_x$	Vertical

From Eqs. (16) and (17) it is seen that pressures P_x , P_y and P_r in the inequalities of Table I, could be replaced by corresponding inequalities in the natural frequencies w_x , w_y and the resonant frequency $w_r = 94$ rad/sec. In Table II these inequalities are shown after dividing the expressions by the resonant frequency w_r .

TABLE II.
SELF-SYNCHRONIZATION FOR THE SYSTEM IN FIG. (3)
IN TERMS OF RELATIVE FREQUENCIES.

Case	Frequency Relations	Observed Motion
1	$w_x/w_r < w_y/w_r < 1$	Horizontal
2	$w_y/w_r < w_x/w_r < 1$	Vertical
3	$w_y/w_r < 1 < w_x/w_r$	Horizontal
4	$w_x/w_r < 1 < w_y/w_r$	Vertical
5	$1 < w_x/w_r < w_y/w_r$	Horizontal
6	$1 < w_y/w_r < w_x/w_r$	Vertical

The observed motion of mass M as a function of the frequency ratios w_x/w_r and w_y/w_r is shown graphically in Fig. 4 where also the corresponding values of the phase angle σ are indicated.

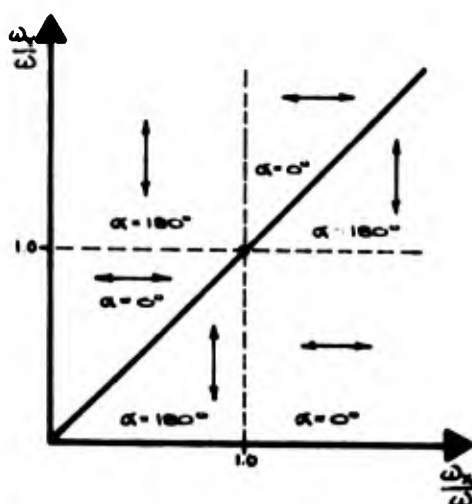


FIG. 4 PICTORIAL REPRESENTATION OF THE PHASE ANGLE BETWEEN ROTORS FOR SYSTEM IN FIG. 3 (HORIZONTAL AND VERTICAL ARROWS INDICATE DIRECTION OF THE RESULTING MOTION.)

CONCLUSIONS

The case of self-synchronization of two motors with eccentric rotating masses producing rectilinear motion has been presented. The condition for self-synchronization has been determined by an approximate solution of the corresponding differential equations of motion. Observations from experiments corroborate the analytical results giving also the direction of ensuing motion in terms of relative resonant frequencies.

NOMENCLATURE

Symbols are defined where they are first introduced in the text and are also defined here for convenience.

- e = Eccentricity of rotors
- g = Acceleration of gravity
- K_x = Spring constant in the x direction
- K_y = Spring constant in the y direction
- $K.E.$ = Kinetic energy
- m = Mass of a rotor
- M = Mass of body in Fig. 2
- $M^0 = M + 2m$
- $P.E.$ = Potential energy
- t = time
- T_0 = Average moment of electromagnetic forces
- w_r = Resonant frequency
- w_x = Natural frequency in x direction
- w_y = Natural frequency in y direction
- x = Horizontal displacement center of mass
- y = Vertical displacement center of mass
- α = Phase angle
- θ, θ_1 = angular displacements of the rotors

REFERENCES

1. Morris, John M. and Guthrie, James J., Jr., "Electromechanical Feeding and Proportioning of Bulk Solids", ASME Paper No. 65-MH-61 ASME-IEEE Materials Handling Conference, Pittsburgh, Pennsylvania, October 1965.
2. Blekhman, I. I., "Rotation of an Unbalanced Rotor Produced by Harmonic Oscillation of the Axis", Bulletin of Academy of Sciences, USSR, Division of Technical Sciences, No. 8, 1954.

PROPAGATION OF THE ERROR IN COMPUTED FREQUENCIES AND MODE SHAPES
RESULTING FROM A DISCRETE MASS REPRESENTATION OF UNIFORM, SLENDER BEAMS
WITH VARYING HEIGHT-TO-LENGTH RATIOS

Francis M. Henderson
Naval Ship Research and Development Center
Washington, D. C. 20034

This paper considers the question of how accurately one can predict the errors in frequencies and modes of transverse vibration (without shear or rotary inertia) resulting from an n-mass modeling of continuous, uniformly rectangular beams with free ends using a knowledge of these errors for a single reference beam.

INTRODUCTION

The dynamic analysis of long, slender structures often involves the calculation of their beam or beam-like frequencies and modes of vibration. This is usually accomplished through an idealization of the structure by an equivalent continuous beam which in turn is approximated for computational purposes by some type of discrete mass-elastic system.

Certain discrete systems [1, 2] consisting of linear arrays of point masses connected by weightless elastic members have had considerable usage in the modeling of ships for the calculation of the first few frequencies and modes.

Reference [2] presents a detailed analysis of transverse vibration frequencies and modes obtained using this discrete model for both uniform and nonuniform beam representations of the SS Gopher Mariner. The calculations were made with digital and analog computers. The general dependence of frequency error upon number of masses is demonstrated for bending vibrations (no shear or rotary inertia) of the uniform model.

This paper will illustrate, with numerical results that, to a practical degree of accuracy, the errors in frequencies and modes resulting from discretizing the Euler-Bernoulli model of an arbitrary continuous rectangular beam can be used to rapidly predict the corresponding errors for other rectangular beams. The method of prediction uses the simple relationships for the theoretical frequencies and modes of rectangular beams.

SYMBOLS

- h Height of rectangular beam cross section in the plane of bending
- w Width of rectangular beam cross section
- ℓ Beam length
- E Young's modulus of elasticity
- I Area moment of inertia of the cross section of a beam about a principal axis perpendicular to the plane of bending
- A Area of beam cross section
- μ Mass per unit length of the beam
- ρ Density of beam material
- γ Weight of beam material per unit volume
- g Acceleration of gravity

- A. BASIS FOR PROJECTING FREQUENCIES AND ERRORS IN FREQUENCIES OBTAINED FOR AN N-MASS MODEL

The circular frequencies of transverse vibration for a uniform rectangular beam with free ends can be expressed [3] ,

$$f_1 = \frac{k_1^2 a}{2\pi} = \left(\frac{k_1}{\ell}\right)^2 \frac{1}{2\pi} \sqrt{\frac{EIg}{A\gamma}}$$

$$= \left(\frac{k_1}{\ell}\right)^2 \frac{1}{2\pi} \sqrt{\frac{EI}{\mu}} \quad (1)$$

where k_i are the roots of

$$\cos k_i \cosh k_i = -1 \quad (2)$$

Since $b = bh$, $A = bh$, and $I = 1/12 bh^3$ for rectangular beams, one obtains by substitution into (1), the dependence of frequency upon the section dimensions and material properties,

$$f_i = \frac{1}{2\pi} \sqrt{\frac{E}{\rho}} k_i^2 \quad (3)$$

From this it is seen that for any other rectangular beam of height, $h' = bh$, and length, $l' = bl$, and with material properties $E' = E$ and $\rho' = \rho$, the corresponding theoretical frequencies will be

$$f_i' = M f_i \quad (4)$$

$$\text{where } M = \frac{1}{2} \sqrt{\frac{h'}{h}}$$

If the corresponding model frequencies, which shall be denoted

$f_i^{n'}$ and f_i^n , n indicating n -masses, can be assumed to properly reflect the dependence shown in Eq. (4), then the absolute error between model and theoretic frequencies for any two beams will be

$$f_i' - f_i^{n'} = M (f_i - f_i^n), \quad (5)$$

and the proportional error will be constant, since Eq. (4) and Eq. (5) combine to give

$$\frac{f_i' - f_i^{n'}}{f_i'} = \frac{M (f_i - f_i^n)}{M f_i} = \frac{f_i - f_i^n}{f_i} \quad (6)$$

B. BASIS FOR PROJECTING MODAL DISPLACEMENTS AND ASSOCIATED ERRORS OBTAINED FOR AN N-MASS MODEL

The analytic expression for the deflection mode shapes of uniform free-free beams, according to Ref. [3], is

$$X = C_1 (\cos kx + \cosh kx) + C_3 (\sin kx + \sinh kx) \quad (7)$$

with x equal to distance along the beam.

Using the end condition equations [3] to solve for C_1 in terms of C_3 and then letting C_3 equal unity, one has

$$X = \frac{\sin k^2 - \sinh k^2}{-\cos k^2 + \cosh k^2} (\cos kx + \cosh kx + \sin kx + \sinh kx) \quad (8)$$

where the k^2 's are roots of Eq. (2)

Equation (8) shows that two beams of equal length, but of different heights, will have the same mode displacement at corresponding points x . On the other hand, for beams of different lengths, say l and l' , the corresponding points of equal displacement in any mode will be x and lx . This suggests that the modal displacements and displacement errors for n -mass models of a beam of length l can be easily predicted from the corresponding n -mass models of beams of length l' by a simple mapping process.

C. PREDICTED VS. COMPUTED ERRORS IN FREQUENCIES AND MODE SHAPES OF DISCRETE MODELS

Tables 2 through 9 demonstrate the accuracies with which frequencies and errors in frequencies were predicted for several n -mass representations of uniform rectangular beams using the reference beam data in Table 1. Tables 13, 14, and 15 illustrate the use of the mapping process described in B. to predict the deflection and errors in deflection for models of a test beam using computed data (Tables 10, 11, and 12) for models of the reference beam.

The height-to-length ratios of the beams for which predictions were made satisfy a necessary requirement for slenderness discussed in Appendix B.

The procedures used to obtain computed results for the beam models and descriptions of the model configurations are given in Appendix A.

Prediction of per cent error in frequencies in Tables 2 through 8 was accomplished by comparing predicted model frequencies with analytic frequencies rather than by using directly the reference beam errors as suggested by Eq. (6). This allowed the calculation of additional significant digits in some of the errors and thus afforded a better verification of Eq. (6). In Table 9 for the Gopher Mariner beam, however, the predicted errors in frequencies are more accurately taken to be the errors for the reference beam, because of the reduced significance of predicted model frequencies.

The modeling of beams with height-to-length ratios of 0.15 or greater using 12 masses led to a general breakdown of the computed solutions. This is indicated in Tables 4 through 7 by the abrupt disagreement between the computed and predicted frequencies and errors for the 12-section model.

TABLE 1
Computed Frequencies and Errors for Reference Beam Models

Beam Description Dimensions: $h = 0.6'$ $\ell = 20'$ $w = 0.6'$ $h/\ell = 0.03$ Material: aluminum alloy 6061-T6 * Material Properties $E = 10 \times 10^6 \text{ lbs/in}^2$ $\rho = 2.53886 \times 10^{-4} \frac{\text{lbs-sec}^2}{\text{in}} / \text{in}^3$				
Frequencies (CPS)				
Mode	Theory	12 Sections	22 Sections	42 Sections
1	25.50	25.62	25.53	25.51
2	70.29	69.22	70.06	70.24
3	137.80	130.42	136.15	137.40
4	227.80	202.83	222.09	226.41
5	340.29	278.69	325.91	336.79
% Errors in Frequencies				
Mode		12 Sections	22 Sections	42 Sections
1		-0.47	-0.1	-0.04
2		1.52	0.33	0.07
3		5.36	1.20	0.29
4		11.0	2.51	0.610
5		18.1	4.23	1.03

TABLE 2
Computed vs. Predicted Frequencies (CPS) and Errors for Models of Test Beam 1

Beam Description Dimensions: $h = 1.2'$ $\ell = 20'$ $w = 1.2'$ $h/\ell = 0.06$ Material: Same as reference beam Multiplying Factor: $M = 2$							
Frequencies (CPS)							
Mode	Theory	Computed			Predicted:	2 x computed frequencies in Table 1	
		12 Sections	22 Sections	42 Sections	12 Sections	22 Sections	42 Sections
1	51.00	51.24	51.07	51.02	51.24	51.06	51.02
2	140.59	138.44	140.13	140.48	138.44	140.12	140.48
3	275.61	260.84	272.30	274.80	260.84	272.30	274.80
4	455.59	405.66	444.19	452.82	405.66	444.18	452.82
5	680.57	557.38	651.82	673.58	557.38	651.82	673.58
% Errors in Frequencies							
Mode		Computed			Predicted		
		12 Sections	22 Sections	42 Sections	12 Sections	22 Sections	42 Sections
1		-0.47	-0.1	-0.04	-0.47	-0.1	-0.04
2		1.53	0.33	0.078	1.53	0.33	0.078
3		5.36	1.20	0.29	5.36	1.20	0.29
4		11.0	2.50	0.608	11.0	2.50	0.608
5		18.1	4.22	1.03	18.1	4.22	1.03

* Ref. [7]

TABLE 3
Computed vs. Predicted Frequencies (CPS) for Models of Test Beam 2

Beam Description Dimensions: $h = 2'$ $\ell = 20'$ $w = 2'$ $h/\ell = 0.10$ Material: Same as reference beam Multiplying Factor: $M = 3 \frac{1}{3}$ <div style="float: right;"> $\alpha = 3 \frac{1}{3}$ $\beta = 1$ $\delta = 1$ $n = 1$ </div>							
Frequencies (CPS)							
Mode	Theory	Computed			Predicted: $3 \frac{1}{3} \times$ computed frequencies in Table 1		
		12 Sections	22 Sections	42 Sections	12 Sections	22 Sections	42 Sections
1	85.00	85.40	85.11	85.03	85.40	85.10	85.03
2	234.31	230.74	233.54	234.13	230.73	233.53	234.13
3	459.34	444.74	453.83	458.01	434.73	453.83	458.00
4	759.32	676.09	740.31	754.71	676.10	740.30	754.70
5	1134.29	928.97	1086.37	1122.63	928.97	1086.37	1122.63
% Errors in Frequencies							
Mode	Computed			Predicted			
	12 Sections	22 Sections	42 Sections	12 Sections	22 Sections	42 Sections	
1	-0.47	-0.13	-0.04	-0.47	-0.12	-0.04	
2	1.52	0.33	0.077	1.53	0.33	0.077	
3	5.36	1.20	0.290	5.36	1.20	0.292	
4	10.96	2.504	0.607	10.96	2.505	0.608	
5	18.10	4.225	1.028	18.10	4.225	1.028	

TABLE 4
Computed vs. Predicted Frequencies (CPS) for Models of Test Beam 3

Beam Description Dimensions: $h = 3'$ $\ell = 20'$ $w = 3'$ $h/\ell = 0.15$ Material: Same as reference beam Multiplying Factor: $M = 5$ <div style="float: right;"> $\alpha = 5$ $\beta = 1$ $\delta = 1$ $n = 1$ </div>							
Frequencies (CPS)							
Mode	Theory	Computed			Predicted: $5 \times$ computed frequencies in Table 1		
		12 Sections	22 Sections	42 Sections	12 Sections	22 Sections	42 Sections
1	127.50	128.09	127.66	127.54	128.10	127.66	127.55
2	351.46	346.10	350.31	351.18	346.10	350.30	351.20
3	689.00	652.09	680.73	687.00	652.10	680.75	687.00
4	1138.95	1014.12	1110.44	1132.04	1014.15	1110.45	1132.05
5	1701.40	1747.56	1629.52	1683.91	1393.45	1629.55	1683.95
% Errors in Frequencies							
Mode	Computed			Predicted			
	12 Sections	22 Sections	42 Sections	12 Sections	22 Sections	42 Sections	
1	-0.46	-0.13	-0.03	-0.47	-0.13	-0.04	
2	1.53	0.330	0.080	1.53	0.330	0.074	
3	5.36	1.20	0.290	5.36	1.20	0.290	
4	11.0	2.50	0.607	11.0	2.50	0.606	
5	-2.71	4.22	1.03	18.1	4.22	1.03	

TABLE 5
Computed vs. Predicted Frequencies (CPS) for Models of Test Beam 4

Beam Description Dimensions: $h = 4'$ $\ell = 20'$ $w = 4'$ $h/\ell = 0.2$ Material: Same as reference beam Multiplying Factor: $M = 6 \frac{2}{3}$							
Frequencies (CPS)							
Mode	Theory	Computed			Predicted: $6 \frac{2}{3} \times$ computed frequencies in Table 1		
		12 Sections	22 Sections	42 Sections	12 Sections	22 Sections	42 Sections
1	170.00	170.79	170.21	170.05	170.80	170.20	170.07
2	468.61	461.47	467.08	468.25	461.47	467.07	468.27
3	918.67	869.46	907.64	916.00	869.47	907.67	916.00
4	1518.60	1352.16	1480.59	1509.38	1352.20	1480.60	1509.40
5	2268.53	2330.09	2172.69	2245.22	1857.93	2172.73	2245.27
% Errors in Frequencies							
Mode		Computed			Predicted		
		12 Sections	22 Sections	42 Sections	12 Sections	22 Sections	42 Sections
1		-0.46	-0.12	-0.03	-0.47	-0.12	-0.04
2		1.52	0.326	0.077	1.52	0.329	0.073
3		5.36	1.20	0.291	5.36	1.20	0.291
4		11.0	2.50	0.607	11.0	2.50	0.606
5		-2.71	4.22	1.03	18.1	4.22	1.03

TABLE 6
Computed vs. Predicted Frequencies (CPS) for Models of Test Beam 5

Beam Description Dimensions: $h = 5'$ $\ell = 20'$ $w = 5'$ $h/\ell = 0.25$ Material: Same as reference beam Multiplying Factor: $M = 8 \frac{1}{3}$							
Frequencies (CPS)							
Mode	Theory	Computed			Predicted: $8 \frac{1}{3} \times$ computed frequencies in Table 1		
		12 Sections	22 Sections	42 Sections	12 Sections	22 Sections	42 Sections
1	212.50	213.49	212.77	212.57	213.50	212.75	212.58
2	585.78	576.85	583.86	585.32	576.83	583.83	585.33
3	1148.36	1086.84	1134.57	1145.02	1086.83	1134.58	1145.00
4	1898.29	1690.23	1850.78	1886.76	1690.25	1850.75	1886.75
5	2835.72	2912.67	2715.92	2806.58	2322.42	2715.92	2806.58
% Errors in Frequencies							
Mode		Computed			Predicted		
		12 Sections	22 Sections	42 Sections	12 Sections	22 Sections	42 Sections
1		-0.47	-0.13	-0.03	-0.471	-0.12	-0.04
2		1.52	0.328	0.079	1.53	0.333	0.077
3		5.36	1.20	0.291	5.36	1.20	0.293
4		11.0	2.50	0.607	11.0	2.50	0.608
5		-2.7	4.22	1.03	18.1	4.22	1.03

TABLE 7
Computed vs. Predicted Frequencies (CPS) for Models of Test Beam 6

Beam Description Dimensions: $h = 6'$ $l = 20'$ $w = 6'$ $h/l = 0.3$ Material: Same as reference beam Multiplying Factor: $M = 10$							
Frequencies (CPS)							
Mode	Theory	Computed			Predicted: 10 x computed frequencies in Table 1		
		12 Sections	22 Sections	42 Sections	12 Sections	22 Sections	42 Sections
1	255.01	256.19	255.33	255.09	256.2	255.3	255.1
2	702.93	692.22	700.63	702.38	692.2	700.6	702.4
3	1378.04	1304.21	1361.48	1374.02	1304.2	1361.5	1374.0
4	2277.95	2028.28	2220.93	2264.12	2028.3	2220.9	2264.1
5	3402.87	3495.20	3259.10	3367.89	2786.9	3259.1	3367.9
% Errors in Frequencies							
Mode		12 Sections	Computed 22 Sections	42 Sections	12 Sections	Predicted 22 Sections	42 Sections
1		-0.463	-0.13	-0.03	-0.47	-0.1	-0.04
2		1.52	0.327	0.078	1.52	0.33	0.07
3		5.36	1.20	0.291	5.36	1.20	0.29
4		11.0	2.50	0.607	11.0	2.51	0.610
5		-2.71	4.22	1.03	18.1	4.23	1.03

TABLE 8
Computed vs. Predicted Frequencies (CPS) for Models of Test Beam 7

Beam Description Dimensions: $h = 1.8'$ $l = 60'$ $w = 1.8'$ $h/l = 0.03$ Material: Same as reference beam Multiplying Factor: $M = 1/3$							
Frequencies (CPS)							
Mode	Theory	Computed			Predicted: 1/3 x computed frequencies in Table 1		
		12 Sections	22 Sections	42 Sections	12 Sections	22 Sections	42 Sections
1	8.50	8.54	8.51	8.50	8.54	8.51	8.50
2	23.43	23.07	23.36	23.41	23.07	23.35	23.41
3	45.93	43.47	45.38	45.80	43.47	45.38	45.80
4	75.93	67.58	74.03	75.47	67.61	74.03	75.47
5	113.43	92.81	108.63	112.26	92.90	108.64	112.26
% Errors in Frequencies							
Mode		12 Sections	Computed 22 Sections	42 Sections	12 Sections	Predicted 22 Sections	42 Sections
1		-0.5	-0.1	0	-0.5	-0.1	0
2		1.5	0.3	0.09	1.5	0.3	0.09
3		5.36	1.2	0.28	5.36	1.2	0.28
4		11.0	2.50	0.61	11.0	2.50	0.61
5		18.2	4.23	1.03	18.1	4.22	1.03

TABLE 9
Computed vs. Predicted Frequencies (CPM) for Models of Test Beam 8 (Gopher Mariner Beam)

Beam Description Dimensions: $h = 102'$ $l = 525'$ $w = 0.08786'$ $h/l = 0.194$ Material: steel $E = 1.93 \times 10^6$ ton/ft^2 $\rho^* = 0.3894$ $\frac{\text{ton-sec}^2}{\text{ft}} / \text{ft}^3$ Multiplying Factor: $\eta = 0.0332$							
$\alpha = 2.1875$ $\beta = 14.167$ $\delta = 0.193$ $\eta = 0.15338 \times 10^4$							
Frequencies (CPM)							
Mode	Theory	Computed			Predicted; 0.0332 x computed frequencies in Table 1		
		10 Sections	20 Sections	40 Sections	10 Sections	20 Sections	40 Sections
1	50.82	51.06	50.89	50.84	51.0	50.9	50.8
2	140.05	138.00	139.60	140.00	138.	140.	140.
3	274.67	259.80	271.30	273.80	260.	271.	274.
4	453.80	404.00	442.60	451.20	404.	442.	451.
5	677.91	554.70	649.50	671.20	555.	649.	671.
% Errors in Frequencies							
Mode		Computed			Predicted		
		12 Sections	22 Sections	42 Sections	12 Sections	22 Sections	42 Sections
1		-0.47	-0.1	-0.04	-0.47	-0.1	-0.04
2		1.46	0.32	0.04	1.52	0.33	0.07
3		5.41	1.23	0.32	5.36	1.20	0.29
4		11.0	2.47	0.57	11.0	2.51	0.610
5		18.2	4.20	0.990	18.1	4.23	1.03

* value of ρ includes the effect of the surrounding water

TABLE 10
Reference Beam - Error in Displacements for 12 Section Model

Beam * Section	Mode 1 (symmetric)			Mode 2 (anti-symmetric)		
	Analytic	Computed	% Error	Analytic	Computed	% Error
1	1.000	1.000	0	1.000	1.000	0
2	0.7653	0.7710	-0.74	0.6031	0.6316	-4.73
3	0.3095	0.3180	-2.7	-0.1226	-0.09557	22.0
4	-0.1014	-0.09563	5.7	-0.5886	-0.5860	0.44
5	-0.4160	-0.4147	0.31	-0.6265	-0.6397	-2.11
6	-0.5872	-0.5890	-0.31	-0.2633	-0.2712	-3.0
Beam Section	Mode 3 (symmetric)			Mode 4 (anti-symmetric)		
	Analytic	Computed	% Error	Analytic	Computed	% Error
1	1.000	1.000	0	1.000	1.000	0
2	0.4461	0.5206	-16.7	0.2916	0.4340	-48.8
3	-0.4485	-0.4215	6.02	-0.6345	-0.6698	-5.56
4	-0.6233	-0.6673	-7.06	-0.2532	-0.3612	-42.7
5	-0.04229	-0.07456	-76.3	0.6125	0.6520	-6.45
6	0.6116	0.6324	-3.40	0.4625	0.5279	-14.1
Beam Section	Mode 5 (symmetric)					
	Analytic	Computed	% Error			
1	1.000	1.000	0			
2	0.1417	0.3696	-161.			
3	-0.6543	-0.8470	-29.5			
4	0.2856	0.2207	22.7			
5	0.6076	0.8039	-32.3			
6	-0.4641	-0.5576	-20.1			

* Appendix A, Fig. 1, (a)

TABLE 11
Reference Beam - Error in Displacements for 22 Section Model

Beam & Section	Mode 1 (symmetric)			Mode 2 (anti-symmetric)		
	Analytic	Computed	% Error	Analytic	Computed	% Error
1	1.000	1.000	0	1.000	1.000	0
2	0.8814	0.8821	-0.08	0.7991	0.8030	-0.49
3	0.6496	0.6512	-0.25	0.4099	0.4174	-1.8
4	0.4211	0.4231	-0.48	0.04347	0.05125	-17.9
5	0.2007	0.2027	-1.0	-0.2723	-0.2662	2.2
6	-0.005598	-0.003910	30.2	-0.5082	-0.5049	0.65
7	-0.1911	-0.1899	0.63	-0.6411	-0.6405	0.09
8	-0.3492	-0.3485	0.2	-0.6597	-0.6611	-0.21
9	-0.4738	-0.4736	0.04	-0.5671	-0.5693	-0.39
10	-0.5598	-0.5600	-0.04	-0.3815	-0.3834	-0.50
11	-0.6038	-0.6041	-0.05	-0.1344	-0.1351	-0.5

Beam Section	Mode 3 (symmetric)			Mode 4 (anti-symmetric)		
	Analytic	Computed	% Error	Analytic	Computed	% Error
1	1.000	1.000	0	1.000	1.000	0
2	0.7186	0.7298	-1.56	0.6380	0.6614	-3.67
3	0.1835	0.2013	-9.70	-0.02964	0.0004825	102.
4	-0.2740	-0.2599	5.15	-0.5115	-0.4973	2.78
5	-0.5751	-0.5696	0.96	-0.6645	-0.6714	-1.0
6	-0.6635	-0.6665	-0.45	-0.4585	-0.4782	-4.30
7	-0.5317	-0.5399	-1.5	-0.01301	-0.03190	-145.
8	-0.2291	-0.2379	-3.8	0.4489	0.4404	1.9
9	0.1494	0.1436	3.9	0.7016	0.7044	-0.40
10	0.4892	0.4878	0.29	0.6218	0.6293	-1.2
11	0.6888	0.6905	-0.25	0.2464	0.2501	-1.5

Beam Section	Mode 5 (symmetric)		
	Analytic	Computed	% Error
1	1.000	1.000	0
2	0.5575	0.5988	-7.41
3	-0.2222	-0.1818	18.2
4	-0.6442	-0.6429	0.20
5	-0.5309	-0.5628	-6.01
6	-0.01072	-0.04512	-321.
7	0.5322	0.5208	2.14
8	0.7099	0.7232	-1.87
9	0.3945	0.4138	-4.89
10	-0.1952	-0.1887	3.3
11	-0.6481	-0.6562	-1.2

* Appendix A, Fig. 1, (b)

TABLE 12
Reference Beam - Error in Displacements for 42 Section Model

Beam* Section	Mode 1 (symmetric)			Mode 2 (anti-symmetric)		
	Analytic	Computed	% Error	Analytic	Computed	% Error
1	1.000	1.000	0	1.000	1.000	0
2	0.9395	0.9396	-0.01	0.8975	0.8980	-0.06
3	0.8233	0.8235	-0.02	0.7009	0.7021	-0.17
4	0.7073	0.7077	-0.06	0.5060	0.5077	-0.34
5	0.5920	0.5924	-0.07	0.3152	0.3171	-0.60
6	0.4777	0.4781	-0.08	0.1315	0.1335	-1.5
7	0.3650	0.3655	-0.1	-0.04140	-0.03951	4.57
8	0.2547	0.2552	-0.2	-0.1997	-0.1981	0.80
9	0.1475	0.1480	-0.3	-0.3398	-0.3384	0.41
10	0.04429	0.04474	-1.0	-0.4581	-0.4570	0.24
11	-0.05419	-0.05379	0.74	-0.5517	-0.5510	0.1
12	-0.1470	-0.1467	0.2	-0.6184	-0.6180	0.06
13	-0.2335	-0.2332	0.1	-0.6566	-0.6566	0.0
14	-0.3126	-0.3124	0.06	-0.6659	-0.6660	-0.02
15	-0.3837	-0.3836	0.03	-0.6465	-0.6469	-0.06
16	-0.4461	-0.4460	0.02	-0.5999	-0.6004	-0.08
17	-0.4991	-0.4990	0.02	-0.5284	-0.5289	-0.09
18	-0.5421	-0.5422	-0.02	-0.4351	-0.4356	-0.1
19	-0.5748	-0.5749	-0.02	-0.3241	-0.3244	-0.09
20	-0.5968	-0.5969	-0.02	-0.1998	-0.2001	-0.2
21	-0.6079	-0.6080	-0.02	-0.06753	-0.06761	-0.1

Beam Section	Mode 3 (symmetric)			Mode 4 (anti-symmetric)		
	Analytic	Computed	% Error	Analytic	Computed	% Error
1	1.000	1.000	0	1.000	1.000	0
2	0.8563	0.8578	-0.18	0.8150	0.8182	-0.39
3	0.5816	0.5850	-0.58	0.4629	0.4696	-1.4
4	0.3130	0.3173	-1.4	0.1266	0.1344	-6.2
5	0.05873	0.06316	-7.54	-0.1742	-0.1670	4.1
6	-0.1713	-0.1673	2.3	-0.4176	-0.4122	1.3
7	-0.3668	-0.3635	0.90	-0.5843	-0.5814	0.50
8	-0.5183	-0.5160	0.44	-0.6614	-0.6610	0.06
9	-0.6184	-0.6173	0.18	-0.6445	-0.6465	-0.31
10	-0.6627	-0.6627	0.00	-0.5396	-0.5433	-0.69
11	-0.6502	-0.6511	-0.1	-0.3620	-0.3668	-1.3
12	-0.5835	-0.5851	-0.27	-0.1356	-0.1405	-3.6
13	-0.4690	-0.4710	-0.43	0.1106	0.1062	4.0
14	-0.3162	-0.3183	-0.66	0.3453	0.3419	0.98
15	-0.1372	-0.1392	-1.5	0.5389	0.5369	0.37
16	0.05387	0.05215	3.19	0.6673	0.6665	0.1
17	0.2424	0.2411	0.54	0.7143	0.7145	-0.03
18	0.4140	0.4132	0.2	0.6738	0.6747	-0.1
19	0.5555	0.5551	0.07	0.5507	0.5518	-0.20
20	0.6563	0.6562	0.02	0.3600	0.3608	-0.2
21	0.7086	0.7088	-0.03	0.1251	0.1254	-0.2

* Appendix A, Fig. 1, (c)

TABLE 12 (continued)

Beam Section	Mode 5 (symmetric)		
	Analytic	Computed	% Error
1	1.000	1.000	0
2	0.7736	0.7795	-0.76
3	0.3436	0.3569	-3.27
4	-0.04918	-0.03725	24.3
5	-0.3722	-0.3630	2.5
6	-0.5864	-0.5818	0.78
7	-0.6668	-0.6674	-0.09
8	-0.6081	-0.6130	-0.81
9	-0.4269	-0.4347	-1.8
10	-0.1603	-0.1692	-5.6
11	0.1403	0.1323	5.7
12	0.4183	0.4126	1.4
13	0.6218	0.6190	0.45
14	0.7128	0.7129	-0.01
15	0.6742	0.6766	-0.36
16	0.5129	0.5164	-0.68
17	0.2580	0.2616	-1.4
18	-0.04383	-0.04100	6.46
19	-0.3375	-0.3359	0.47
20	-0.5693	-0.5690	0.05
21	-0.6968	-0.6973	-0.07

TABLE 13
Test Beam 7 - Computed vs. Predicted Errors in Displacements for 12 Section Model

Beam* Section	Mode 1 (symmetric)			Mode 2 (anti-symmetric)		
	Computed Displacement	% Error	% Error Predicted	Computed Displacement	% Error	% Error Predicted
1	1.000	0	0	1.000	0	0
2	0.7710	-0.74	-0.74	0.6316	-4.73	-4.73
3	0.3180	-2.7	-2.7	-0.09557	22.0	22.0
4	-0.09563	5.7	5.7	-0.5860	0.44	0.44
5	-0.4147	0.31	0.31	-0.6397	-2.11	-2.11
6	-0.5890	-0.31	-0.31	-0.2712	-3.0	-3.0

Beam Section	Mode 3 (symmetric)			Mode 4 (anti-symmetric)		
	Computed Displacement	% Error	% Error Predicted	Computed Displacement	% Error	% Error Predicted
1	1.000	0	0	1.000	0	0
2	0.5206	-16.7	-16.7	0.4340	-48.8	-48.8
3	-0.4215	6.02	6.02	-0.6698	-5.56	-5.56
4	-0.6673	-7.06	-7.06	-0.3612	-42.7	-42.7
5	-0.07456	-76.3	-76.3	0.6520	-6.45	-6.45
6	0.6324	-3.40	-3.40	0.5279	-14.1	-14.1

Beam Section	Mode 5 (symmetric)		
	Computed Displacement	% Error	% Error Predicted
1	1.000	0	0
2	0.3696	-161.	-161.
3	-0.8470	-29.5	-29.5
4	0.2207	22.7	22.7
5	0.8039	-32.3	-32.3
6	-0.5576	-20.1	-20.1

* Appendix A, Fig. 2, (a)

TABLE 14
Test Beam 7 - Computed vs. Predicted Errors in Displacements for 22 Section Model

Beam* Section	Mode 1 (symmetric)			Mode 2 (anti-symmetric)		
	Computed Displacement	% Error	% Error Predicted	Computed Displacement	% Error	% Error Predicted
1	1.000	0	0	1.000	0	0
2	0.8821	-0.08	-0.08	0.8030	-0.49	-0.49
3	0.6512	-0.25	-0.25	0.4174	-1.8	-1.8
4	0.4231	-0.48	-0.48	0.05125	-17.9	-17.9
5	0.2027	-1.0	-1.0	-0.2662	2.2	2.2
6	-0.003910	30.2	30.2	-0.5049	0.65	0.65
7	-0.1899	0.63	0.63	-0.6405	0.09	0.09
8	-0.3485	0.2	0.2	-0.6611	-0.21	-0.21
9	-0.4736	0.04	0.04	-0.5693	-0.39	-0.39
10	-0.5600	-0.04	-0.04	-0.3834	-0.50	-0.50
11	-0.6041	-0.05	-0.05	-0.1351	-0.5	-0.5

Beam Section	Mode 3 (symmetric)			Mode 4 (anti-symmetric)		
	Computed Displacement	% Error	% Error Predicted	Computed Displacement	% Error	% Error Predicted
1	1.000	0	0	1.000	0	0
2	0.7298	-1.56	-1.56	0.6614	-3.67	-3.67
3	0.2013	-9.70	-9.70	0.0004825	102.	102.
4	-0.2599	5.15	5.15	-0.4973	2.78	2.78
5	-0.5696	0.96	0.96	-0.6714	-1.0	-1.0
6	-0.6665	-0.45	-0.45	-0.4782	-4.30	-4.30
7	-0.5399	-1.5	-1.5	-0.03190	-145.	-145.
8	-0.2379	-3.8	-3.8	0.4404	1.9	1.9
9	0.1436	3.9	3.9	0.7044	-0.40	-0.40
10	0.4878	0.29	0.29	0.6293	-1.2	-1.2
11	0.6905	-0.25	-0.25	0.2501	-1.5	-1.5

Beam Section	Mode 5 (symmetric)		
	Computed Displacement	% Error	% Error Predicted
1	1.000	0	0
2	0.5988	-7.41	-7.41
3	-0.1818	18.2	18.2
4	-0.6429	0.20	0.20
5	-0.5628	-6.01	-6.01
6	-0.04512	-321.	-321.
7	0.5208	2.14	2.14
8	0.7232	-1.87	-1.87
9	0.4138	-4.89	-4.89
10	-0.1887	3.3	3.3
11	-0.6562	-1.2	-1.2

* Appendix A, Fig. 2, (b)

TABLE 15
Test Beam 7 - Computed vs. Predicted Errors in Displacements for 42 Section Model

Beam* Section	Mode 1 (symmetric)			Mode 2 (anti-symmetric)		
	Computed Displacement	% Error	% Error Predicted	Computed Displacement	% Error	% Error Predicted
1	1.000	0	0	1.000	0	0
2	0.9396	-0.01	-0.01	0.8980	-0.06	-0.06
3	0.8235	-0.02	-0.02	0.7021	-0.17	-0.17
4	0.7077	-0.06	-0.06	0.5077	-0.34	-0.34
5	0.5924	-0.07	-0.07	0.3171	-0.60	-0.60
6	0.4781	-0.08	-0.08	0.1335	-1.5	-1.5
7	0.3655	-0.1	-0.1	-0.03951	4.57	4.57
8	0.2552	-0.2	-0.2	-0.1981	0.80	0.80
9	0.1480	-0.3	-0.3	-0.3384	0.41	0.41
10	0.04474	-1.0	-1.0	-0.4570	0.24	0.24
11	-0.05379	0.74	0.74	-0.5510	0.1	0.1
12	-0.1467	0.2	0.2	-0.6180	0.06	0.06
13	-0.2332	0.1	0.1	-0.6566	0.0	0.0
14	-0.3124	0.06	0.06	-0.6660	-0.02	-0.02
15	-0.3836	0.03	0.03	-0.6469	-0.06	-0.06
16	-0.4460	0.02	0.02	-0.6004	-0.08	-0.08
17	-0.4990	0.02	0.02	-0.5289	-0.09	-0.09
18	-0.5422	-0.02	-0.02	-0.4356	-0.1	-0.1
19	-0.5749	-0.02	-0.02	-0.3244	-0.09	-0.09
20	-0.5969	-0.02	-0.02	-0.2001	-0.2	-0.2
21	-0.6080	-0.02	-0.02	-0.06761	-0.1	-0.1

Beam Section	Mode 3 (symmetric)			Mode 4 (anti-symmetric)		
	Computed Displacement	% Error	% Error Predicted	Computed Displacement	% Error	% Error Predicted
1	1.000	0	0	1.000	0	0
2	0.8578	-0.18	-0.18	0.8182	-0.39	-0.39
3	0.5850	-0.58	-0.58	0.4696	-1.4	-1.4
4	0.3173	-1.4	-1.4	0.1344	-6.2	-6.2
5	0.06316	-7.54	-7.54	-0.1670	4.1	4.1
6	-0.1673	2.3	2.3	-0.4122	1.3	1.3
7	-0.3635	0.90	0.90	-0.5814	0.50	0.50
8	-0.5160	0.44	0.44	-0.6610	0.06	0.06
9	-0.6173	0.18	0.18	-0.6465	-0.31	-0.31
10	-0.6627	0.00	0.00	-0.5433	-0.69	-0.69
11	-0.6511	-0.1	-0.1	-0.3668	-1.3	-1.3
12	-0.5851	-0.27	-0.27	-0.1405	-3.6	-3.6
13	-0.4710	-0.43	-0.43	0.1062	4.0	4.0
14	-0.3183	-0.66	-0.66	0.3419	0.98	0.98
15	-0.1392	-1.5	-1.5	0.5369	0.37	0.37
16	0.05215	3.19	3.19	0.6665	0.1	0.1
17	0.2411	0.54	0.54	0.7145	-0.03	-0.03
18	0.4132	0.2	0.2	0.6747	-0.1	-0.1
19	0.5551	0.07	0.07	0.5518	-0.20	-0.20
20	0.6562	0.02	0.02	0.3608	-0.2	-0.2
21	0.7088	-0.03	-0.03	0.1254	-0.2	-0.2

* Appendix A, Fig. 2, (c)

TABLE 15 (continued)

Beam Section	Mode 5 (symmetric)		% Error Predicted
	Computed Displacement	% Error	
1	1.000	0	0
2	0.7795	-0.76	-0.76
3	0.3569	-3.27	-3.27
4	-0.03725	24.3	24.3
5	-0.3630	2.5	2.5
6	-0.5818	0.78	0.78
7	-0.6674	-0.09	-0.09
8	-0.6130	-0.81	-0.81
9	-0.4347	-1.8	-1.8
10	-0.1692	-5.6	-5.6
11	0.1323	5.7	5.7
12	0.4126	1.4	1.4
13	0.6190	0.45	0.45
14	0.7129	-0.01	-0.01
15	0.6766	-0.36	-0.36
16	0.5164	-0.68	-0.68
17	0.2616	-1.4	-1.4
18	-0.04100	6.46	6.46
19	-0.3359	0.47	0.47
20	-0.5690	0.05	0.05
21	-0.6973	-0.07	-0.07

APPENDIX A

BEAM MODELING AND NUMERICAL CALCULATIONS

Solutions for natural frequencies and modes of vibration of the discrete mass models of the reference beam and test beams (excepting Gopher Mariner) were obtained using the digital computer program described in Refs. [4] and [5]. For the calculation procedure, which is based upon a finite-difference method [4, 5], the continuous beams were represented by discrete systems consisting of 12, 22, and 42 masses connected by weightless members. The reference and test beams of Tables 1 through 10 were partitioned for lumping of continuous inertial and elastic properties as shown in Fig. 1.

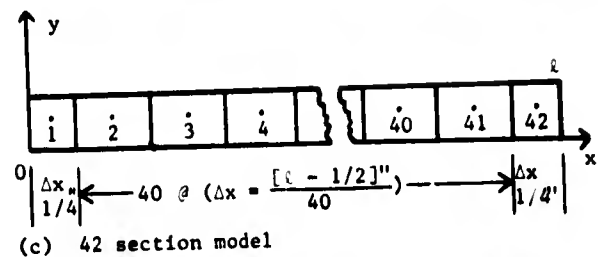
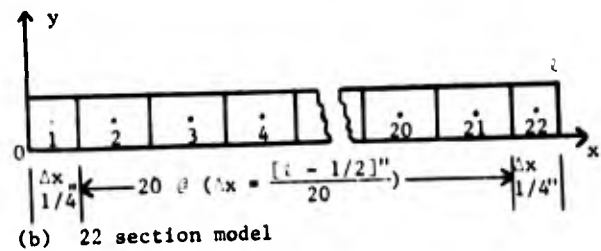
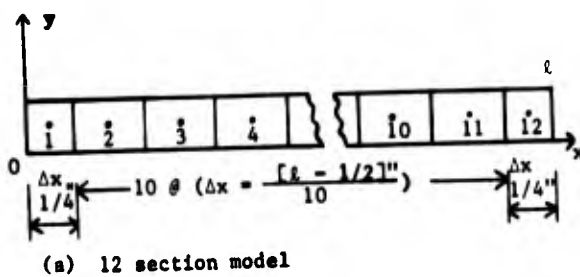


Fig. 1 - Reference and Test Beam Models Used in Tables 1 through 10

The total mass, $\mu\Delta x$, and bending compliance, $\Delta x/EI$, of each beam section are considered concentrated at the section midpoints (numbered points in Fig. 1). With this data the computer program calculates the natural frequencies of the discrete system and the normalized bending moment and displacement at each mass point.

... of the beam, the total section length ... in order ... will be varied ... end point ... are

... of the beam ... the ... mode shapes ... for the ... beam of length ... the ... of the ... beam of length ...

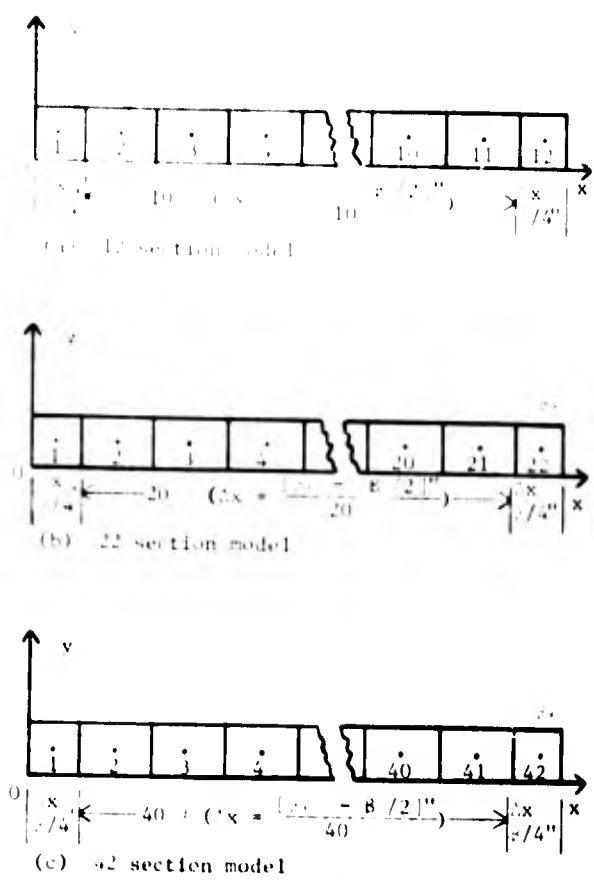


Fig. 2 - Mapping of Reference Beam Models

The computation of displacement modes for the models of test beam 7 (Tables 13, 14, 15) was done using $\beta_1 = 720''$ and $\gamma = 3$.

The model frequencies calculated by the program are considered accurate to within $\pm 10^{-6}$ radians. The calculation of mode

shapes yielded about four significant figures in displacements.

Analytic values for modal displacements were obtained with Eq. (8) using the following values for k_i : $k_1 = 4.73004074$, $k_2 = 7.8542046$, $k_3 = 10.9956078$, $k_4 = 14.1371655$ and $k_5 = 17.2787596$.

* Roots of Eq. (2) obtained from Ref. [6]

APPENDIX B

A GEOMETRIC CRITERION FOR SLENDER BEAMS

A necessary condition on the height-to-length ratios of beams, which might qualify as slender in the sense of Euler Bernoulli theory, can be obtained from a criterion given in Ref. [1]. According to this criterion a slender beam is one which can be bent into circular form in the plane of bending as shown in Fig. 3.

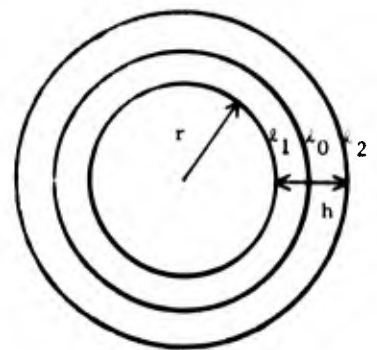


Fig. 3 - Circular Beam

In Fig. 3, l_0 denotes the neutral axis of the beam and is equal to the beam length, l . The beam height is denoted by h .

From this condition one obtains,

$$l_1 = 2\pi r \quad (9)$$

and

$$l_0 = 2\pi(r + 1/2 h). \quad (10)$$

Substituting (9) into (10) gives

$$l_1 = l_0 - \pi h \quad (11)$$

If one assumes $r > 0$, then $l_1 > 0$ and from (11)

$$l_0 > \pi h \quad (12)$$

Eq. (12) yields the limiting value on h/l under the criterion stated above,

$$h/l_0 = h/l < \frac{1}{\pi} \quad (13)$$

Eq. (13) was the condition governing the selection of h/l ratios included in this paper.

REFERENCES

1. R. T. McGoldrick, "Ship Vibration," DTMB Rept. 1451, December, 1960
2. Ralph C. Leibowitz and E. H. Kennard, "Theory of Freely Vibrating Nonuniform Beams, Including Methods of Solution and Application to Ships," DTMB Rept. 1317, May, 1961
3. S. Timoshenko, "Vibration Problems in Engineering," pp. 336-337. D. Van Nostrand Co., Princeton, New York, 1955
4. E. H. Cuthill and F. M. Henderson, "Description and Usage of General Bending Response Code 1 (GBRC1)," DTMB Rept. 1925, July, 1965
5. Francis M. Henderson, "Computer Program for General Ship Vibration Calculations," The Shock and Vibration Bulletin, Bulletin 36, Part 6, pp. 115-130, February, 1967
6. Adams, "Smithsonian Mathematical Formulae and Tables of Elliptic Functions," Smithsonian Institution, City of Washington, 1947
7. "ALCOA Structural Handbook," p. 36, Aluminum Company of America, Pittsburgh, Pennsylvania, 1960

BLANK PAGE

DYNAMIC STRESS ANALYSIS

A DISCUSSION ON THE ANALYTICAL DYNAMICS, STRESS, AND DESIGN INTERFACES

Irvin P. Vatz
Teledyne Brown Engineering
Huntsville, Alabama

The objective of this paper is to review the structural analysis work flow path. Present practices will be evaluated relative to future requirements. The following questions are discussed:

- (1) What is the effect of the analytical outputs on the efficiency of the design process?
- (2) What is the effect of the analytical process on the efficiency of the finalized design?
- (3) What is the ideal interface between dynamics analysis and stress analysis?
- (4) Can the stress analysts use their dynamics analysis inputs to make the ultimate efficient use of the information?
- (5) What is the meaning of structural design reliability?
- (6) Do we take into account the cumulative history effect on the life of structures?
- (7) How do all these factors influence the determination of the static equivalent of the dynamic load?

Recommendations will be made in the areas of administration and engineering technology.

INTRODUCTION

Large aerospace design-analysis facilities generally have an organizational division that is either line-functional or project-oriented. The engineering analysis areas, in turn, must serve one of these organizational systems - or both - according to the environment. In any case, there is a flow of requirements, documents, and finished work elements from organization to organization. These communication paths can be defined as organizational interfaces. The manner in which these interfaces operate affects the efficiency of the design operation and the quality of the final product.

Each interface possesses characteristics from the following outline.

- I. Direction
 - A. One-Way Flow Path
 - B. Two-Way (back and forth) Flow Path
- II. Route
 - A. Direct to Receiver
 - B. Indirect Through Reviewers to Receiver

III. Addressees

- A. Single
- B. Finite Few
- C. Limited Distribution
- D. General Distribution

IV. Authority

- A. Absolute Authority
- B. Staff Authority

V. Other Functions

- A. Review and Recommend
- B. For Information Only
- C. Distribution Only

The characteristics of each interface will influence its importance to the administrative system as a whole. This fact should be obvious and presents one of the basic theses of this paper.

A mature system usually has interfaces that operate without question in an automatic manner. The processes in such a system were born of need and modified to eliminate problems that experience elicited. In an unchanging environment, the mature system will usually function in a satisfactory manner. Under the pressure of slowly changing requirements, a mature system will bend, modify, and allow additions in such a way that operational stress is relieved.

The mature system will have become inflexible; that is, it will resist any gross change. But the mature system reduces visibility across interfaces and may mask the true nature of transmitted information. Thus Force is Force. The physical theorist, the dynamicist, the stress analyst, and the designer will each have his own definition and concept of Force. Through each interface Force is Force. But is all the necessary information transmitted across the interface? Has the communication been technically successful?

The success of communication across an interface depends on the ultimate objective of the system. A communication may adequately perform its mission relative to current system objectives, but a change in the objectives may require extensive overhaul of communication requirements. Some of the required changes are likely to be masked by the adequacy of past performance and the existence of one-way informational flow paths. One facet that may be masked is the factor of safety each division of the design process adds

to the design requirements. As long as the effect of a large multi-factor of safety is acceptable within the system's ultimate objectives, there is no problem. The future requirements of spacecraft and reusable launch-boosters will put forth a more demanding evaluation of design criteria. An increase in the ratio between payload and total weight is probably essential. A more complete concept of structural reliability is needed. Neither of these two demands on the design process can afford to tolerate excessive factors of safety or masked information. This paper will take a critical look at a typical structural analysis work flow system relative to foreseeable future demands.

A TYPICAL STRUCTURAL ANALYSIS WORK FLOW SYSTEM

There are probably as many variations of organizational pattern as there are organizations. It is not the purpose herein to get involved in organizational structure, but to present a dynamics analysis work flow diagram (Figure 1) that would be typical of a majority of organizations.

The flow lines are placed to exemplify the flow of information to and from the Dynamics Analysis Organization. Other lines of communication are omitted from the chart. Only the basic lines are presented so that a lot of detail will not overrun the ideas to be presented.

The chronological path starts with the receipt of the conceptual designs by Dynamics Analysis. Preliminary loads and preliminary qualifications are generated. The loads are transmitted to Stress Analysis where combined loads design criteria are established. The stress area receives and inputs loads from other applicable sources. These other loads influence the dynamics indirectly by their effect on the preliminary design drawings that will follow. Dynamics analysis may or may not be required for the first or first few design iterations. These will be stress analyzed. Generally, a reasonably firm design is forwarded to the Dynamics Analysis Group for the first iteration towards the final design analysis. This inner loop of Figure 1 will be repeated until a design satisfies both the Stress and Design organizations.

Several characteristics of this flow diagram are worth noting. Communication between Dynamics and Design is indirect and one-way. It will also follow that Dynamics has basically a review and recommendation

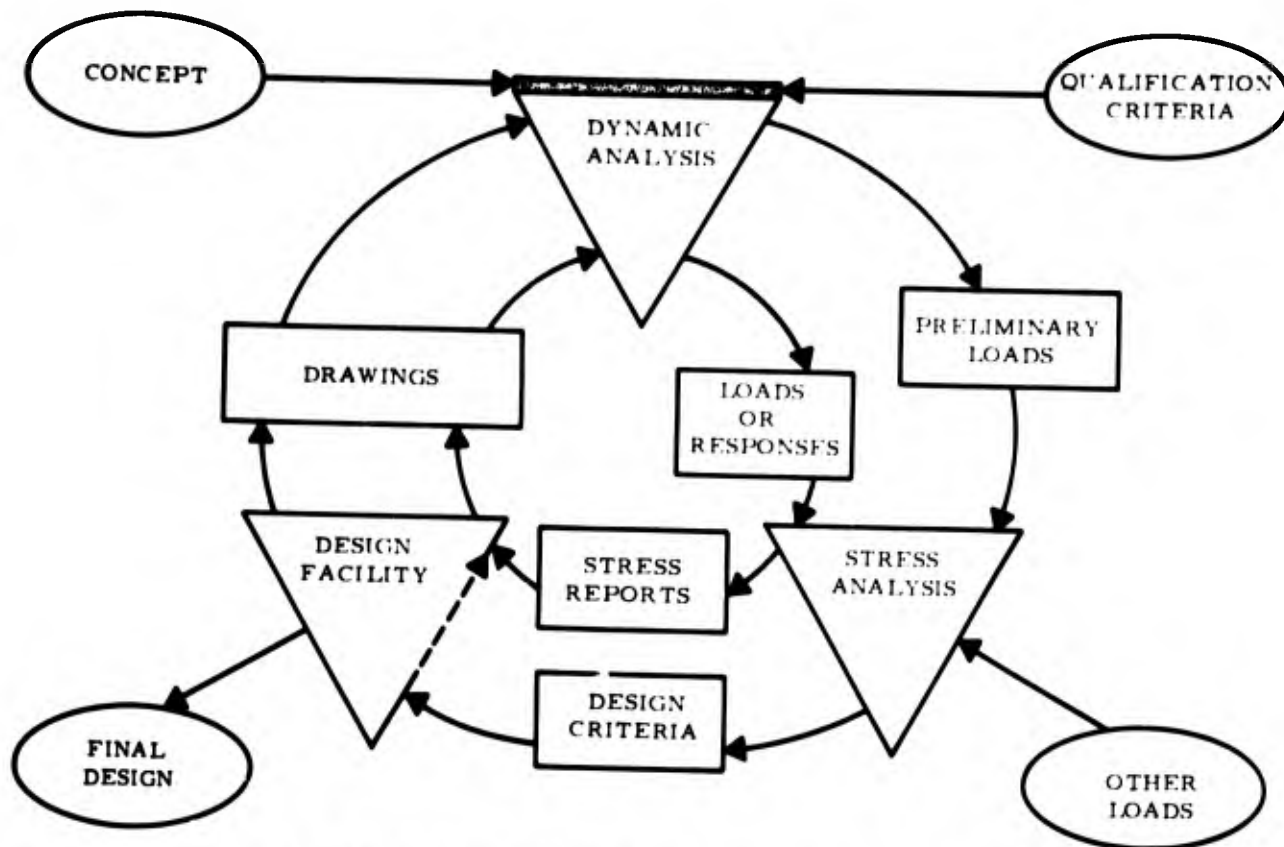


Fig. 1. Dynamic analysis in its organizational environment

function and that Dynamics has a single recipient for its product - Stress Analysis.

Several other concepts may be deduced:

- (1) The influence of dynamics on Design is filtered by the stress analysis function.
- (2) Communication (Stress to Dynamics) is generally of a Go/No-Go type in terms of allowable static stress.
- (3) Communication (Design to Dynamics) is generally filtered by the Stress organization.
- (4) More mutual grounds generally exist for good communication between Stress and Design than between either of these and Dynamics.

The fourth item above follows from the fact that designers and stress analysts communicate with a mutually understood language. Going back to the statement that Force is

Force, both Stress and Design engineers visualize Force as "a cause of the deformation of the material in bodies, ($F = -kx$). This force is "static" and in axial excitation is related to area by $F = PA$, where P is pressure or stress and A is area. Thus $PA = -kx$. This may sound very elementary -- and its being so elementary is the crux of the problem; it is believable and unquestionable. On the other hand, the dynamicist sees force as derived from some form of $F(t) = \ddot{x}M + (1 + j\eta)kx$, which is a complex differential equation in which force is time dependent. The dynamicist sees $F(t)$ as being transient, pulse-like, periodic, or random. What is the static equivalent of $F(t)$? In the author's opinion, there is no direct mathematical equivalence. The ultimate objectives and the design life will influence the relationship of $F(k, x)$ to $F(t)$.

An example of the communication problem can be stated like this. A dynamicist will state that he can calculate the structural stresses in a dynamic system. When this is true, the resultant stress is time variant. This time variant stress does not have the same relation to failure as a static stress.

A dynamic stress, when considerably below yield stress, can cause failure by fatigue. There are design and operational criteria which influence fatigue and which probably bypass the dynamicist and go to some other analytical area such as Stress, Design, Reliability, or Test. Actually, the role of Reliability relative to Structures in many organizations is rather vague. There are also dynamic stresses (those below the asymptote to the S/N curve) that will have no effect on failure whatsoever in the absence of other stresses. It may be concluded that a great deal more than mere loads, forces, or responses is required to expedite the efficient transmittal of dynamic effects on structure.

There is a vast gray area masking structural reliability. Since it is so gray, it is the author's opinion that the dynamicist automatically produces numbers, believing them to be related to $F(t)$. The stress analyst receives these same numbers and believes them to be an additive $F(k, x)$ function. This procedure may induce a positive or negative safety factor, depending on the situation. In aerospace design of short-lived hardware, the induced safety factor is generally grossly positive. As long as the total objectives of the design can absorb the safety margin, the procedure is adequate. As stated earlier, the criteria for the space shuttle program may be much more demanding. Therefore, the author has asked a series of questions that may reveal the significance of this gray area.

- (1) What Is The Effect Of The Analytical Outputs On The Efficiency Of The Design Process?

Both analytical design criteria and loads analysis affect the complexity and the number of iterations a design must go through. To increase the design process efficiency, the number of iterations must be reduced. Better initial communications in the form of more realistic preliminary loads can go a long way in reducing the need for iterations. Inadequate information during the concept stages is usually compensated by excessive safety factors. In many engineering circumstances this is good engineering practice, but future demands of space-design may require a more finite evaluation of risk. Perhaps preliminary design criteria should be produced that are marginal instead of statistically safe. Over-designed structure gets into the system because of the preliminary load requirements and then sets like concrete -- that is, it is most difficult to correct by the restraints of

the design system. Underdesigned structure is readily correctable by the system. The design process efficiency would be increased by the critical editing of preliminary loads when close safety factor tolerances must be accepted in the final product.

The inadequate and indirect communication between Design and Dynamics and the related problem between Stress and Dynamics sponsors designs that are produced without any regard to dynamics. It appears that Dynamics Analysis, as a late comer, was added to the design process to overcome designed-in-failure-mechanisms. It is true that not too long ago it was almost always more economical not to design against dynamic failure. It was better to correct dynamics problems by test, correction, and retest. This philosophy has deeply penetrated the design system. As designs advance in complexity, size, and cost, it becomes more economical to design away from dynamic problems. A more meaningful communication between Dynamics and Design should improve the design process efficiency.

The Design-Stress-Dynamics communication problem leads to the misinterpretation of dynamic design criteria -- especially for transients and shocks. The efficiency of the design process would be increased if the $F(t)$ and $F(k, x)$ interpretations were better understood by all involved parties. This may be asking too much. Perhaps a new function should be created to coordinate load summation. This suggestion will be discussed under the last question.

Better efficiency could also be achieved where mathematical models are well coordinated. Question (3) will expand this idea.

- (2) What Is The Effect Of The Analytical Process On The Efficiency Of The Finalized Design?

The analytical process has a profound effect on the design criteria. The design cycle is tuned to prevent failure, not especially to produce design efficiency. The characteristics of the analytical interfaces do influence the weight versus reliability attitude of the designers. This is very much a part of the gray area in the design process. The discussion of the design process efficiency (Question 1) applies to this question also.

- (3) What Is The Ideal Interface Between Dynamics Analysis and Stress Analysis?

The structural analysis process for large aerospace hardware is becoming more and more dependent on the digital computer. As we look to the future, communication may very well be best served by computer language. Therefore, the technical discussion under this question will be in matrix algebra. We will define $[K]$, $[M]$, $[R]$, and $[T]$ as square matrices of stiffness, mass, damping, and transfer function, respectively. We will also define $[K]$, $[R]$, $[M]$ as elements of $[Z]$, the impedance square matrix, and $[M]^{-1/2} [K]$ $[M]^{-1/2}$ as the dynamics matrix $[D]$. $\{F\}$ and $\{X\}$ are column matrices of force and response. $\{X\}^T$ is the transpose of the response matrix, and $\{\phi\}$ is a function of $[M]^{-1/2}$ and $\{X\}$.

The dynamics analysis area may work with the following matrix equations:

$$\{\dot{X}\}^T \{F\} = \{\dot{X}\}^T [Z] \{\dot{X}\} \quad (1)$$

$$\{\phi\} [w^2] = [D] \{\phi\} \quad (2)$$

Both these equations require the generation of a mass and a stiffness matrix. An $\{X\}$ matrix may be assumed to be an input by using statistical data, and the resulting loads calculated; or a load matrix $\{F\}$ can be assumed, and the response determined. Both of these processes are complicated by the mode shape summation requirement. The equation

$$\{X_2\} = [T] \{X_1\} \text{ or } \{\ddot{X}_2\} = [T] \{\ddot{X}_1\} \quad (3)$$

is quite often used to simplify response prediction after the natural frequencies and mode shapes have been determined.

Now what part of the dynamics analysis process is the stress analyst interested in? It is the author's opinion that a stress analyst wants a static equivalent of $\{F\}$ or $\{X\}$ and is really not interested in a factual $\{F\}$ or $\{X\}$. A second part to Equation (3) may be asked. What good would the static equivalent of the dynamic load or response do if it could be given to the stress analyst? In the author's opinion not much value would be received. Many factors would affect the continued value of a discrete matrix. These factors are not now generally reviewed by the dynamics analyst. In other words, the dynamics analyst is not a structures reliability expert. We are talking about the accumulated history effect of temperature, radiation, de/re gassing, variable static load, shock, vibration, etc., and how these affect structural reliability. Is the stress analyst a structures reliability expert?

To a point the answer should be yes. But does his expertise cover the scope of the above accumulated history effects? It is the author's opinion that we will be extended beyond the state-of-the-art; additional engineering technology is needed.

After much thought and deliberation on Question (3), a conclusion has been reached that, in light of possible future requirements, there is no ideal interface between Stress and Dynamics. This conclusion will be brought up again later in this paper. In light of present and past requirements, current practices are reasonably practical.

The mathematical model the dynamicist uses requires a stiffness matrix, $\{K\}$. Depending upon the analysis objectives, many stiffness matrices may have to be generated. The stress analyst also uses stiffness matrices. His basic equation is

$$\{F\} = [K] \{X\} \quad (4)$$

The stress requirements for stiffness matrices generally require more detail than is practical for Dynamics. Conservation and computerized reduction of the stress stiffness matrices would help efficiency and communication. Coordination of node points with thermal engineering would also help communication.

- (4) Can The Stress Analysts Use Their Dynamics Analysis Inputs To Make The Ultimate Efficient Use Of The Information?

This is probably a bad question because the answer is an obvious "no." The use of the word "ultimate" takes the requirement beyond realism. It is asked because the "ultimate" is our objective and any change in the design process should be a step towards the ultimate. It is possible that uncorrelated problem solutions to today's gray area of structural reliability may impede rather than help growth to the ultimate.

- (5) What Is The Meaning of Structural Design Reliability?

Component reliability may be defined as "the probability of specified performance for a given period of time when used in a specified manner." Structural reliability may be defined as "the scientific analysis of a specific structure to determine the probability of successful performance considering the accumulated influence of its environments

during its design life. The word "scientific" is used here to imply more than just a statistical determination that is associated with the "Black Box" theory of reliability.

Structural design reliability is really the goal of all structural designs. We design to provide a satisfactory probability of successful performance over the design life. Even though all engineering will accept this philosophy, no separate and distinct engineering discipline has been developed; the technology is dispersed throughout a number of disciplines and organizational elements.

(6) Do We Take Into Account The Cumulative History Effect On The Life Of A Structure?

Depending upon the design objectives, the answer could be a qualified yes. There are a great many areas that are strong-armed by the test of the finalized design in an accelerated environment. This is done because the state-of-the-art of some of the engineering prediction methods is not dependable enough to stand on its own merit.

We may not be able to afford empiricism on the large, costly, multi-environmental space vehicles of the future. One of the reasons for qualifying the "yes" is that some structural reliability areas are tested by part, not the full assembly, in simulated environments not ideally identical with those experienced during design life. As the environments become more complicated, the effects of each influence become more masked by the empirical approach. Analytical predictions will become more necessary.

(7) How Do All These Factors Influence The Determination Of The Static Equivalent Of The Dynamic Load?

Systems analysis has a theory which states:

"The recognition of symptoms and the repetitive attempt to correct them will not necessarily uncover the basic problem and provide a permanent solution."

Symptoms do not by themselves define the problem, isolate the strategic kernel, or uncover the critical path. The author must confess that this paper was motivated by the recognition of a symptom -- a communication deficiency between Dynamics and Stress.

Peter Drucker states, "Strategic decisions -- whatever their magnitude, complexity, or importance -- should never be taken through problem-solving."¹ Engineers by natural inclination are problem-solvers. We would have a better professional environment and a better engineered product if we sat back and did a little more philosophizing and rationalizing. The author set out to recommend a solution to a symptom. It was discovered that there was no ideal interface between Dynamics and Stress. If we have a symptom, what is the underlying problem? The strategic fact is that there are so many influences on reliability relative to the dynamic load that the output of the dynamicist has not been fully processed. Additional refinement is needed before it is passed to the stress analyst. Is this not also true of other load inputs? And don't they have intra-dependence? Environmental conditions can add damage or damage-relief to a structure.

The author proposes changes in the structural design and analysis work flow path. (Refer to Figure 2.) Conceptual design would be processed to and through the presently construed load determination areas. But, instead of loads going to Stress, they would go to the newly conceived group that performs analysis on loads relative to structural reliability. The processed and summarized loads are then passed on for stress analysis. Another new area receives the stressing results. It is called, for lack of a better name, the Analysis Review Committee. Experts from each of the analysis areas would be included. This committee would review the stress reports for evaluation of design criteria and pass their findings to any applicable groups in the design team. They would also work closely with the designers so that the proper technology would positively influence the design -- not be reviewed after design completion. The new structural reliability group would be strongly represented on the committee.

Think about the improved use and definition of technology, and the greater importance placed on two-way communication. This idea is too new to be very positive on every advantage and disadvantage.

¹Peter F. Drucker, The Practice of Management (New York: Harper & Row, 1954).

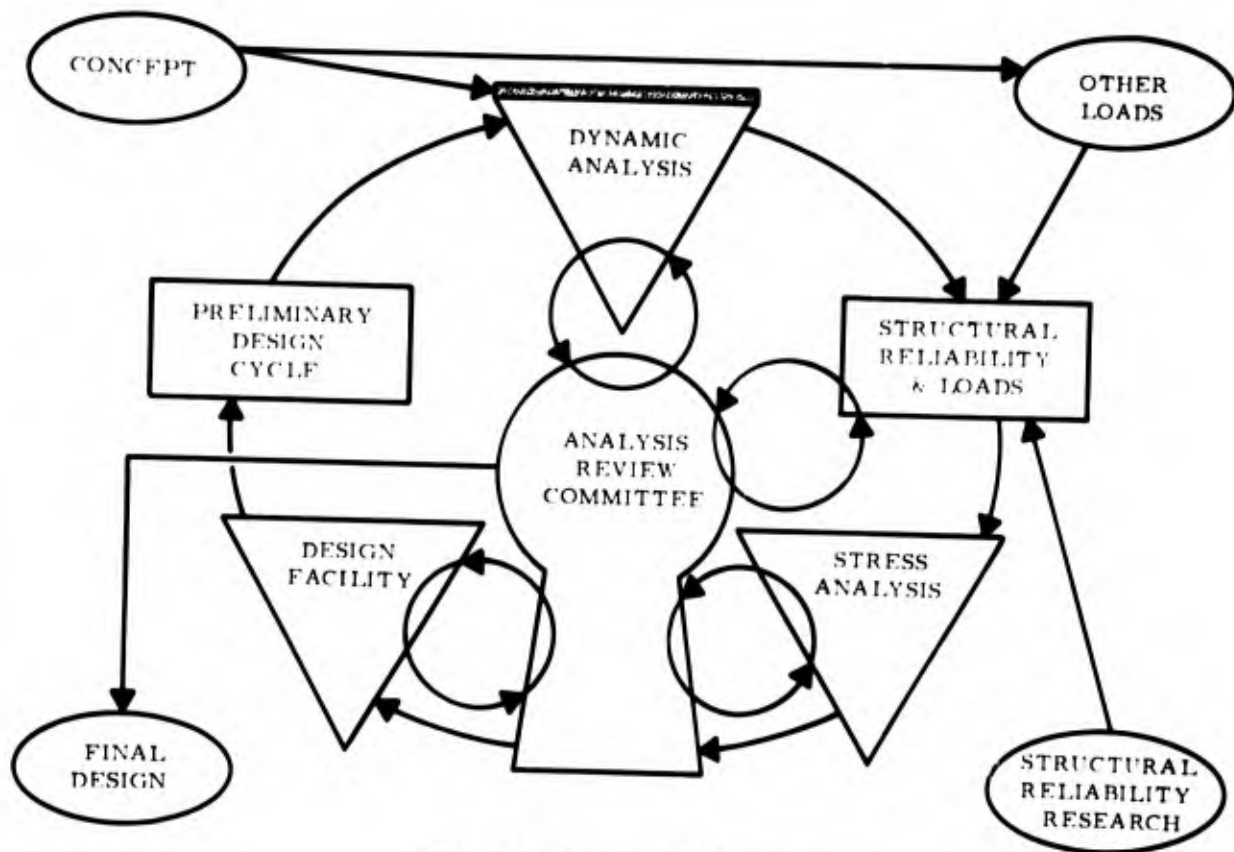


Fig. 2. Insertion of new concepts

We will close with another strategic kernel. The responsibility for improvements in structural reliability technology has never been centralized. It has always been in rather unfair competition for funding with technology

more near and dear to specialists (in other fields) who have made the decisions. New technology is needed. Squarely placing the responsibility will most certainly put this wrong to right.

DISCUSSION

Mr. McCasill (Bell Helicopter): I concur with many of the statements that you have made, many of the desires that you have expressed, and I would like to point out that many of these are our desires, too. Whether or not the stress group knows structural reliability, in the end they are stuck with structural reliability, because submitting the reports and representing the design side of the house, the stress group by nature, is stuck with the results of their handwork, at least in our product, we wind up in that position. Therefore, we ardently desire this communication and this predictive capability. As stress people representing the design side of the house we have some other pressures that are brought to bear on us as a company. In bidding a contract there is very little in any of the specifications or in any of the contractual negotiations to guide us in the area that you discussed. We wind up being the victims of cost, of available funds, and yet we have to look into the future and realize that somewhere down the line we will wind up in the position that you described of being the victims of structural reliability because of the lack of communication and the lack of predictive capabilities. So we have a share of concern and yet somewhere there is a state-of-the-art that we seem to be missing since this very preliminary process of negotiations, of specification, of Government communication to us of what is desired in structural reliability in the

product is not well defined. There are some vague machine life data, but entire giant pieces of structure are not well defined.

Mr. Cronkite (Bell Helicopter): Do you feel that one way to obtain static stress analysis and dynamic stress analysis together is to have one analysis to do both, such as the NASTRAN programs, or the other large structural analysis programs that are designed to this end?

Mr. Vatz: I will not answer that question, because that is an opinion question and there are people here who have different opinions than I. But I will say that some people have told me that the dynamicist can calculate instantaneous stress. This is true but that is not the answer, what we want is reliability. The instantaneous stress is not the peg on which to hang structural reliability completely. It is part of that hat rack, so to speak.

Mr. Cronkite: I was not as much interested in that as I was in your comments about communications between the static stress and dynamics groups. I feel that one way you can get them together is to have one analysis for both.

Mr. Vatz: Well, I do not object to that.

DYNAMIC STRESS ANALYSIS IN A STRATIFIED MEDIUM

Jackson C. S. Yang
Ames Research Center, NASA
Moffett Field, California 94035

Stress waves generated in a structure consisting of alternating plane, parallel, isotropic, and homogeneous elastic layers by the application of pressure pulses of various shapes and duration are analyzed. The method of characteristics is employed to compute the transient stresses at various points in the structure. Numerical computations were made using both the "Effective Modulus Theory", where the layered structure is replaced by a homogeneous, transversely isotropic material, and by following the stress wave through each layer in conjunction with appropriate procedures to satisfy the boundary conditions and interface conditions. Comparisons of the results using the two approaches are presented in several graphs and it is shown that the smoothness of the applied pressure pulse, the rise and unloading times, has far more influence on the reliability of the "Effective Modulus Theory" than the generally accepted concept that it depends on the duration of the pressure pulse.

INTRODUCTION

In problems of impact, such as those experienced by a vehicle landing on a planet, any surface, entering into water, being struck by a meteoroid or being subjected to high-rate disturbances of the external pressure, such as blast loads, the pressure disturbances may give rise to appreciable stress waves propagating into the interior of the vehicle. This may cause severe damage to the vehicle or to the various components within the vehicle. The usage of multilayered structures has been increasing in importance, i.e., bumper-hull structures, heat shields, etc. The purpose of this investigation is to study the transient stresses generated in a laminated medium by high-rate pressure loads in a direction normal to the layers.

In a multilayered structure the pattern of transient stress waves is rather complicated due to the repeated reflections and refractions of the waves at the interfaces between layers of materials of different mechanical properties. The reflections and refractions of stress waves in a multilayered structure require a careful examination because they may generate somewhat unexpected effects such as the appearance of high tensile stresses in the interior of the body under compressive external loads. Excessive dynamic tensile stresses are undesirable

because they cause spalling of brittle elastic materials and delamination at the interfaces.

With this complexity of following the waves and matching boundary conditions, the customary approach in constructing a theory to describe the mechanical behavior of a laminated composite consists of replacing the composite by a homogeneous but usually an isotropic medium whose material constants are determined in terms of the geometry and in terms of the material properties of the constituents of the composite. Theories of this type are termed "effective modulus theories." For a laminated medium, the effective elastic constants have been computed by Riznichenko, Postma, White and Angona, and Rytov, (see references 1-4) on the basis of both static and dynamic considerations. It appears that the effective modulus theory yields good results for static analysis. In considering dynamic problems, however, this theory has to be viewed with some suspicion especially if the wave length and the rise time of the input pressure pulse are small.

In this paper the method of characteristics is employed to analyze the propagation of stress waves in a direction normal to the layering in laminated plates. A numerical integration of the characteristic equations in each layer, in conjunction with appropriate procedures to ensure that the conditions on the

external boundaries as well as the continuity conditions at the interfaces are satisfied, yields the stress and the particle velocity at an arbitrary location.

As a specific example we consider the stress distribution in a layered structure subjected to various types of pressure loads of varying durations, rise and unloading times. The structure treated consists of alternating limestone and sandstone layers. This is the example given by Postma (see reference 2) where the effective modulus theory was applied based on the assumption that the layered medium behaves on the whole as a homogeneous but transversely isotropic continuum. Numerical results for the dynamic stress field using Postma's effective modulus theory will be compared with the results obtained by following the wave and matching boundary conditions in every layer.

EFFECTIVE MODULUS THEORY

In this section the mechanical behavior of the laminated layers is described in an approximate manner by a homogeneous continuum model. The simplest model of that type is provided by the effective modulus theory, whereby the mechanical behavior is described by a homogeneous but anisotropic continuum.

To make the paper reasonably self-contained, the salient equations governing the elasticity of anisotropic bodies are stated. Let x_i be a rectangular cartesian coordinate system with $i = 1, 2, 3$, and let u_i be the displacement vector field. The elastic strain tensor is then defined by

$$e_{kl} = \frac{1}{2}(u_{k,l} + u_{l,k}) \quad (1)$$

where

$$u_{k,l} = \frac{\partial u_k}{\partial x_l} \quad (2)$$

For a homogeneous, anisotropic, linearly elastic medium, the stress tensor σ_{ij} is related to the strain tensor by the generalized Hooke's law

$$\sigma_{ij} = c_{ijkl} e_{kl} \quad (3)$$

In Eq. (3) it is understood that the tensor summation convention should be invoked whenever indices $i, j, k, l = 1, 2$ or 3 are repeated. The elastic coefficients satisfy the symmetry conditions

$$c_{ijkl} = c_{jikl} = c_{ijlk} = c_{klij} \quad (4)$$

Thus, of the 81 coefficients c_{ijkl} , only 21 are independent.

In applied science and engineering the following contracted notation for the stresses and the strains is generally found more convenient (see reference 5).

$$\sigma_1 = \sigma_{11}, \sigma_2 = \sigma_{22}, \sigma_3 = \sigma_{33}, \sigma_4 = \sigma_{23}, \sigma_5 = \sigma_{13}, \sigma_6 = \sigma_{12} \quad (5)$$

$$\epsilon_1 = \epsilon_{11}, \epsilon_2 = \epsilon_{22}, \epsilon_3 = \epsilon_{33}, \epsilon_4 = 2\epsilon_{23}, \epsilon_5 = 2\epsilon_{13}, \epsilon_6 = 2\epsilon_{12} \quad (6)$$

The generalized Hooke's law then becomes

$$\sigma_q = c_{qr} \epsilon_r \quad (7)$$

By comparison of Eqs. (3) and (7) we find

$$c_{11} = c_{1111}, c_{12} = c_{1122}, \dots, c_{16} = c_{1112}, \text{ etc.} \quad (8)$$

In a transversely isotropic medium all directions which make the same angle with an axis of symmetry are equivalent. If we choose the x_1 -axis as the axis of symmetry, the elastic constants c_{qr} may be arranged in the following form

$$c_{qr} = \begin{vmatrix} c_{11} & c_{12} & c_{12} & \cdot & \cdot & \cdot \\ c_{12} & c_{22} & c_{23} & \cdot & \cdot & \cdot \\ c_{12} & c_{23} & c_{22} & \cdot & \cdot & \cdot \\ \cdot & \cdot & \cdot & \frac{c_{22} - c_{23}}{2} & \cdot & \cdot \\ \cdot & \cdot & \cdot & \cdot & c_{55} & \cdot \\ \cdot & \cdot & \cdot & \cdot & \cdot & c_{55} \end{vmatrix} \quad (9)$$

As is evident from the array (9), the stress-strain relations for a transversely isotropic medium assume a simple form if the x_1 -axis coincides with the axis of symmetry.

We now consider a stratified medium consisting of a large number of homogeneous, isotropic, elastic materials (see figure 1). The Lamé's elastic constants and the thicknesses of the alternating layers are denoted by λ_l, μ_l, d_l and λ_m, μ_m, d_m respectively.

According to the effective modulus theory, the gross elastic behavior of the laminated medium is transversely isotropic with the x_1 -axis as the axis of symmetry. The stress-strain relations can then be described by equations of the general form (3). The effective elastic constants c_{11} , etc., can now be derived in terms of the elastic constants and the thicknesses of the layers by a method which was discussed in detail by Postma. The results are

$$\begin{aligned}
c_{11} &= \frac{1}{D} [(d_f + d_m)^2 (\lambda_f + 2\mu_f)(\lambda_m + 2\mu_m)] \\
c_{12} &= \frac{1}{D} [d_f + d_m] [\lambda_f d_f (\lambda_m + 2\mu_m) \\
&\quad + \lambda_m d_m (\lambda_f + 2\mu_f)] \\
c_{22} &= \frac{1}{D} [(d_f + d_m)^2 (\lambda_f + 2\mu_f)(\lambda_m + 2\mu_m) \\
&\quad + 4 d_f d_m (\mu_f - \mu_m)(\lambda_f + \mu_f - \lambda_m - \mu_m)] \\
c_{23} &= \frac{1}{D} [(d_f + d_m)^2 \lambda_f \lambda_m \\
&\quad + 2(\lambda_f d_f + \lambda_m d_m)(\mu_m d_f + \mu_f d_m)] \\
c_{55} &= (d_f + d_m) \mu_f \mu_m / (d_f \mu_m + d_m \mu_f)
\end{aligned} \quad (10)$$

where

$$D = (d_f + d_m) [d_f (\lambda_m + 2\mu_m) + d_m (\lambda_f + 2\mu_f)] \quad (11)$$

ANALYSIS OF WAVE PROPAGATION

In the analysis we restrict the attention to one-dimensional wave motions for an elastic solid (constant density and wave speed). For this type of wave motion the stress equation of motion may be written in the following form:

$$\sigma_{1j,1} = \rho u_j \quad (12)$$

The solutions of equations (12) may be written in the general form:

$$u_j = U_j(t - x_1/c) \quad (13)$$

It is known that the wave velocity c can in general assume three values, which are the three roots of the following cubic equation:

$$\det |c_{1j1k} - \rho c^2 \delta_{jk}| = 0. \quad (14)$$

where δ_{jk} is the Kronecker delta. It can easily be shown that in general a normal external disturbance produces three waves whose wave fronts propagate with the wave velocities that are computed from equation (14). One of these waves is longitudinal, the other two are transverse waves. This effect does not occur for an isotropic medium, where a normal surface disturbance produces a longitudinal wave only. It also does not occur for a transversely isotropic medium if the axis of symmetry is normal to the boundary.

A numerical analysis of the wave propagation problem is conveniently carried out by the method of characteristics. The characteristic curves are those curves in the x_1 - t plane along which the system of partial differential equations can be replaced by differential expressions containing total differentials.

We first introduce the particle velocity $v_1(x_1, t)$ as

$$v_1(x_1, t) = \frac{\partial u_1(x_1, t)}{\partial t}. \quad (15)$$

In terms of the particle velocity, the equation of motion, equation (12), is then rewritten as

$$\frac{\partial v_1}{\partial t} = \frac{1}{\rho} \frac{\partial \sigma_1}{\partial x_1}. \quad (16)$$

From the strain-displacement relation, equation (1), for one dimension, differentiation yields

$$\frac{\partial \epsilon_1}{\partial t} = \frac{\partial v_1}{\partial x_1}.$$

Also, defining

$$\rho c^2 = \frac{\partial \sigma_1}{\partial \epsilon_1} \quad (17)$$

we can show that c is the wave speed in the medium and equation (17) can be written in the form

$$\frac{\partial \sigma_1}{\partial t} = \rho c^2 \frac{\partial \epsilon_1}{\partial t} = \rho c^2 \frac{\partial v_1}{\partial x_1} \quad (18)$$

It is now seen that total differentials can be obtained along $\frac{dx_1}{dt} = \pm c$, where c is defined by equation (17):

$$\begin{aligned}
\frac{d}{dt} \left(v_1 \mp \frac{\sigma_1}{\rho c} \right) &= \frac{\partial v_1}{\partial t} + \frac{\partial v_1}{\partial x_1} \frac{dx_1}{dt} \mp \left(\frac{1}{\rho c} \frac{\partial \sigma_1}{\partial t} + \frac{1}{\rho c} \frac{\partial \sigma_1}{\partial x_1} \frac{dx_1}{dt} \right) \\
&= \frac{\partial v_1}{\partial t} - \frac{1}{\rho} \frac{\partial \sigma_1}{\partial x_1} \pm \left(c \frac{\partial v_1}{\partial x_1} - \frac{1}{\rho c} \frac{\partial \sigma_1}{\partial t} \right).
\end{aligned} \quad (19)$$

From equations (16), (18) and (19) we have:

$$\text{along } \frac{dx_1}{dt} = +c: \quad \frac{d}{dt} \left(v_1 - \frac{\sigma_1}{\rho c} \right) = 0 \quad (20)$$

along

$$\frac{dx_1}{dt} - c : \quad \frac{d}{dt} \left(v_1 + \frac{\sigma_1}{\rho c} \right) = 0 \quad (21)$$

In multilayered structures materials of different material properties are joined. Across the interfaces the stresses and the particle velocities are continuous. The conditions at an interface between two materials f and m then are of the form

$$(\sigma_1)_f = (\sigma_1)_m \quad (22)$$

$$(v_1)_f = (v_1)_m \quad (23)$$

The plate can be subjected to external disturbances at either boundary, or both. The input can be applied suddenly or gradually in any specified time function for σ and v . Since it is assumed that the body is initially at rest and undisturbed, the field variables vanish identically ahead of the first wave front.

NUMERICAL PROCEDURE

Consider the grid system of the characteristic lines in the x_1 - t plane as shown in figure 2. The ordinate $x_1 = 0$ represents the boundary of the body, where the external disturbances are applied. A numerical procedure involving stepwise integration along the characteristics of equations (20) and (21) is employed to compute the response for various inputs. The stresses and the particle velocity are calculated at all grid points.

When the external input has a finite rise time, σ_{11} and v_1 vanish identically along and ahead of the wave fronts $ABG \dots D$. If the external input has a step discontinuity it is for computational purposes assumed that the step is applied over an infinitesimally small time, so that the magnitude is reached along $CHM \dots F$, but the field quantities still vanish along $ABG \dots D$.

The grid points are divided into three groups: interior points, boundary points and interface points.

BOUNDARY POINTS

Along the boundaries $x_1 = 0$ one of the two variables σ_{11} and v_1 is prescribed as a function of time. The remaining variable may be determined from the characteristic equations along the characteristic curves. Referring to figure 2 we note that since the field variables vanish at A and B, for the boundary $x_1 = 0$, only the equation along c^+ (B to C) is used.

INTERIOR POINTS

The field variables vanish at B and G, and they have been computed at the boundary point C. The values of σ_{11} and v_1 at the grid point H can then be computed by employing the characteristic equations along GH (c^+) and CH (c^-). The computation at other interior points proceeds by a step by step procedure. Thus, to compute the field variables at S, we employ the values at P and R, which have previously been computed, and we use the characteristic equations along c^- and c^+ , respectively.

INTERFACE POINTS

To compute the field variables near an interface we consider the points N_1 and N_2 , which are located on different sides of an interface but infinitesimally close to the interface, as shown in figure 3. There are altogether four unknown field variables at the points N_1 and N_2 . Above the interface the characteristic equation along MN_1 can be utilized. Underneath the interface we can use the characteristic equation along LN_2 . Two additional equations, adding to a total of four equations, are obtained from the interface conditions (22) and (23) which relate the field variables at N_1 and N_2 . The four field variables at the interface can thus be computed by solving four algebraic equations simultaneously.

The computations described above were carried out on a digital computer. It is apparent that the smaller the characteristic grid, the more accurate the numerical results will be.

Care must be exercised to insure that the c^- characteristic lines reaching an interface meet up with the c^+ characteristics from the grid points in the next layer. This can be accomplished by relating the increments Δx in the i th layer (first material) and $(i+1)$ th layer (second material) by the relation

$$c_i \Delta x_i = c_{i+1} \Delta x_{i+1}$$

where c_i and c_{i+1} are the dilatational wave speeds in the i th and $(i+1)$ th layers.

NUMERICAL EXAMPLES

Eve and Keys (see reference 6) give the following numerical values for elastic constants of typical earth materials:

Limestone:

$$\rho = 2.69-2.72 \quad ; \quad \mu = (2.1-3.0) \times 10^{11} \\ \kappa = (3.75-5.7) \times 10^{11}; \quad \nu = 0.25-0.28 \text{ (c.g.s. units)}$$

Sandstone:

$$\rho = 2.3 \quad ; \quad \mu = 0.61 \times 10^{11} \\ \kappa = 1.25 \times 10^{11} ; \quad \nu = 0.29 \quad (\text{c.g.s. units})$$

κ is the bulk modulus; $\kappa = \lambda + \frac{2}{3}\mu$; ν is Poisson's ratio.

For a demonstration of the anisotropy under realistic conditions, we take the d_f layers to be limestone and the d_m layers sandstone, with the following parameters:

Limestone:

$$\rho_f = 2.7; \mu_f = 2.5 \times 10^{11}; \lambda_f = 3.0 \times 10^{11}; \nu_f = 0.273$$

Sandstone:

$$\rho_m = 2.3; \mu_m = 0.6 \times 10^{11}; \lambda_m = 0.8 \times 10^{11}; \nu_m = 0.286$$

Let $d_f = 1$; $d_m = 3$; and using equations (10) and (11), we find

$$c_{11} = 3.36 \times 10^{11} \frac{\text{DYNE}}{\text{CM}^2} \quad c_{33} = 2.46 \times 10^{11}$$

$$c_{12} = 1.21 \times 10^{11} \quad c_{44} = 0.74 \times 10^{11}$$

$$c_{13} = 0.97 \times 10^{11} \quad c_{66} = 1.08 \times 10^{11} \\ \rho = 2.4$$

$$\left(\frac{c_{11}}{\rho}\right)^{\frac{1}{2}} = 3.73 \text{ km-sec}^{-1}; \left(\frac{c_{44}}{\rho}\right)^{\frac{1}{2}} = 1.76 \text{ km-sec}^{-1}$$

$$\left(\frac{c_{33}}{\rho}\right)^{\frac{1}{2}} = 3.21 \text{ km-sec}^{-1}; \left(\frac{c_{66}}{\rho}\right)^{\frac{1}{2}} = 2.12 \text{ km-sec}^{-1}$$

If each layer is considered in the laminated structure:

Limestone:

$$c_1 = \left[\frac{\lambda_f(1 - 2\nu_f)}{\nu_f(1 - \nu_f)\rho_f} \right]^{\frac{1}{2}} = 5.05 \text{ km-sec}^{-1}$$

Sandstone:

$$c_2 = \left[\frac{\lambda_m(1 - 2\nu_m)}{\nu_m(1 - \nu_m)\rho_m} \right]^{\frac{1}{2}} = 2.7 \text{ km-sec}^{-1}$$

Four different types of input pulses are investigated in this paper: step, rectangular, triangular, and half sine. In all cases, five different pulse lengths were considered: $\bar{t}_1 = 40, 80, 160, 320$, and 640 microseconds per kilometer of layer thickness. For each type of input pulse and for each pulse length, the stresses and particle velocities were computed at certain specific locations in the laminated structure with 18 layers of alternating limestone and sandstone. The results for the stresses at a point

in the middle of the ninth layer of sandstone of a few of the cases are presented in figures 4-6. The stresses were rendered dimensionless by dividing by σ_0 where σ_0 is the maximum value of the externally applied pressure, i.e.,

$$\bar{\sigma} = \frac{\sigma(x_1, t)}{\sigma_0} \quad (24)$$

The time scale is dependent upon the thickness of the laminated layers:

$$t = 0.2 \bar{t} d$$

where the dimensions of \bar{t} are in microsec. per kilometer of layer thickness and d is in kilometers.

The effect of the rise and unloading times of the input pulse were investigated. Five different rise and unloading times for two different types of input pulses were considered: $\bar{t}_1 = 0, 5, 10, 15, 20$ microsec. per kilometer of layer thickness. The results for the trapezoidal and triangular input pulses are presented in figures 7 and 8.

General plots of the effects of wave length, rise and unloading time with respect to the percentage of the deviation of the "Effective Modulus Theory" to the theory that takes into account the wave propagation in all the layers are presented in figures 9 and 10.

It is observed in figure 9 that the differences in the peak stress values predicted by the two theories are between 32% to 42% for various lengths of rectangular and step pulses. However, the comparisons were very good for the triangular and half-sine pulses, between 6% to 20% and 2% to 10% respectively. It is also observed in figure 10 that the effect of the rise and unloading time of the input pulse gave an error difference in the peak stress values predicted by the two theories of about 10% (compare errors at $t = 0$ and $\frac{t}{5\bar{\alpha}} = 4$).

CONCLUSIONS

In this paper the propagation of stress waves in laminated composite structures was analyzed by means of the method of characteristics. A numerical integration of the characteristic equations in conjunction with appropriate procedures to ensure that the conditions on the external boundaries as well as the continuity conditions at the interfaces are satisfied yields the stresses and the particle velocities at any point in the structure as functions of the time for external pressure loads of arbitrary time variation.

Specific computations for a periodic structure consisting of alternating limestone and sandstone layers using both the "Effective Modulus Theory" and by following the stress wave and matching boundary conditions in every layer resulted in a number of conclusions which should provide guidelines as to the reliability of the "Effective Modulus Theory" and its dependence upon the wavelength, rise time, unloading time and the smoothness of the applied pressure pulse.

The comparisons between the two approaches gave the following conclusions:

1. Contrary to general belief, the duration of the applied pressure pulse does not have strong influence on the validity of the "Effective Modulus Theory."

2. The effect of the rise time and the unloading time of the applied pressure pulse is far more dominating than the wavelength. The slower the rise and unloading time, the more reliable the "Effective Modulus Theory."

3. The "Effective Modulus Theory" gives very reliable results for a very smooth pressure pulse such as a half sine pressure pulse.

4. The "Effective Modulus Theory" gives very unreliable results for zero rise time even though the wave length is allowed to approach infinity.

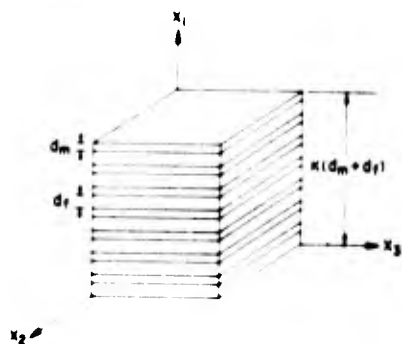


Fig. 1 Elementary volume of stratified medium.

REFERENCES

1. Ryznichenko, Yu. V., "Seismic Quasi-Anisotropy," *Izvest. Akad. Nauk. SSSR, Ser. Geozh i. Geogr.*, Vol. 13, 1949, pp. 518-544.
2. Postma, G. W., "Wave Propagation in a Stratified Medium," *Geophysics*, Vol. 20, 1955, pp. 780-806.
3. White, J. E., and Angona, F. A., "Elastic Wave Velocities in Laminated Media," *J. of the Acoustical Society of America*, Vol. 27, 1955, pp. 311-317.
4. Rytov, S. M., "Acoustical Properties of a Thinly Laminated Medium," *Soviet Phys. Acoustics*, Vol. 2, 1956, pp. 68-80.
5. Hearmon, R. F. S., *Applied Anisotropic Elasticity*, Oxford University Press, 1961.
6. Eve, A. S. and Keys, D. A., 1929, *Applied Geophysics*: Cambridge, Cambridge University Press.

ACKNOWLEDGEMENT

The work was supported by the National Aeronautics and Space Administration while the author held a National Research Council Senior Postdoctoral Resident Research Associateship at the Ames Research Center.

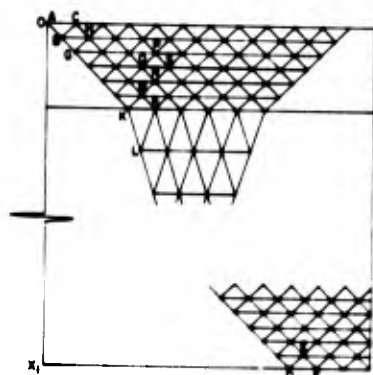


Fig. 2 Characteristic grid system.

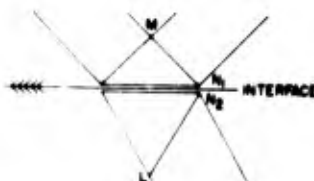


Fig. 3 Detail of grid near interface.

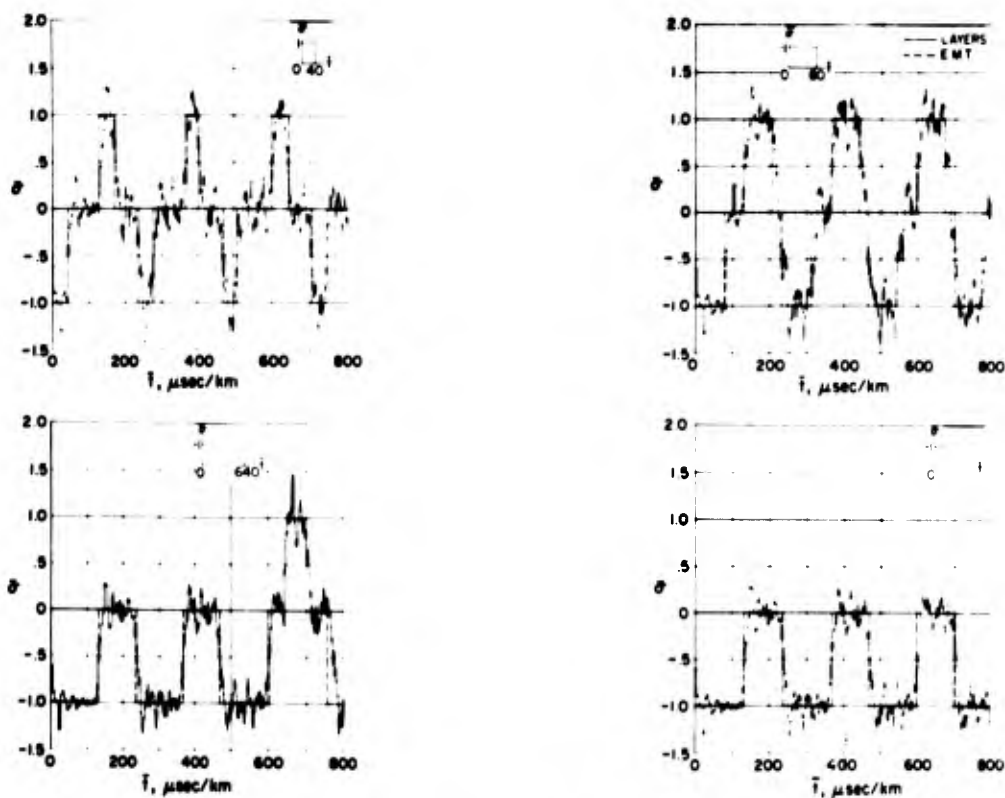


Fig. 4 Dimensionless stresses at a point in the ninth sandstone layer of the structure for a rectangular pressure input with various wave lengths.

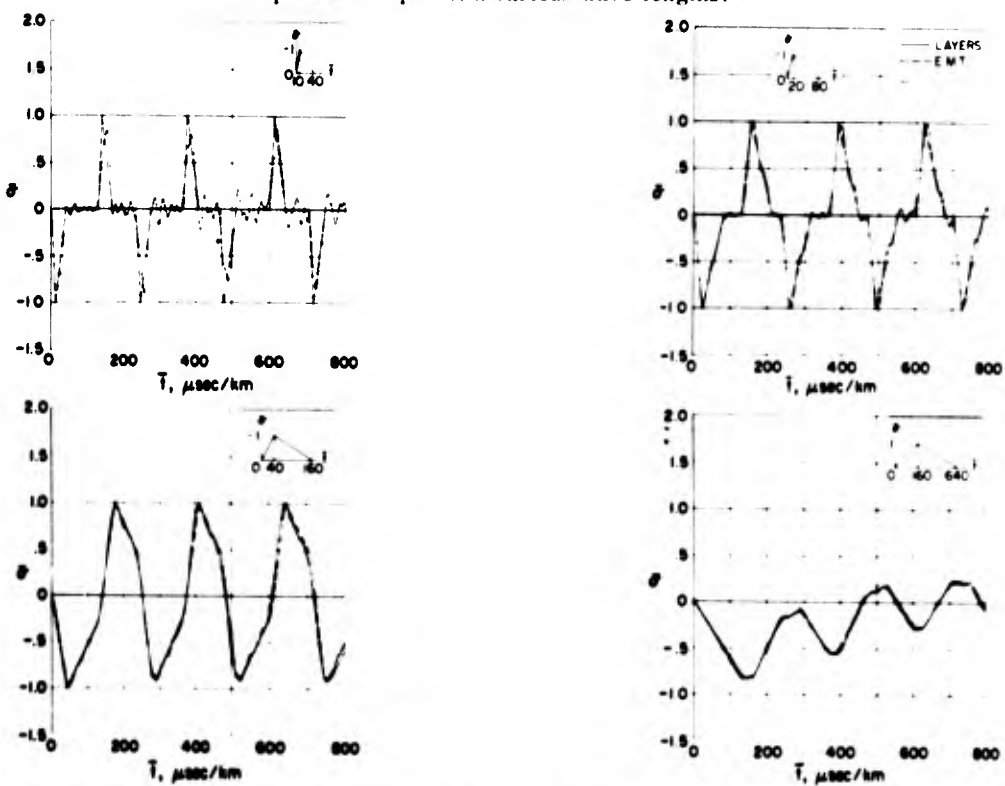


Fig. 5 Dimensionless stresses at a point in the ninth sandstone layer of the structure for a triangular pressure input with various wave lengths.

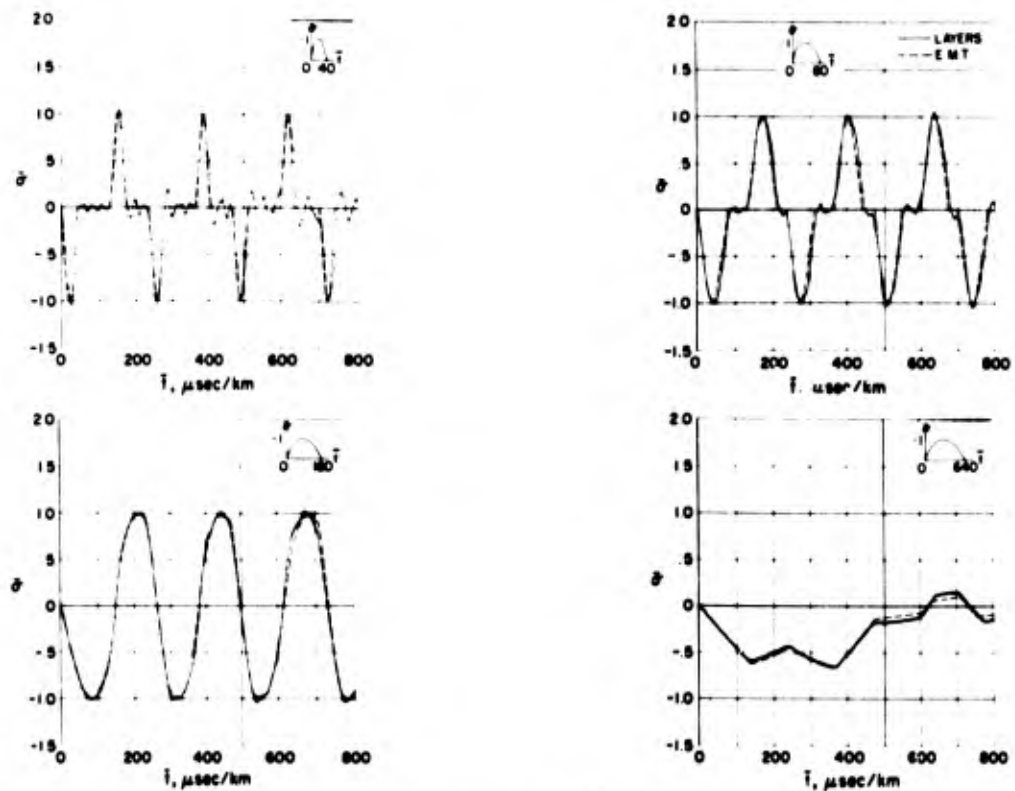


Fig. 6 Dimensionless stresses at a point in the ninth sandstone layer of the structure for a half-sine pressure input with various wave lengths.

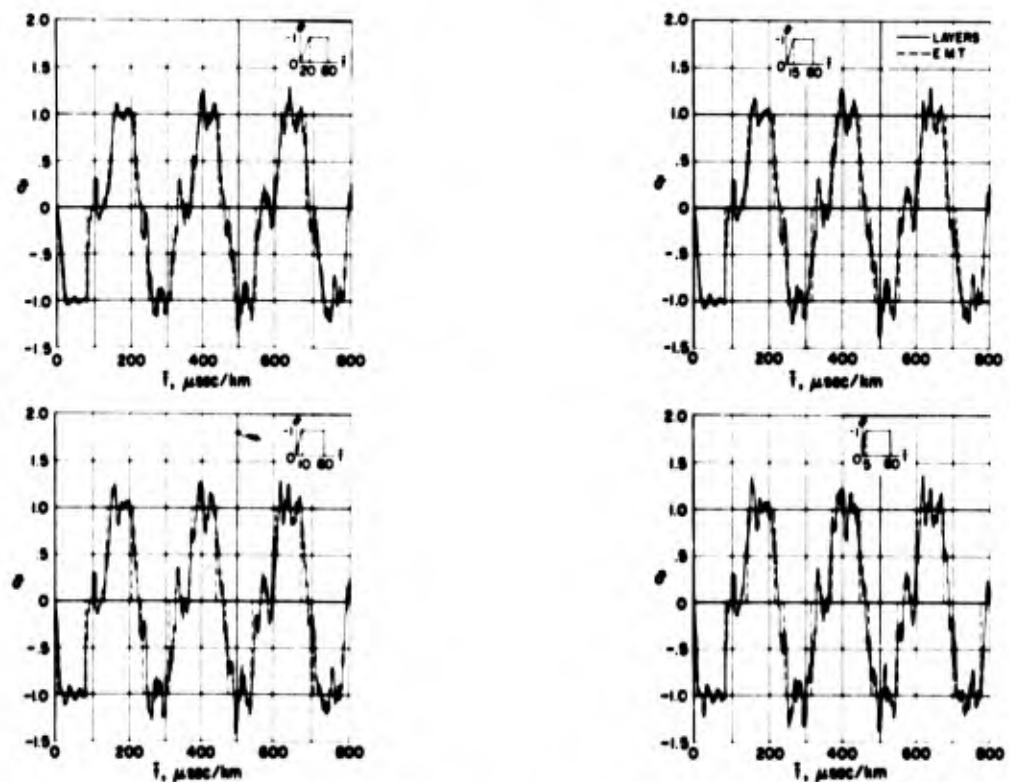


Fig. 7 Dimensionless stresses at a point in the ninth sandstone layer of the structure for a trapezoidal type pressure input with various rise times.

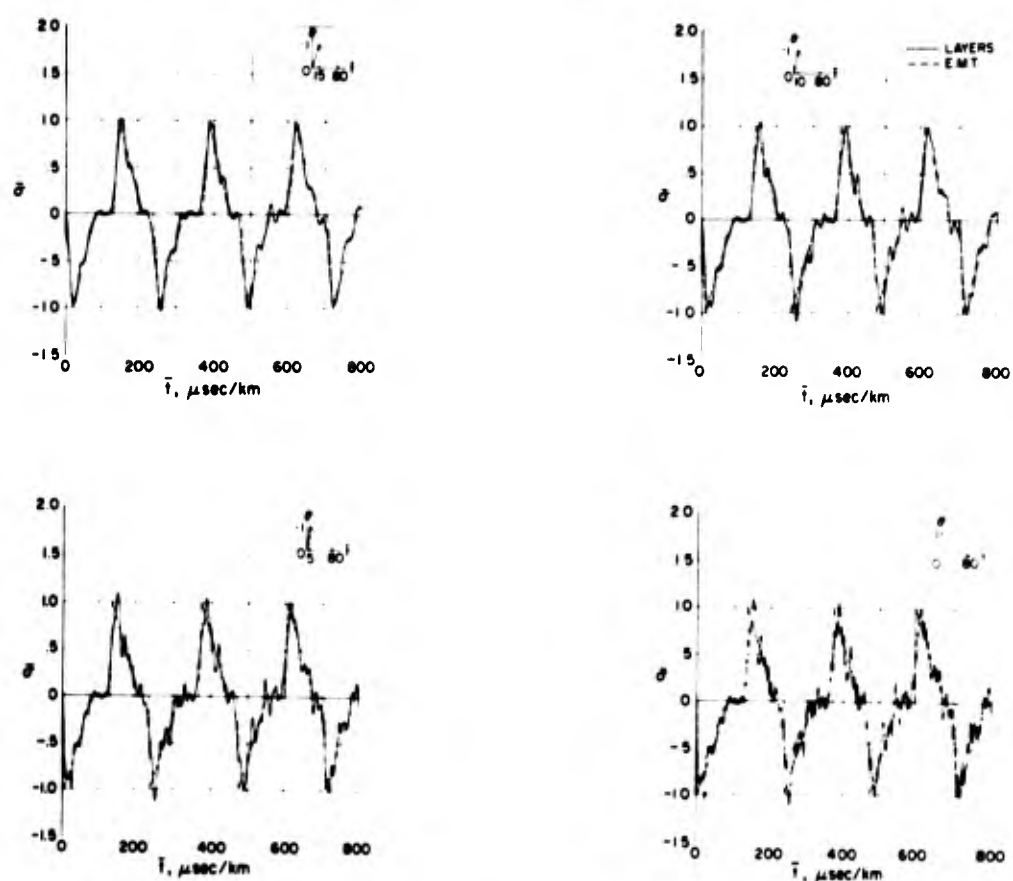


Fig. 8 Dimensionless stresses at a point in the ninth sandstone layer of the structure for a triangular pressure input with various rise times.

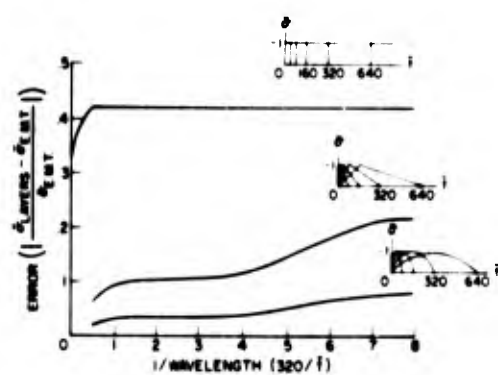


Fig. 9 Effect of wavelength and shape of pressure input on the error in peak stress values.

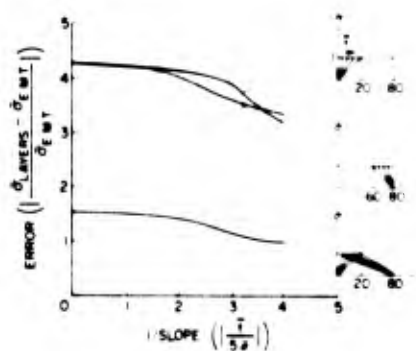


Fig. 10 Effect of rise time and unloading time on the error in the peak stress values.

DISCUSSION

Mr. Howard (Acrospace Corporation): How well does this effective modulus theory work when your acoustic impedances reaching the media are very much different than the ones that you selected?

Mr. Yang: If I were to select materials that exhibit a great difference in the impedance ratio then probably what has been said about the effective modulus as far as the long duration is true. In this particular example, I chose limestone and sandstone, and as I pointed out, the difference in the impedances is not great, it is about 1.4. If one chooses a ratio of 3 to 1 then some other results might be obtained. I am presently studying this.

Mr. Howard: The other point that is not quite clear is the significance of the little square pulses on the bottom of one of your plots. What time are you talking about, is that one transit time through the medium, or is it at each interface at each lamina?

Mr. Yang: No. This is a plot of stress versus time at a particular point in the laminated medium, at the middle for instance. So if you were sitting in the middle of this laminated medium you have a pressure pulse come through you. Now, if the pressure pulse duration is short you would see the complete pulse pass by you first, that is one square. Then if you sat there a while longer you would see the reflected wave coming back and it becomes a tensile wave. So if you sat there and let that wave go by then you would see a tensile wave which is the rectangular wave that you saw going back. If you sat there longer you would see waves coming back and forth, back and forth, back and forth.

Mr. Howard: The question is how can one monitor that if one has an effective modulus versus each one of these reflections that one might obtain from each one of the interfaces? If you were concerned with de-lamination between two layers, how could an effective modulus theory be applied?

Mr. Yang: No, the effective modulus theory just gives the overall effect, whereas I can study the interface with the other one.

Mr. Howard: I was wondering about the relationship of that mitigator. Is that a separate study or does that have something to do with this effective modulus theory?

Mr. Yang: No, that is a separate study.

Mr. Bachman (Holmes and Narver): Why could you not use a finite element analysis to perform the same type of work?

Mr. Yang: You can. I am sure a lot of people have done that. As a matter of fact there are a couple of papers out on that and on the finite difference method also.

Mr. Bachman: I just was wondering whether there are certain advantages to your method?

Mr. Yang: Definitely. I like my method because to calculate through 18 layers I put it on a computer and I only need 20 statements in the program. It can be easily picked up by various people to read and it only took me about two seconds to go through the analysis for each plot. Now, I do not know how long it takes to do this with the finite element method.

Mr. Ripperger (University of Texas): I suppose I will have to read the paper to get the answer to my question. Those plots that you showed for the effects of rise time and pulse duration and so on, I understand that they represent nothing but computed results?

Mr. Yang: That is right.

Mr. Ripperger: The thing that I do not understand is how the rise time and duration enter into the computed results when you are using the effective modulus. How do they get in there?

Mr. Yang: When I used the effective modulus theory I looked at it as a homogenous transversely isotropic material, so I was able to calculate these coefficients which in turn gave me the wave speed. Now, that is one separate item. Then I used the wave propagation theory and the method of characteristic and watched the applied load, which could be any kind of pulse, travel back and forth in the homogenous transversely isotropic material. So, whatever pulse one has, whatever variation one has, there will be a difference. It will definitely give one a difference effect whatever stress calculation one has.

Mr. Ripperger: How did you arrive at the values to use for your constants in the effective modulus theory?

Mr. Yang: First of all, the author of another paper, which I have referenced in my paper, has calculated these five coefficients by working them out in his paper as a function of the thickness of the two alternating layers and the two elastic constants. He has calculated the values for these coefficients and the procedure for this is shown, I think, step by step in his paper. I chose sandstone and limestone because I was a little bit lazy for this particular initial try. I will have to refer you to his paper.

Mr. Vatz (Teledyne Brown Engineering): I used the finite element method in a very similar problem once to calculate an acoustic transformer where I wanted to match acoustic impedances across an interface.

COMPARISON OF STRUCTURAL LOADS; STATIC VERSUS DYNAMIC

Paul J. Jones and William J. Kacena, III
Martin Marietta Corporation
Denver, Colorado

A method is presented for obtaining static equivalent loads for structures subjected to random excitation that yields stresses consistent with the dynamic condition. The technique for determining equivalent static loads applies specifically to normal mode analyses of lumped parameter systems. The governing equations are derived and an example structure consisting of a simple truss is analysed to illustrate the developed methodology. A comparison of the derived stresses for the equivalent static loads, and for other combinations of static loads, is presented to show the conservatism that this method eliminates. The method presented for determining static equivalent loads due to random excitation appears to be readily adaptable, with minor modifications, to existing dynamic response and finite element structural analysis programs.

INTRODUCTION

Structural analysts in the aerospace industry are charged with the responsibility of designing flight hardware to withstand specified random excitation levels. One classical method employed by analysts to determine response loads for complex structures subjected to random forcing functions is the modal approach applied to lumped parameter models of structural systems [1,2]. This paper expounds on this basic method to provide methodology for determining static equivalent loads that can be used to determine stresses consistent with the dynamic response condition.

Computation of equivalent static loads that can then be used to determine stresses offers the following advantages over direct computation of stresses:

- 1) The number of degrees of freedom required to adequately define a complex structure using finite element techniques generally exceeds the size capability of dynamic programs (eigenvalue/eigenvector programs, modal response analysis programs). In these cases, static reduction techniques [3] must be used to reduce sizes of the stiffness and mass matrices. To compute internal loads or stresses directly, the reduction transformation must be applied to

the internal loads matrix of the stress transformation matrix, a procedure that requires much computer time. Computation of static equivalent loads eliminates the requirement for collapsing the internal loads or stress transformation;

- 2) Computation of static equivalent loads by dynamic analysts, which are in turn provided to stress analysts, is consistent with responsibility assignments for most aerospace companies;
- 3) Static equivalent loads due to random excitation can be superimposed with other simultaneous loading conditions such as steady state accelerations. The total loads matrix can then be used in finite element structural analysis computer programs to calculate total stresses for the combined loading situation.

THEORETICAL DEVELOPMENT

The following development provides a derivation of the basic random response methodology [1,2] and the static equivalent load technique. Consider the equations of motion of a lumped parameter system subjected to a specified base motion

$$[M] \ddot{z} + (1 + i g_r) [K] \dot{z} = -[M] \ddot{x} \quad (1)$$

where z denotes the motion of the collocation points, x represents the imposed base motion, $[M]$ and $[K]$ are the mass and stiffness matrices, and $[I]$ is a matrix containing elements for all degrees of freedom consistent with the direction of excitation. The normal modes $[\phi]$ corresponding to the natural frequencies ω_r provide a coordinate transformation to the normal coordinates:

$$z = [\phi] \eta \quad (2)$$

and

$$\dot{z} = [\phi] \dot{\eta} \quad (3)$$

Substituting (2) and (3) into (1) and premultiplying by $[\phi]^T$ yields

$$[\phi]^T [M] [\phi] \ddot{\eta} + (1 + i g_r) [\phi]^T [K] [\phi] \dot{\eta} = -[\phi]^T [M] [I] \ddot{x} \quad (4)$$

Using the properties of normal coordinates, (4) can be further simplified into

$$\begin{aligned} [M_{eq}] \ddot{\eta} + (1 + i g_r) [M_{eq}] \dot{\eta} &= -[\phi]^T [M] [I] \ddot{x} \\ &= -[\phi]^T [M] [I] \ddot{x} \end{aligned} \quad (5)$$

where $[M_{eq}]$ is a matrix of equivalent masses. Since the normal modes uncouple the equations of motion, the r^{th} modal response can be written as

$$\begin{aligned} \ddot{\eta}_r + (1 + i g_r) \dot{\eta}_r &= \frac{-(\phi_r^T [M] [I])}{M_{eq_r}} \ddot{x} \\ &= \frac{\Gamma_r}{M_{eq_r}} \ddot{x} \end{aligned} \quad (6)$$

The term Γ_r is generally referred to as the modal participation factor and is a measure of the degree of response for a given mode. If the input \ddot{x} is a random excitation, the i^{th} mean square response acceleration can be written as in [1]

$$\overline{\ddot{z}_i} = \frac{\pi}{2} \sum_{r=1}^n \phi_{ir}^2 \frac{\Gamma_r^2}{g_r M_{eq_r}^2} f(\omega_r) \omega_r \quad (7)$$

where $f(\omega_r)$ is the input acceleration spectral density value at ω_r . It should be noted that Eq (7) uses an input PSD generated with the definition

$$f(\omega) = |\ddot{X}(\omega)|^2 / 2\pi T \quad (8)$$

and is subject to the assumptions of a relatively flat PSD, small damping, and little coupling between modes. The i^{th} mean square displacement can be written as

$$\overline{z_i} = \frac{\pi}{2} \sum_{r=1}^n \phi_{ir}^2 \frac{\Gamma_r^2}{g_r M_{eq_r}^2} \frac{f(\omega_r)}{\omega_r^3} \quad (9)$$

and the mean square value of the i^{th} internal load as

$$\overline{L_i} = \frac{\pi}{2} \sum_{r=1}^n (k\psi_r) \phi_{ir}^2 \frac{\Gamma_r^2}{g_r M_{eq_r}^2} \frac{f(\omega_r)}{\omega_r^3} \quad (10)$$

The internal loads transformation is represented in Eq (10) as $k\psi$. Member stresses can be expressed in a similar manner.

$$\overline{\sigma_i^2} = \frac{\pi}{2} \sum_{r=1}^n (S k\psi_r)^2 \phi_{ir}^2 \frac{\Gamma_r^2}{g_r M_{eq_r}^2} \frac{f(\omega_r)}{\omega_r^3} \quad (11)$$

where S is a stress combination matrix.

The above equations for internal loads and stresses apply to direct computation of these quantities. As previously stated, the purpose of the study is to present a procedure for developing equivalent static loads that can be used to determine internal member loads and stresses in a subsequent analysis. The procedure consists of developing an acceleration vector for each mode whose terms in the r^{th} mode are

$$\ddot{z}_{ir} = \phi_{ir} \frac{\Gamma_r}{M_{eq_r}} \sqrt{\frac{\pi}{2g_r}} \frac{f(\omega_r)}{\omega_r} \quad (12)$$

This acceleration vector, whose elements have signs consistent with the mode shape, can then be used with the mass matrix to form an applied force vector for each mode. For the r^{th} mode the applied force vector is written

$$\{L_{ex}\}_r = [M] \{\ddot{z}\}_r \quad (13)$$

The internal loads for the r^{th} mode are related to the external loads through

$$\{L\}_r = [k\psi] [K]^{-1} \{L_{ex}\}_r \quad (14)$$

However, most finite element structural analysis computer programs eliminate the above matrix inversion method in favor of other forms of simultaneous equation solutions. A similar expression can be written for the stresses in the r^{th} mode,

$$\{\sigma\}_r = [Sk\psi] [K]^{-1} \{L_{ex}\}_r \quad (15)$$

To obtain values for internal loads and stresses consistent with the dynamic values, the modal results must be root-sum-squared as indicated by

$$\{L\}_{rms} = \left[\sum_{r=1}^n \{L\}_r^2 \right]^{1/2} \quad (16)$$

and

$$\{\sigma\}_{rms} = \left[\sum_{r=1}^n \{\sigma\}_r^2 \right]^{1/2} \quad (17)$$

This method will produce internal loads and stresses which have essentially the same values as those indicated by the dynamic computations (10) and (11). Figure 1 illustrates the interchange between dynamic and finite element computer programs required to implement the methodology for determining internal loads and stresses in structures subjected to random excitation.

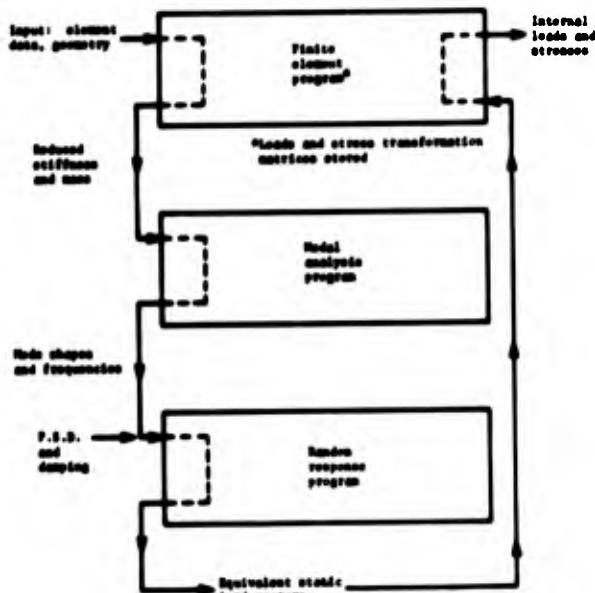


Fig. 1 - Program usage for equivalent static load method

SAMPLE PROBLEM

A simple truss subjected to a random base excitation can be used to illustrate the methodology for determining and applying static equivalent loads. The truss is shown in Fig. 2 along with the input PSD, the direction of excitation, and the assumed damping. The mass data and the structural properties are presented in Tables 1 and 2, respectively. The member loads in the truss will be determined by

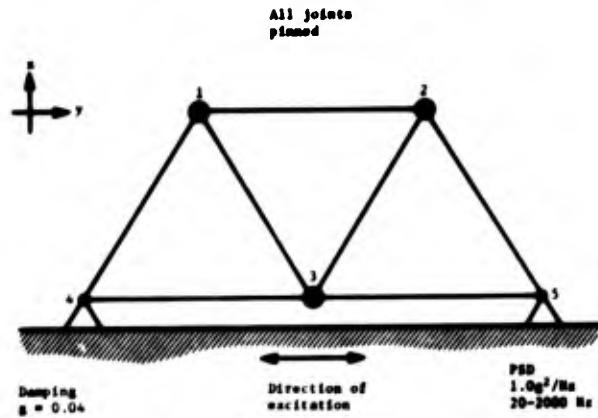


Fig. 2 - Sketch of simple truss (sample problem)

TABLE 1
Mass Data and Degree-of-Freedom

Collocation Point Number*	Lumped Mass (lb-sec ² /in.)	Degrees of Freedom	
		x	y
1	0.1295	1	2
2	0.1295	3	4
3	0.0026	5	6
4	0.0026	7 ⁺	8 ⁺
5	0.0026	9 ⁺	10 ⁺

*See Fig. 2

⁺Degrees of freedom 7, 8, 9, 10 restrained.

TABLE 2
Structural Data for Truss Members

Member Number*	Area (in. ²)	Length (in.)	Modulus of Elasticity (lb/in. ²)
1-2	0.5	25	10 ⁷
4-3	0.25	25	10 ⁷
3-5	0.25	25	10 ⁷
4-1	0.25	25	10 ⁷
1-3	0.25	25	10 ⁷
3-2	0.25	25	10 ⁷
2-5	0.25	25	10 ⁷

*See Fig. 2

- 1) Direct computation of internal loads using a dynamic analysis of the total system, which generally exceeds in size the capabilities of the dynamic programs (300 or more degrees-of-freedom);
- 2) Direct computation of internal loads using a dynamic analysis of a reduced system (degrees-of-freedom associated with the small mass at collocation

point 3 are eliminated). The computer time required to collapse the internal loads or stress transformation is generally prohibitive;

- 3) Computation of static equivalent loads for the reduced system which are in turn used to calculate internal loads. This represents the static equivalent load methodology developed in the preceding section;
- 4) Computation of internal loads using the worst combination of response accelerations as inertial loads.

The following description considers calculation of internal loads; however, member stress calculations are analogous.

The mass and restrained stiffness matrix for the truss are:

$$[M] = \begin{bmatrix} 0.1295 & & & & & \\ & 0.1295 & & & & \\ & & 0.1295 & & & \\ & & & 0.1295 & & \\ & & & & 0.0026 & \\ & & & & & 0.0026 \end{bmatrix} \frac{\text{lb-sec}^2}{\text{in.}}$$

and

$$[K] = \begin{bmatrix} 1.5 & & & -0.75 & 0.433 & \\ & 2.5 & & 0.433 & -0.25 & \\ & & 1.5 & -0.75 & -0.433 & \\ -0.75 & 0.433 & -0.75 & 2.5 & -0.433 & -0.25 \\ 0.433 & -0.25 & -0.433 & -0.25 & 1.5 & \\ & & & & & 1.5 \end{bmatrix} \frac{\text{lb}}{\text{in.}} \times 10^5.$$

The internal load transformation matrix is

$$[k_v] = \begin{bmatrix} 0 & -2.0 & 2.0 & & & \\ & & & 1.0 & & \\ & & & -1.0 & & \\ 0.866 & 0.5 & & & & \\ & & 0.866 & 0.5 & -0.866 & -0.5 \\ 0.866 & -0.5 & & & -0.866 & 0.5 \\ & & 0.866 & -0.5 & & \end{bmatrix} \frac{\text{lb}}{\text{in.}} \times 10^5.$$

The normal modes and natural frequencies for the total system are

$$[\phi] = \begin{bmatrix} 0.3277 & 1.939 & 1.934 & 0.2492 & 0.1152 & 0.1968 \\ -1.936 & -0.2382 & 0.3319 & 1.947 & -0.0656 & -0.1184 \\ -0.3277 & 1.939 & -1.934 & 0.2492 & -0.1152 & 0.1968 \\ -1.936 & 0.2382 & 0.3319 & -1.947 & -0.0656 & 0.1184 \\ 0 & 2.096 & 0 & -0.9281 & 0 & -19.48 \\ -0.8388 & 0 & -1.023 & 0 & 19.57 & 0 \end{bmatrix}$$

and

$$\{f\} = \begin{Bmatrix} 87.53 \\ 116.1 \\ 157.7 \\ 289.8 \\ 1212.0 \\ 1217.0 \end{Bmatrix} \text{ Hz.}$$

Since the mass associated with degrees of freedom 5 and 6 is small compared to the other masses, these degrees of freedom can be eliminated using reduction techniques [3]. The collapsing or reduction transformation for this process is

$$[T_c] = \begin{bmatrix} 1 & & & & & \\ & 1 & & & & \\ & & 1 & & & \\ & 0.5 & -0.288 & 0.5 & 0.288 & \\ -0.288 & 0.1667 & 0.288 & 0.1667 & & \end{bmatrix}.$$

The reduced mass, stiffness, and internal loads transformation are

$$[M_c] = [T_c]^T [M] [T_c].$$

$$[K_c] = [T_c]^T [K] [T_c].$$

$$[k_v]_c = [k_v] [T_c].$$

For the reduced system, the normal modes and natural frequencies are:

$$\phi_c = \begin{bmatrix} 0.3277 & 1.939 & 1.934 & 0.2485 \\ -1.936 & -0.2382 & 0.3318 & 1.947 \\ -0.3277 & 1.939 & -1.934 & 0.2485 \\ -1.936 & 0.2382 & 0.3318 & -1.947 \end{bmatrix}$$

and

$$\{f_c\} = \begin{Bmatrix} 87.5 \\ 116.1 \\ 157.7 \\ 289.8 \end{Bmatrix} \text{ Hz.}$$

The total system modal properties can be used in Eq (10) to compute the dynamic internal loads that represent an exact solution. The reduced system modal properties also can be used in Eq (10) to compute internal loads. The static equivalent loads method consists of using the reduced system properties in Eq (12) and (13) to produce modal external load vectors which, in turn, can be used in Eq (14) to determine internal loads for each mode. The final internal loads can then be determined using the root-sum-square procedure indicated by Eq (16). The root mean square static equivalent loads for the truss as computed from Eq (12) and (13) are

$$\{L_{ex}\}_r = \begin{Bmatrix} \text{Mode 1} \\ \text{Mode 2} \\ \text{Mode 3} \\ \text{Mode 4} \end{Bmatrix} = \begin{Bmatrix} 482.0 \\ -2848.0 \\ -482.0 \\ -2848.0 \end{Bmatrix}, \begin{Bmatrix} 0 \\ 0 \\ 0 \\ 0 \end{Bmatrix}, \begin{Bmatrix} 647.0 \\ 111.0 \\ -647.0 \\ 111.0 \end{Bmatrix}, \begin{Bmatrix} 0 \\ 0 \\ 0 \\ 0 \end{Bmatrix} \text{ lb.}$$

The fourth method uses the reduced system modal properties to compute response accelerations from Eq (7), which, when premultiplied by the mass matrix, results in the applied loads. The signs of these loads are then manipulated to produce a maximum value of each internal load. This method is included to show the conservatism that can result from some methods of static load application.

Table 3 presents the resulting root mean square (one-sigma) internal loads for the four methods. The dynamic calculations using both total and reduced system modal properties produce the same internal loads. The proposed static equivalent load method results in the identical values of internal loads. The fourth method produces conservative results.

TABLE 3
Comparison of Dynamically and Statically
Calculated Member Loads

One-Sigma Member Loads (lb)				
Member Number	Dynamic Solution Total System	Dynamic Solution Reduced System	Static Equivalent Load Method	Maximum Static Load
1-2	0	0	0	3344
4-3	3173	3144	3143	3329
3-5	3173	3144	3143	3329
4-1	2620	2615	2617	3796
3-2	3146	3146	3143	3331
1-3	3146	3146	3143	3331
2-5	2620	2615	2617	3796

DISCUSSION

A method of determining equivalent static loads for structures subjected to random excitation has been developed and applied to a sample problem which demonstrated that the static equivalent load method does yield results consistent with the dynamic response condition. This method is intended for use on structures that can be represented by lumped parameter models. The general category of systems to which this method should be applied are those large enough that static reduction techniques must be used to make the system size compatible with existing modal analysis programs and too large to allow reduction of internal loads and stress transformation matrices without spending excessive amounts of computer time.

Because of the wide variety of structural analysis programs in general use, it is impossible to provide exact numbers for the sizes of systems for which this method is optimum. An evaluation of the usefulness of this method must be based on the capabilities of structural analysis programs available to the reader. The modifications to existing computer programs before this methodology can be used are rather simple:

- 1) The random response program must be modified to generate the modal external load vectors;
- 2) The finite element program capability must be expanded so that the external load vectors for each mode are applied individually to the structure producing modal internal loads or modal mem-

ber stresses which are stored;

- 3) Finally, the finite element program needs the additional capability of root-sum-squaring internal effects over the number of modes.

Several items relative to the application of this methodology are worthy of mention. First, it is not necessary to determine and apply modal external loads for all the modes of the dynamic system; only those modes of importance need be retained for these analyses. However, a close look at the modal external loads can provide the analyst with useful information regarding the relative importance of the modes. As the equivalent static load method is presented here, root mean square or the one-sigma magnitudes are determined. These magnitudes must then be multiplied by an appropriate factor to yield meaningful design criteria. The reader is warned to calculate modal member stresses and then root-sum-square the results when stresses are desired. The reason for this precaution is that the phase relationships among the internal reactions can be important in determining stresses when combined loading exists. Nonadherence to this precaution would defeat the purpose of the static equivalent load method, which accounts for the phase relationships as specified by the mode shapes in an effort to eliminate erroneous or over-conservative results.

SYMBOLS

$[M]$	mass matrix
$[K]$	stiffness matrix
g	structural damping coefficient
\ddot{x}	base acceleration
$\{z\}$	discrete displacements
$\{\ddot{z}\}$	discrete accelerations
$\{T\}$	excitation transformation vector
$\{q\}$	modal coordinates
$[I]$	normal mode matrix
$\{\omega\}$	natural frequency matrix
$[M_{eq}]$	equivalent mass matrix
$\hat{X}(\omega)$	Fourier transform of $\ddot{x}(t)$
$f(\omega)$	acceleration spectral density
$\{p\}$	modal participation vector
$[k_i]$	internal loads transformation matrix
$[S]$	stress combination matrix
$\{L\}$	internal loads vector
$\{s\}$	stress vector
$\{L_{ex}\}$	external loads vector
r	index denoting r^{th} mode
i	index denoting i^{th} degree of freedom

REFERENCES

1. Walter C. Hurty and Moshe F. Rubinstein, Dynamics of Structures, pp. 285-290 and pp. 404-409. Prentice-Hall, Inc., New Jersey, 1965.
2. W. T. Thompson and M. V. Barton, "The Response of Mechanical Systems to Random Excitation," Journal of Applied Mechanics, June 1957, pp. 248-251.
3. W. A. Benfield and R. F. Huda, "Vibration Analysis of Structures by Component Mode Substitution," Presented at the AIAA/ASME 11th Structures, Structural Dynamics, and Materials Conference, Denver, Colorado, April 22-24, 1970.

EGGSHELLING AND VIBRATIONS OF A HIGH SPEED SHAFT WITH NASTRAN ANALYSIS

Dennis J. Martin and William C. Walton, Jr.
NASA Langley Research Center
Hampton, Virginia

The NASA recently initiated a research investigation of methods of noise reduction in aircraft turbojet engines. Of particular interest was a high speed multistage axial flow compressor. An interesting coupling-shaft vibration problem was encountered in the design and operation of the system. The solution to the vibration problem revealed an "eggshelling" phenomenon, an unusual balancing procedure, and the corresponding analytical study of the complete system using NASTRAN provided excellent agreement with experiment and indicated the design changes required for the system.

INTRODUCTION

Vibration, unbalance, or critical speed problems in rotating devices have existed for many years. A recent Shock and Vibration Information Center Monograph, SVM-4, "Dynamics of Rotating Shafts" by Loewy and Piarulli has surveyed our knowledge in this area and has presented an extensive bibliography of 554 references. The state of the art of balancing high speed shafts is quite advanced, however a thin wall shaft of a multistage, axial flow compressor system used in a noise reduction research program encountered cross-sectional deformations due to the addition of balance weights that required the development of a new and unique balancing procedure.

Analytical predictions of critical speeds of high speed shafts require a calculation of the natural frequencies of the non-rotating shaft on its appropriate supports. The NASTRAN computer program that is approaching full operational status is suited to the computation of natural frequencies of very complex structural systems and can be economically used for detailed analysis of shaft type systems.

This paper describes the thin wall shaft, the compressor-shaft-motor system, the balancing procedure developed, and a NASTRAN analysis of the complete system.

THE EXPERIMENTAL COMPRESSOR

The experimental compressor selected for the noise reduction program was mounted for test within an anechoic chamber as shown in figure 1.



Fig. 1 - Experimental compressor mounted in anechoic chamber

In order to minimize noise interference the drive motor and gear box were mounted outside the anechoic chamber. The overall compressor - gear box - motor installation is shown schematically in figure 2. The connecting coupling-

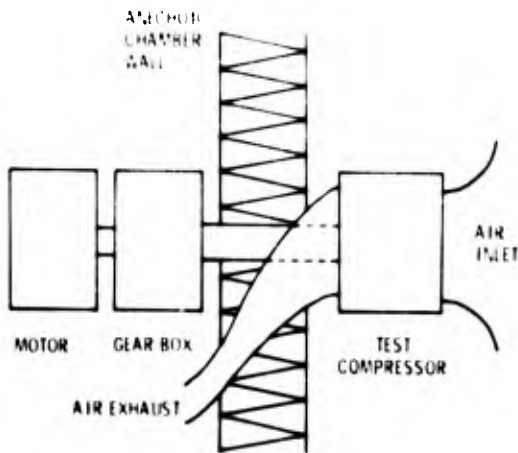


Fig. 2 - Schematic of compressor system in the anechoic chamber

shaft had a splined gear at each end and was designed to transmit 3,000 horsepower at 25,000 revolutions per minute. In order to maintain high critical speeds within the compressor it was desirable to make the coupling-shaft hollow, and therefore light so that the loads upon the compressor bearings would be small. The torque loading on the coupling-shaft was small and the shaft wall thickness was reduced to .0625 inch (.159 cm) still with low shear stresses. The coupling shaft was 22.5 inch (57.2cm) in length and 4.0 inch (10.2 cm) in diameter. The shaft was balanced in a dynamic balancing machine at 1,200 rpm; however initial test runs at 18,000 rpm clearly indicated that further balancing was needed.

CONVENTIONAL BALANCING METHOD

Conventional in situ balancing procedures were unsuccessful. Generally the addition of balance weights increased the magnitude of the unbalance - and in a very inconsistent manner. Further study revealed an interesting coupling-shaft unbalance phenomenon.

The high-speed coupling-shaft and the instrumentation are shown graphically in figure 3. A displacement sensor was mounted at the midspan of the coupling-shaft to sense the maximum deflection of the shaft due to unbalance. Balance weights were added internally and were distributed along the length of the coupling-shaft. Although the distortion is three dimensional, it may be illustrated with a two dimensional cross sectional sketch through the midspan of the coupling-shaft, figure 4. The coupling-shaft may have an inherent unbal-

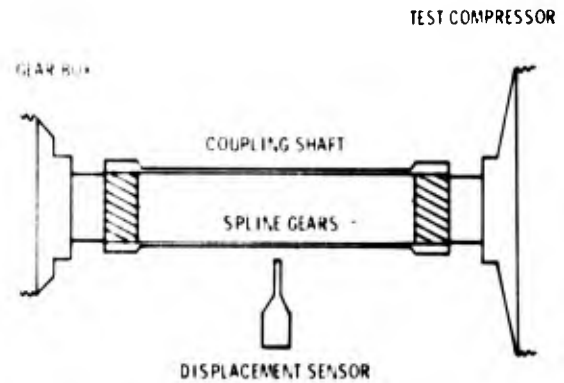


Fig. 3 - Schematic of thin-wall coupling-shaft

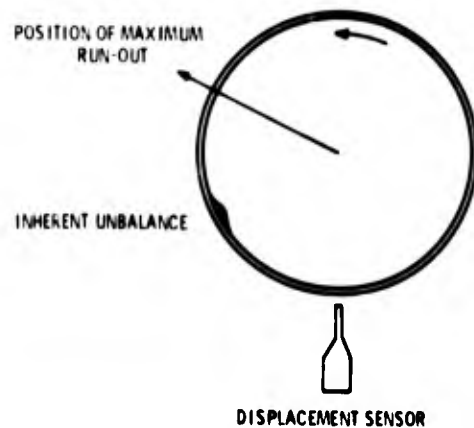


Fig. 4 - Cross section of coupling-shaft

ance due to a manufacturing imperfection or tolerance. The vector is plotted at the angular position of the maximum run-out. The length of the vector is proportional to the magnitude of the run-out. The run-out vector may be measured directly, however, to determine the balance weights to be added, it is first necessary to locate the effective angular position of the inherent unbalance, and second, to determine its magnitude. The angular position of the inherent unbalance can be determined by observing its dynamic effects, the run-out, or the forces created on the supports at either end of the shaft. The supports were not easily accessible and the deflections of the coupling-shaft at its midspan were a good indication of the unbalance.

The amount and location of the position of maximum deflection can be determined with a strobe light, a scribe, or an electronic probe as was used here. When the design speed is well below the coupling-shaft first critical the

position of the unbalance and the balance weights may be added diametrically opposite the angular position of maximum run-out. For operation at higher speeds or for systems with high damping, the deflection lags the force by a phase angle. In order to determine the correct place to attach balance weights it is necessary to determine the phase angle.

There is a standard procedure for determining this phase angle and it is illustrated in figure 5. A small balance weight is added at

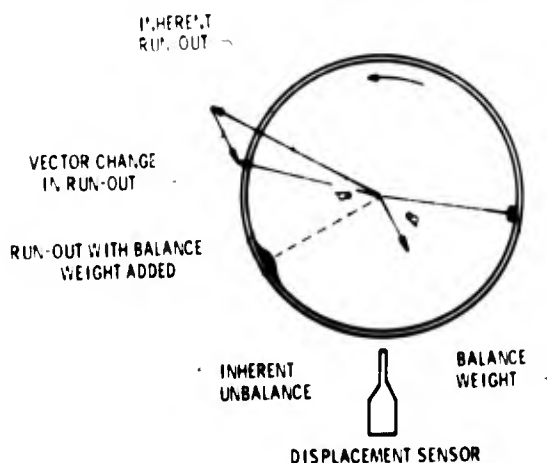


Fig. 5 - Conventional in situ balancing

an arbitrary point and the incremental change in the run-out vector is observed. The vector change in the location of maximum deflection is due to the added balance weight. The direction of the incremental change in run-out, when compared to the direction of the force produced by the added weight determines the phase angle, β , between the force and the response. The ratio of the magnitude of the change in run-out to the magnitude of the balance weight added determines the dynamic compliance of the system at the rpm selected for balancing. The angular location of the inherent unbalance is thus determined as it is assumed to be the same phase angle, β , ahead of the initially measured run-out. The magnitude of the inherent unbalance is also determined by applying the dynamic compliance factor to the magnitude of the initial inherent run-out. Balance may be achieved by adding the computed weight opposite the angular location of the inherent unbalance. Iterations of this procedure may be required to achieve final balance.

MODIFIED BALANCING METHOD

The conventional balancing procedure was used on the thin-wall coupling-shaft connecting the multistage axial flow compressor to the gear box in the noise reduction program and was unsuccessful. Iterations were inconsistent

and tended to be divergent. The conventional balancing procedure requires only a measurement of magnitude and angular position of the run-out. The instantaneous run-out signal was recorded and the real time history of the run-out appeared to contain considerable second harmonic content. To further study this phenomenon a second sensor was installed diametrically opposite the first and a typical result is shown in figure 6.

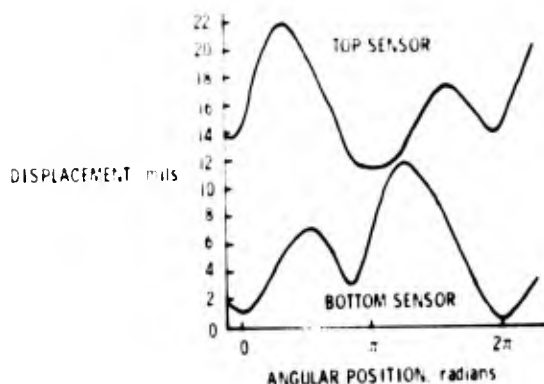


Fig. 6 - Displacement of coupling-shaft wall

It can be seen that if the shaft remained round, that lateral deflection of the shaft would produce time histories that would be similar and exactly 180° out of phase. When the shaft moved toward one sensor, it would move an equal amount away from the opposite sensor. If the shaft remained round, the sum of the two sensor outputs would thus remain constant. It is also evident that the difference of the two outputs would indicate twice the actual displacement or run-out.

The sums and differences of the outputs of the two sensors were determined and are shown in figure 7. The sum trace indicates

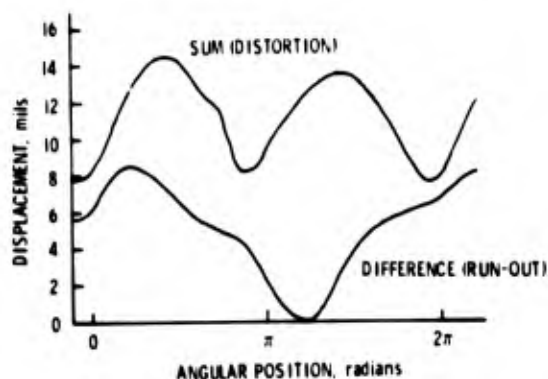


Fig. 7 - Sum and difference of diametrically opposite transducer outputs

that the shaft has experienced considerable cross-sectional distortion. The distortion fluctuates at twice per revolution. The difference contains some harmonic distortion but is principally one per revolution.

A harmonic analysis was applied to the difference (run-out) trace to obtain the magnitude and phase of the fundamental of the run-out. A trial balance weight was added as in the conventional procedure to determine the phase angle and dynamic compliance factor. The amount and location of balance weight was thus determined. These computed weights were attached in the proper place and again the individual run-out sensors indicated larger displacements and were at dangerous levels. Recording the sums and differences of the two sensors was very encouraging, however. These sums and differences are shown in figure 8.

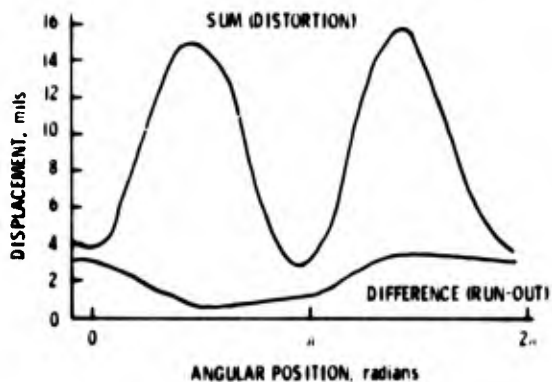


Fig. 8 - Sum and difference measurements with balance weights added

It can be seen that the shaft is nearly balanced but is badly distorted. This is illustrated in figure 9. The centrifugal forces from the inherent unbalance and the

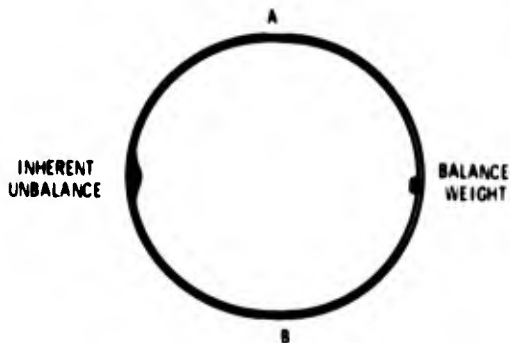


Fig. 9 - Illustration of elliptical (eggshelling) distortion mode

added balance weights have combined to distort the shaft into an apparent elliptical section, since the trace is predominantly two per revolution. The shaft has experienced what was termed an "eggshelling" type of distortion. The addition of two equal weights at A and B was then successful in reducing the distortion stresses and the measured run-out was thus reduced to acceptable levels.

The foregoing description treated the shaft as an angular ring and the coupling-shaft, having length, required that the balance weights be distributed along the length of the coupling-shaft.

ANALYTICAL STUDY

The modified balancing procedure was successful in allowing operation of the compressor at design speed with the thin-wall coupling-shaft. The thin-wall coupling-shaft later required replacement because of excessive spline gear wear and a thicker wall, smaller diameter shaft was installed. It was found, however, that the new system was operating uncomfortably close to a critical speed. Small changes in the system resulted in large deflections. An analytical study was initiated to understand the compressor - coupling-shaft - gear box system and to investigate methods of raising the critical speed of the complete system. One approach was to forego some of the noise isolation and move the motor - gear box closer to the compressor, thus reducing the length of the coupling-shaft. This would obviously raise the critical speed of the coupling-shaft alone but it was not known how much this would raise the critical speed of the complete system.

For the analysis the NASTRAN computer program was utilized. NASTRAN is a very large capability general purpose, finite element structural analysis program developed under NASA sponsorship over the past several years. The program is currently operational on a trial basis at a number of government and private installations using different computers. Release to the general public is imminent. It will be possible to obtain the NASTRAN program with detailed documentation including an engineer users manual for only a nominal charge. Information concerning NASTRAN may be obtained from COSMIC.* Steps are being taken to establish the necessary organizations within NASA to continually upgrade the program, periodically releasing improved versions.

The objectives in the following part of the paper are to show the method and the results of the design study and to bring out the applicability of NASTRAN for design studies of high speed shafting.

* COSMIC, Barrow Hall, University of Georgia, Athens, Georgia 30601

SYSTEM DESCRIPTION

Figure 10 illustrates the essential features of the shafting system of the research

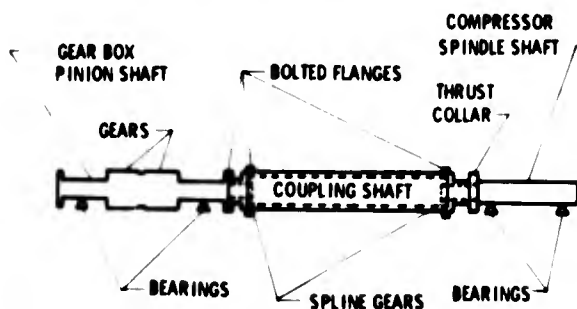


Fig. 10 - Schematic drawing of the shafting system

compressor installation. The gears of the drive motor (not shown) engage the gears on the gear box pinion shaft which is seated on two bearings. The gear box pinion shaft is bolted through a flange to the male part of a spline gear. The teeth of the male part of the spline gear mesh with the teeth in the female part of the spine gear and this female part is in turn bolted through flanges to the coupling-shaft. The other end of the coupling-shaft is bolted through flanges to the female part of a second spline gear. The male part of this second spline gear fits over the end of the compressor spindle shaft and butts against a heavy thrust collar. The gear box pinion shaft and the compressor spindle shaft are constructed of steel. The coupling-shaft is aluminum.

APPROACH

The basic information initially available to guide an approach is shown in figure 11. In

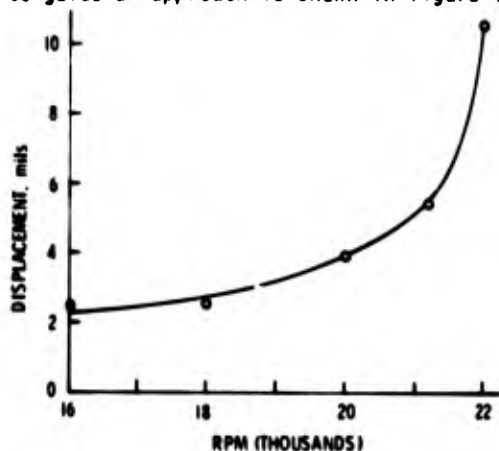


Fig. 11 - Displacement at center of coupling-shaft as a function of operating speed.

figure 11 the peak to peak vibratory displacement at the center of the coupling-shaft is plotted as a function of operating speed. This displacement was measured during trial runs of the compressor system. The data of figure 11 strongly suggest that a critical speed is being approached as the operating speed is increased to 22,000 rpm.

VIBRATION TEST PROCEDURES AND RESULTS

It was first desired to confirm the critical speed by a ground vibration test. The non-rotating coupling-shaft was forced throughout the frequency range of interest by a small electromagnetic shaker placed near the center of the coupling-shaft. The response was measured by a roving accelerometer. The test was run with the compressor connected and with it disconnected. As figure 12 indicates, resonant

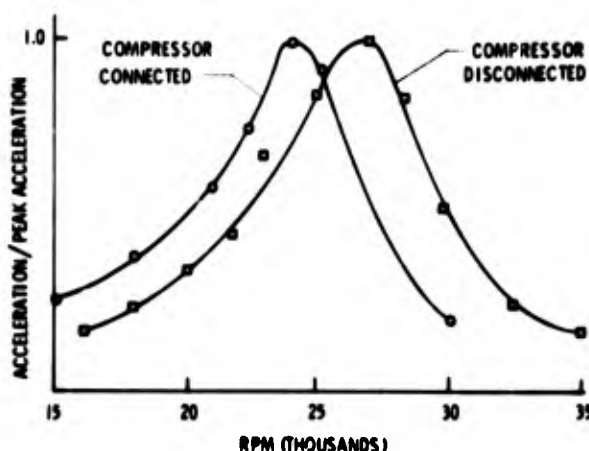


Fig. 12 - Results of the vibration test of the complete shafting system

peaks quite clearly are found at approximately 24,000 rpm (400 Hertz) with the compressor connected and at about 27,000 rpm (450 Hertz) with the compressor not connected. It is noted that the compressor spindle shaft is still a part of the system even though the compressor is not connected. Two decisions were made based upon the results shown in figure 12. First it was decided that the rapid increase of deflection amplitude indicated in figure 11 was indeed a classical critical condition in which the speed of rotation nears the fundamental structural frequency of the shaft. Second, it was decided that it would be sufficient for the purposes of the study to carry out the NASTRAN analysis for the system with the compressor disconnected and then to reduce the calculated critical speeds by about 3,000 rpm to account for the presence of the compressor. All results henceforth cited are for the case where the compressor is not connected.

The deflection mode shape of the funda-

mental mode was also measured with the moving accelerometer. The results of this measurement are shown in figure 13 along with a calculated mode shape.

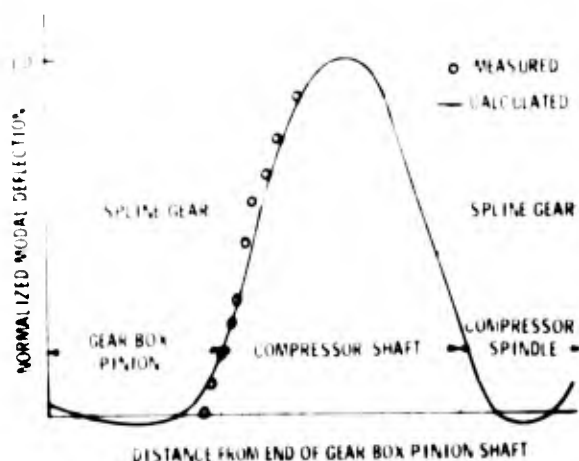


Fig. 13 - Comparison of calculated and measured natural mode shapes for the first mode of the shafting system

NASTRAN ANALYSIS PROCEDURES

In the NASTRAN analysis, the shafting system consisting of the gear box pinion, the coupling-shaft, and the compressor spindle shaft were treated as connected beams. The bearings were treated as four rigid pins allowing free rotation but zero deflection. A basic beam finite element from the NASTRAN element library was utilized with section shearing stiffness set so high that shearing deformations were in effect excluded. Typical elements are shown in figure 10. The bolted flanges were considered to carry bending moments as though the material through the flange joints was continuous. This was considered reasonable since the bolts were highly torqued and the joints could therefore be expected to remain in compression for the small vibration amplitudes. Some question arose as to whether the teeth of the spline gears could support bending moments. It was decided to treat these joints first as pinned joints and then as continuous joints in hopes of bracketing the true condition. In the connection between the coupling shaft and the compressor spindle shaft the male part of the spline gear was represented as attached to the compressor spindle shaft inboard of the end of the spindle shaft allowing overhang as in the real structure.

The masses were represented in the NASTRAN analysis as being continuously distributed with the exception of flange masses, the thrust collar, and parts of the spline gears. These latter pieces were represented by concentrated masses. In the continuously distributed part of the mass, rotary inertia was ignored, but the

rotary inertias of the connecting masses were included. Great care was exercised to input the mass and bending stiffness correctly in detail.

All aspects of the system idealization described were readily represented with the various options open to the NASTRAN user. For this relatively simple application it was easy to learn to use the program from the documentation accompanying the program. The design analysis was run after four or five trial runs with uniform beams to assure understanding of the inputting procedure. Misunderstandings, all of which were of a minor nature, were cleared up on these trial runs. Of four runs made for the actual study, all ran correctly the first time. The computer time to calculate the first three frequencies and mode shapes using a Langley Research Center CDC 6600 computer, was typically about one minute.

RESULTS OF STUDY

Natural frequencies calculated using the NASTRAN program are presented in Table I along

TABLE I. - COMPARISON OF CALCULATED AND MEASURED NATURAL FREQUENCIES (UNITS, rpm) FOR THE COMPLETE SHAFTING SYSTEM WITH THE COMPRESSOR DISCONNECTED

MODE NUMBER	CALCULATED FREQUENCY		MEASURED FREQUENCY
	PIN JOINTS	CONTINUOUS JOINTS	
1	26,575	26,877	26,800
2	36,709	53,837	

with the frequency measured for the first mode. It appears that the calculated frequency measured for the first mode is little affected by the assumptions about the rigidity of the spline gear joints. Good agreement with the test result is achieved with either the case of the joints represented as pins or as continuous beams. This relieves the concern about correct representation of the spline joints. It is of some interest to note that the second mode frequency computed for continuous joints is much higher than the second mode frequency for pinned joints. In the test results of figure 12 there is no evidence of a second mode response at 35,000 rpm although the analysis for pin joints predicts a second mode frequency of 36,700 rpm. This suggests that the spline gears act more nearly as continuous joints and affect primarily the second mode.

As mentioned previously, figure 13 shows a correlation between calculated and measured mode shapes for the fundamental mode. The calculated mode shape shown is for the case of continuous joints. Because of accessibility problems the mode shape was measured only over part of the shaft. The mode shape correlation

is considered good and along with the good frequency correlation inspires confidence in the analysis. The mode shape calculated for the case of pin joints has a very similar deflection curve to that for continuous joints and is not shown. The calculated slopes for the case of pin joints, however, indicates jumps in the slope at the spline joints as would be expected.

Figure 14 shows the effect on critical speed brought about by reducing the distance

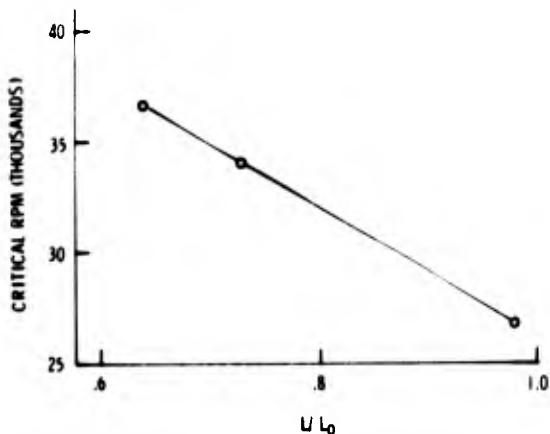


Fig. 14 - Critical speed as a function of the ratio of coupling-shaft length, L , to the original length, L_0 .

between the gear box and the compressor. Calculated critical speeds are plotted against the ratio of the reduced length of the coupling-shaft to its original length. The values of

this ratio at the data points at L/L_0 of .64 and .73 correspond to reductions of 8 inch (20.3 cm) and 6 inch (15.2 cm) in the length of the coupling-shaft. Its original length was 22.5 inch (57.2 cm). As can be seen, with the 8 inch reduction, an increase in critical speed to 36,500 rpm can be expected with the compressor disconnected. With the previously discussed correction for the presence of the compressor, a critical speed of over 33,000 rpm is indicated. On the basis of these calculations it was decided to move the motor and gear box 8 inches closer to the compressor even though this requires some alteration to the motor foundation and some sacrifice in motor-gear box noise isolation from the anechoic test chamber.

CONCLUDING REMARKS

This paper has shown that significant cross sectional distortions may be found in high speed shafts having thin walls and that conventional balancing techniques require modifications to achieve acceptable results. An alternate procedure, using a combination of two displacement sensors is described. A harmonic analysis of the sensor signals and the addition of multiple balance weights is seen to lead to acceptable balance with greatly reduced wall distortions.

It has also been demonstrated that the NASTRAN computer program, which belongs to the nation, can be used effectively to predict critical frequencies of complicated shafting systems. Considering the apparent effectiveness of the program and considering its general availability, we can now economically employ detailed analysis in the design of shafting systems and we can therefore aspire to rather high standards in justification of designs.

DISCUSSION

Mr. Paz (University of Louisville): I am aware that you mentioned that the problem was three dimensional but your explanation was two dimensional. How did you locate these corrective weights longitudinally along the shaft?

Mr. Martin: We calculated the shape for the first mode of a free-free shaft and we arbitrarily

distributed the weights in proportion to this deflection mode shape.

Mr. Vatz (Teledyne Brown Engineering): I want to compliment the author in getting experimental results that agreed with his computer program.

BLANK PAGE

**PARAMETRIC STUDY OF A BEAM WITH A COMPOUND SIDE-
BRANCH RESONATOR AS A DEVICE TO EVALUATE
PRELIMINARY DESIGN LOADS**

J. Roger Ravenscraft
Teledyne Brown Engineering
Huntsville, Alabama

The object of this paper is to present modal displacement ratios of a simulated skin-mounted component system. The results will provide an understanding of the responses relative to a point on the skin, a point at the attachment of the component to the skin, and a point located at the centroid of the mounted component. This is accomplished through a finite element model of the beam and attached component. The component centroid is sidebranched off the beam by a pair of springs. This support system will permit (a) three degrees of freedom to describe the motion of the component, and (b) a stiffened component beam interface element between the mounting attachment points on the beam simulated skin. This finite element model is then analyzed on the digital computer for various mass and stiffness values of the sidebranch. The parametric study of this simulated system is performed to show how the component parameter changes affect the modal displacement ratios.

The beam sidebranch system was chosen because it represents:

- (1) A rather elementary model
- (2) The response of the skin to acoustic excitation
- (3) The transfer of energy from the skin to an internally mounted component.

The modal density of the simulated skin mounted component is restricted by this concept to a simulation of the planar circumferential modes represented by the beam. The resulting motions will help in understanding the generation of preliminary design data from the statistics of skin response.

INTRODUCTION

The design cycle of Aerospace Vehicles generally starts with a configuration concept. The preliminary design process requires the documentation of loads that will be used to generate design criteria. Since no hardware drawings exist, the dynamic loads can be estimated by statistical methods, drawing on past experience.

One type of the required loads is represented by equipment mounted to a shell structure. The attachment is made through a

bracket. Vibration and acoustic energy will excite the shell. The response of the components mounted on this shell will depend upon configuration and system parameters of mass, stiffness, and damping.

The objective of this study is to present "modal displacement ratios" (MDR) obtained by computer solution for simulated skin mounted components. The modal displacement ratio is the quotient of v_i and v_r taken from a mode shape of a particular system. In this paper v_i is always the mode shape at the sidebranch mass in the x direction. The

mode shape on the y direction of the beam is v_y and will be specified at either y max (v_{ry}) or at the attachment location (v_{ra}). The mathematical model of a shell and sidebranch is rather involved. Therefore, the skin and mounted component modes were limited to the modal density of a beam with an attached mass. This model was chosen so that the results, although limited in scope, would yield information suitable to show the effects of varying the parameters of the more complex system. These parameters were (a) the mass properties of the simulated component, and (b) the stiffness of the sidebranch structure.

FINITE ELEMENT MODEL

The finite element model used to determine the eigenvector ratios presented in this study is shown in Figure 1.

The beam has uniform cross-section properties, except at the location between the foundation attachment points. This location is assumed to be very stiff when compared with the basic beam.

A mass is attached (as shown in Figure 1) by a pair of parallel linear springs side-branched off the beam.

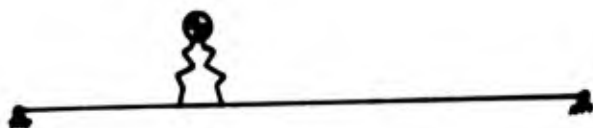


Figure 1 - Beam and Sidebranch Lumped Mass Model

The distributed mass model retains 72 degrees of freedom to describe the motion of the beam and sidebranched mass. The degrees of freedom include translation in the x and y axes and rotation about the z axis (at 23 intermediate locations along the pin-ended beam and at the center of gravity of the simulated component).

After the model was selected and the scope of input data was resolved, the model and data were processed by the DACS [1] digital computer program. Outputs of both tabular and graphical mode shapes were received. Because of the almost overwhelming quantity, the raw data are not presented in this paper. Extracted data from modes 1 and 2 are presented in Tables 1 through 3. These data are consolidated into applicable ratios for easy comprehension.

TABLE 1

MODAL DISPLACEMENT RATIOS IN THE FIRST MODE

(As a Function of Sidebranch Mass & Frequency)

$f_{n \text{ system}}$	f_{no-y}	$\frac{M_{sb}}{M_b}$	$\frac{v_{1x}}{v_{1y}}$	$\frac{v_{1x}}{v_{ra}}$	$\frac{v_{1y}}{v_{ry}}$
32.14 Hz	40 Hz	3.37	.19	3.34	4.35
35.67	51		1.93	2.13	1.71
37.65	68		3.24	1.54	1.19
41.78	95		3.67	1.27	0.97
46.36	130		2.73	1.15	0.89
52.76	185		1.32	1.09	0.88
28.26	40	7.7	0.23	2.44	2.06
32.48	51		0.48	1.81	1.52
34.51	68		0.68	1.43	1.2
37.17	95		0.77	1.22	1.01
39.84	130		0.70	1.11	0.93
41.82	185		0.53	1.05	0.88
24.15	40	15.4	0.29	1.72	1.46
24.03	51		0.33	1.42	1.21
28.65	68		0.48	1.22	1.02
30.14	95		0.46	1.12	0.94
29.8	130		0.4	1.06	0.90
28.9	185		0.36	1.03	0.87
15.9	40	30.8	0.28	1.36	1.16
17.24	51		0.33	1.22	1.03
21.45	68		0.36	1.12	0.95
20.67	95		0.34	1.06	0.90
21.08	130		0.32	1.03	0.88
20.64	185		0.32	1.01	0.86
11.57	40	61.6	0.32	1.17	0.98
10.13	51		0.32	1.1	0.93
12.11	68		0.43	1.05	0.87
13.4	95		0.32	1.03	0.87
14.15	130		0.37	1.01	0.84
13.05	185		0.35	1.0	0.84

DISCUSSION

Preliminary design loads for components mounted on structures are often required when the attachment hardware and the particular attachment location are not specified. In addition, vibration and acoustic criteria are determined from various statistical analyses of preliminary design criteria. Because of the uncertainties, conservative methods have been developed for providing preliminary loads. Feasible design concepts can then be initiated with subsequent analysis reviews to determine the adequacy of preliminary dynamic design parameters.

- [1] J. R. Hackney, Dynamic Analysis of Complex Structures by Direct Stiffness Methods, Technical Note SE-291, Teledyne Brown Engineering, September 1969.

TABLE 2
MODAL DISPLACEMENT RATIOS IN THE
FIRST MODE
(As a Function of Generalized Stiffness)

f_n system	$\frac{K_{gs}}{K_{gb}}$	$\frac{M_{gs}}{M_{gb}}$	$\frac{v_{1x}}{v_{1y}}$	$\frac{v_{1y}}{v_{ra}}$	$\frac{v_{1y}}{v_{ry}}$
32.14 Hz	0.035	3.35	0.19	3.44	4.35
35.67	0.07	3.35	1.93	2.13	1.71
28.26		7.7	0.22	2.44	2.06
37.65	0.14	3.35	3.24	1.54	1.19
32.48		7.7	0.48	1.81	1.52
24.15		15.4	0.29	1.72	1.41
41.78	0.28	3.35	3.07	1.27	0.97
34.51		7.7	0.68	1.43	1.2
24.03		15.4	0.33	1.42	1.21
15.9		30.8	0.28	1.36	1.16
46.36	0.56	3.35	2.73	1.15	0.89
37.17		7.7	0.77	1.22	1.01
28.65		15.4	0.48	1.22	1.02
1724		30.8	0.33	1.215	1.03
11.57		61.6	0.32	1.17	0.98
52.76	1.12	3.35	1.32	1.09	0.88
39.84		7.7	0.70	1.11	0.93
30.14		15.4	0.46	1.12	0.94
21.45		30.8	0.36	1.12	0.95
10.13		61.6	0.32	1.1	0.93
41.82	2.24	7.7	0.53	1.05	0.88
29.78		15.4	0.4	1.06	0.89
20.67		30.8	0.34	1.06	0.90
12.11		61.6	0.43	1.05	0.87
28.87	4.5	15.4	0.36	1.03	0.87
21.08		30.8	0.32	1.01	0.88
13.4		61.6	0.32	1.03	0.87
20.64	9.0	30.8	0.32	1.01	0.86
14.15		61.6	0.37	1.015	0.84
13.05	18.	61.6	0.35	1.005	0.84

TABLE 3
MODAL DISPLACEMENT RATIOS IN THE
SECOND MODE
(As a Function of Sidebranch Mass & Stiffness)

f_n system	Mode Type	$\frac{M_{gs}}{M_{gb}}$	$\frac{K_{gs}}{K_{gb}}$	$\frac{v_{2x}}{v_{2y}}$	$\frac{v_{2y}}{v_{ra}}$	$\frac{v_{2y}}{v_{ry}}$
36.5 Hz	B	3.35	0.035	3.74	19.0	12.
40.8			0.07	0.453	3.0	2.7
47.			0.14	0.276	2.0	1.8
53.8			0.28	0.251	1.5	1.3
58.2			0.56	0.367	1.3	1.1
65.3	A		1.12	0.731	1.0	1.1
36.4	B	7.7	0.07	1.7	19.0	2.7
39.			0.14	1.85	2.6	2.6
41.8			0.28	1.32	1.7	1.6
45.5			0.56	1.17	1.4	1.3
51.			1.12	1.3	1.2	1.15
59.7	A		2.25	1.75	1.1	1.1
35.2	B	15.4	0.14	3.06	5.6	6.3
37.1			0.28	2.67	2.4	2.0
39.2			0.56	1.84	1.5	1.4
42.4			1.12	1.95	1.3	1.2
47.2			2.25	2.18	1.2	1.1
55.2	A		4.5	2.54	1.1	0.9
33.7	B	30.8	0.28	3.2	3.4	1.9
34.3			0.56	2.88	1.9	1.4
35.3			1.12	2.51	1.4	1.15
37.6			2.25	2.65	1.2	0.98
42.8			4.5	2.82	1.1	0.85
48.4	B		9.0	2.83	1.1	0.74
28.7	B	61.6	0.56	8.75	2.3	1.15
30.5			1.12	2.85	1.7	0.98
30.5			2.25	2.12	1.24	0.93
32.6			4.5	2.78	1.16	0.74
34.1			9.0	2.48	1.1	0.72
35.3	B		18.0	2.5	1.05	0.63

Evaluation of the preliminary dynamic design parameters is an early task to perform in providing preliminary dynamic design information. The study of a model will aid in the evaluation of preliminary load generation by giving visibility to a practical situation. Beam sidebranch system mode shapes are investigated by varying the quantitative values of the mass and sidebranch stiffness. To reduce the analysis to a workable scope, three modal displacement ratios were selected for study. These ratios are based on:

- The x to y modal displacement of the sidebranch mass (v_{1x} , v_{1y}).
- The y to y modal displacement between the sidebranch mass and beam attachment location (v_{1y} , v_{ra}).
- The y modal displacement of the sidebranch mass to the point of maximum beam modal displacement (v_{1y} , v_{ry}).

Figure 2 shows the beam resonant frequencies and mode shapes without the sidebranch. Note that the lowest natural frequency is at 152 Hz.

The stiffness of the sidebranch spring-mass system was chosen so that (a) the fundamental

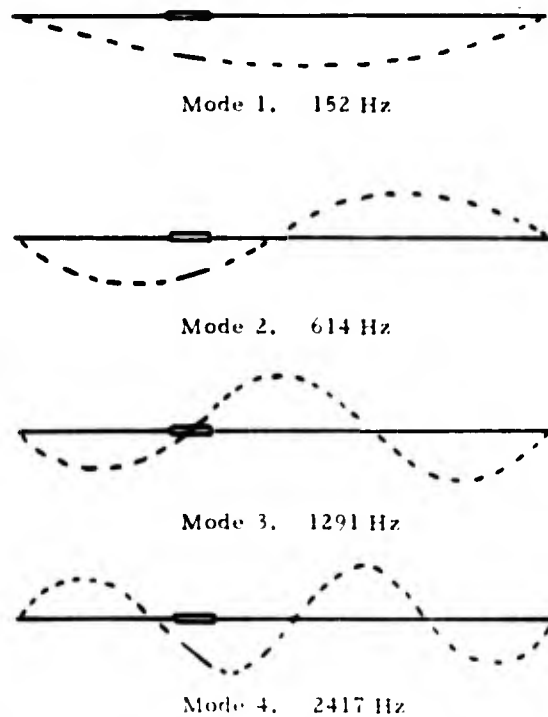


Figure 2 - Beam Without Sidebranch
Frequencies and Mode Shape

frequency of the selected sidebranch systems would be above the combined system fundamental frequency, and (b) it would allow a wide range of mass changes, while keeping the principal mode resonant frequency between 10 and 100 Hz. This allows a study of modal displacement ratios by changing the parameters of the sidebranch system.

A typical first mode shape for the combined system is shown in Figure 3. The natural frequencies ranged from 10 to 50 Hz -- considerably lower than the beam by itself. This type of mode shape resulted for all the mass and spring sidebranches studied. The mass translational and rotational deflections are in phase with the beam and thus reinforce the combined mode without reactive cancellation.



Figure 3 - System First Mode

Three general types of parametric classifications are noted from the data presented in Figure 4. The data are tabulated in Tables 1 and 2. The first can be classified as having a

low ratio of sidebranch mass to beam mass. Typically, this classification will have a ratio of less than 10 with the sidebranch support structure approaching the generalized stiffness of the beam. The modal displacement ratios are mass and stiffness dependent. Although directly related to the ratio of the sidebranch mass to the beam mass, the MDR's are more sensitive to stiffness than to mass.

The second can be classified as having a sidebranch mass greater than 10 times that of the beam and a sidebranch stiffness less than that of the beam. The MDR's are not sensitive to mass changes and are inversely related to the ratio of sidebranch to beam generalized stiffness.

The third includes any sidebranch with a stiffness greater than twice the generalized stiffness of the beam. The MDR's of this classification were not sensitive to mass or stiffness changes within practical consideration.

The second system mode is shown in Figure 5. The expected mode shape is exemplified by Type A. The sidebranch mass translational and rotational deflections are out-of-phase and oppose the beam first mode shape. The sidebranch mass reacts against the natural response of the beam and distorts the mode shape of the beam section away from a half sine wave pattern. When the relative rotational or x translational deflection of the sidebranch

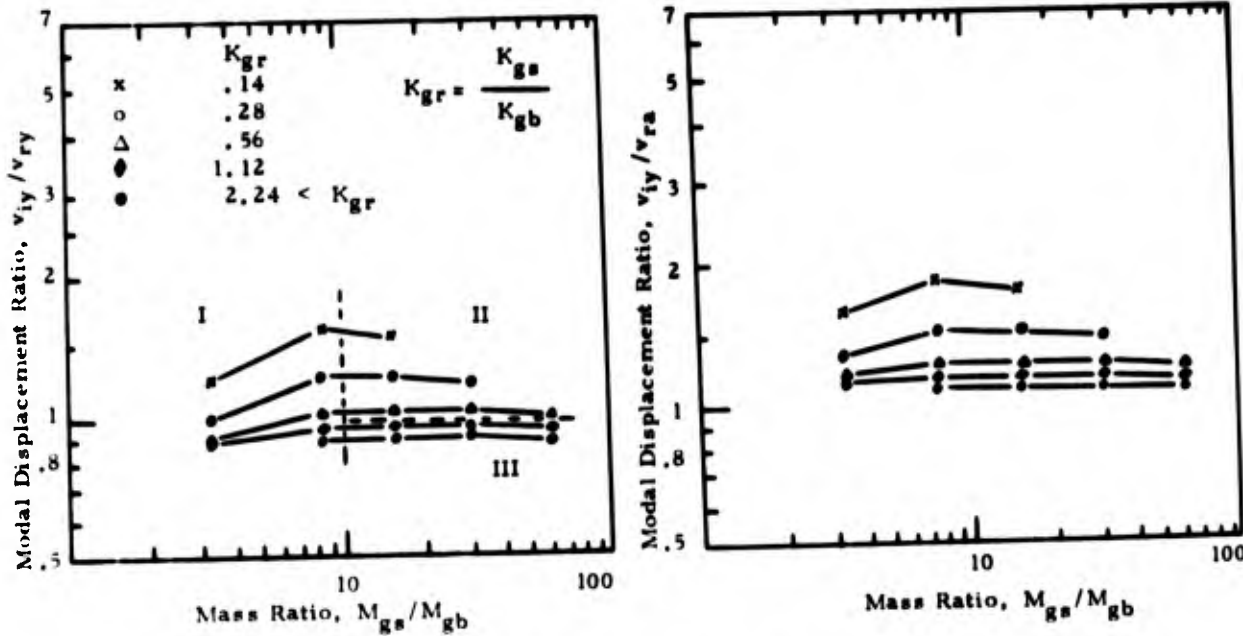


Figure 4 - Modal Displacement Ratio Versus Mass Ratio for the First Mode

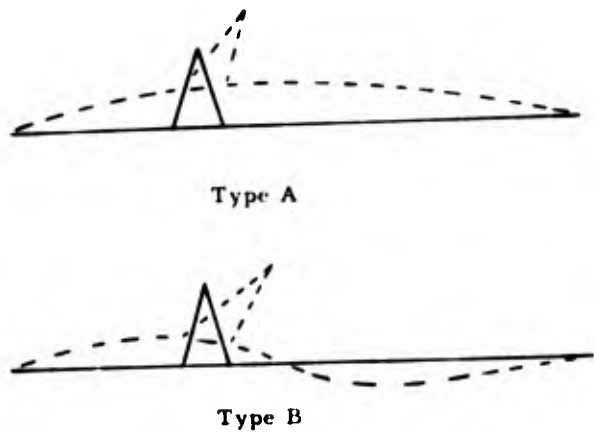


Figure 5 - Second System Mode

is large (caused by either low stiffness or high mass), the beam is forced into an apparent second mode of Type B (the data are tabulated in Table 3). In Figure 6 the translation from one mode shape to the other is in the area around the dashed line. The v_{iy} to v_{ry} ratios of the second mode are based on the maximum y eigenvector of the beam regardless of the location of that point on the beam. The v_{iy} to v_{ry} ratios exhibit two classification areas. The low mass ratio area (up to 16) is similar to classification 1 of the first mode. Our computer program instructions did not include data similar to the second classification of the first

mode. The remaining data show the trends of classifications 2 and 3.

The v_{iy}/v_{ra} ratio exhibits trends of classification 1 throughout.

The MDR's are graphed versus the normalized stiffness in Figures 7 through 10. Plotting the data in this manner clearly shows the consistency of the data to this ratio and convergence of the MDR's at the high stiffness ratios.

If environmental data are available for the vehicle shell (simulated by the beam) the environment of the mass in the y direction will be related to the shell environment as simulated by our model. Although our model has freedom in the x direction, it is my opinion that the model is unrealistic for analysis of sidebranched components in the x direction. Therefore, the only mention of x deflection is in the deflection ratio v_{ix}/v_{iy} located in Tables 1, 2 and 3.

The reader is left to his own initiative to apply the displayed data. It must be pointed out that, although many computer runs were performed, only one basic model configuration was used. A change in beam configuration or a change in the sidebranch location relative to the beam will alter the results.

A true plate model would have a greater modal density and more degrees of freedom for the equivalent number of finite elements. If the

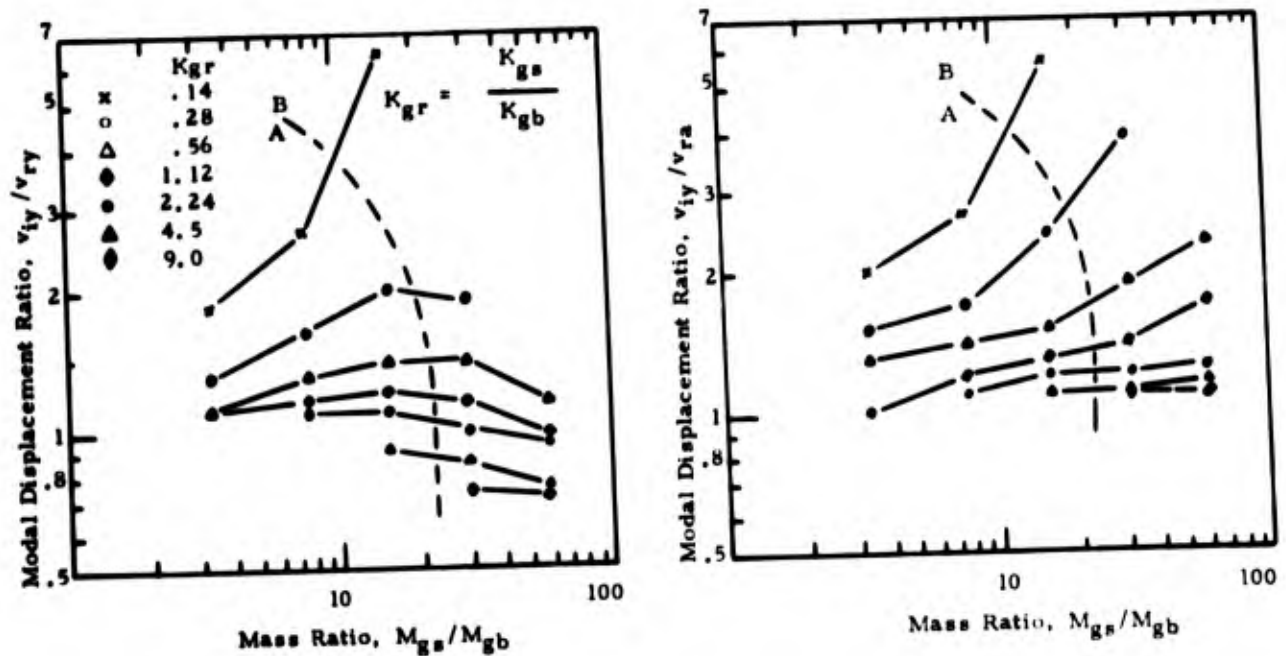


Figure 6 - Modal Displacement Ratios Versus Mass Ratios for the Second Mode

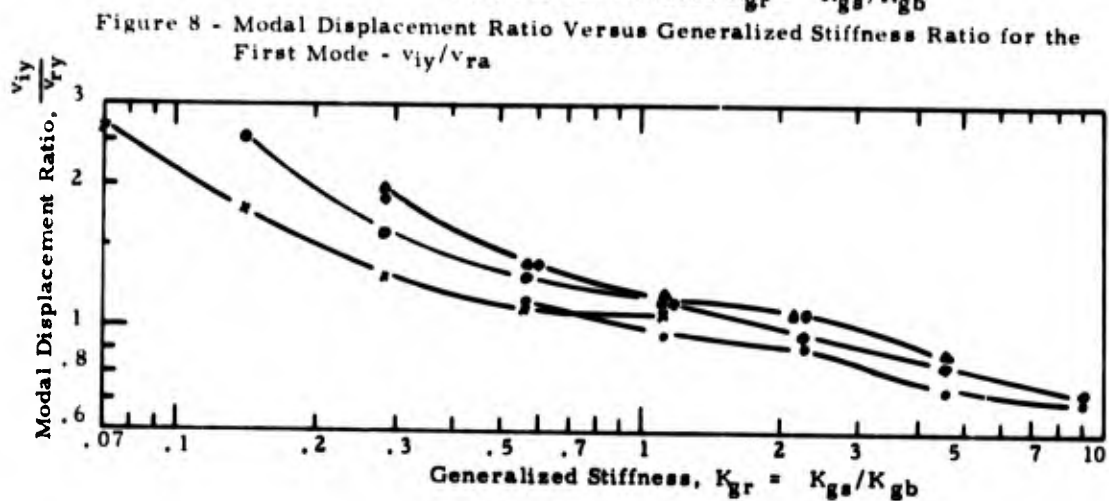
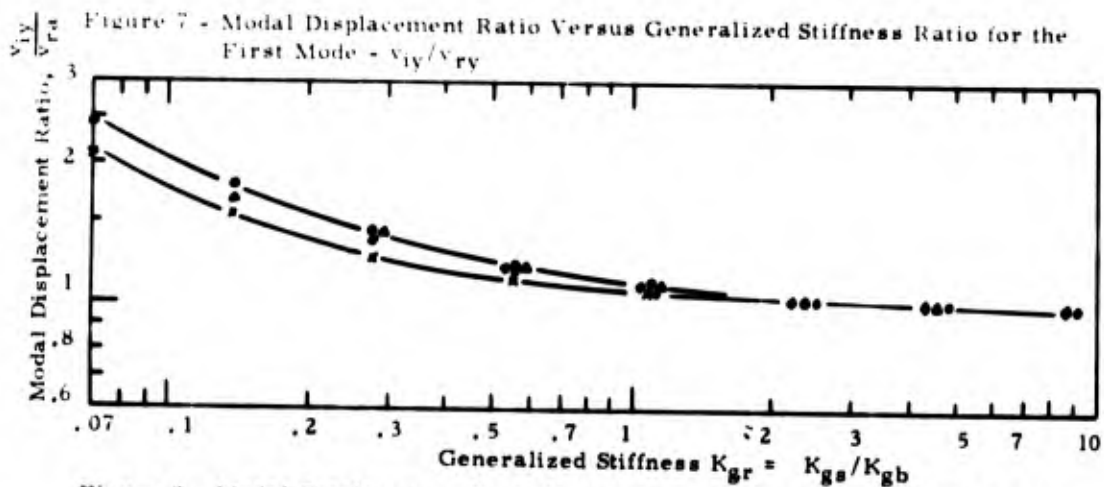
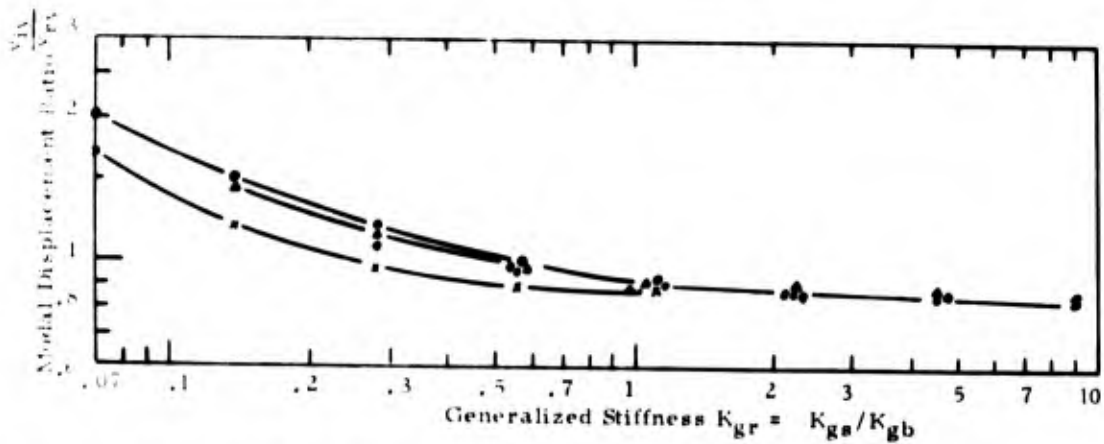


Figure 9 - Modal Displacement Ratio Versus Generalized Stiffness Ratio for the Second Mode - v_{iy}/v_{ry}

plate is considered a lattice of crossed beams, the results would be a rough equivalent of the model as used. Since only relative displacements are presented in the data, the effect of

the crossed beam lattice should be no different than the single beam within the scope of the model data as presented.

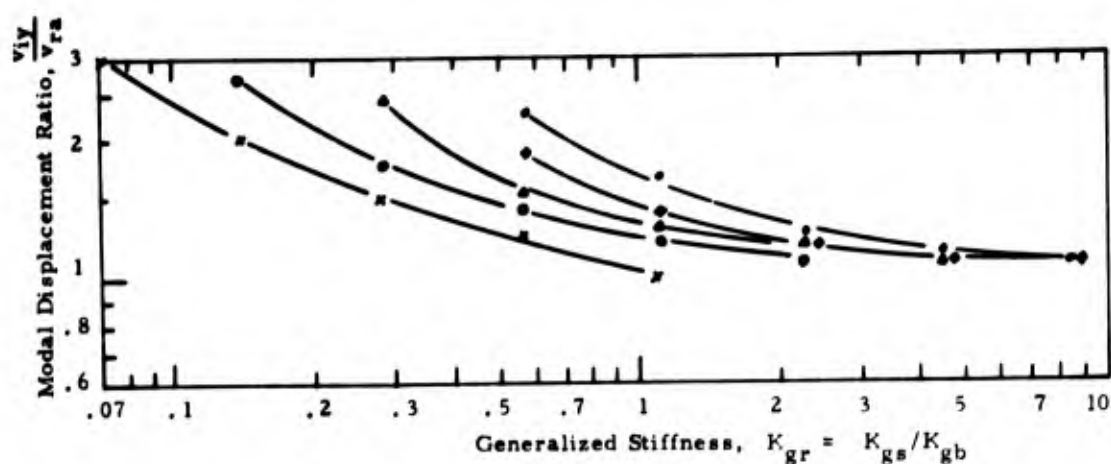


Figure 10 - Modal Displacement Ratio Versus Generalized Stiffness Ratio for the Second Mode - v_{iy}/v_{ra}

CONCLUSIONS

Three general trends should be noted:

- (1) The relative y deflection of the mass goes down with increased sidebranch stiffness until an asymptote is reached (Figures 7 through 10).
- (2) Except for very large relative side-branch masses, increasing the mass either increases the relative deflection of the mass or has little effect. Only

at the upper mass extremes of our data ensemble did increased mass decrease the relative response of the mass. Even here the negative slope is nominal.

- (3) When the mass ratio is not at the high extreme and the stiffness ratio is not at the low extreme, the MDR's are in an average range of 1 to 1.5.

BLANK PAGE

RAIL LAUNCHING DYNAMICS OF THE SAM-D SURFACE-TO-AIR MISSILE *

Martin Wohltmann, Leonard A. Van Gulick, H. Carlton Sutphin
Structure Analysis Department
Martin Marietta Corporation
Orlando, Florida

This paper describes the dynamic motions of a single-stage, surface-to-air missile launched from a container-canister. The missile and canister are each about 17 feet in length. Missile and canister diameters are 16 inches and 36 inches, respectively. The principal interface between the missile and canister is a 10 inch wide continuous rail contoured to the missile circumference. No mechanical parts, such as shoes interconnect the missile and the rails. The rocket motor provides the launching force. As the missile exits the canister, it picks up angular rate and position prior to the development of stabilizing aerodynamic forces. Requirements for the missile to fly through established target windows restrict the rate and position to be within specified magnitudes. The problem, usually called "tipoff" and "mal launch" is to determine for this particular missile the angular rate and position as it exists from the canister.

INTRODUCTION

SAM-D is being developed as a highly mobile, tactical air defense system for use by the U.S. Army in battlefield. The system is designed to provide defense against high-performance aircraft. It will be capable of engaging several targets simultaneously. A vehicle will carry several of the single-stage, solid propellant supersonic missiles in launching-shipping canisters. The missile is cradled within the canister, supported by a trough-like launch rail. Missiles are capable of being fired singly or in close-sequence salvos. The weatherproof canister provides protection for the missile from the time it is manufactured until fired.

Requirements for the missile to fly through established target windows restrict the angular rate and position of the missile as it exits the canister, to specified magnitudes. This problem, usually called "tipoff" or "mal launch" is analyzed in this paper.

Figure 1 illustrates the basic system concept. The major components are a track vehicle, launch platform, and six missile-containing canisters. Figure 2 illustrates a SAM-D launching.

Parameters that affect missile exit angular velocity and position are:

- 1 Weight and moment of inertia
- 2 Rail curvature or irregularity



Figure 1. SAM-D Basic System Concept



Figure 2. SAM-D Launch

*Work performed under contract to Raytheon Company, Lexington, Massachusetts.

- 3 Friction between rail and missile
- 4 Thrust misalignment
- 5 Missile center of gravity offset
- 6 Rail length
- 7 Rail elasticity
- 8 Canister and launcher flexibility
- 9 Winds
- 10 Backflowing asymmetric-motor exhaust pressures
- 11 Launch angle.

Two separate analyses were made taking into account several of the above parameters.

Mathematical Symbols

A,B,C,D	Coefficients
F_k	Spring force/unit length
K	radius of gyration
L	Distance from missile,c.g., to missile aft end
I	Pitch inertia
P,V,S	Refer to Figure 6 (distances)
N	Normal force
Q_1	Generalized force
R	Radius of curvature or generalized coordinate
T	Kinetic energy or thrust
W	Weight
a_0, b_0	Constants for spring properties
f_k	Friction force/unit length
d	Distance (refer to Figure 5)
g	Acceleration due to gravity
h	Height
l	Rail length
M	Mass
q_1	Generalized coordinate
r	Missile radius
t	Time
x,y	Cartesian coordinates or integration variables
q	Generalized coordinates
α	Generalized coordinate or launch angle
μ	Thrust misalignment
μ	Coefficient of friction
d/dt	Total derivative
$\partial/\partial t$	Partial derivative
.	First derivative with respect to time
..	Second derivative with respect to time

Rail Curvature Analysis

In this analysis the following assumptions were made:

- 1 The launcher and canister are both rigid;
- 2 The missile is straight and rigid;

- 3 The rail is rigid and circularly curved (0.2 inch in height per the 209 inch length).

The following factors are considered in the analysis of the effects of rail curvature:

- 1 Friction
- 2 Thrust misalignment
- 3 Canister launch angle
- 4 Planar motion
- 5 Canister length.

Figure 3 illustrates the model used to obtain the equations of motion during the early part of the launch. The two degrees-of-freedom are the coordinates ϕ and ψ . Forces included are missile weight, thrust, and friction. LaGrange equations, in the following form, are used to obtain the equations of motion:

$$\frac{d}{dt} \left(\frac{\partial T}{\partial \dot{q}_1} \right) - \frac{\partial T}{\partial q_1} = Q_1 \quad (1)$$

$$Q_1 = X \frac{\partial x}{\partial q_1} + Y \frac{\partial y}{\partial q_1} \quad (2)$$

where

T = kinetic energy
 q_1 = independent coordinates ϕ and ψ
 Q_1 = generalized forces
X,Y = X and Y components of the forces
x,y = Cartesian coordinates
t = time.

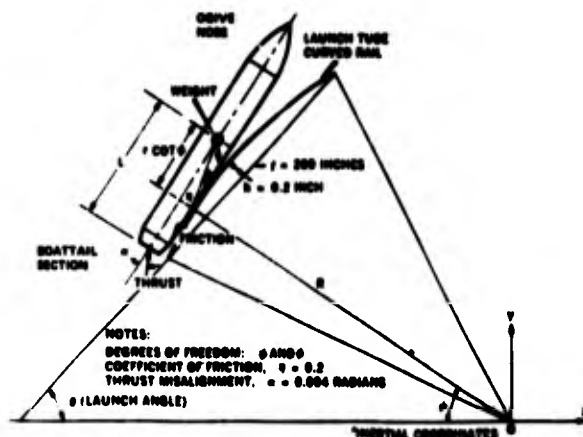


Figure 3. Dynamic Model for a Straight Missile on a Curved Rail

The missile kinetic energy is

$$T = \frac{1}{2} m (\dot{x}_{cg}^2 + \dot{y}_{cg}^2) + \frac{1}{2} I_{cg} \dot{\psi}^2 \quad (3)$$

where

m = missile mass
 I_{CG} = missile pitch inertia = 1.

By geometry (see Figure 3),

$$X_{CG} = -(R+r) \cos \psi + r \cot \phi \sin \psi \quad (4)$$

and

$$Y_{CG} = (R+r) \sin \psi + r \cot \phi \cos \psi \quad (5)$$

Differentiating equations (4) and (5) with respect to time,

$$\dot{X}_{CG} = (R+r) \dot{\psi} \sin \psi + r \dot{\psi} \cos \psi \cot \phi - r \dot{\phi} \sin \psi \csc^2 \phi \quad (6)$$

$$\dot{Y}_{CG} = (R+r) \dot{\psi} \cos \psi - r \dot{\psi} \sin \psi \cot \phi - r \dot{\phi} \cos \psi \csc^2 \phi \quad (7)$$

Squaring Equations (6) and (7), and substituting into Equation (3) and collecting terms, the system kinetic energy becomes

$$T = \frac{1}{2} m \left[(R+r)^2 \dot{\psi}^2 - 2r(R+r) \dot{\psi} \dot{\phi} \csc^2 \phi + r^2 \dot{\phi}^2 \cot^2 \phi + r^2 \dot{\phi}^2 \csc^4 \phi \right] + \frac{1}{2} I \dot{\psi}^2 \quad (8)$$

Taking the partial derivative of Equation (8) with respect to $\dot{\psi}$ and the time derivative

$$\frac{d}{dt} \left(\frac{\partial T}{\partial \dot{\psi}} \right) = \frac{1}{2} m \left[2(R+r)^2 \ddot{\psi} - 2r(R+r) \ddot{\phi} \csc^2 \phi + 4r(R+r) \dot{\phi}^2 \csc^2 \phi \cot \phi + 2r^2 \ddot{\psi} \cot^2 \phi - 4r^2 \dot{\psi} \dot{\phi} \cot \phi \csc^2 \phi \right] + I \ddot{\psi} \quad (9)$$

also

$$\frac{\partial T}{\partial \dot{\psi}} = 0 \quad (10)$$

Next, taking the partial derivative of Equation (8) with respect to $\dot{\phi}$ and the time derivative

$$\frac{d}{dt} \left(\frac{\partial T}{\partial \dot{\phi}} \right) = \frac{1}{2} m \left[-2r(R+r) \ddot{\psi} \csc^2 \phi + 4r(R+r) \dot{\psi} \dot{\phi} \csc^2 \phi \cot \phi + 2r^2 \ddot{\phi} \csc^4 \phi - 8r^2 \dot{\psi} \dot{\phi}^2 \csc^4 \phi \cot \phi \right] \quad (11)$$

and next, taking the partial derivative of Equation (10) with respect to ϕ :

$$\frac{1}{I} = \frac{1}{2} r \left[4r(R+r) \dot{\psi}^2 \csc^2 \phi \cot \phi - 2r^2 \dot{\phi}^2 \csc^2 \phi \cot \phi - 4r^2 \dot{\psi}^2 \csc^4 \phi \cot \phi \right] \quad (12)$$

Equations (9), (10), (11), and (12) provide the LHS of the LaGrange Equation (1).

Thrust Force

The generalized force due to thrust, including misalignment, is determined as follows. Rewriting Equation (2),

$$Q_{x,T} = X_T \frac{\partial X}{\partial x} + Y_T \frac{\partial Y}{\partial x} \quad (13)$$

$$Q_{y,T} = X_T \frac{\partial X}{\partial y} + Y_T \frac{\partial Y}{\partial y}$$

The x and y components of thrust are (refer to Figure 3):

$$X_T = T \sin (\psi - \alpha) = T (\sin \psi \cos \alpha - \cos \psi \sin \alpha) \quad (14)$$

$$Y_T = T \cos (\psi - \alpha) = T (\cos \psi \cos \alpha + \sin \psi \sin \alpha) \quad (15)$$

Again, referring to Figure 3, the x and y displacements at the point of thrust application are

$$x = x_{CG} - L \sin \psi = -(R+r) \cos \psi + r \cot \phi \sin \psi - L \sin \psi \quad (16)$$

$$y = y_{CG} - L \cos \psi = (R+r) \sin \psi + r \cot \phi \cos \psi - L \cos \psi \quad (17)$$

Taking the partial derivatives of Equations (16) and (17) with respect to the coordinates ϕ and ψ , and substituting these together with Equations (14), and (15) into Equation (13) provides the thrust generalized forces:

$$Q_{\psi,T} = T (R+r) \cos \alpha - T (r \cot \phi - L) \sin \alpha \quad (18)$$

$$Q_{\phi,T} = -Tr \csc^2 \phi \cos \alpha \quad (19)$$

Weight Force

The generalized force due to the missile weight is determined as follows. The x component of the weight is zero and the y component is

$$Y_w = -mg \quad (20)$$

The cg displacements are given by Equations (4) and (5) and the partial derivatives of these

x and y displacements with respect to the coordinates r and ψ ; when substituted together with Equation (20) into Equation (2), provides the generalized force due to the missile weight

$$Q_{r,W} = -mg [(R+r) \cos \psi - r \sin \psi \cot \psi] \quad (21)$$

and

$$Q_{\psi,W} = mgr \cos \psi \csc^2 \psi. \quad (22)$$

Friction Force

Similarly, for friction, the generalized force components are determined as follows:

$$X_F = -F \sin \psi \quad Y_F = -F \cos \psi. \quad (23)$$

The coordinates of the point of contact are

$$x = -R \cos \psi \quad y = R \sin \psi \quad (24)$$

$$\frac{\partial x}{\partial \psi} = R \sin \psi \quad \frac{\partial y}{\partial \psi} = R \cos \psi. \quad (25)$$

Then

$$Q_{\psi, \text{Friction}} = -F \sin \psi (R \sin \psi) - F \cos \psi (R \cos \psi) \quad (26)$$

$$Q_{\psi, \text{Friction}} = -FR. \quad (27)$$

With $F = \mu N$ where μ is the coefficient of friction and N is the normal force:

$$Q_{\psi, \text{Friction}} = \mu RN. \quad (28)$$

For preliminary analysis, the normal force N is taken to be the weight component perpendicular to the rail surface:

$$N \approx mg \cos \theta. \quad (29)$$

Thus the ψ generalized force is

$$Q_{\psi, \text{Friction}} = -\mu mg R \cos \theta. \quad (30)$$

With the aid of Figure 4, a friction generalized force is developed in the ϕ coordinate.

$$x = r \cot \phi \sin \psi \quad y = r \cot \phi \cos \psi \quad (31)$$

$$\frac{\partial x}{\partial \phi} = -r \csc^2 \phi \sin \psi \quad \frac{\partial y}{\partial \phi} = -r \csc^2 \phi \cos \psi. \quad (32)$$

With the use of Equations (23), (28) and (29), the friction generalized force in the ϕ direction becomes

$$Q_{\phi, \text{Friction}} = \mu mgr \csc^2 \phi \cos \theta. \quad (33)$$

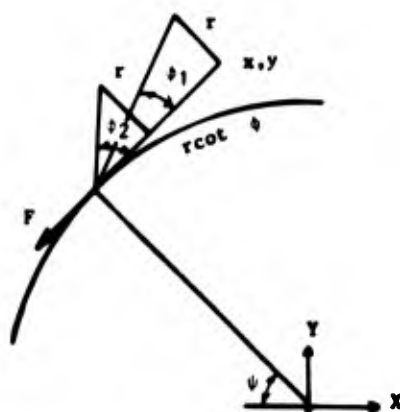


Figure 4. Friction as a Function of Coordinate ϕ

Equations of Motion

Combining Equations (9), (10), (11), (12), (18), (19), (21), (22), (27), and (33), the equations of motion become after dividing the ψ equations by $m(R+r)^2$ and defining $I = mK^2$ where K = missile radius of gyration, the final form of the ψ equation becomes

$$\begin{aligned} & \left[1 + \left(\frac{r}{R+r} \right)^2 \cot^2 \phi + \left(\frac{K}{R+r} \right)^2 \right] \ddot{\psi} \\ & - \left[\left(\frac{r}{R+r} \right) \csc^2 \phi \right] \dot{\psi}^2 = \frac{T/m}{(R+r)} \cos \alpha \\ & - \frac{T/m}{(R+r)^2} (r \cot \phi - L) \sin \alpha - \frac{g}{(R+r)} \cos \psi \\ & + \frac{g r}{(R+r)^2} \sin \psi \cot \phi - \frac{\mu g r}{(R+r)^2} \cos \theta \\ & - 2 \left(\frac{r}{R+r} \right) \dot{\phi}^2 \csc^2 \phi \cot \phi \\ & + 2 \left(\frac{r}{R+r} \right)^2 \dot{\psi} \dot{\phi} \csc^2 \phi \cot \phi \end{aligned} \quad (34)$$

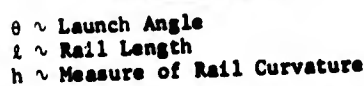
and after dividing the ϕ equation by $m r^2 \csc^4 \phi$ and rearranging, the final form of the ϕ equation becomes

$$\begin{aligned} & \left[- \left(\frac{R+r}{r} \right) \sin^2 \phi \right] \ddot{\phi} + \dot{\phi}^2 = - \frac{T}{m r} \sin^2 \phi \cos \alpha \\ & + \frac{g}{r} \sin^2 \phi \sin \psi + \frac{\mu g}{r} \sin^2 \phi \cos \theta \\ & + 2 \dot{\phi}^2 \cot \phi - \dot{\psi}^2 \sin^2 \phi \cot \phi. \end{aligned} \quad (35)$$

Equations (34) and (35) may be written simply as:

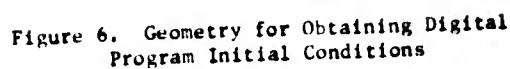
$$\begin{aligned} A \ddot{\psi} + B \dot{\psi} &= F_1(\phi, \psi, \dot{\phi}, \dot{\psi}), \\ C \ddot{\phi} + D \dot{\phi} &= F_2(\phi, \psi, \dot{\phi}, \dot{\psi}). \end{aligned} \quad (36)$$

Figure 5 illustrates the geometry necessary to compute the rail radius of curvature. The geometrical relations are:

$$L = 2 \sqrt{R^2 - d^2} \text{ and } d = R - h. \quad (37)$$
$$R = \frac{\ell^2}{8h} + \frac{h}{2}. \quad (38)$$
$$\Psi_T = \frac{2}{R} \quad (39)$$


Referring to Figure 6, Ψ_1 is determined from

$$\psi_1 \approx 90^\circ - \theta \quad (40)$$

$$\phi_1 = \psi_1 + \psi_2 = \psi_1 \quad (41)$$
$$S = \frac{r}{\tan \phi} = \frac{r}{\tan (\psi_1 + \psi_2)} \quad (42)$$

$$P = V - S = V - \frac{r}{\tan(\psi_1 + \psi_2)} \quad (43)$$
$$P = RY_2^* \quad (44)$$
$$V = \frac{r}{\tan(\psi_1 + \psi_2)} = R\psi_2 \quad (45)$$
$$\tan (\psi_1 + \psi_2) = \frac{\tan \psi_1 + \tan \psi_2}{1 - \tan \psi_1 \tan \psi_2} \quad (46)$$
$$\psi_2 = \frac{V \tan \psi_1 - r}{(R-r) \tan_1 - V} \quad (47)$$

The equations of motion (34) and (35) are valid only while the contact point between

the missile and the rail is: 1) between the rail ends, and 2) between the boattail and ogive sections of the missile.

These conditions are met only if the following stopping conditions are not exceeded. Referring to Figure 6, if

$$\dot{\psi} = \dot{\psi}_1 + \dot{\psi}_2$$

and

$$\dot{\psi} < 0.0,$$

the equations are not valid. Also referring to Figure 7 if

$$\dot{\psi} < \tan^{-1} \frac{r}{V}$$

and $\dot{\psi} < 0.0$, the equations are not valid. The missile is tipping backwards on boattail. Similarly, as shown in Figure 8:

$$\text{if } \dot{\psi} > 180^\circ - \tan^{-1} \frac{r}{V}$$

and $\dot{\psi} < 0.0$, the equations are not valid. The missile is tipping forward on the ogive section.

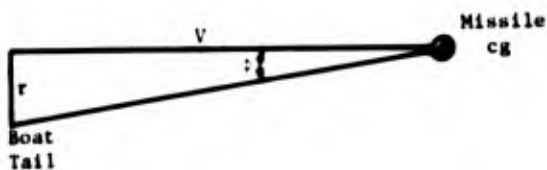


Figure 7. Constraint on Coordinate ψ , Missile Tipping Backwards

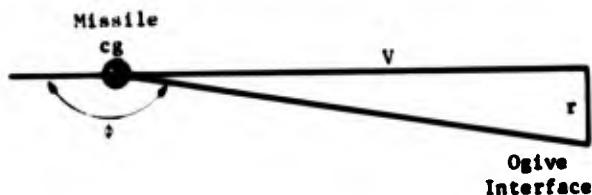


Figure 8. Constraint on Coordinate ψ , Missile Tipping Forwards

Once the ψ stopping conditions are exceeded, the equations of motion change. The new equations are called Gravity Tipoff equations.

Gravity Tipoff Analysis

Figure 9 illustrates the dynamic model. The two degrees-of-freedom are taken to be R and θ . By geometry, the cg displacements in the Cartesian coordinate system are

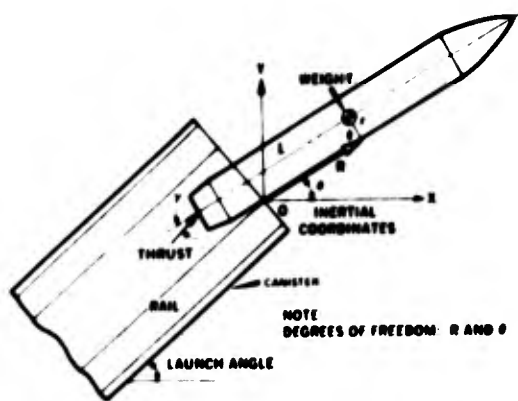


Figure 9. Dynamic Model for Gravity Tip-Off

$$x_{cg} = x = R \cos \theta + r \sin \theta \quad (48)$$

$$y_{cg} = y = R \sin \theta + r \cos \theta. \quad (49)$$

Differentiating Equations (48) and (49) with respect to time, and squaring the results and substituting into the system kinetic energy

$$T = 1/2m (\dot{x}^2 + \dot{y}^2) + 1/2I_{cg} \dot{\theta}^2, \quad (50)$$

the kinetic energy becomes

$$T = 1/2m [\dot{R}^2 - 2R\dot{R}\dot{\theta} + r^2\dot{\theta}^2 + R^2\dot{\theta}^2] + 1/2I_{cg} \dot{\theta}^2. \quad (51)$$

Taking the partial derivative of Equation (51) with respect to \dot{R} and $\dot{\theta}$ and taking the time derivatives

$$\frac{d}{dt} \left(\frac{\partial T}{\partial \dot{R}} \right) = m\ddot{R} - m\dot{R}\ddot{\theta} \quad (52)$$

$$\frac{d}{dt} \left(\frac{\partial T}{\partial \dot{\theta}} \right) = -mR\ddot{R} + mR^2\ddot{\theta} + mR^2\dot{\theta}^2 + 2mR\dot{R}\dot{\theta} + I_{cg}\ddot{\theta}. \quad (53)$$

Taking the partial derivative of Equation (51) with respect to the coordinates θ and R , and substituting together with Equations (52), (53), into Equation (1), the LHS of LaGrange equations become

$$\frac{d}{dt} \left(\frac{\partial T}{\partial \dot{R}} \right) - \frac{\partial T}{\partial R} = m\ddot{R} - m\dot{R}\ddot{\theta} - mR\dot{\theta}^2 \quad (54)$$

$$\frac{d}{dt} \left(\frac{\partial T}{\partial \dot{\theta}} \right) - \frac{\partial T}{\partial \theta} = -mR\ddot{R} + m(R^2 + R^2)\ddot{\theta} + 2mR\dot{R}\dot{\theta} + I_{cg}\ddot{\theta}. \quad (55)$$

The generalized force due to the missile weight is determined as follows:

$$X_W = 0 \quad Y_W = -mg \quad (56)$$

and taking the partial derivatives of the x_{cg} and y_{cg} coordinates in Equation (48) and (49) with respect to R and θ and making use of Equation (2),

$$Q_{R_W} = -mg \sin \theta \quad (57)$$

$$Q_{\theta_W} = -mg R \cos \theta + mgr \sin \theta. \quad (58)$$

The generalized force due to the thrust force is determined as shown in the following analysis. The location of the thrust application point is:

$$\begin{aligned} x_T &= x_{cg} - L \cos \theta = R \cos \theta - r \sin \theta \\ &\quad - L \cos \theta \end{aligned} \quad (59)$$

$$\begin{aligned} y_T &= y_{cg} - L \sin \theta = R \sin \theta + r \cos \theta \\ &\quad - L \sin \theta. \end{aligned} \quad (60)$$

The components of the thrust are

$$X_T = T \cos (\theta + \gamma) \quad (61)$$

$$Y_T = T \sin (\theta + \gamma). \quad (62)$$

Taking the partial derivatives of Equations (59) and (60) with respect to the coordinates R and θ , The generalized thrust force is

$$Q_{R_T} = T \cos \gamma \quad (63)$$

and

$$Q_{\theta_T} = T(R - L) \sin \gamma - Tr \cos \gamma. \quad (64)$$

Making use of Equations (54), (55), (57), (58), (63), and (64); the equations of motion become

$$\begin{aligned} \ddot{R} - r \ddot{\theta} &= -g \sin \theta + \frac{T}{m} \cos \gamma + mR\dot{\theta}^2 \quad (65) \\ -r\ddot{R} + (K^2 + R^2 + r^2) \ddot{\theta} &= -gR \cos \theta + gr \sin \theta \\ &\quad + \frac{T}{m} (R - L) \sin \gamma - \frac{Tr}{m} \cos \gamma - 2R\dot{R}\dot{\theta} \end{aligned} \quad (66)$$

where

$$K^2 = \frac{I_{cg}}{m}.$$

Equations (65) and (66) were solved using the digital computer. The initial conditions for these equations were determined from the end condition results of the rail curvature equations.

This completes the rail curvature analysis results are presented at the end of the paper

Rail Elasticity Analysis

The previous dynamic analysis to determine the tipoff rate as the SAM-D missile exits

from the heavywall canister did not include any elastic effects. This analysis determines the effect of rail elasticity only, on tipoff rate. Figure 10 illustrates the dynamic model. Principal elasticity is in the rubber pad which overlays the bottom foam rail.

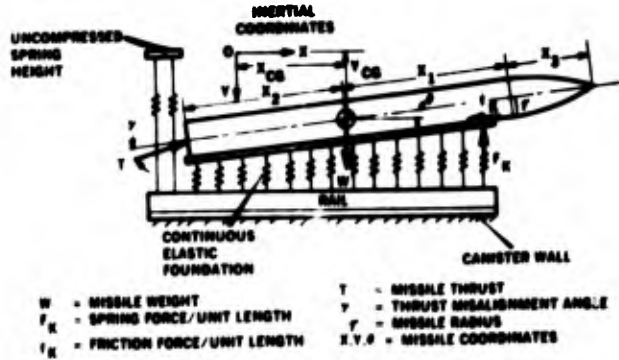


Figure 10. Dynamic Model for Elastic Rail

The equations of motion are (assuming θ and α are small):

$$\Sigma F_x = T - \int_{-x_2}^{x_1} f_k dx = m\ddot{x}_{cg} \quad (67)$$

$$\Sigma F_y = -T(\theta + \alpha) + W - \int_{-x_2}^{x_1} F_k dx = m\ddot{y}_{cg} \quad (68)$$

$$\begin{aligned} \Sigma M_{cg} &= -Tx_2\alpha - \int_{-x_2}^{x_1} rf_k dx \\ &\quad + \int_{-x_2}^{x_1} x F_k dx = I_{cg} \ddot{\theta} \end{aligned} \quad (69)$$

where

- T = missile thrust
- f_k = friction force/unit length
- m = missile mass
- x_{cg}, y_{cg}, θ = missile position coordinates
- α = thrust misalignment angle
- W = missile weight
- F_k = spring force/unit length
- r = missile radius
- x = integration variable
- x_1, x_2 = integration limits
- I_{cg} = missile pitching inertia
- M_{cg} = pitching moment about cg.

The spring force per unit length F_k was determined through the use of the experimental data shown in Figure 11. A quadratic curve was fit through the data of the form

$$F_k = a_0 y + b_0 y^2. \quad (70)$$

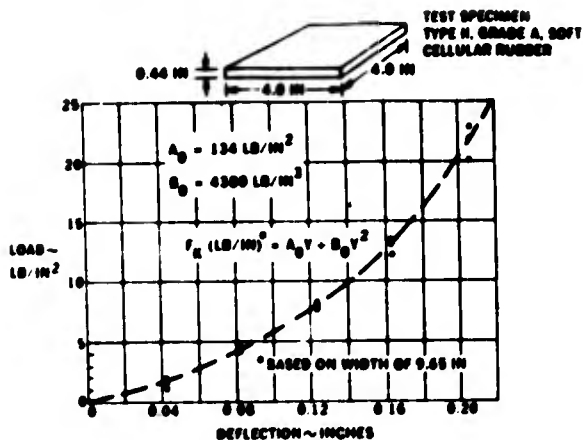


Figure 11. Load Deflection Characteristic of Rail Rubber Pad

The total normal spring force is

$$-\int_{-x_2}^{x_1} F_k dx \quad (71)$$

and with the deflection $y = f(x)$ i.e.,

$$y = y_{cg} - x\theta = y_o - x\theta \quad (72)$$

$$-\int_{-x_2}^{x_1} \left\{ a_o [y_o - x\theta] + b_o [y_o - x\theta]^2 \right\} dx. \quad (73)$$

Expanding Equation (73), and integrating, the total spring force becomes

$$-\int_{-x_2}^{x_1} F_k dx = -(a_o y_o + b_o y_o^2) (x_1 + x_2) + (a_o + 2b_o y_o) \theta \left(\frac{x_1^2 - x_2^2}{2} \right) - (b_o \theta^2) \frac{x_1^3 + x_2^3}{3}. \quad (74)$$

The total friction force is

$$\int_{-x_2}^{x_1} f_k dx = \int_{-x_2}^{x_1} \mu F_k dx \text{ where } \mu = \text{coefficient of friction} \quad (75)$$

or

$$\left(\int_{-x_2}^{x_1} f_k dx = -\mu (a_o y_o + b_o y_o^2) (x_1 + x_2) + \mu (a_o + 2b_o y_o) \theta \left(\frac{x_1^2 - x_2^2}{2} \right) - \mu b_o \theta^2 \left(\frac{x_1^3 + x_2^3}{3} \right) \right). \quad (76)$$

The moment due to friction is

$$\int_{-x_2}^{x_1} r f_k dx = -r\mu (a_o y_o + b_o y_o^2) (x_1 + x_2) + r\mu (a_o + 2b_o y_o) \theta \left(\frac{x_1^2 - x_2^2}{2} \right) - r\mu b_o \theta^2 \left(\frac{x_1^3 + x_2^3}{3} \right). \quad (77)$$

The moment due to spring force is determined as follows:

$$\int_{-x_2}^{x_1} F_k x dx = \int_{-x_2}^{x_1} (a_o y_o + b_o y_o^2) x dx - \int_{-x_2}^{x_1} \theta (a_o + 2b_o y_o) x^2 dx + \int_{-x_2}^{x_1} b_o \theta^2 x^3 dx. \quad (78)$$

Integrating Equation (78),

$$\int_{-x_2}^{x_1} F_k x dx = (a_o y_o + b_o y_o^2) \left(\frac{x_1^2 - x_2^2}{2} \right) - (a_o + 2b_o y_o) \theta \left(\frac{x_1^3 - x_2^3}{3} \right) + b_o \theta^2 \left(\frac{x_1^4 - x_2^4}{4} \right). \quad (79)$$

Substituting Equations (74), (76), (77), and (79) into Equations (67), (68), and (69), the equations of motion become

$$\ddot{x}_{cg} = \frac{T}{m} - \frac{\mu}{m} (a_o y_o + b_o y_o^2) (x_1 + x_2) + \frac{\mu}{m} (a_o + 2b_o y_o) \theta \left(\frac{x_1^2 - x_2^2}{2} \right) - \frac{\mu}{m} b_o \theta^2 \left(\frac{x_1^3 + x_2^3}{3} \right) \quad (80)$$

$$\ddot{y}_{cg} = \ddot{y}_o = -\frac{T}{m} (\alpha + \theta) + \frac{W}{m} - \frac{1}{m} (a_o y_o + b_o y_o^2) (x_1 + x_2) + \frac{1}{m} (a_o + 2b_o y_o) \theta \left(\frac{x_1^2 - x_2^2}{2} \right) - \frac{b_o}{m} \theta^2 \left(\frac{x_1^3 + x_2^3}{3} \right) \quad (81)$$

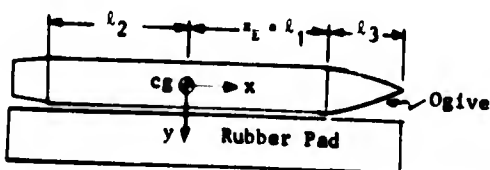
$$\ddot{\theta} = -\frac{T}{I_{cg}} x_2 \alpha - \frac{r\mu}{I_{cg}} (a_o y_o + b_o y_o^2) (x_1 + x_2) + \frac{r\mu}{I_{cg}} (a_o + 2b_o y_o) \theta \left(\frac{x_1^2 - x_2^2}{2} \right) - \frac{r\mu}{I_{cg}} b_o \theta^2 \left(\frac{x_1^3 + x_2^3}{3} \right) + \frac{1}{I_{cg}} (a_o y_o + b_o y_o^2) \left(\frac{x_1^2 - x_2^2}{2} \right) - \frac{1}{I_{cg}} (a_o + 2b_o y_o) \theta \left(\frac{x_1^3 + x_2^3}{3} \right) + \frac{b_o}{I_{cg}} \theta^2 \left(\frac{x_1^4 - x_2^4}{4} \right) \quad (82)$$

The integration limits x_1 and x_2 must be determined within the constraints imposed.

The term x_E is defined as equal to the distance from the cg to the ogive-cylinder interface or as the distance from the cg to the rail front end; the shorter distance is used. When

$$x_{cg} \leq l_3$$

$$x_E = l_1$$



When

$$x_{cg} > l_3$$

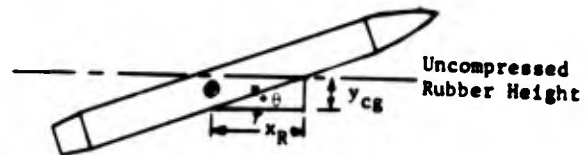
$$x_E = l_1 - (x_{cg} - l_3)$$



Note that when the cg passes the end of the rail, x_E becomes negative.

It is possible for the missile vertical displacement and rotation to be such that a portion of the rubber under the missile is undeformed.

If the rotation is counterclockwise and θ positive, this can occur forward of the missile cg only.



For $\theta > 0.0$

$$x_R = y_{cg} \cot \theta.$$

The integration limit, x_1 , is equal to the lesser of x_R or x_E and x_2 is equal to l_2 .

If $x_R \leq x_E$

$$x_1 = x_R$$

$$x_2 = l_2.$$

If $x_R > x_E$

$$x_1 = x_E$$

$$x_2 = l_2.$$

If the rotation is clockwise and θ negative, it can only occur aft of the cg.



For $\theta < 0.0$

$$x_A = -y_{cg} \cot \theta.$$

The integration limits, x_1 and x_2 , are found as follows:

$$\begin{aligned} \text{If } x_A &= i_2 \\ x_2 &= x_A \\ x_1 &= x_E \end{aligned}$$

$$\begin{aligned} \text{If } x_A &= i_2 \\ x_2 &= i_2 \\ x_1 &= x_E \end{aligned}$$

The equations of motion and the logic constraints were programmed for solution using the CDC 6400 digital computer.

Results and Conclusions

Typical time histories of the angular position and rate of the SAM-D missile during exit, as obtained from the "rail curvature analysis" are presented in Figures 12 and 13. Classification prevents actual values being assigned to the time ordinates. The oscillation of the position and rate is due to the missile rocking as a pendulum on the curved rail surface. About 70 percent of the total tipoff rate is obtained after the missile center of gravity passes the rail end. This portion of the launch process is called "gravity tipoff." Figure 14 presents time histories of the angular rate of the missile as obtained from the "rail elasticity analysis." The oscillation appearing here is due to a rocking motion of the missile on a rubber pad located between the missile surface and the launch rail.

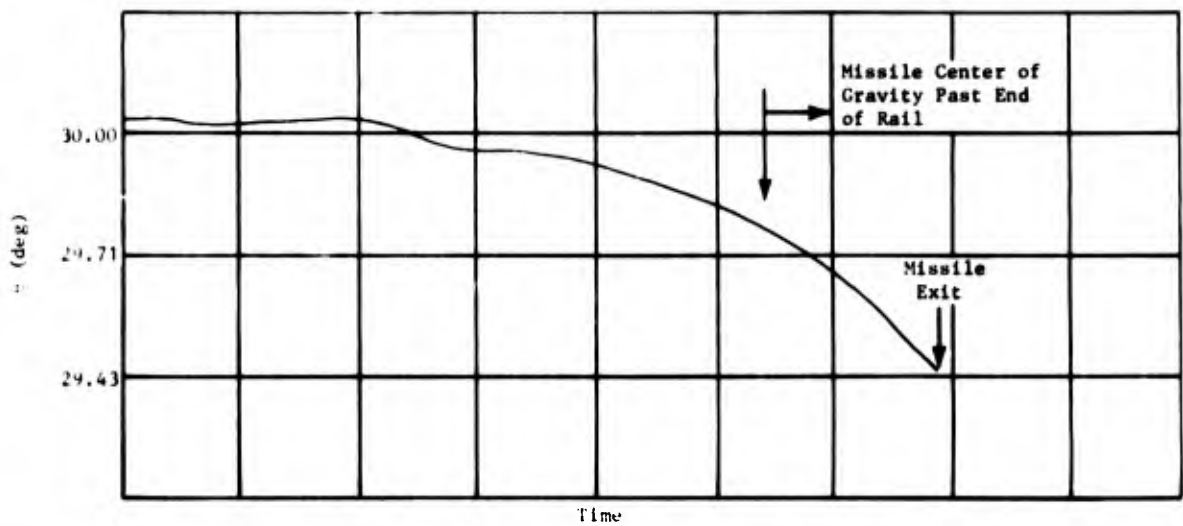


Figure 12. Missile Attitude versus Time

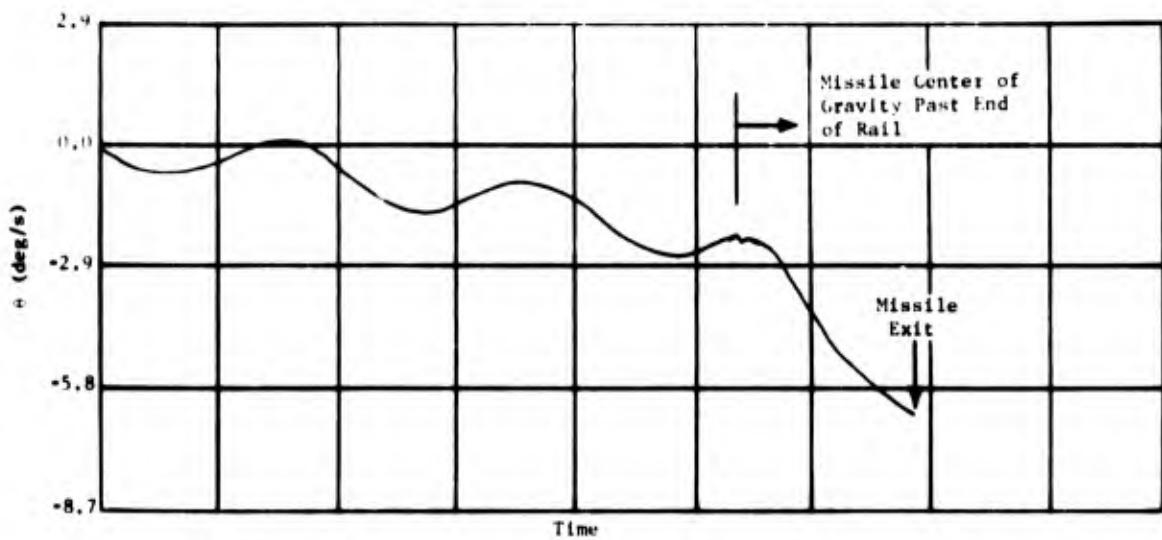


Figure 13. Missile Pitch Rate versus Time

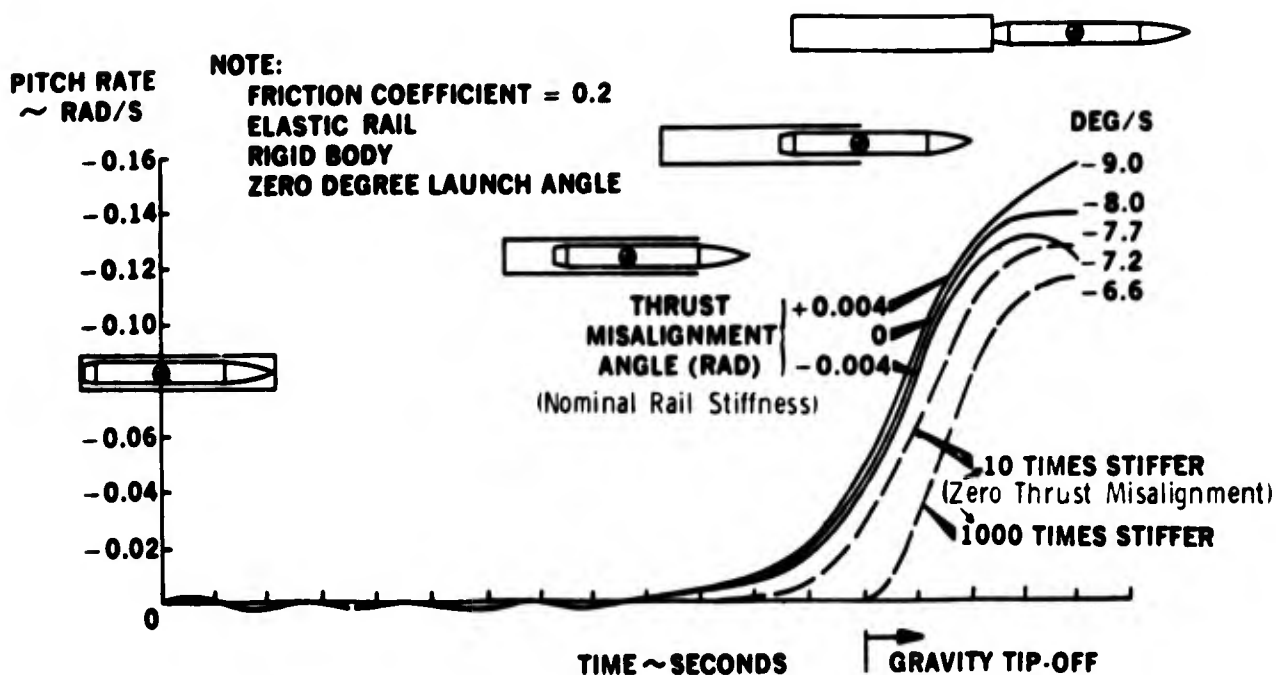


Figure 14. Exit Tip-Off Rate

Table I summarizes the effects of various parameters in the analysis on the missile tipoff rate and positions.

The conclusions reached are as follows:

- 1 Tipoff rate increases with decrease in launch angle, ranging from -6.6 deg/s at a zero degree launch angle to -3.4 deg/s at a 60 degree launch angle.
- 2 Rail curvature increases the position and rate values by 0.4 deg and 1.1 deg/s.
- 3 Thrust misalignment plus cg offset produces changes in the rate and position values of ± 0.13 deg.
- 4 Friction has a negligible effect on rate and position. This is due to thrust forces being much larger than friction forces.

- 5 A decrease in rail length by about 20 percent increases the position and rate values by 0.08 deg and 0.6 deg/s.
- 6 Rail elasticity increases rate by 1.4 deg/s.

Summary

The largest single factor in the analysis of tipoff rate and position is produced during the "gravity tipoff" portion of the launch process. For the SAM-D missile it amounts to about six degrees/second for the 30 degree launch angle. All other factors such as rail curvature, rail elasticity, friction, thrust misalignment, and rail length cause relatively small perturbations in the total tipoff rate and position. The change in missile angular position during launch is not more than 1.0 degree.

TABLE 1. Effects of Various Parameters on Missile Tipoff Rate

Parameter	Exit Angular Position (deg)	Exit Angular Rate (deg/s)	Remarks
Launch angle 30°	-	-6.6	Nominal results
45°	-0.27	-5.7	
60°	-0.20	-3.4	
Rail curvature	0.4	1.1	Curvature of 0.2 inch in 209 inch length
Thrust misalignment plug cg offset	0.13	0.7	Combined effects equivalent to misalignment angle of 0.004 radians
Friction	±0.0	±0.0	$r = 0.0 \rightarrow 0.2$ thrust forces much larger than friction forces
Rail length	0.08	0.6	20 percent decrease in length
Rail elasticity	-	1.4	

DISCUSSION

Mr. Lipeles (Littleton Research and Engineering Corporation): In the testing did you make measurements and verify the tipoff angles and rates?

Mr. Van Gulick: Yes, we did make measurements and while they were within acceptable limits, they were higher than we had predicted. We redid our analysis and found that there was a contribution due to the rigid body motion of the canister, and when we included this we were able to match the measured rates much better.

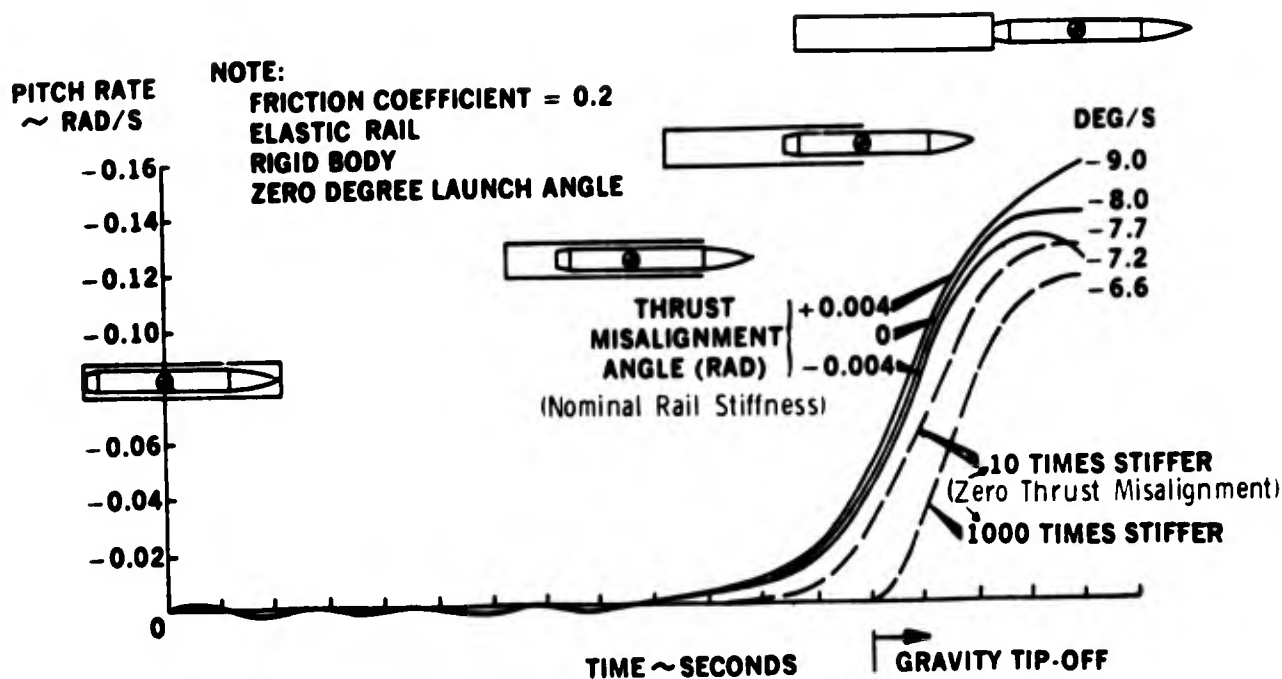


Figure 14. Exit Tip-Off Rate

Table I summarizes the effects of various parameters in the analysis on the missile tipoff rate and positions.

The conclusions reached are as follows:

- 1 Tipoff rate increases with decrease in launch angle, ranging from -6.6 deg/s at a zero degree launch angle to -3.4 deg/s at a 60 degree launch angle.
- 2 Rail curvature increases the position and rate values by 0.4 deg and 1.1 deg/s.
- 3 Thrust misalignment plus cg offset produces changes in the rate and position values of ± 0.13 deg.
- 4 Friction has a negligible effect on rate and position. This is due to thrust forces being much larger than friction forces.

- 5 A decrease in rail length by about 20 percent increases the position and rate values by 0.08 deg and 0.6 deg/s.
- 6 Rail elasticity increases rate by 1.4 deg/s.

Summary

The largest single factor in the analysis of tipoff rate and position is produced during the "gravity tipoff" portion of the launch process. For the SAM-D missile it amounts to about six degrees/second for the 30 degree launch angle. All other factors such as rail curvature, rail elasticity, friction, thrust misalignment, and rail length cause relatively small perturbations in the total tipoff rate and position. The change in missile angular position during launch is not more than 1.0 degree.

TABLE 1. Effects of Various Parameters on Missile Tipoff Rate

Parameter	Exit Angular Position (deg)	Exit Angular Rate (deg/s)	Remarks
Launch angle	-	-6.6	Nominal results
30	-0.27	-5.7	
60	-0.20	-3.4	
Rail curvature	0.4	1.1	Curvature of 0.2 inch in 209 inch length
Thrust misalignment plug cg offset	0.13	0.7	Combined effects equivalent to misalignment angle of 0.004 radians
Friction	±0.0	±0.0	$\mu = 0.0 \pm 0.2$ thrust forces much larger than friction forces
Rail length	0.08	0.6	20 percent decrease in length
Rail elasticity	-	1.4	

DISCUSSION

Mr. Lipeles (Littleton Research and Engineering Corporation): In the testing did you make measurements and verify the tipoff angles and rates?

Mr. Van Gulick: Yes, we did make measurements and while they were within acceptable limits, they were higher than we had predicted. We redid our analysis and found that there was a contribution due to the rigid body motion of the cannister, and when we included this we were able to match the measured rates much better.